

DISS. ETH No. 24283

**Fundamentals of
Carbon Fibre Reinforced Polymer (CFRP)
Machining**

A thesis submitted to attain the degree of
DOCTOR OF SCIENCES of ETH ZURICH
(Dr. sc. ETH Zurich)

presented by

Robert Fabian Voß

M.Sc. RWTH Aachen

born on 04.08.1986 in Paderborn
citizen of Germany

accepted on the recommendation of:

Prof. Dr.-Ing. Konrad Wegener, examiner

Prof. Dipl.-Ing. Dr. techn. Friedrich Bleicher, co-examiner

2017

Preamble

The research reported in this doctoral thesis has been generated at the Institute of Machine Tools and Manufacturing (IWF) affiliated to the Swiss Federal Institute of Technology (ETH) in Zurich. During this time I worked on the optimisation of drilling, orbital drilling and countersinking tools for the preparation of riveted joint connections in carbon fibre reinforced polymer (CFRP) for the aerospace industry. Fundamental knowledge has been generated by means of orthogonal cutting and slot milling experiments. The findings from these principle experiments were applied to develop prototypes and optimise conventional drilling and orbital drilling tools, aiming for increased bore quality and tool lifetime. The focus has been on optimising tool geometry in interaction with the diamond coating and improving the process parameters.

Here I would like to thank Prof. Dr.-Ing. Konrad Wegener for his generous support of my research and the lively discussions in which he has always shown great interest in CFRP machining. Furthermore, I would like to thank Prof. Dipl.-Ing. Dr. techn. Friedrich Bleicher for being the co-supervisor of my thesis.

Thanks to Dr. Fredy Kuster for his support by providing his great know-how and experience in terms of handling research projects. He was always approachable for the PhD candidates in the group "Prozesse" at IWF. My thanks also go to Dr. Wolfgang Knapp for supporting the research with his extensive knowledge in the field of measuring technology.

Many colleagues supported me in my work, in conducting experiments together and subsequently writing publications as well as in supporting during test rig development, preparation and lively discussions. Special thanks to: Dr. Marcel Henerichs, Lukas Seeholzer, Jens Boos, Maximilian Warhanek, Sebastian Böhl, Dr. Thomas Liebrich, Dr. Hidetake Tanaka, David Harsch, Bircan Bugdayci, Dr. Nicolas Jochum, Nikolas Schaal, Darko Smolenicki, Linus Meier, Martina Spahni, Mark Voegtlin, Sandro Wigger and Albert Weber.

Supervision of students, such as master, bachelor and semester thesis was always a great pleasure to me. I would like to thank for the effort of the following students: Stefan Übelin, Kai Neugebauer, Christian Dörig, Tobias Ammann, Martina Spahni, Patrick Meyer-Galow, Lukas Seeholzer, Stephan Rupp, Christoph Walch, Claudio Häfner, Isin Yildirim, David Rieger, Gianluca Capricano and Raphael Richner.

For the intensive and exciting collaboration during the last few years I would like to thank the industry partners, especially Nicolas Vernier from Dixi Polytool SA, Ulf Heule and Harry Studer from Heule Werkzeug AG, John Bexkens and Michael Dietz from Oerlikon Balzers, Stefan Klauser and Manuel Zaugg from RUAG Aerostructures Switzerland and Dominik Raps and Michael Glowania from Airbus Helicopters.

A special thanks to my family who always supported me on my way to achieve the doctoral degree and that I could always rely on them.

Zurich May 2017, Robert Voß

I Table of Contents

I	Table of Contents	I
II	Abbreviations.....	III
III	Symbols	IV
1	Introduction.....	1
2	State of the art in CFRP machining	7
2.1	Generation of process knowledge in CFRP machining.....	9
2.1.1	Fundamental free orthogonal cutting process.....	10
2.1.2	Fundamental milling	19
2.1.3	Drilling process.....	22
2.2	Bore quality in CFRP drilling	28
2.2.1	Form and roughness	28
2.2.2	Evaluation of bore entrance/exit damages.....	30
2.2.3	Bore channel and subsurface damages	34
2.2.4	Mechanical strength of bore	37
2.3	Tool wear and microgeometry.....	40
2.4	Cutting edge treatment of diamond-coated tools for CFRP machining	47
2.5	Force modelling in orthogonal CFRP machining	48
3	Research approach	55
4	Fundamental orthogonal cutting experiments	58
4.1	Free orthogonal cutting test rig setup.....	58
4.2	Results of cutting experiments with focus on forces and wear.....	61
4.3	Evaluation of the friction coefficient.....	69
4.3.1	Results and discussion.....	71
4.3.2	Conclusion of friction evaluation	74
5	Analytical force model	76
5.1	Sub-model $\theta=0^\circ(=180^\circ)$	78
5.1.1	Modelling.....	78
5.1.2	Results of sub-model $\theta=0^\circ$	85
5.2	Sub-model $15^\circ \leq \theta \leq 75^\circ$	87
5.2.1	Modelling.....	88
5.2.2	Results of sub-model $15^\circ \leq \theta \leq 75^\circ$	98
5.3	Sub-model $\theta=90^\circ$	99

5.3.1	Modelling.....	100
5.3.2	Results of sub-model $\theta=90^\circ$	107
5.4	Sub-model $105^\circ+\gamma \leq \theta < 165^\circ$	108
5.4.1	Modelling.....	109
5.4.2	Results of sub-model $105^\circ+\gamma \leq \theta < 165^\circ$	115
5.5	Interconnecting sub-models to overall force model	116
5.6	Conclusion and transferability of model to drilling operation.....	119
6	New approach for bore exit evaluation	123
6.1	Key parameters of the approach.....	123
6.2	Demonstration of analysing procedure.....	125
6.3	Analysing results.....	128
6.4	Conclusion of bore exit evaluation approach.....	134
6.5	Correlation of the damage value Q_d and tool micro-geometry	135
7	Drilling experiments in CFRP	140
7.1	Measuring equipment	140
7.2	Cutting edge treatment of diamond-coated drilling tools.....	144
7.2.1	Experimental setup.....	145
7.2.2	Drilling results.....	149
7.2.3	Conclusion cutting edge treatment	152
7.3	Orbital drilling vs. conventional drilling	154
7.3.1	Experimental setup.....	154
7.3.2	Drilling results.....	156
7.3.3	Conclusion of process strategy comparison	161
8	Overall conclusion and outlook.....	162
IV	Bibliography.....	164
V	Appendix	178

II Abbreviations

Notation	Description
A&D	Aerospace and Defence
AFRP	Aramid Fibre Reinforced Polymer/Plastic
CBN	Cubic Boron Nitride
CEA	Cutting Edge Analyser approach for micro-geometry evaluation
CFRP	Carbon Fibre Reinforced Polymer/Plastic
CP-T	cutting-process-tribometer
FEM	Finite Element Modelling
FRP	Fibre Reinforced Polymer/Plastic
GFRP	Glass-Fibre Reinforced Polymer/Plastic
GUI	Graphical User Interface
HSS	High Speed Steel
MD	Multi-Directional
MPEM	Minimum Potential Energy Method
NC	Numerical Control
PCD	Poly Crystalline Diamond
POD	Pin-On-Disk Tribometer
RVE	Representative Volume Element
SEM	Scanning Electron Microscope
UD	Uni-Directional

III Symbols

Notation	Unit	Description
A_d	[mm ²]	Damaged area around the bore
A_{free}	[mm ²]	Uncovered bore area
A_m	[mm ²]	cross sectional area of the idealised matrix layer surrounding the fibre (RVE)
A_{max}	[mm ²]	Circular area of diameter D_{max}
A_{mb_1}	[mm ²]	Projected area of region1 at cutting edge for <i>micro-buckling</i>
A_0	[mm ²]	Circular bore area
a_c	[μm]	Actual cutting depth in orthogonal turning
a_E	[μm]	First semi axis in x-direction of resulting contact ellipse between the tool and the carbon fibre (sub-Model: $\theta=90^\circ$)
a_e	[mm]	Machining width in orthogonal turning equal to workpiece width, due to full section
b	[mm]	Width of the workpiece
b_c	[μm]	Spring-back height of the material in region 3 of a cutting edge
\check{b}_c	[μm]	Spring-back height of the material at previous rotation
b_E	[μm]	Second semi axis in y-direction of resulting contact ellipse between the tool and the carbon fibre (sub-Model: $\theta=90^\circ$)
c_{cur}	[-]	Exact solution of the curvature of a bending beam (sub-Model 4)
$d = 2r$	[mm]	Tool diameter
$d_{80\%}$	[mm]	80% of the tool diameter (d)
d_{out}	[mm]	Outer diameter of the ring shaped CFRP workpiece in turning
D	[mm]	Bore diameter
D_e	[mm]	Equivalent delamination diameter
D_{max}	[mm]	Maximum diameter in the damage zone
D_2	[mm]	Diameter of the cutting edge in the contact point B (sub-Model: $\theta=90^\circ$)
$D_{95\%} = 0.95D$	[mm]	95% of the bore diameter D
E^*	[MPa]	Effective <i>Young's</i> modulus perpendicular to the fibre axis
E_{c2}	[MPa]	<i>Young's</i> modulus of CFRP transverse to fibre axis in region 2
E_{c3}	[MPa]	<i>Young's</i> modulus of CFRP transverse to fibre axis in region 3
E_{f1}	[MPa]	<i>Young's</i> modulus of carbon fibre in axial direction
E_{f2}	[MPa]	<i>Young's</i> modulus of carbon fibre in transversal direction
E_m	[MPa]	<i>Young's</i> modulus of matrix material in CFRP

III Symbols

Notation	Unit	Description
$E_{m,0}$	[MPa]	Young's modulus of matrix material in CFRP at low strain rate (according to datasheet)
$E_{m,real}$	[MPa]	Young's modulus of matrix material in CFRP at actual strain rate
$F_{A,cov}$	[-]	Parameter describing the relative bore area covered with uncut fibres
$F_{A,d}$	[-]	Parameter representing the relative damaged area A_d
F_N	[N]	Normal force of pin on CFRP surface
F_c	[N]	Cutting force (in cutting velocity direction)
F_d	[-]	Delamination factor
F_{da}	[-]	Adjusted delamination factor
F_{ed}	[-]	Equivalent delamination factor
F_f	[N]	Thrust force (in feed direction)
$F_{i,Rn,z}$	[N]	Systematic designation of force in model interval 'i', region of the tool 'n' and direction z or y
$F_{L,95\%}$	[-]	Relative circumferential length at 95% of D being punctured by fibres
F_{nd}	[-]	Normalised delamination factor
F_n	[-]	Factor based on tanh() representing n_{uncut}
F_y	[N]	Friction force in y-direction
F_z	[N]	Friction force in z-direction
F_t	[N]	Friction Force in sliding velocity direction
f	[mm]	General feed rate
f_z	[mm/rev]	Feed per revolution and cutting edge
$f_{z,a}$	[μ m/rot]	Feed rate per tooth in axial direction (orbital drilling)
$f_{z,t}$	[μ m/rot]	Feed rate per tooth in tangential direction (orbital drilling)
G_m	[MPa]	Shear modulus of the matrix material in the CFRP
H_1	[μ m]	Height of region 1 of the cutting edge in y direction
h	[mm]	Thickness of the workpiece
h^*	[μ m]	Vertical crack length from tool/fibre contact in B in y direction (sub-Model: $\theta=90^\circ$, section2)
I_f	[kg m ²]	Moment of inertia of carbon fibre
K_c	[-]	Variable describing the contacting share during cutting $\theta=150^\circ$ with saw teeth topography (sub-Model 4; region 1)
K_{Em}	[-]	Correction factor for Young's modulus at actual strain rate
K_f	[-]	Correction factor for tool-fibre contact in region 1 of sub-model 1
$K_{\sigma Tf}$	[-]	Correction factor for tensile strength of fibre at actual strain rate

Notation	Unit	Description
k	[-]	Normalised stiffness of the elastic foundation
k_b	[-]	Second WINKLER constant of the matrix/fibre connection in section 3 of sub-Model: $\theta=90^\circ$
k_{cush}	[-]	Dimensionless cushion factor of the elastic foundation
k_m	[-]	First WINKLER constant of the foundation
L	[μm]	Wavelength of the fibre during micro-buckling
$L_{95\%}$	[mm]	Complete circumferential length at 95% of D
L^*	[μm]	Distance from free fibre end to crack position/origin of coordinate system (sub-Model 4, region 1)
L_c	[μm]	Half projected contact length of the indented cylinder in half-space
L_{pf}	[mm]	Projected friction length in region 3 of a cutting edge
L_z	[mm]	Distance from one saw-teeth to the next one (in $\theta=150^\circ$)
l_c	[m]	Cutting length = Path length due to primary motion
l_f	[mm]	Feed travel = Length of path transverse by the tool in feed direction
l_{fr}	[μm]	Distance from the tool/fibre contact point K to the free end of the fibre (sub-Model: $15^\circ \leq \theta \leq 75^\circ$; region 2)
l_{sh}	[mm]	Shear length in force model of interval $15^\circ \leq \theta \leq 75^\circ$
L_z	[mm]	Distance between two saw teeth of the topography of $\theta=150^\circ$ CFRP
l_α	[μm]	Length in cutting velocity direction, where material is increasingly compressed \rightarrow Horizontal semi-axis of the ellipse, describing the cutting edge rounding (region2)
l_γ	[μm]	Length in feed direction, where material is forced underneath cutting edge \rightarrow Vertical semi-axis of the ellipse, describing the cutting edge rounding (region2)
M_{max}	[Nm]	Maximum torque of a spindle
N	[N]	Substitution variable, used in the $\theta=0^\circ$ force model
n_f	[-]	Number of bend fibres over workpiece width
n_{uncut}	[-]	Number of uncut fibres
P_{max}	[kW]	Maximum power of a spindle
P_{mb}	[N]	Theoretical force on fibre during micro-buckling
\bar{P}_{mb_1}	[N]	Average resulting force by <i>micro-buckling</i> in region 1
$\bar{P}_{mb_2.1}$	[N]	Average resulting force by <i>micro-buckling</i> in region 2.1
$P_{mb_{cr}}$	[N]	Critical compressive force on fibre at failure due to <i>micro-buckling</i>
$P_{P0_{cr}}$	[N]	Critical bending force at initial fibre failure (sub-Model: $15^\circ \leq \theta \leq 75^\circ$; region 2)
$\bar{P}_{P0_{cr}}$	[N]	Average bending force until initial fibre failure (sub-Model: $15^\circ \leq \theta \leq 75^\circ$; region 2)

III Symbols

Notation	Unit	Description
$P_{pr_2.2}$	[N]	Resulting pressing force, exemplary in sub-region 2.2
Q	[N/m ²]	Substitution variable, used in the $\theta=0^\circ$ force model
Q_d	[-]	Damage value containing various parameters describing the bore exit/entrance quality
R^*	[μm]	Radius in elliptical shape of cutting edge approximated with least square method in region 2 of force model interval I
R_a	[μm]	Arithmetic average roughness - the arithmetic deviation of the surface profile from the centreline
R_z	[μm]	Ten-point height - average distance between the five highest peaks and the five deepest valleys within the sampling length
R_p	[μm]	Peak height - average distance between the five highest peaks and the centreline within the sampling length
r_e	[μm]	Nose radius of cutting edge
r_f	[μm]	Radius of carbon fibre
r_{fm}	[μm]	Radius of carbon fibre embedded in matrix material (RVE)
r_{peak}	[μm]	Peak radius in transition from rake to flank face
r_{sg}	[μm]	Radius of surface generation, according to [101, 232]
s	[μm]	Length of matrix slippage during <i>micro-buckling</i>
VB	[μm]	Width of flank wear (flank wear criterion)
V_f	[%]	Volume fraction of carbon fibres in CFRP
V_m	[%]	Volume fraction of matrix in CFRP
$v_{f,a,h}$	[m/min]	Feed velocity of helix in axial direction (orbital drilling)
$v_{f,t,h}$	[m/min]	Feed velocity of helix in tangential direction (orbital drilling)
w_t	[mm]	Wall thickness of the CFRP workpiece in turning
X_f	[MPa]	Tensile strength of fibre
X_{pr_cr}	[MPa]	Compressive strength of carbon fibre transverse to fibre axis (sub-Model: $\theta=90^\circ$)
θ	[$^\circ$]	Fibre orientation
α, β, γ	[$^\circ$]	Clearance -, wedge- and rake angle
α^*	[$^\circ$]	Angle of straight-line in region 3 relative to cutting velocity direction
$\hat{\alpha}$	[1/ μm]	Substitution variable, used in the $\theta=0^\circ$ force model
$\hat{\beta}$	[1/ μm]	Substitution variable, used in the $\theta=0^\circ$ force model
γ^*	[$^\circ$]	Angle of straight-line in region 1 relative to feed direction
Δd_j	[μm]	Systematic pressing displacement lengths transverse to fibre direction (sub-Model: $15^\circ \leq \theta \leq 75^\circ$; region 2)
$\Delta \omega_i$	[μm]	Systematic bending displacement lengths transverse to fibre direction (sub-Model: $15^\circ \leq \theta \leq 75^\circ$; region 2)
$\Delta \omega_{max}$	[μm]	Maximum necessary deflection of a fibre transverse to fibre axis to

Notation	Unit	Description
		“dive” below the cutting edge (sub-Model: $15^\circ \leq \theta \leq 75^\circ$; region 2)
η	[-]	Parameter describing interfacial fibre-matrix bonding during micro-buckling
κ	[deg]	tool setting angle
λ	[deg]	Tool inclination angle
μ	[-]	Friction coefficient
μ_{app}	[-]	Apparent friction coefficient represents superposition of adhesion and plastic deformation effects
ν_{c12}	[-]	<i>Poisson's</i> ratio of CFRP transverse to fibre axis
ξ	[-]	Parameter describing ratio of matrix slippage to the wavelength of the fibre in <i>micro-buckling</i>
Π	[J]	Total potential energy
σ_{Pr}	[MPa]	Compressive stress at contact between cutting edge and fibre (sub-Model: $\theta=90^\circ$)
σ_{T_freal}	[MPa]	Tensile strength of the carbon fibre at actual strain rate
σ_{T_f0}	[MPa]	Tensile strength of the carbon fibre at low strain rates (from data sheet)
τ	[MPa]	Interfacial shear strain of the matrix
τ_c	[MPa]	Ultimate shear strength of interfacial (matrix-fibre) shear strain
ω	[μm]	Transverse deflection of carbon fibre
$\omega_{Z''_{cr}}$	[μm]	Critical deflection in <i>C</i> , above which a crack is initiated (sub-Model: $\theta=90^\circ$)
Φ	[deg]	Shear angle in the force models
ϕ	[deg]	Fibre cutting angle: Measured between fibre axis and cutting velocity direction

Kurzbeschreibung

Seit Einführung des Airbus A380 (Erstflug in 2005) werden aufgrund hervorragender Leichtbaueigenschaften von kohlenstoff-faserverstärkten Kunststoffen (CFK) zunehmend mehr Strukturbauteile eines Flugzeugs aus diesem Material gefertigt. Bei dem aktuellsten Flugzeug, dem Airbus A350, beträgt der CFK-Anteil mehr als 50 Gewichtsprozent. Während die bislang übliche Verwendung von Aluminiumlegierungen geringe fertigungstechnische Herausforderungen mit sich brachte, birgt die CFK-Zerspanung Schwierigkeiten bzgl. Bearbeitungsqualität und Werkzeugstandzeit. Die Zerspanung von Luftfahrt-CFK mit hohem Fasergehalt erzeugt einen extrem starken Werkzeugverschleiss und das Material neigt zu Schäden wie bspw. Delaminationen. Da Nietverbindungen nach wie vor das Hauptfügeverfahren von Bauteilen in zivilen Flugzeugen darstellen, sind eine grosse Anzahl an Bohroperationen zur Nietvorbereitung auch in CFK notwendig; Im A350 müssen bspw. 1,2 Mio. Bohrungen eingebracht werden. Nach aktuellem Stand der Technik werden viele dieser Bohrungen in CFK manuell nachbearbeitet, um die strengen Qualitätsanforderungen der Luftfahrtindustrie zu erfüllen. Dies verursacht hohe Kosten und lange Prozesszeiten. An dieser Stelle setzt die Forschung am Institut für Werkzeugmaschinen und Fertigung (IWF) der ETH Zürich an: Schwerpunkt sind grundlegende Analysen der Spanbildung zur Steigerung des Prozessverständnisses und darauf aufbauend Optimierungen von Prozessparametern, Werkzeuggeometrie und -beschichtungen sowie der Bearbeitungsstrategien.

Die vorliegende Dissertation knüpft thematisch an die Arbeit von HENERICHS [101] aus dem Jahr 2015 an. Dabei wird thematisch ein Bogen gespannt, ausgehend von der grundlegenden Verschleisscharakterisierung, Reibungsuntersuchung und Kraftmodellierung über die Entwicklung einer neuartigen Bewertung der Bohrungsqualität bis hin zur Untersuchung des Einflusses optimierter Werkzeug Mikro-Geometrien und verschiedener Bearbeitungsstrategien beim Bohren von CFK. Im Detail werden hier folgende Themen rund um die CFK-Zerspanung behandelt:

- Grundlegende Zerspanversuche von unidirektionalem CFK im orthogonalen Schnitt
 - Charakterisierung von Werkzeugverschleiss mit Hilfe «Gerade – Ellipse – Gerade»
 - Reibungsuntersuchung beim Bearbeitungsprozess
- Entwicklung eines analytischen Kraftmodells für die orthogonale Bearbeitung von unidirektionalem CFK
- Neuartiger Ansatz zur Bewertung der Bohrungsaustrittsqualität
- Angewandte Forschung: Optimierung der Bohroperationen in CFK
 - Einfluss lokaler Schneidkantenpräparation auf die Bearbeitungsqualität beim Bohren
 - Orbitalbohren im Vergleich zum konventionellen Bohren mit Spiralbohrer

Die von HENERICHS [101] schwerpunktmässig vorgestellten Grundlagenversuche im orthogonalen Schnitt von unidirektionalem (UD) CFK werden in dieser Arbeit weitergeführt und Modellansätze daraus abgeleitet. Der Ansatz zur Verschleisscharakterisierung mittels «Gerade – Ellipse – Gerade» ermöglicht eine reproduzierbare und effiziente Beschreibung der Schneiden-Mikro-Geometrie. Diese Beschreibung ist neben der Reibungsuntersuchung unmittelbar beim Bearbeitungsprozess notwendig, um ein aussagekräftiges analytisches Kraftmodell für die CFK-Zerspanung im orthogonalen Schnitt zu ermöglichen. Das Kraftmodell bildet erstmals den gesamten Faserorientierungsbereich von $0^\circ \leq \theta < 180^\circ$ ab,

wobei gewisse Faserorientierungsbereiche mit ähnlichen Spanbildungsmechanismen zu faserwinkelbereichsspezifischen Teilmodellen zusammengefasst werden. In der abschließend präsentierten Anwendungsforschung wird das gesteigerte Prozessverständnis auf die Bohrbearbeitung von CFK übertragen. Um eine Optimierung der Bearbeitungsprozesse hinsichtlich Bohrungsqualität charakterisieren zu können, wird zunächst ein neuartiger Ansatz zur Bewertung der Bohrungsaustrittsqualität vorgestellt. Dabei werden neben üblicherweise betrachteten Schäden ausserhalb der Bohrung auch ungeschnittene Fasern berücksichtigt, die Nietoperationen ebenfalls behindern können. Anschließend werden zwei Möglichkeiten zur Steigerung der Bearbeitungsqualität präsentiert: Erstens wird durch lokale Schneidkantenpräparation eines diamantbeschichteten Werkzeugs mittels Laserabtrag die Mikrogeometrie optimiert und die Verschleisswiderstandsfähigkeit entlang der Freifläche gezielt reduziert. Zweitens wird durch Variation der Bearbeitungsstrategie die Bohrungsqualität gesteigert. Beide Möglichkeiten führen zum Teil sogar zu erheblichen Verbesserungen hinsichtlich Qualität und Standzeit.

Abstract

Since the introduction of the Airbus A380 (first flight in 2005), an increasing number of structural components of an aircraft are made of carbon fibre reinforced polymers (CFRP), due to its excellent lightweight properties. In the most recent aircraft, the Airbus A350, the CFRP content is more than 50% by weight. While the use of conventional aluminium alloys has led to minor manufacturing challenges, the CFRP machining process presents difficulties with regard to processing quality and tool lifetime. The machining of aviation-CFRP with its high fibre content produces an extremely strong tool wear and the material tends to damages, such as delaminations. Since rivet connections continue to be the main joining method of components in civilian aircrafts, a large number of drilling operations in CFRP are necessary for the preparation of rivets; e.g. in the A350 1.2 million bores have to be introduced. According to the current state of the art, manual rework is necessary for many of these holes in CFRP to meet the stringent quality requirements of the aviation industry. This causes high costs and long process times. That is where the research at the Institute for Machine Tools and Manufacturing (IWF) of the Swiss Federal Institute of Technology (ETH Zurich) starts: The main focus of the research is on fundamental analyses of chip formation to increase process knowledge and based on this to optimise process parameters, tool geometry and coatings as well as processing strategies.

This thesis is thematically linked to the work of HENERICHS [101] from the year 2015. In this most recent thesis an arch is drawn up, starting from the basic wear characterisation, friction analysis and force modelling through the development of a new evaluation of the drilling quality up to the investigation of the influence of optimised tool micro-geometries and different machining strategies in CFRP drilling. The following topics around CFRP machining are covered in detail:

- Fundamental orthogonal machining of unidirectional (UD) CFRP
 - Characterisation of tool wear by means of «straight line – ellipse – straight line»
 - Friction analysis close to a machining operation
- Introduction of an analytical force model for orthogonal machining of UD CFRP
- Novel approach for bore exit evaluation
- Applied research: Optimisation of drilling operations in CFRP
 - Influence of local cutting edge preparation on the machining quality during drilling
 - Orbital drilling compared to conventional drilling with spiral drills

The fundamental investigations in orthogonal machining of UD CFRP by HENERICHS [101] are continued in this thesis and modelling approaches are derived therefrom. The approach of tool wear characterisation by means of «straight line – ellipse – straight line» enables a reproducible and efficient description of the cutting edge micro-geometry. This description is necessary besides the friction analysis close to a machining operation to enable a powerful analytical force model for orthogonal CFRP machining. For the first time, an analytical force model maps the entire fibre orientation range of $0^\circ \leq \theta < 180^\circ$, whereby specific fibre orientation ranges with similar chip formation mechanisms are combined to so-called sub-models. In the finally presented application oriented research, the increased process knowledge is transferred to drilling operations in CFRP. In order to be able to characterise

the optimisation of the machining processes with respect to drilling quality, a novel approach for evaluating the bore exit quality is proposed. In addition to the typically analysed damages in the vicinity of the bore, uncut fibres protruding inside are also taken into account, which can also hinder rivet inset. Subsequently, two possibilities are presented to significantly improve the drilling quality in CFRP: Firstly, the micro-geometry is optimised and the wear resistance along the flank face is reduced by treating the cutting edge of a diamond coated tool locally with laser ablation. Secondly, a significant increase of the bore quality by variation of the processing strategy is shown. Both possibilities lead to considerable improvements of quality and tool lifetime.

1 Introduction

Carbon-fibre-reinforced polymer (CFRP), also known as carbon-fibre-reinforced plastic, is a composite material consisting of carbon fibres embedded in polymeric matrix material. A distinction is made between continuous strand, long and short fibre reinforced materials. While in short CFRPs the fibre segments are more or less randomly arranged in the matrix, in continuous strand reinforced materials single fibres are arranged to rovings with preferential direction. One roving typically consists of 5.000-15.000 fibres with a fibre diameter in the range of 6-7 μm . This small fibre diameter is chosen, because a material in form of a fibre has a considerably higher strength than any other form and the smaller the diameter the higher the strength, which has been found by GRIFFITH [87]. He showed that a smaller fibre diameter results in a lower density of lattice defects relative to the fibre length. According to SCHÜRMAN [203] a defect generates large notch effects and is the initial point of crack propagation. A single lattice defect results in fibre failure but in a roving the local defect is supported by a few thousand adjacent fibres and crack propagation may be stopped at the fibre-matrix interfaces. The stochastically distribution of such defects results in a rather constant load capacity of a roving. Due to these properties CFRP components show an excellent fatigue resistance but in case of an impact mechanical damages are difficult to detect. The manufacturing methods drawing, spinning and stretching of carbon fibres further improve the strength and stiffness by orienting the crystallographic plane of the carbon in fibre direction, as stated by SCHÜRMAN [203]. Accordingly CFRP fibres are highly anisotropic and the high strength and stiffness in fibre direction is payed with worse mechanical properties transverse to the fibre direction.

In terms of polymeric composites, a flat laminate is manufactured by stacking several layers of unidirectional (UD) or woven plies. One ply is a manufactured assembly of long carbon fibres and is also referred to as fabric. A categorisation of different fabrics is generally done by the orientation of the fibres in the fabric. The left picture in Figure 1.1 shows schematically the stacking sequence in a laminate with UD fabrics. PETERS [171] explains the goal of composite design as to achieve the lightest and most efficient structures by orienting a maximum amount of fibres in the direction of the load in the CFRP component. The potential weight reduction of a composite material as compared to a homogeneous material e.g. metal is therefore highly dependent on the expected load on the component. In UD fabrics the majority of fibres is oriented in one direction and is straight and uncrimped, resulting in the best possible mechanical properties of the component in this direction. During design phase with UD fabrics the symmetry and balance of a stack needs to be considered, to avoid bending or distortion of a component, as explained inter alia by PETERS [171]. The picture in the middle of Figure 1.1 shows common weave styles of woven fabrics, where warp fibres in longitudinal direction (0°) and weft fibres in transverse direction (90°) interlace in a regular pattern to generate a mechanical interlock. According to VAUGHAN [229], the plain weave shows the maximum yarn slippage stability, while other fabrics with two or more warp yarns interlocking two or more filling yarns are more pliable and can more easily be draped to simple contours. Other manufacturing methods of CFRP, e.g. winding or pultrusion for round CFRP parts or certain profiles will not be discussed, since the focus of this thesis is on flat UD and woven CFRP laminates.

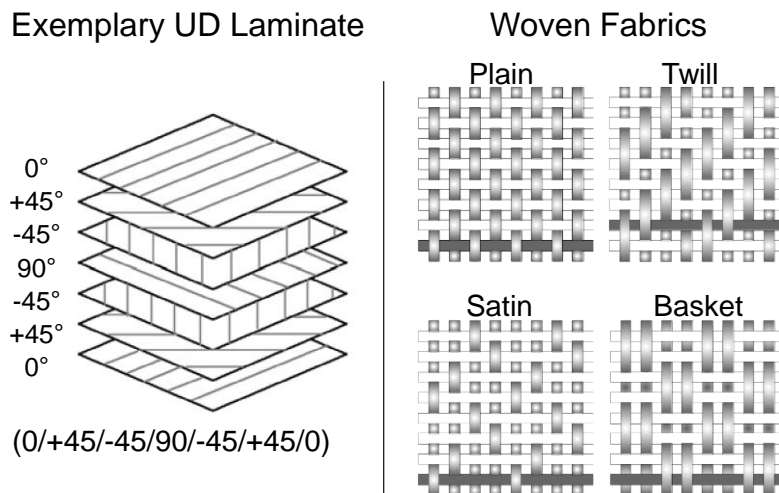


Figure 1.1: Exemplary stacking sequence of UD laminate (left) and woven fabrics (right), according to [65].

Different processing routes exist to impregnate the fibres with the matrix (resin) material and cure the component. The selection of the appropriate method depends on the component size, matrix material, geometrical constraints, etc. In the method with the lowest tool costs, the resin is applied either by spraying, rollers or brushes, while the laminate is placed in a one-sided mould. Subsequently, the components cure either under standard atmospheric conditions or vacuum bagging is used to apply pressure to the laminate and improve the solidification. Another manufacturing technique, explained in detail by FONG [78], is Resin Transfer Moulding (RTM) where the fabrics are placed as dry stack into a first mould and pre-pressed together with a binder. In a second mould the resin is injected into the fabric and cures under pressure and optional vacuum. A third processing route, which allows for more process automation, uses pre-impregnated fabric (prepreg) with pre-catalysed resin as raw material. These fabrics are cut to size, put into a mould and typically heated in an autoclave to 120°C - 180°C. Under these conditions the resin reflows and cures. For large structures, this process may be adapted to “out of autoclave” by applying pressure with vacuum bagging instead of the tool and using an oven to cure the component. In aerospace industry most CFRP components are manufactured from autoclave-cured prepregs, as stated by HOREJSI [118] and LÄSSIG et al. [144]. Accordingly, RTM or infusion processes are only used, if significant cost savings outmatch risks of material availability, aerospace certifications and factory capabilities.

The technical requirements of a component and the selection of a certain manufacturing method directly influence the selection of an appropriate matrix material. According to REINHART [187], in composite CFRP material the matrix system has the function of binding the fibres by its adhesive characteristic, transferring the loads between fibres and protecting the fibres against environmental influences. SCHÜRMAN [203] states that the matrix on the one hand fulfils an important tasks by holding the fibres in place but is on the other hand the weak component of the CFRP. The matrix systems being utilised with carbon fibres today are most commonly thermosets (49%) followed by thermoplastics (15%), as presented by KRAUS and KÜHNEL [138]. In the high-performance aerospace industry the mechanical properties, like the impact strength or *Young's* modulus of epoxy based CFRP matrix materials may be improved by appropriate selection of additives (<3%) like thermoplastics or elastomers, as being explained by WITTEN [249]. Nevertheless, most of the matrix materials exhibit quite different mechanical and physical properties from the fibres. According to

FLEMMING [77], two-component-matrix systems consisting of resin and hardener, are mostly used in industrial application, due to easy handling. In RTM processes the two components are mixed before impregnation and immediately curing starts, which is a chemical thermosetting reaction. The more expensive one-component-matrix systems are almost only utilised in aerospace industry, as stated by FLEMMING et al. [77]. These systems start curing by exceeding a certain temperature ($>150^{\circ}\text{C}$) and allow for production of high quality CFRP components.

For the future it is expected by KRAUS and KÜHNEL [138] that thermoplastics will have an increased market share, especially in high volume applications with short cycle times and where good recyclability is necessary (e.g. automotive industry). But this thesis with focus on the aerospace industry, concentrates on the most utilised epoxy-based CFRP (thermoset).

CFRP in Industrial Applications

Fibre Reinforced Polymers (FRP) are introduced in industrial applications in the early 1930s, as investigated by KÖNIG et al. [135]. In the meantime applications for FRPs have changed from initially secondary parts to mainly high performance engineering parts in the aerospace and automotive industry as well as energy and sports & leisure applications today. Figure 1.2 (left) shows the market for carbon composites (CC) of 2015 divided into its applications according to the market report by KRAUS and KÜHNEL[139]. It needs to be considered that the different markets have dissimilar demands on quality and manufacturing methods. The authors state that aerospace and defence (A&D) claims for 30% of the global CC-volume but makes 61% of the global turnover. Accordingly A&D high performance applications utilise costly raw material and manufacturing methods. But in the interpretation of the data it needs to be considered that the high quality standards in A&D may cause extra costs for material approval and testing. KRAUS and KÜHNEL [139] calculate the imaginary average costs for CFRP in each branch of industry, resulting in 310 USD/kg for A&D but just 86 USD/kg and 97 USD/kg respectively in automotive industry and the wind energy sector. Referring to this market report [139] from 2016, an estimated annual growth of the CFRP market of 10-13% to 191 kt in 2022 is expected. Both the automotive as well as the aerospace industry are expected to be the main growth drivers in the next few years, due to the European regulations to reduce the CO_2 consumption and pushing on lightweight manufacturing. In retrospective, the CFRP demand has more than doubled in six years' time (2009-2015), as displayed Figure 1.2 (right).

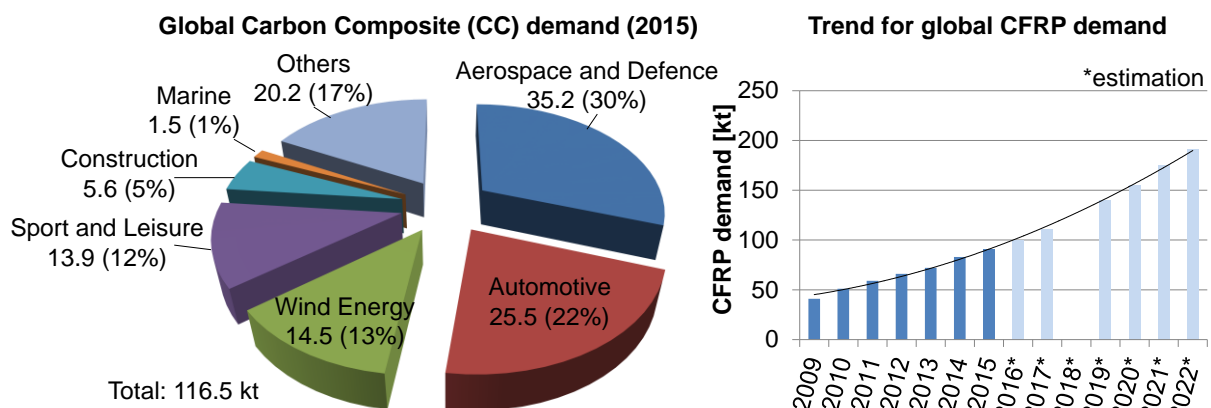


Figure 1.2: Global CF demand (2015) in kt divided into industries (left) and trend for future demand (right), according to [138, 139].

This thesis focuses on applications in the aerospace industry, which is known as an early adopter of new technologies and according to SCHÜRMAN [203] is the pioneer in utilising CFRP components. The first structural FRP-components in aviation are installed in gliders starting in the mid-1950s, as described by EHRENSTEIN [65] and SCHÜRMAN [203]. The first plane with a CFRP structural wing of 29 m wingspan, which was impossible to build out of glass fibre, was developed in 1972 by the university glider team in Braunschweig [203]. In the meantime the amount of FRP-components in airplanes has drastically increased. In modern aircrafts like the Airbus A350 or the Boeing 787 (Dreamliner) more than 50 weight percent of the plane are made of CFRP [138, 205], as presented in Figure 1.3. Even in the Airbus A380 and the Boeing 777 with wings made of CFRP a considerable amount of carbon fibres is installed. The current ramp-up of the A350 and the Boeing 787, which are mostly made of CFRP, promises an annual growth rate in A&D of 13% being above the average market growth of 11% [138]. Furthermore, the statistic in Figure 1.3 shows not only a reduction of aluminium alloys accompanied with the increasing utilisation of CFRP but also an increasing amount of titanium. Titanium seems to be the enabler for the increasing use of CFRP in the aerospace industry. SCHÜRMAN [203] explains this effect with the electrical properties of carbon fibres at presence of an electrolyte, like water in moisture environment, which generates an electrochemical potential in contact with metals. This may result in anodic corrosion of metals. Therefore either titanium or stainless steel has to be used in applications with direct contact to CFRP or certain insulation of aluminium is necessary to prevent contact corrosion.

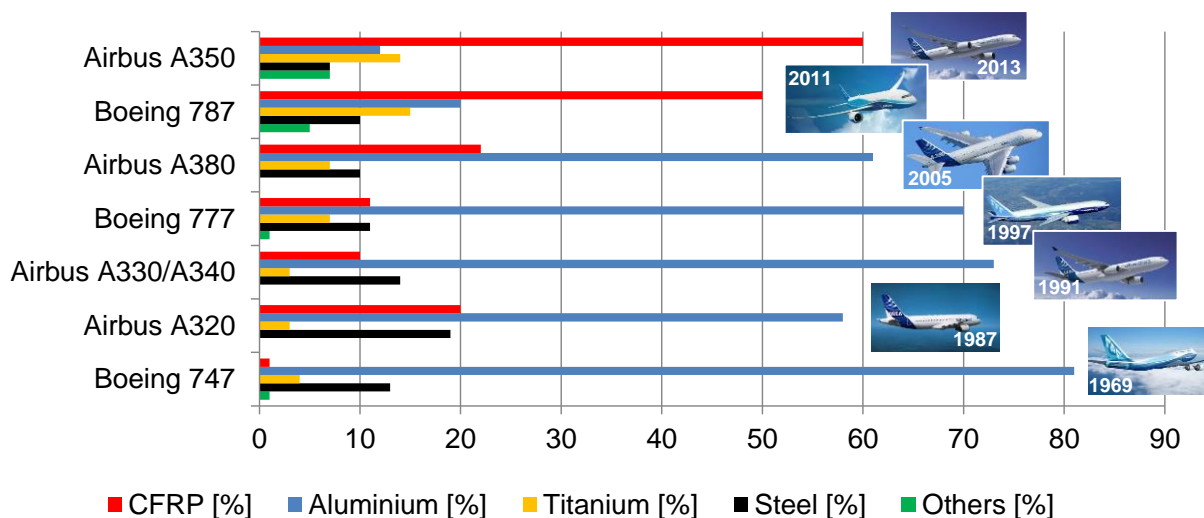


Figure 1.3: Material distribution in weight% in different Airplanes, according to [85, 138, 205].

The main reason for CFRP having prevailed in the above mentioned industries are the improved physical and mechanical properties such as high damping capacity, corrosion resistance, fatigue strength as well as high specific stiffness and strength, as stated by KÖNIG et al. [135]. SHEIKH-AHMAD [205] highlights the ability to tailor the fibre properties in a wide range during fabrication. Exemplary fibre types are High Tenacity (HT), High Modulus (HM) and Intermediate Modulus (IM) plus certain special fibres. In fibre direction the tensile strength of CFRP with exemplary intermediate modulus fibres (IM-CFRP) is 4.7 to 5.8 times larger compared to an aluminium alloy (7075 T6) and the *Young's* modulus is up to 2.7 times higher, as shown in Table 1.1. Furthermore carbon fibres are chemical substantially inert, infusible, resistant to high temperatures, biocompatible and permeable to X-rays, as stated by WITTEN [249]. These properties and an up to 36% lighter weight compared to aluminium

alloy are the enabler for production of high performance and light weight structural components, according to SHEIKH-AHMAD [205]. In this thesis the following two CFRP/epoxy materials are used for the experiments:

- Unidirectional inter-modulus fibres IMA-12K with 12.000 fibres per roving and a high performance matrix material HexPly® M21. According to the datasheet by *Hexcel* [105], the fibre fraction by weight in the laminate is 66% and the tensile strength is 3.050 MPa while the *Young's* modulus is 178 GPa. The fibre diameter is 7 μm .
- Woven AS4-6K with 6.000 fibres per roving and the same resin HexPly® M21. The fibre fraction by weight in the laminate is 65%, the tensile strength is 880 MPa and the *Young's* modulus is 73.9 GPa [105]. The fibre diameter is 7 μm .

Table 1.1: Properties of fibres, FRPs and Al-alloy, according to [65, 66, 106, 205, 249]

	Tensile strength [MPa]	Young's Modulus [GPa]	Density [g/cm ³]	Costs*** [€/kg]
Aluminium alloy (7075 T6)	~572	~71	~2.8	1 - 3
Carbon fibres*				
Standard (HT, IM)	3'600 - 4'700	240 - 295	1.77 – 1.78	20-80
High Modulus (HM)	1'750 – 3'000	300 - 500	1.8 - 1.96	100-500
Special types	/	/	/	100-1'000
Glass fibres*	2'400 – 4'600	55 - 90	2,14 - 2,72	2 - 3
Aramid fibres*	2'800 – 3'000	65 - 130	1,44 - 1,45	20 - 30
CFRP – IM**	2'700 - 3'300	164 - 190	1.78	/
CFRP – HM**	2'400	255	1.81 - 1.83	/
GFRP**	3'100 - 4'600	80 - 91	2.46 - 2.5	/

*In fibre direction

**Cured material at room temperature;
normalised to 60% fibre volume

***Considers raw material Data
and production costs

According to EHRENSTEIN [65] the costs for a CFRP component under consideration of raw material and production costs varies heavily, as shown in the right column in Table 1.1. High performance fibres HT, HM and IM made of costly raw material and with pricey production methods are much more expensive than aluminium alloys or glass fibre reinforced plastics (GFRP). LÄSSIG et al. [144] estimate a total cost reduction for CFRP components of up to 30% until 2020, based on cycle time reductions, a higher degree of automation, simplification of processes and improved technologies for CFRP production. According to KRAUS and KÜHNEL [138], an increased utilisation of thermoplastic CFRP may result in further cost reductions, due to shorter cycle times by avoiding chemical reactions (necessary in thermosets), unproblematic storability and good recycling conditions. However, these matrix materials require a larger added value of the material manufacturer.

STÖCKLE [209] shows in Figure 1.4 an exemplary change from an aluminium welding construction to an integrated CFRP cabin framework in a helicopter. The change from aluminium to CFRP in this application does not only result in lighter weight (-10%) but is even 30% cheaper when applying highly automated CFRP production techniques.

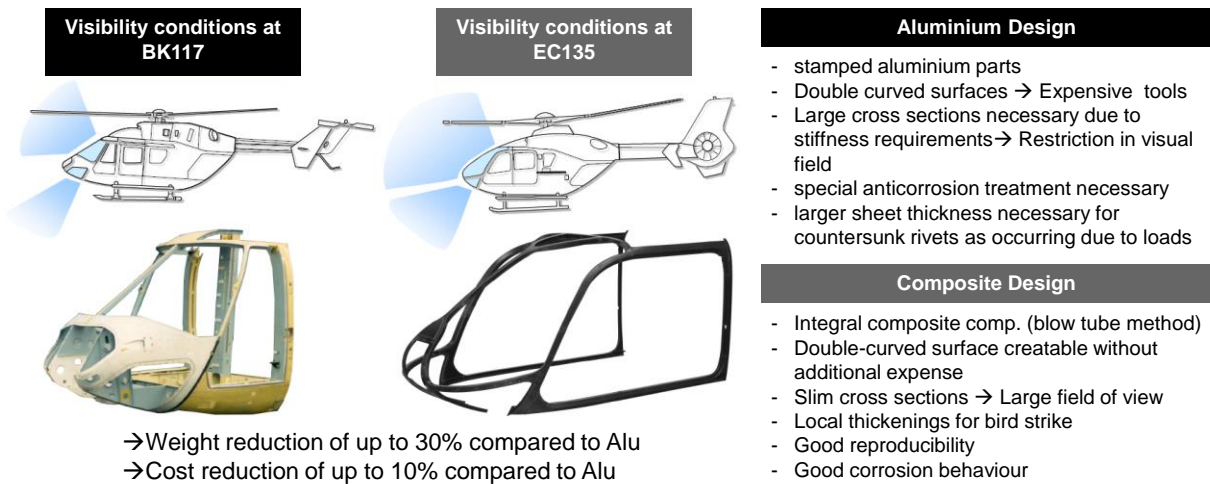


Figure 1.4: Comparison of Al vs. CFRP design of cabin framework in a helicopter [209].

This thesis focusses on CFRP machining with defined cutting edges for the aerospace industry: Fundamental orthogonal turning is used for generation of process knowledge and the findings are applied to optimise conventional CFRP drilling and orbital drilling processes. The detailed state of the art concerning these topics is presented in the following Chapter 2. This introduction provides the reader with an overview regarding carbon fibres, CFRP manufacturing methods, characteristic properties of CFRP, its main applications and the market trend. In case of further demand for information concerning CFRP, the detailed manufacturing methods or applications beyond the aerospace industry the reader is given the following literature recommendations: WITTEN [249], FLEMMING et al. [77], SHEIKH-AHMAD [205], DAVIM [54], SCHÜRMAN [203], PETERS [171].

2 State of the art in CFRP machining

Manufacturing of Carbon Fibre Reinforced Polymers (CFRP) is a near-net-shape technology. Nevertheless a large number of machining operations e.g. contour milling, drilling, orbital drilling or waterjet machining are still necessary for finishing and are investigated in the research community. This chapter summarizes the research areas in the field of CFRP machining, with a special focus on drilling.

Early CFRP machining research starts in the 1970th by EVERSTINE and ROGERS [69] who were the first to develop a deformation and material separation model for cutting CFRP. SUNG and SUH [212] analysed in fundamental friction and wear experiments the behaviour of graphite fibre-epoxy with 52100 steel. It was found that the carbon fibre orientation in the probe relative to the sliding direction (normal, transverse and longitudinal) has a huge influence on the friction coefficient μ_{app} and the wear volume. The friction coefficient varies in range of $0.2 < \mu_{app} < 0.8$. Minimum friction force occurs, when sliding with normal oriented graphite fibres embedded in epoxy over a steel surface. In the early 1980th KOPLEV et al. [137] conducted an experimental orthogonal cutting study with maximum 40 m/min in UD CFRP, where the fibre orientation was parallel and perpendicular to the cutting velocity direction. The authors focused on chip formation with quick stop devices, workpiece surface quality and process forces. They found the cutting process in CFRP consisting of several fractures and no distinctive plastic deformation occurs, as known from metal machining. Furthermore the clearance angle is identified as the main influencing factor on the thrust force. The larger the clearance angle, the more the thrust force decreases. The cutting force on the other hand is mainly influenced by the feed rate (cutting depth). Extensive comparisons of drilling and turning (facing) in CFRP and Glass Fibre Reinforced Polymer (GFRP) were conducted by SAKUMA et al. [197-199], who found that tool wear in CFRP is several times the wear in GFRP. The authors tested different cutting inserts made of sintered carbide, ceramic and cermet. The wear rate of these various tool materials shows a correlation to the tool material hardness; apart from a few exceptions it applies that the harder the tool material, the lower the wear rate. According to SAKUMA et al. [199], this correlation may be superimposed by thermal effects. The heat conductivity is specified as 4.19 W/m·K in CFRP and 0.3 W/m·K in GFRP and leads to accumulated heat at the cutting edge of poor thermal conducting tool materials e.g. ceramics in GFRP machining. Accordingly, the thermal conductivity of the tool material had a high influence on improving the tool wear in GFRP machining, but just a little influence in CFRP. The experiments showed that cemented carbide tools (K10) performed best in CFRP machining, followed by ceramic tools. In contrast the latter tool material showed maximum wear in GFRP machining. SAKUMA et al. [199] stated that the cutting speed has a smaller influence on the tool wear. In 1985 KÖNIG et al. [135] highlight the differences in material properties between metal and FRPs and point out the differences in machining. The following four typical damages, when machining FRPs are identified: Delamination, spalling, fuzzing and burning. Therefore the major parameters determining the cutting quality are discussed. Furthermore the authors indicate waterjet cutting as being suitable for machining of thin laminates. But the edge quality is found to highly depend on the cutting parameters and the material composition as well as the fibre orientation. BOLDT and CHANANI [18] presented tools for graphite composites and aramid composites as well as a comparison between conventional drilling and pecking. A so called spade drill/countersink tool for CFRP drilling is recommended to eliminate the

need for material backup at the bore exit side. A version for a power feed motor and one for manual drilling/reaming is presented. With this tool the bore exit quality is rapidly increased in relation to conventional drilling tools, however the conventional tools are not presented. Furthermore BOLDT and CHANANI [18] recommend a tool with a rake angle of 10° for manual countersinking in CFRP and a spiral drill with C-shaped cutting edges for aramid composites to cut from the outside to the centre.

In the next several years the Fibre Reinforced Polymers (FRP) research is characterised by extensive studies of a few research teams. At the WZL of the RWTH Aachen three consecutive theses can be found, starting with GRASS [86] in 1988 with research about drilling in fibre reinforced thermosets. RUMMENHÖLLER [193] finishes his thesis in 1996 about the material oriented process design for CFRP milling. The third thesis at the WZL is written by WÜRTZ [252] in 2000 focussing on the dust emissions during the milling of components made of CFRP. This is an important topic, since CFRP forms particles during machining in the range of micrometres which might be harmful when inhaled by the operator.

At the university of Darmstadt, REIMANN [186] evaluated in 1991 high-speed milling of CFRP thermosets and short fibre reinforced thermoplastics (PEEK). The experiments with a milling cutter head and poly-crystalline diamond (PCD) tools were conducted in a cutting speed range of 2000-5000 m/min. The material separation mechanism is described and a failure hypothesis is defined. Based on this theory and experimental data an ideal depth of cut of 40-60 μm and cutting speed of 2000-3000 m/min for optimum surface quality was identified. The tool geometry of 8° rake angle and 18° flank angle was recommended.

In contrast to REIMANN [186], HOHENSEE [117] focused on contour milling with lower cutting speeds in the range of 100-500 m/min and laser cutting at the university in Hannover. Glass-, aramid- as well as carbon fibre reinforced thermosets were investigated. It was stated that the machining quality and process forces are mainly influenced by the type of fibre and the fibre orientation. CFRP materials generate maximum process forces compared to the other two materials. It is recommended to use tools with geometrically defined cutting edges.

In the United States a group under the leadership of RAMULU [3-7, 47, 48, 181, 182, 238-240, 247] from the University of Washington in Seattle conducted research in fundamental orthogonal cutting of FRPs including machining induced surface textures and chip formation, starting in 1991. Additionally to the above mentioned topics, this group focused on edge trimming and machining-induced surface ply damages as well as a first study [182] about drilling CFRP/Titanium stack material in 2001.

In parallel a research group headed by HOCHENG [110-115, 175, 176, 222-225] from the Tsing Hua University in Taiwan presented their first relevant publication in 1992 and focused on drilling FRP thermosets and milling of polymer composites. In a later phase from 2004 to 2006 the publications [113-115, 223-225] of this group focused on delamination analysis in CFRP drilling.

Further FRP research in this early phase was conducted at the University of Naples under the leadership of CAPRINO and TETI [28-40, 194, 217] and focusses on single aspects especially in the fields of static and dynamic material failure, surface quality after machining and the influence of fibre orientation on the process forces at low cutting velocities and feed rates in FRPs. The keynote paper by TETI [218] "Machining of Composite Materials" summarises the findings about machining of CFRP until 2002 and somehow marks the end of this early research phase with a clear number of research groups. Afterwards a

diversification of FRP research to many different institutes occurs and the publications tend to focus either on single materials, e.g. epoxy-based CFRP, CFRP/Titanium-stack or certain processes e.g. orbital drilling, contour milling or certain process technologies e.g. PCD tools, diamond coated cemented carbide tools. The below described state of the art focuses on cutting of continuous strand epoxy based CFRP with defined cutting edge. As a consequence of the presented research content in this thesis (Chapter 4 ff.) it is distinguished between fundamental orthogonal cutting and drilling with continuous cutting edge contact. To get a more general overview on FRP machining it is referred to the literature from DAVIM [54], EHRENSTEIN [65], SHEIKH-AHMAD [205] and WITTEN [249].

As shown in the above mentioned publications of KOPLEV et al. [137], SUNG and SUH [212] and KÖNIG et al. [135], the fibre orientation θ in the material has a huge influence on the machining quality, forces and tool wear. Usually the fibre orientation θ is defined as the angle between the fibre axis and the cutting velocity, but the angular orientation may vary within various publications. To ensure uniform definition in this thesis, the fibre orientation θ is defined as the angle counter clockwise from the cutting velocity to the fibre axis, shown in Figure 2.1. If it is referred to publications with differing definition, the fibre orientation θ is adapted to the definition in Figure 2.1.

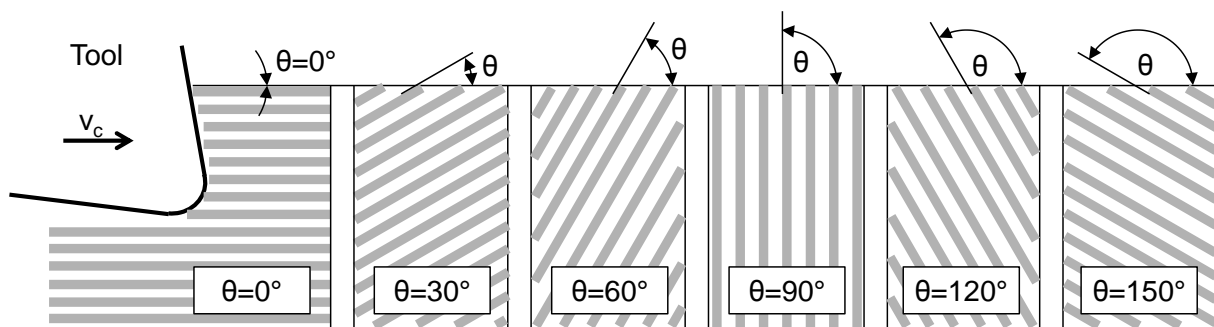


Figure 2.1: Definition of fibre orientation θ in this thesis in accordance with HENERICHS [101]

2.1 Generation of process knowledge in CFRP machining

The machinability of CFRP in literature is generally analysed based on fundamental orthogonal cutting experiments [30, 31, 33, 34, 75, 96, 101, 102, 137, 176, 193, 207, 230, 239, 240], but insights can also be obtained from tests in drilling [10, 61, 67, 73, 86, 88, 89, 98, 109-111, 135, 146, 147, 157, 158, 162, 173, 179, 198, 220, 222, 234, 251, 252] and milling [47, 48, 52, 83, 90, 107, 108, 117, 193]. The following three Chapters 2.1.1, 2.1.2 and 2.1.3 focus on publications, which condense the machinability of CFRP using one of these three processes. All publications indicate on the material-related difficulties in CFRP machining, based on the inhomogeneity of the CFRP material and the high abrasiveness of carbon fibre machining. The inherent inhomogeneous and mostly anisotropic mechanical properties of CFRP lead to significantly different machining conditions and usually rougher machined surfaces compared to metal, as stated by KÖNIG et al. [135, 136]. The authors identified that CFRP shows brittle behaviour and breaks more or less without plastic deformation at comparatively low loads. Furthermore, the above mentioned mechanical properties of CFRP cause undesirable effects, such as delamination and heavy tool wear. It is reported by various authors [15, 53, 64, 107, 152, 156, 218] that delamination, in which

two layers in a CFRP component detach locally, is the principle damage of CFRP laminates. While single authors analyse machining of CFRP with grinding tools [47, 48, 74, 170, 226], the predominant number of authors recommend the use of geometrically defined cutting edges [30, 31, 33, 34, 47, 48, 52, 75, 83, 90, 96, 101, 102, 107, 108, 117, 137, 161, 170, 176, 193, 207, 230, 239, 240, 247] made of cemented carbide, diamond coated carbide or poly-crystalline diamond (PCD).

2.1.1 Fundamental free orthogonal cutting process

In drilling operations of unidirectional (UD) CFRP, the cutting velocity magnitude and effective direction angle change along the main cutting edge from the outside to centre of the tool. Additionally, the fibre orientation θ at the cutting edge changes with tool rotation and repeats every 180° . Usually the tip angle is smaller than 180° and thus the cutting edge machines several laminate layers simultaneously. At the same time the peripheral land reams along the bore wall. Consequently, various effects superimpose during exemplary drilling operations and thereby are not suitable for detailed fundamental process analysis. That is why the majority of fundamental machining processes research was conducted with orthogonal cutting. As stated by KLOCKE and KÖNIG [132], free orthogonal cutting is a particular case of a turning operation with maximum complexity reduction. Turning is defined in the standard DIN8589a as a machining operation with defined cutting edge, rotating cutting motion and an arbitrary transverse translational feed movement. According to [132], free orthogonal cutting is characterised by the following boundary conditions:

- Only the main cutting edge engaged (free)
- The tool setting angle κ_r is 90° (orthogonal)
- The tool inclination angle λ_s is 0° (orthogonal)

Applying free orthogonal cutting to unidirectional CFRP facilitates constant cutting speed, feed rate, chip thickness and fibre orientation θ . Due to this advantageous properties, many researchers [30, 31, 33, 34, 75, 96, 101, 102, 137, 176, 193, 207, 230, 239, 240] applied free orthogonal cutting processes, partly altered from a turning operation to a planing (stationary tool) or shaping (stationary workpiece) process. The different setups with low process complexity are presented in Figure 2.2.

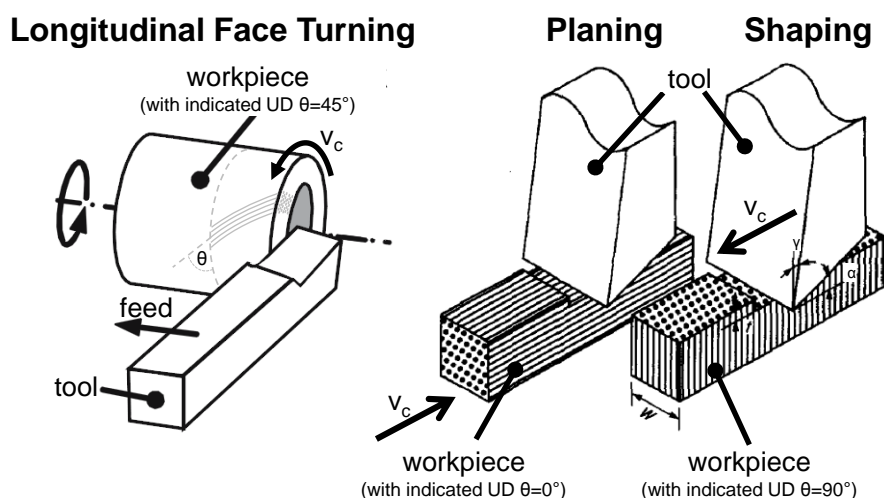


Figure 2.2: Cutting processes with maximum complexity reduction: Turning, planing and shaping, according to [132, 137]

In contrast to turning, planing and shaping are processes with main translational cutting motion and gradual feed movement perpendicular to the cutting direction, defined in the standard DIN8589e. Since CFRP is often manufactured as plane sheet material, the samples of the two latter mentioned processes with straight cutting motion are easier to obtain. In turning operations, a round tube-shaped CFRP probe is necessary to enable free orthogonal cutting. Planing and shaping are mostly reciprocating processes with run-in and -out behaviour at the beginning and end of the engagement during translational motion, while free orthogonal turning is a process with continuous cut.

KOPLEV et al. [137] were the first to conduct experimental machining of UD CFRP/epoxy with simplified cutting kinematics. The authors applied shaping with a cutting length of each reciprocating cut of 220 mm as well as quick-stop experiments to better understand the cutting processes in CFRP. Two different fibre orientations, parallel and perpendicular to the cutting velocity direction were investigated. The research in [137] with CFRP/epoxy ($V_f=61\%$) focused on the influence of process parameters and tool macro-geometry on chip dimensions, workpiece quality and process forces. It was stated that the cutting forces on the one hand depend on the rake angle as well as the cutting depth and the feed forces on the other hand depend mainly on the clearance angle and the tool wear. Figure 2.3 shows the cutting and feed forces plotted over the total cutting length. The authors do not show a tool wear analyses, but conclude the above mentioned feed force and tool wear correlation based on the force increase with cumulative total cutting length. It was generally stated by KOPLEV et al. [137] that UD CFRP/epoxy machining consists of several brittle fractures, in which each fracture creates a chip and no distinctive plastic deformation occurs.

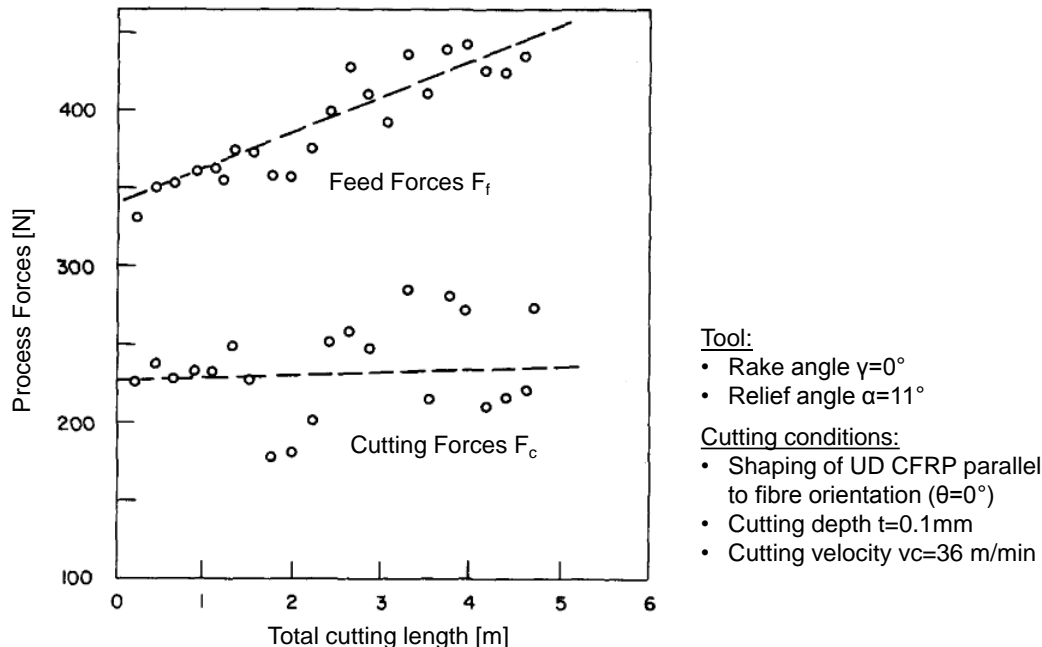


Figure 2.3: Process forces in orthogonal machining of UD CFRP/epoxy according to [137]

CAPRINO et al. [30, 31, 33, 34] conducted orthogonal cutting experiments with a planing setup in unidirectional glass-fibre reinforced polymer (GFRP). Despite the different fibre material, similar chip formation mechanisms occurred. The authors focused on the cutting and feed forces and the influence of tool wear of HSS tools. The reciprocating linear motion parallel to the fibre orientation ($\theta=0^\circ$) of each 400 mm length was performed at a low cutting speed of 0.46 m/min. The authors stated that this low speed is chosen intentionally to avoid thermal

effects. It is assumed that the machining characteristics at such low cutting speeds vary significantly from those at realistic process parameters. The regular analyses of rake and flank face wear validate the findings of KOPLEV et al. [137] that an increasing clearance angle significantly reduces the feed force and the cutting force is only slightly affected by the clearance angle.

WANG et al. [239, 240] present an orthogonal cutting study split into part I about UD and part II about multi-directional graphite/epoxy material. In part I [240] the authors utilized PCD tools in orthogonal machining without considering tool wear, due to a comparably short cutting length. The influence of tool macro-geometry as well as cutting parameters on the chip formation, process forces and the surface topography were analysed. Tests were conducted with tools of 0° , 5° and 10° rake angle and 7° and 17° clearance angle in $\theta=0^\circ$, 15° , 30° , 45° , 60° , 75° and 90° UD CFRP. Low cutting speeds of $v_c = 4, 9$ and 14 m/min were tested. WANG et al. [240] identified the fibre orientation as the key parameter on the material removal, in which mainly three effects and combinations of those occur: Fibre cutting, shearing and fracture along the fibre/matrix interface. Figure 2.4 shows an overview of the identified effects.

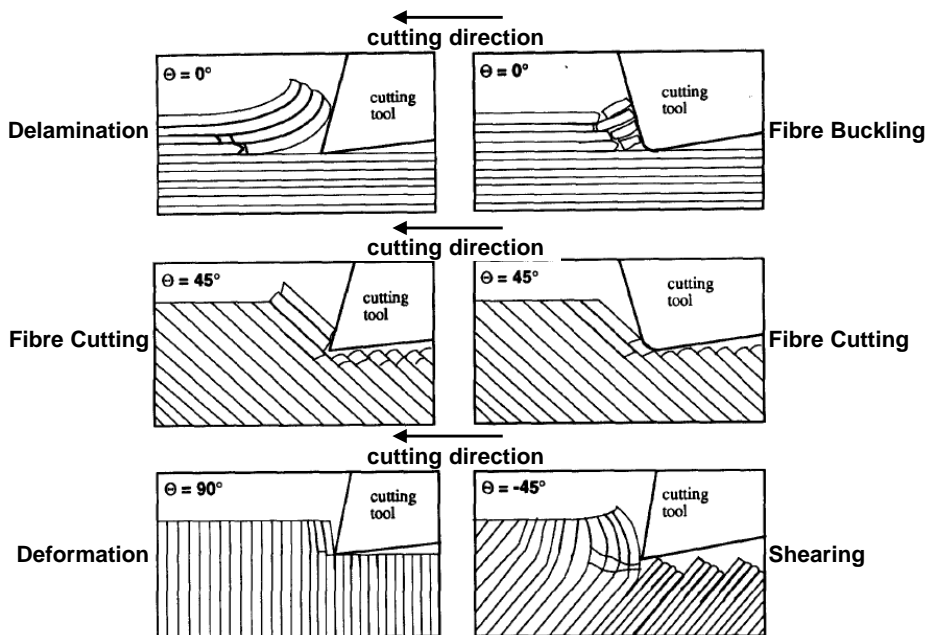


Figure 2.4: Cutting mechanisms in orthogonal machining of UD Gr/Epoxy according to [240]

Furthermore, macro-chip analyses including dimensional measurements were conducted by WANG et al. [240]. Accordingly macro-chips were only obtained for $0^\circ \leq \theta \leq 60^\circ$ and encompass many fractured fibre bundles. Generally stated for $\theta < 45^\circ$ larger chips were formed, while for $\theta > 45^\circ$ discontinuous powder-like chips were noted. For $\theta = 0^\circ$ chips occurred with maximum length of $1500 \mu\text{m}$ and a height being equal to the depth of cut. Machining fibre orientations $90^\circ > \theta > 180^\circ$ generated rather irregular chips, due to a high degree of material displacement, which prevented macro-chip analysis. By means of quick-stop experiments WANG et al. [240] identify that for $0^\circ < \theta < 90^\circ$ chip release always occurred along the fibre/matrix interface, which was confirmed by HENERICHS [101].

A layer of matrix smearing on the machined surface was correspondingly identified by KOPLEV et al. [137] and WANG et al. [240]. With increasing fibre orientation between $0^\circ < \theta < 90^\circ$ the amount of smeared matrix material increased and served to reduce the surface

roughness. The results of the comprehensive analyses by WANG et al. [240] were taken into account for various models e.g. by AROLA and RAMULU [4, 5] or USUI et al. [228]. The findings in part II of the study in multi-directional CFRP/epoxy material by WANG et al. [239] agreed mostly with the findings in part I [240] (UD CFRP/epoxy). Accordingly slightly fewer damages were introduced, due to the support provided by adjacent plies with multiple fibre orientations. The authors suggested an optimum tool geometry for this multi-directional CFRP/epoxy material of 6-7° rake angle and a clearance angle of $\alpha=17^\circ$.

RUMMENHÖLLER [193] focused on the chip generation not only in orthogonal cutting of CFRP but also in contour milling with cutter and milling-heads. The orthogonal machining kinematic was realised by means of a turning insert mounted to a cantilever beam, in which the travelled path is significantly large compared to the engagement conditions. In this setup with cemented carbide inserts of variable geometry, realistic cutting speeds between 50-100 m/min were reached at cutting depths of 20-50 μm . Both the milling cutter and the milling head tools were equipped with PCD and had a diameter of 8 mm and 50 mm, respectively. The processes were investigated by means of high-speed camera recordings as well as SEM analyses of the generated surfaces and particles. A comparison between the failure behaviour of individual carbon fibres under defined load conditions, shown in Figure 2.5, and the findings from the machining operations allowed for conclusions on the chip formation mechanisms.

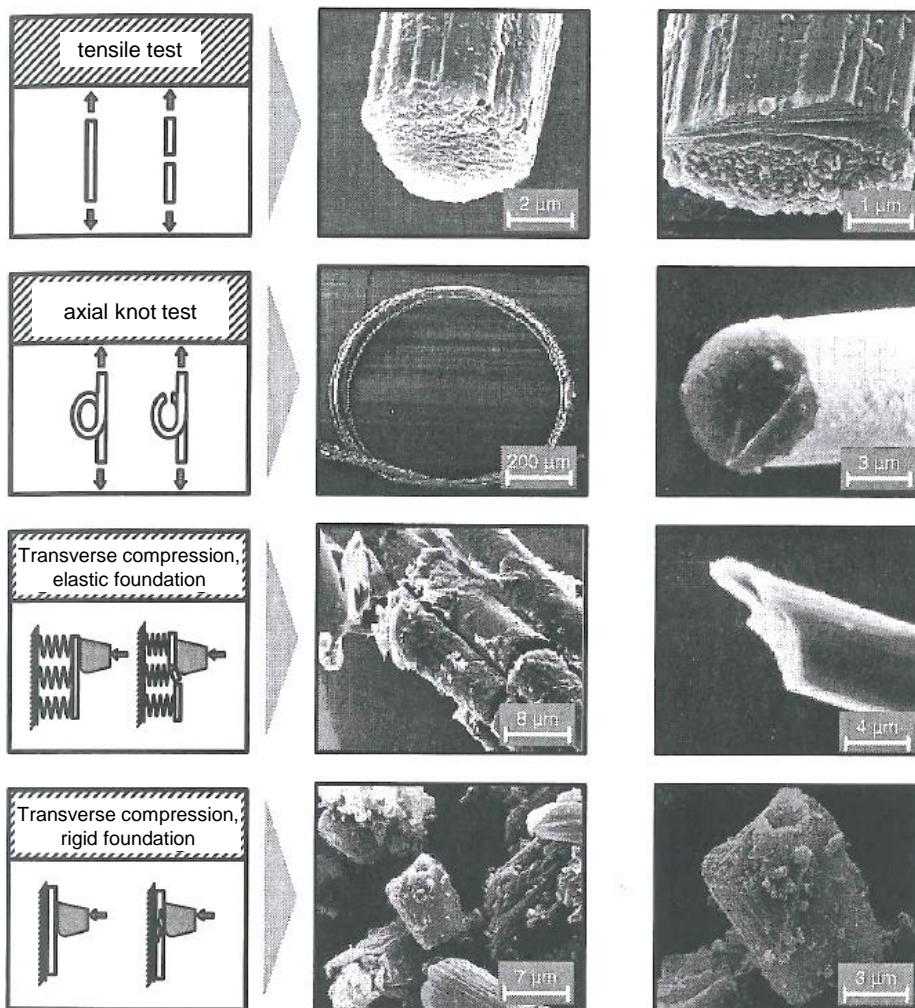


Figure 2.5: Failure behaviour of individual carbon fibres under defined load conditions, according to [193]

RUMMENHÖLLER [193] divided machining of unidirectional CFRP with different fibre orientations into four sections, based on the inherent chip formation mechanisms occurring, as shown in Figure 2.6. These sections were $\theta=0^\circ$ and $\theta=90^\circ$, where the material is cut in fibre orientation and perpendicular, as well as the angular transition regions $0^\circ < \theta < 90^\circ$ and $90^\circ < \theta < 180^\circ$ in between.

$\theta=0^\circ=180^\circ$:

RUMMENHÖLLER [193] detected for $\theta=0^\circ$, where the fibres are parallel to the cutting velocity direction, two possible chip formation mechanisms. These mechanisms are *buckling* and *peeling*, each with single fibre cracks perpendicular to the fibre axis and an advancing interlaminar crack in the laminate. Which of the two mechanisms occurs depends mainly on the tool rake angle and the CFRP properties but also the cutting edge radius has an influence. Due to high cutting speeds and multi-axial stresses further micro-cracks were expected. RUMMENHÖLLER [193] and KOPLEV et al. [137] reported unanimously smooth surfaces with no damages deeper than 1-2 fibre layers below the surface. Furthermore regular, rather large chips in the size of the cutting depth were formed. According to RUMMENHÖLLER [193], machining $\theta=0^\circ$ CFRP with interlaminar cracks is an energy-effective separation mechanism, resulting in low forces and tool wear.

$\theta=90^\circ$:

The load initiation in the composite material is transverse to the fibres and generally results in bending and produces an interlaminar failure, due to shear deformation. The interlaminar cracks spread perpendicular to the cutting velocity and enable chip generation. According to RUMMENHÖLLER [193], these cracks may approach the deeper material levels, which result in (subsurface-)damages of the machined surface. The fibre immediately in front of the cutting edge fails due to exceeding the maximum tensile strength at the outer fibre radius. Subsequently, a crack extends due to the released deformation directly to the next fibre in cutting direction and stops until this fibre is also bent and exceeded the maximum tensile strength. In contrast to CFRP with $\theta=0^\circ$, in $\theta=90^\circ$ each fibre has to be cut by the cutting edge individually. This results in smaller particles and generates strong tool wear. The observations of destroyed surfaces, covered with a layer of matrix material and uncut fibres by KOPLEV et al. [137] are consistent with this theory. The analyses showed damages by bending and breakage up to a depth of 100-300 μm below the surface and the formation of rather irregular chips.

$90^\circ < \theta < 180^\circ$:

Worst machining results were observed by RUMMENHÖLLER [193] in machining fibre orientations between $90^\circ < \theta < 180^\circ$, in particular in the range of 120° - 150° , in which a superposition of the mechanisms of the above two extremes occurs. This fibre orientation leads to an increased bending load on the composite and the pressure on the fibre is reduced. A stress decomposition by buckling of the fibres, comparable to $\theta=0^\circ$, is not possible and the fibres, touching the rake face of the tool, break when exceeding the bending strength. Shear in the matrix layers, due to bending of the fibres, results in interlaminar cracks, which affect the machined surface. According to RUMMENHÖLLER [193], machining CFRP with this fibre orientation ($90^\circ < \theta < 180^\circ$) results in uneven chip formation and poor surface quality. Furthermore disadvantageous chip removal leads to unfavourable wear on the tool rake surface. HENERICHS and VOSS et al. [96, 101, 102, 230] verified a saw-teeth

shaped profile on the machined surface of $\theta=150^\circ$ CFRP material, according to the chip formation mechanisms explained by RUMMENHÖLLER [193] and shown in Figure 2.6.

$0^\circ < \theta < 90^\circ$:

For a range of fibre orientation between $0^\circ < \theta < 90^\circ$ RUMMENHÖLLER [193] stated that the fibres are compressed transverse to the fibre direction and separated by local pressure-peaks right at the cutting edge. Subsequently the separated layer slides along an interlaminar crack and is conveyed along the tool rake face as a chip. This chip forming mechanism was described the same way by HOHENSEE [117]. Comparable to $\theta=0^\circ$ a favourable surface quality is expected.

All the above mentioned idealised cutting mechanisms are superimposed by squeezing and compression processes below the cutting edge. This leads to intensive wear on the flank face, resulting in so-called waterfall wear profiles. To reduce these processes and induce high local stresses, RUMMENHÖLLER [193] recommended tools for CFRP machining with minimum cutting edge radii.

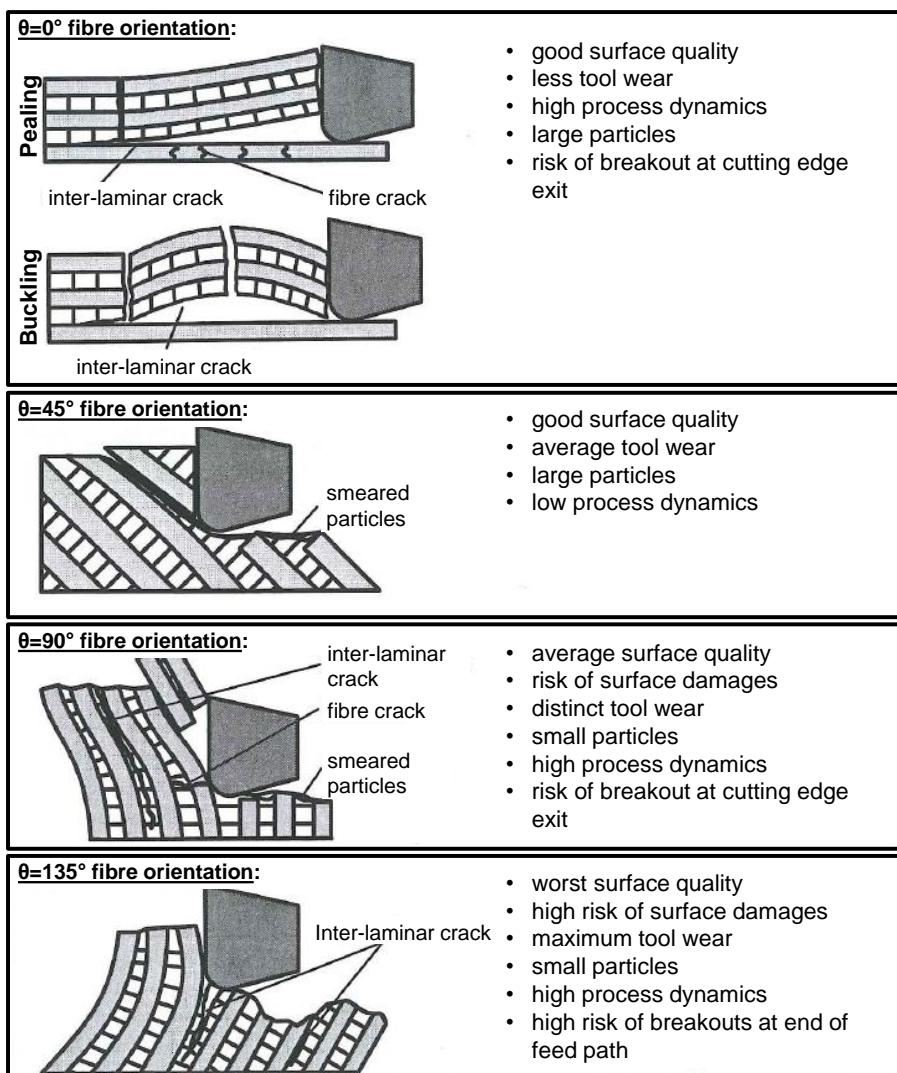


Figure 2.6: Machining mechanisms in UD CFRP and effects on the process, according to [193]

PWU and HOCHENG [176] derived from orthogonal planing experiments in UD CFRP a further chip formation model with a focus on $\theta=90^\circ$ in which most of the findings by KOPLEV [137], WANG [239, 240] and RUMMENHÖLLER [193] were confirmed. Matching these results, the fibre

orientation was found to be the dominant influencing parameter, while the cutting conditions e.g. speed are rather insignificant. In $\theta=90^\circ$ bending is the failure and chip formation mechanism, which was modelled regarding forces, chip length and thickness by beam theory, linear elastic fracture mechanics and laminate mechanics. The model could show the major trend of the experimental planing results in UD CFRP. The authors stated concordantly to SCHÜTTE [204] that defined shearing of the fibres vertical to the fibre-axis cannot be expected, because the cutting edge radius is usually larger (range 10-20 μm) than the fibre diameter (7-10 μm). Instead, the fibres are deflected and fail by exceeding the bending strength, in which the fibres are fractured in tension. With tool advancement, chips are formed assisted by fracture of the matrix between the fibres. The material was modelled as cantilever beam clamped at one end and stressed with a perpendicular concentrated load. Dimensions of the beam were defined by the measured chip thickness and actual depth of cut as well as the measured chip length, which might be larger than the depth of cut, as shown in Figure 2.7.

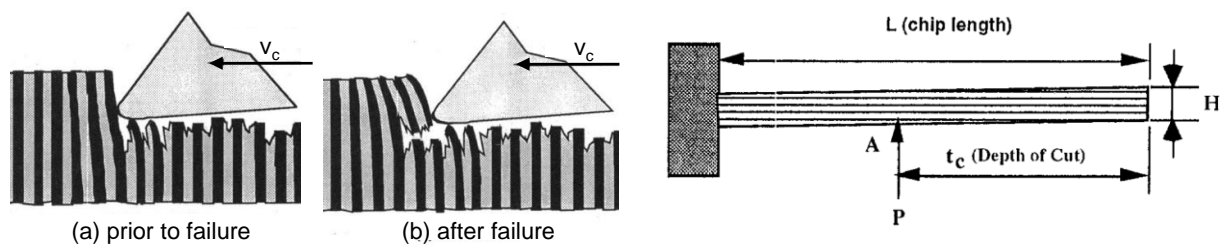


Figure 2.7: Schematic of bending failure in $\theta=90^\circ$ and model as cantilever beam, according to [176]

FERREIRA et al. [75] compared cutting inserts made of various materials, namely ceramics, cemented carbide, cubic boron nitride (CBN) and poly-crystalline diamond (PCD) during turning experiments in CFRP/phenolic material ($V_f=0.35-0.4$). Details about the test rig setup were not presented, but the tests were conducted on a CNC lathe machine with variable cutting velocities between 50 m/min and 310 m/min. The feed rate has been varied in a range of 50-250 $\mu\text{m}/\text{rev}$. Except PCD, all other materials showed a high tool wear rate, in which CBN presented a better wear resistance than ceramics or cemented carbide, as shown on the left in Figure 2.8. While the feed force, which is known to correlate to tool wear and machining quality in machining with PCD tools remained almost constant, in carbide or ceramic tools the feed force increase was remarkable. Consequently PCD tools generated best surface quality. These results extend the experiments by SAKUMA et al. [197, 199], where the tungsten carbide K10 showed best wear resistance but Al_2O_3 , CBN and PCD have not been tested at this time. In contrast to metal machining, the tools in CFRP machining did not show crater wear but distinct asymmetric cutting edge rounding with stronger wear along the flank face (Waterfall profile), due to the abrasiveness of the carbon fibres. SEM analyses by SREEJITH et al. [207] indicated that the PCD tool wear is associated with the well-known abrasion and fatigue induced modes. According FERREIRA et al. [75], the variation of cutting speed showed a strong influence on the tool flank wear, presented on the right in Figure 2.8. The larger the cutting speed, the more intense flank wear (VB) occurs at a certain cutting length, which is more significant for speeds larger than 150 m/min. This may be due to a higher thermo-mechanical load and insufficient heat dissipation at high cutting velocities, which weakens the carbide material, according to SREEJITH et al. [207]. FERREIRA et al. [75]

concluded that cutting conditions are very important and need to be adapted to the chosen tool material and geometry.

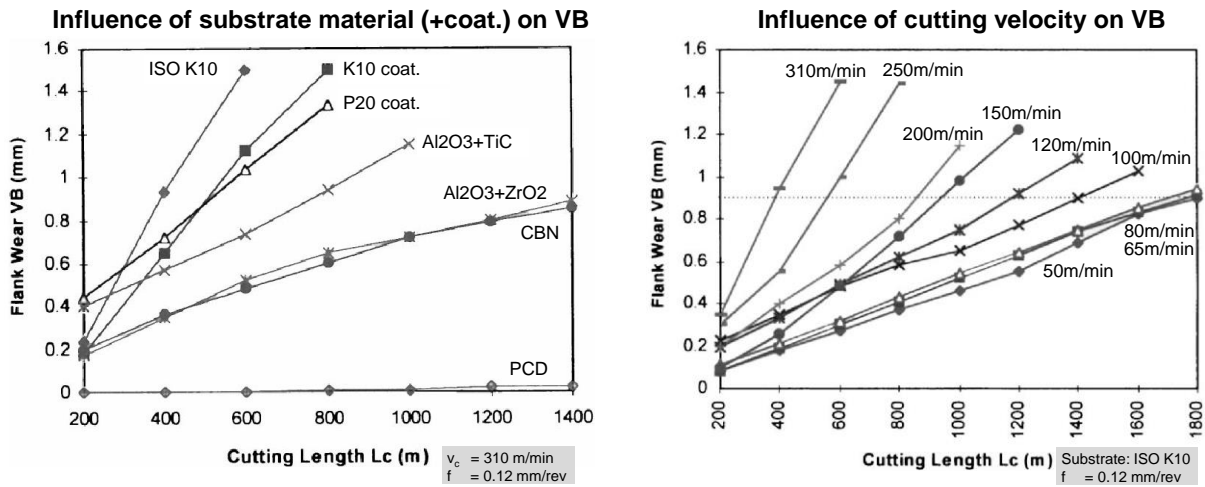


Figure 2.8: Influence of different substrate materials and cutting velocities on the flank wear (VB), according to [75].

SREEJITH et al. [207] also identified the importance of process parameters in face turning operations with PCD tools in CFRP/phenolic material ($\theta=0^\circ$, filament wound) focusing on specific cutting pressures and thermal effects, shown in Figure 2.9. CFRP/phenolic is known for its high temperature resistance. Most effective machining for the specific composite was identified between $v_c=200\text{-}300 \text{ m/min}$ and a critical cutting speed ($v_{c,crit}=300 \text{ m/min}$) exists above which the machining performance deteriorates. Temperature measurements with infrared pyrometer showed almost a steady state ($T=300\text{-}350^\circ\text{C}$) in the most effective machining range and a dramatic temperature increase beyond the critical cutting speed up to a maximum of 475°C at $v_c=400 \text{ m/min}$. The authors concluded that in the steady state the heat dissipation by the carbon and phenolic material is sufficient to keep the temperature constant, but above $v_{c,crit}$ dissipation is not sufficient and temperature increases.

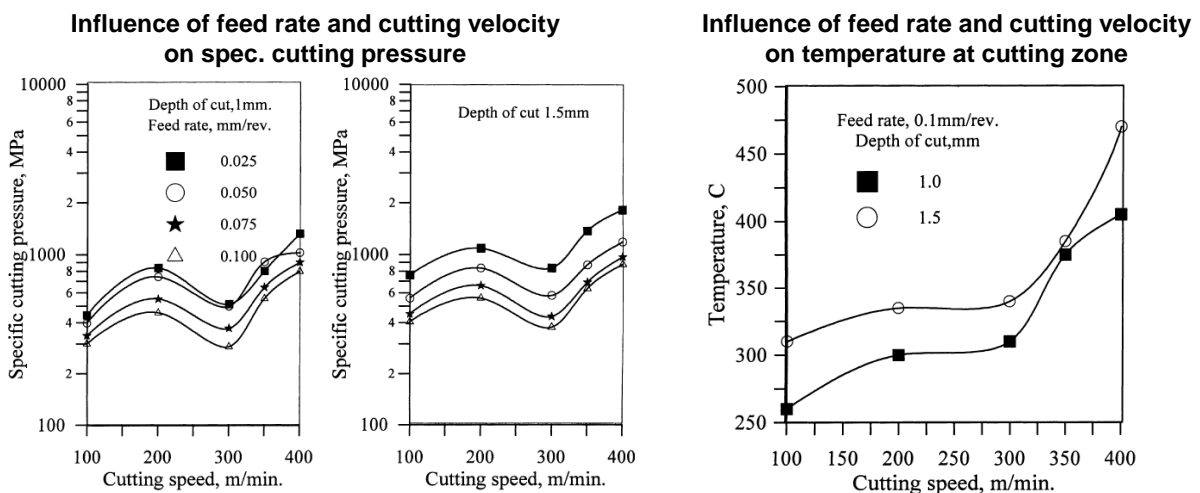


Figure 2.9: Influence of feed rate and cutting speed on specific cutting pressure and temperature in CFRP/phenolic with PCD tools, according to [207]

SCHÜTTE [204] provides an important contribution to the optimisation of CFRP machining by specifically analysing the influence of the setting (κ_r) and inclination angles (λ_s) in fundamental planing. But certainly the large wedge angle of the utilised tools and the rather

low cutting speed impede the direct transferability to a drilling process. Generally the influence of the fibre cutting angle, the setting angle (κ_r) and the inclination angle (λ_s) were analysed during fundamental planing experiments in UD CFRP/epoxy laminates. A certain PCD tool with constant side clearance (12°) and side rake (0°) angle was utilised for several experiments. The experiments were conducted in free orthogonal machining setup with $\kappa_r=90^\circ$ and $\lambda_s=0^\circ$, as shown on the top right in Figure 2.10, but also with deviating angles from the free orthogonal cutting setup ($\kappa_r<90^\circ$ and $\lambda_s<0^\circ$). This variation of setting and inclination angle corresponds to the cutting conditions in drilling. Furthermore according to SCHÜTTE [204], the constant chip thickness and cutting speed of $30\ \mu\text{m}$ and $5\ \text{m/min}$ match the values during drilling operations in CFRP. However, the influence of tool wear on the chip formation mechanisms was neglected in the experimental data analysis, based on the fact that the initial cutting edge radius $r_{\text{peak}}=10\ \mu\text{m}$ already exceeds the fibre diameter ($\sim 5\text{-}8\ \mu\text{m}$).

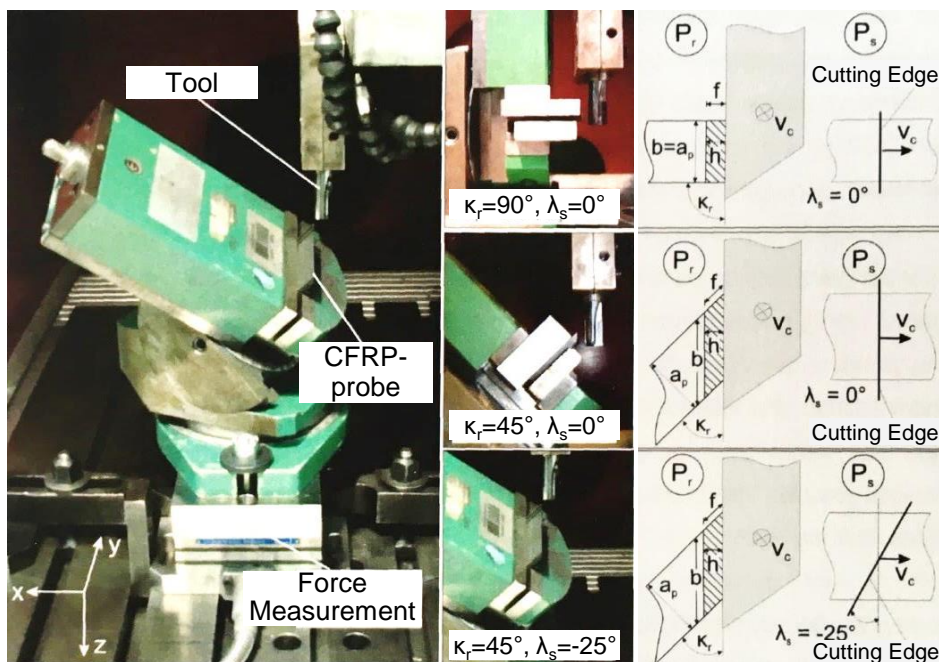


Figure 2.10: Test rig for planing of UD CFRP/Epoxy, according to [204]

HENERICHS and VOSS et al. [62, 96, 101, 102, 230] developed a test rig setup enabling orthogonal machining of unidirectional CFRP in a turning operation. It has the advantage over planing and shaping of potential cutting velocities up to $500\ \text{m/min}$ and an effective continuous cut. The force analyses were in accordance with the observations by KOPLEV et al. [137] and WANG et al. [238-240]. HENERICHS and VOSS et al. [96, 101, 102, 230] took a deeper look to the influence of tool geometry on tool wear. Basically, the smaller the clearance angle α , the significantly larger is the width of flank wear (VB) at a certain cutting length. Increasing the rake angle leads to a minor reduction of flank wear. The fibre orientations $\theta=30^\circ$ and $\theta=60^\circ$ caused maximum tool wear whereas $\theta=150^\circ$ generated minimum process forces and tool wear. Detailed 3D measurements of worn tool profiles showed a significant influence of fibre orientation on the tool micro-geometry. In two additional works [62, 96] ground PCD fine grain tools were compared in orthogonal cutting to lasered PCD mix grain tools and lasered CVD diamond tools, generated with a nano-second pulsed laser system. The differences in machining forces between the ground and lasered PCD tools were rather small but the utilisation of lasered CVD diamond tools improved the wear resistance significantly, due to an increased hardness and the avoidance of washing out of cobalt matrix compared to PCD.

2.1.2 Fundamental milling

As explained in 2.1.1, most of the fundamental experiments for process knowledge generation were conducted in orthogonal cutting. Conducting fundamental milling experiments, which is a process with interrupted cuts was given less attention in the research community; but nevertheless it may obtain important insights on the machinability of CFRP. Comparable to orthogonal cutting experiments, single-edged milling experiments aim to increase process knowledge by reducing complexity of a conventional slot milling process. Common simplifications are the utilisation of cutter heads with one cutting edge installed to assign the forces to a single engaged blade, and tools with 0° helix angle to generate forces only in laminate plane direction. In contrast to orthogonal turning, milling is characterised by interrupted cuts and variation of theoretical chip thickness during tool rotation. Most challenging in CFRP machining are introduced workpiece damages and the enormous tool wear, described by FERREIRA et al. [75], HENERICHS et al. [102] and HOCHENG et al. [112].

AN et al. [2] compared the process forces for two different UD CFRP materials namely T700 and T800 in machining with a tool mounted to an adapted flywheel. Material T700 and T800 differ in the tensile strength of 2450 MPa compared to 2840 MPa and the tensile modulus of 125 GPa and 168 GPa respectively. Cutting speeds and cutting depths were varied in a range of 100-300 m/min and 5-25 $\mu\text{m}/\text{rev}$. According to the measurements, larger cutting and feed forces occurred for T800, the material with larger tensile strength and modulus. The trend of the cutting forces F_c plotted over the fibre orientation corresponds to experiments by HENERICHS et al. [102] and WANG et al. [240] but the feed forces F_f slightly differ; maximum feed forces occurred at $\theta=90^\circ$, instead of $30^\circ \leq \theta \leq 60^\circ$ as shown in the aforementioned orthogonal machining experiments [102, 240]. Furthermore, AN et al. [2] calculated the specific cutting energy, which was decreasing with increasing cutting depth. Accordingly improved machinability occurs for increased cutting depths. An exception occurs for the fibre orientation of $\theta=90^\circ$, in which the specific cutting energy maintained stable after the cutting depth exceeded the fibre diameter (6-8 μm). Consequently, the authors concluded that the machinability of $\theta=90^\circ$ is not affected by the cutting depth.

COLLIGAN and RAMULU [47, 48] conducted edge trimming experiments at CFRP plates with various laminate layers and fibre orientations. The authors classified three fundamental types of delamination, shown in Figure 2.11. Type I shows broken fibres some distance inward from the trimmed edge. Type II has protruding uncut fibres and may be delaminated from the ply below at a certain distance from the milled edge. Type III describes loose fibres which are partially attached to the milled edge, causing a fuzzy appearance. The authors stated in [47, 48] that delamination in milling is mainly caused by lacking support of the top laminate layers.

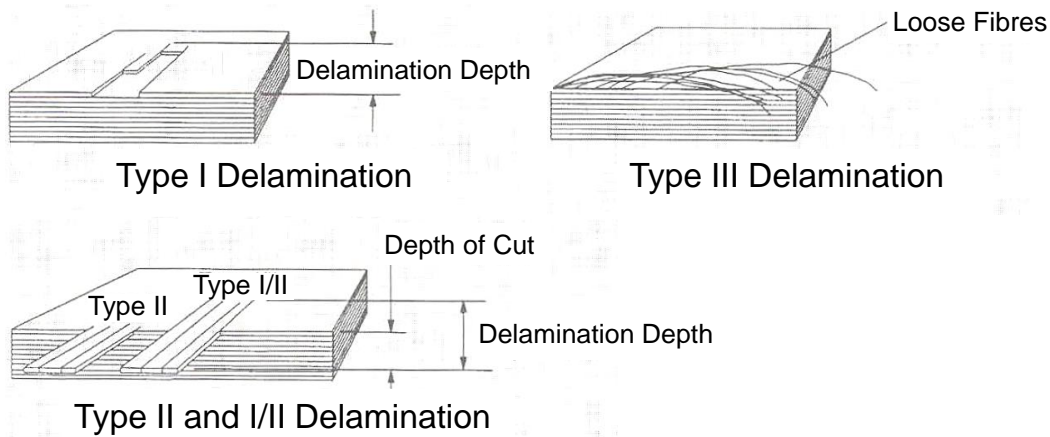


Figure 2.11: Classification of Delamination, according to COLLIGAN and RAMULU [47, 48].

HOHENSEE [117] and RUMMENHÖLLER [193] confirmed the finding of mainly top layers delaminating in milling and identify a huge influence of tool sharpness on the resulting workpiece quality. HOHENSEE [117] defined the angle between cutting velocity and fibre direction as the fibre cutting angle which changes continuously during tool rotation. ZHANG et al. [265] conducted CFRP drilling experiments and identified a *main* and *secondary spalling region* around the bore exit where delamination primarily exists but does not show a systematic relationship to the fibre cutting angle. This systematic scheme between fibre cutting angle and delamination was explained by HINTZE et al. [107] in milling experiments with variable fibre orientations. The authors distinguished two delamination effects: *Generation of delamination* and *propagation of delamination*, as presented in Figure 2.12. The first effect occurs in the fibre cutting angle range $0^\circ < \phi < 90^\circ$ of the milled edge, where fibres tend to evade the cutting edge and thus delamination may be generated. The latter effect occurs, if a certain fibre is initially delaminated under critical fibre cutting angle $0^\circ < \phi < 90^\circ$ and propagates with progressing feed rate to an actually non-critical fibre cutting angle range of $90^\circ \leq \phi < 180^\circ$. Consequently, the history of delamination propagation of the top layer fibres is considered. Furthermore HINTZE et al. [107] confirmed the statement of various research teams [48, 83, 117] that the condition of the tool has a key influence on the occurrence of delamination. A worn CFRP cutting tool is characterised by a rounded cutting edge with increasing peak radius and generates more damages along the milled edge.

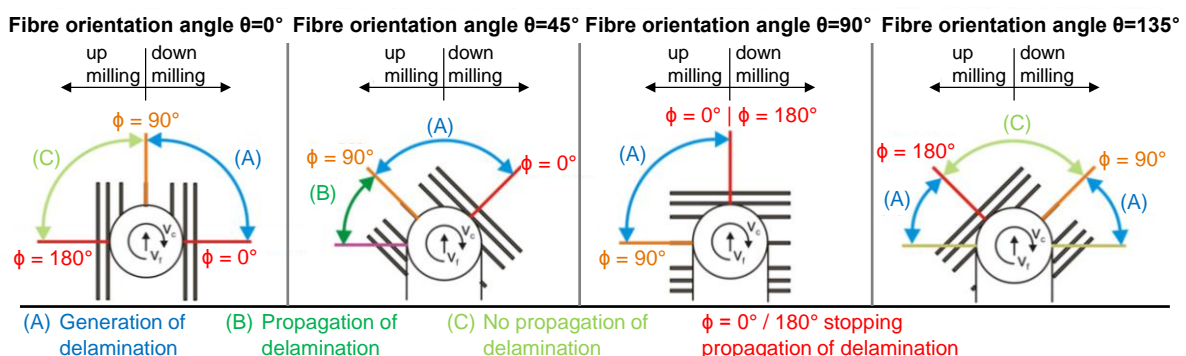


Figure 2.12: Systematic scheme for describing the occurrence of delamination in milling, according to [107]

Based on the experimental study in [107], HINTZE and HARTMANN [108] modelled the relation between the minimum damage depth, the fibre orientation and fibre properties as well as the actual occurring uncut fibres. The authors used elementary bending models to state that

fibre-protrusion at milled edges is always associated with delamination. Deflection and delamination occur as long the damage depth Δ_i of the fibres, initiated by the milling process, is larger than the required damage depth Δ_c for fibre or fibre bundle deflection. Calculations of the required damage depths are based on the ultimate tensile strain as well as the fibre diameter or fibre bundle diameter.

Slot-milling experiments were conducted by DAVIM et al. [52], which come up with the feed rate as main influencing variable on both the delamination factor and surface roughness but an explanation of these effects was missing. However, surface roughness is not a sufficient parameter to describe the machining quality in CFRP since subsurface damages may occur, among others stated by AROLA and RAMULU [7] as well as GHIDOSSI et al. [83]. Nevertheless many authors e.g. in [90, 112, 152] used the simple measurable surface roughness at least as one of many analysing methods to describe CFRP surface quality in milling.

According to TETI [218], top layer delamination in contour milling may be avoided only by using tools with opposed helix which orient the forces from the top and bottom CFRP layers to the middle. In these processes an accurate axial alignment of the workpiece relative to the tool is necessary. TETI [218] stated that a limitation of these tools is the insufficient chip transport which tends to clog-up the chip flutes when milling thick workpieces. In these cases, split helix milling cutters, which introduce alternating stresses on the two top layers, could reduce delamination compared to standard tools. But the dynamic stresses could certainly result in unacceptable vibration and chatter. Some additional studies [52, 92, 131] compared fundamentally different tool concepts such as compression end mills, multi-tooth end mills, slot cutter heads or insert cutter heads, as shown in Figure 2.13. HAGINO and INOUE [90] tested three different tools with variable helix angle but constant rake and clearance angle in side milling operations (edge trimming). With increasing helix angle the axial force increases, which generates damage-free edges by compression at the lower CFRP surface but at the same time the extend and number of delaminated layers at the top CFRP surface increases.

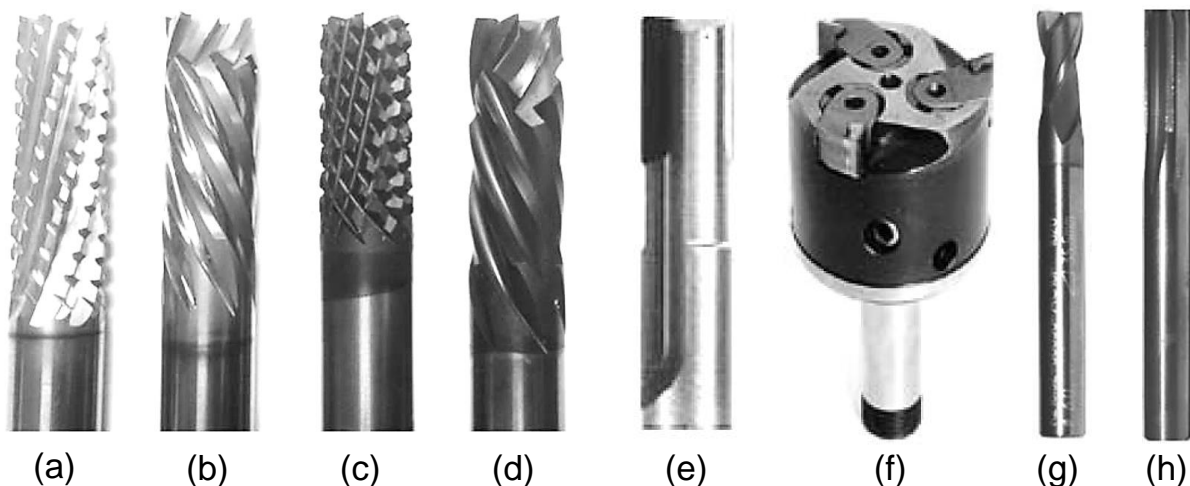


Figure 2.13: Exemplary multitooth (a,c), compression double helix (b,d), slot cutter (e,h), insert cutter (f) and two flute single helix (g) milling tools for CFRP according to [52, 92, 131]

2.1.3 Drilling process

The overview of industrial applications in Chapter 1 shows that about 50% of modern airplanes are manufactured of CFRP components. Even though the CFRP laminating technologies have advanced and it is possible to produce these components near-net-shape, it is still necessary to perform machining operations for joining and assembly, as stated by ENEYEW [67]. According to AURICH [10] and ENEYEW [67], these components are still joint by rivet or fastener connections, since the epoxy based CFRP cannot be welded. SCHOMAKER et al. [200] stated that adhesives e.g. liquid shims are currently not used for joining of structural components in large civil airplanes but for sealing and spacers to fill gaps in between two components. WITTEN [249] noted that bolt connections, in contrast to adhering and welding are not the ideal joining method for FRPs, because of spot wise force introduction and material weakening by interrupting the fibre flow in the component. Nonetheless fasteners have prevailed in large civil aircrafts due to maintenance friendliness by detachability as well as diverse applicability by joining possibility of different materials. For large size holes, a core can be placed in the mold during laminating and curing to prevent interruption of fibre flow in the component. But for smaller sized holes, such as for rivets and small fasteners, drilling is the preparation method of choice, as stated by ENEYEW [67]. According to KLOCKE and KÖNIG [132], drilling is a manufacturing method with a main rotational cutting motion and a superimposed axial movement. Drilling is specified in the standard DIN8589b and distinguished by the following characteristics:

- Varying cutting velocity along the main cutting edges down to zero in the tool centre
- Difficult chip evacuation
- Unfavourable heat distribution at the cutting edges
- Increased wear at the sharp cutting edge corners
- Rubbing at the peripheral land of the drill

The zero cutting velocity in the tool centre results in an effective direction angle of $\eta=90^\circ$, which is continuously reduced with increasing radii along the cutting edges to usually $\eta \ll 1^\circ$ at the cutting edge corner. Figure 2.14 shows an illustration of a drilling operation in multilayer CFRP with two exemplary cutting velocities. It is apparent on the left in Figure 2.14 (top view) that the main cutting edges of a spiral drill are usually offset to the main axis of symmetry due to the core of the drill. This geometric conditions result in a not orthogonally oriented cutting force to the main cutting edge and the rake and clearance angle in the tool-in-use system vary along the tool radius. DAVIM [54] stated that in CFRP drilling usually low forces occur and delicate tools may be applied, but nevertheless a core and thus a chisel edge is still necessary, visible on the left in Figure 2.14. This chisel edge usually has unfavourable negative rake and clearance angles in contrast to the main cutting edges. Due to a lack of plastic deformation of CFRP, this area of negative rake angle is the starting point of delamination, as stated by TSAO and HOCHENG [222]. With advancing of the tool in feed direction and complete penetration of the workpiece, the delamination may extend to or even exceed the bore edge. Whether the starting delamination in the tool centre exceeds the bore edge or is removed before by a clean cut is influenced by the tool geometry, CFRP material properties and process parameters. LAZAR [146] stated that roughly 50% of the thrust force in drilling with an exemplary web thickness equal to 20% of the diameter attribute to the chisel edge. To improve the geometry along the chisel edge, several authors [67, 98, 146, 173] recommend the application of a web thinning in CFRP machining. According to TOENSHOFF

[220], this method reduces the initial length of the chisel edge and thus reduces the feed forces, while it has almost no influence on the torque. Nevertheless disadvantageous conditions of low cutting velocity ($v_c \ll v_{c,max}$) and large effective direction angles ($\eta \gg 0^\circ$) are still present at the chisel edge and lead to difficulties in machining. In literature and industrial applications a wide variety of drill point geometries such as web thinned point, split point or conical point etc. have been developed to improve the drilling performance regarding centre ability, thrust force and rigidity.

In contrast to metal machining, CFRP forms dust-like chips in the dimension of micrometres and thus chip extraction through the chip flute may be simplified by fluid dynamical conditions, as analysed by WÜRTZ [252]; grinding of the chips along the bore channel, as known from metal machining is omitted.

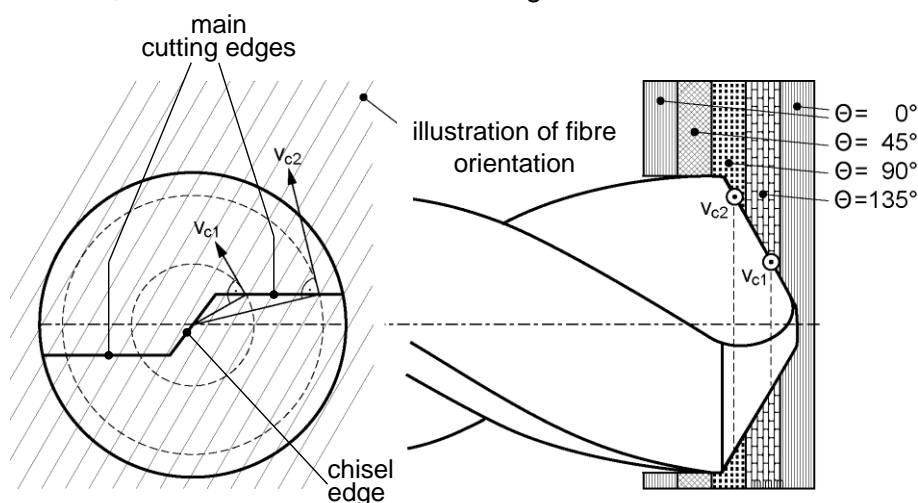


Figure 2.14: Illustration of drilling operation in CFRP with exemplary cutting velocities, according to [101].

Research in CFRP drilling started in 1984 with an experimental study by SAKUMA and SETO [198], comparing wear and machining quality in GFRP and CFRP. Cemented carbide K01 was found to show better tool wear resistance compared to HSS and ultra-fine grain carbides, but in general the wear amount in CFRP drilling is several times the wear in GFRP. The wear width on flank face (VB) increased from the drill centre to the peripheral part as well as throughout the drilling series except at the early stage. SAKUMA and SETO [198] identified *combing wear* along the flank face, which presumably was produced by chipping in the early stage of the drilling series and fine faults. These initial defects lead to concentration of the fibres in the hollows and thus groove-like wear is accelerated.

GRASS [86] conducted fundamental drilling experiments in GFRP, CFRP and AFRP thermoset materials. The fundamental fibre fracture mechanisms were analysed as well as typical drilling quality evaluations in FRP with a focus on the bore channel surface, the bore exit damages and the dimensional accuracy. GRASS [86] identified the damages of top layers at the bore exit side as critical, which are mainly influenced by the workpiece material and the load. The load introduced by the machining operation depends on the process parameters as well as the tool geometry and material. According to the experiments in [86], thermal measurements show higher temperatures of up to 200°C in CFRP drilling compared to 170°C in GFRP drilling. Although the thermal conductivity is better in CFRP, the higher fibre strength of CFRP is responsible for these results. The larger the tool diameter, which leads to a higher heat capacity of the tool and reduced specific machined volume, the lower

is the maximum temperature in the drilling operation. Figure 2.15 shows the energy distribution divided into the main three shares: Tool, workpiece and chip. Compared to metal drilling, in FRPs a significantly smaller amount of energy is conveyed with the chips and the relative thermal load on the tool is increased. The better heat conductivity of CFRP compared to GFRP leads to a higher heat capacity of the workpiece. A reduction of the thermal stress in a FRP drilling process is possible by selectively short immersion lengths, short dwell times and high re-feed speeds. Consistently PIQUET [173] states that the tool mainly removes the heat produced by the machining. In agreement with the free orthogonal machining results in 2.1.1, GRASS [86] identified in the drilling experiments intensive tool wear in form of cutting edge rounding amplified at the flank face, leading to rapidly increasing feed forces and decreasing machining quality. Based on the criterion “damage free”, a tool lifetime ratio of PCD to carbide drills from 50/15 is achieved. MILLER [162] presented further experimental data on drilling CFRP/epoxy with a focus on minimum machining damages and optimum drilling conditions.

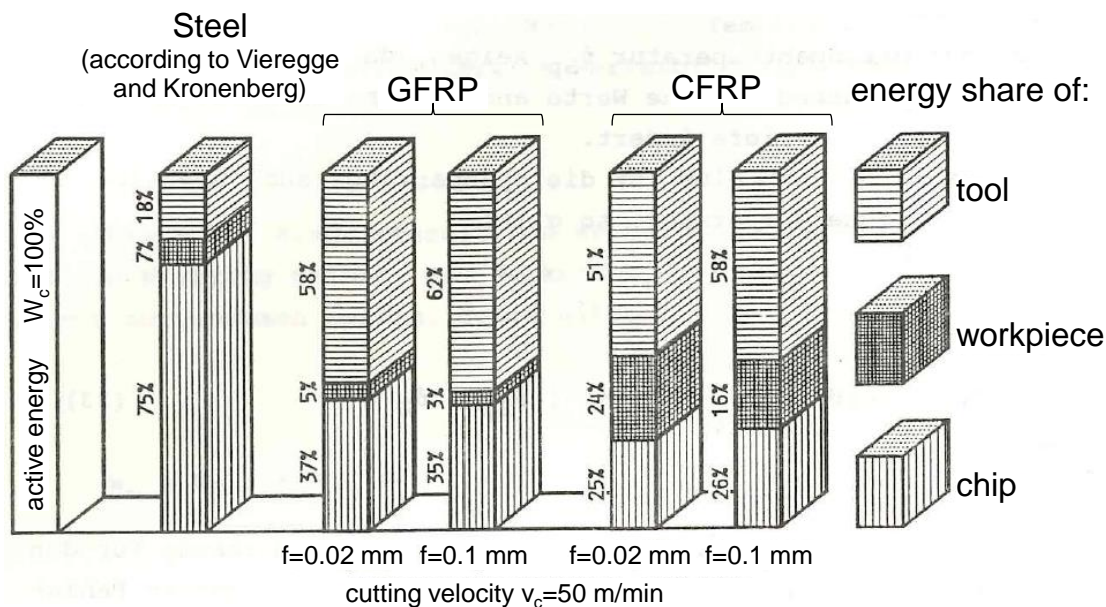


Figure 2.15: Energy distribution in drilling of CFRP and GFRP, according to [86]

Several publications [10, 67, 88, 89, 109-111, 135, 147, 158, 179, 234] in CFRP drilling focused on the most frequent damages, which are delamination, fibre pull-out, interlaminar cracking and thermal defects. To reduce these damages some publications [61, 135, 157, 158, 162, 173] focused on the optimisation of process parameters while others [73, 89, 109, 173, 251] analysed the influence of tool geometry variation. Experimental studies in CFRP drilling were mostly conducted with uncoated [44, 51, 64, 72, 173, 198] or diamond coated carbide tools [98, 121, 244] but also PCD tools [23, 125-127] were utilised. Former publications e.g. by TETI [218] reported a much shorter tool lifetime for diamond coated carbide tools at reasonable cutting speeds, due to a degradation of coating adhesion to the substrate material. But nowadays CVD diamond coating adhesion has improved and MAEGAWA et al. [153] showed possible advantages of two layer tools with different hardness distribution. In general the publications in CFRP drilling compare various drill geometries, coatings and process parameters, which were evaluated based on the bore quality, process forces and tool life time. Chapter 2.2 in this thesis summarises evaluation criteria for the bore quality in CFRP drilling. The key findings in CFRP drilling mostly confirm the results of the fundamental experiments, as shown by SCHÜTTE [204]. He transferred the findings from

fundamental planing experiments in UD CFRP/epoxy laminates to conventional drilling operations. The complex geometrical conditions in drilling differ from planing in variable fibre cutting angle, setting angle $\kappa \neq 90^\circ$ and inclination angle $\lambda < 0$. SCHÜTTE [204] provides an important contribution to the generation of process knowledge and optimisation of CFRP drilling. But an exceptionally large wedge angle of the utilised tools and a low cutting speed ($v_c = 5$ m/min) in the fundamental planing experiments impede the direct transferability to common drilling operations in CFRP.

WU [251] analysed the influence of multifacet drills (MFD), which showed chisel edge lengths of only 2% of the tool diameter to reduce the thrust force. In conjunction with other features the authors expected to achieve reduced cutting forces, strengthening of the drill centre, speeding up heat transfer, improving center-up tendency and facilitating chip extraction. Based on the experimental data, a point angle decrease to 100° - 110° was recommended in order to reduce the temperature of the periphery and the feed forces. MATHEW [158] compared conventional drilling with trepanning in UD FRPs and developed a critical feed rate model for each process. It was found that trepanning enables utilisation of up to 16 times higher feed rates compared to spiral drills. The main influencing variable on the critical feed rate for push-out delamination is the uncut material thickness (sub-laminate).

KÖNIG and GRASS [136] stated that drilling operations on cured parts are mostly conducted at the end of the production sequence and thus fail safe drilling of these components is of particular importance. WONG [250] estimated that 60% of all part rejections in aerospace industry account for poor hole quality. According to RAMULU [181] and ENEYEW [67], non-traditional bore generating methods e.g. (abrasive-)water jet (WJ), electron discharge machining (EDM) and electro chemical machining (ECM) show currently various drawbacks, such as melted matrix material or moisture absorption of the CFRP. Consequently, conventional drilling with spiral drills is still the most economic and convenient operation for bore initiation in composites, as stated by HOCHENG [116], even though this method may reach its limits in certain hard to machine UD CFRP requiring rework. These limits are mostly reached in terms of workpiece quality and tool lifetime (heavy wear). Several authors [10, 67, 73, 88, 147, 179, 234, 266] report that the inherent inhomogeneity and anisotropy of CFRP in combination with unfavourable conditions in the drilling tool centre may lead to critical damages in drilling, such as pull-out of single fibres, delamination and matrix cracking due to intrinsic weakness of the epoxy, uncut fibres, deviation of roundness and bore diameter, in extreme cases even resin degradation caused by low head conductivity. To overcome these limits different process strategies were established. ZACKRISSON et al. [263] developed a new process strategy at the Department of Aeronautics at Royal Institute of Technology (KTH) in Stockholm. This strategy was called KTH-method and superimposed an additional eccentrically revolution on the conventional drilling process resulting in a helical path, as shown in Figure 2.16. In this process the material is machined both, axially and radially by rotating the cutting tool about its own axis, as well as eccentrically about the principle axis while feeding the tool through the material. This method is characterised by elimination of the stationary tool centre and thus a substantially reduction of the axial forces. Furthermore the tool diameter is smaller than the bore diameter, resulting in improved chip transport and heat dissipation (cooling). By adjusting the eccentricity of the revolving motion, several bore diameters may be generated with a tool of one diameter. It was stated by ZACKRISSON et al. [263] that the bore diameter precision is determined by the precision of the tool positioning, rather than by the precision of the tool itself. PERSSON [170] compares the mechanical

strength of bores introduced by conventional drilling and the so called KTH-method in CFRP, in which the bores generated by KTH showed a better quality. Subsequently several authors [10, 13, 20, 21, 56, 57, 70, 71, 123, 130, 145, 149, 150, 168, 196, 202, 214] recommended machining of CFRP with the KTH-method or slightly adjusted strategies, each trying to avoid the unfavourable conditions in conventional drilling. From 2001 to 2004 researchers [123, 130, 145, 149, 150] at the Linköping University in Sweden analysed the influence of orbital drilling (KTH-method), also called circular milling or helical milling on the machining quality in CFRP. Helical milling is characterised by continuous cuts at the frontal cutting edges, represented by the red volume in Figure 2.16 (right) and discontinues cutting at the peripheral lands, marked green/blue. The bore diameter depends on both the tool geometry and the eccentricity of the tool axis to the principle bore axis. KIHLMAN et al. [130] identified a thrust force reduction by factor 8 compared to conventional drilling. Boosted by promising bore qualities in CFRP this machining process was further investigated by BRINKSMEIER and FANGMANN et al. [20, 21, 70, 71], DENKENA et al. [56, 57], BECKE and SCHULZE [13, 202], SAKAMOTO et al. [196] and AURICH et al. [10]. BRINKSMEIER and FANGMANN [20] showed the potential for high tolerance boreholes by static and dynamic adjustments of the process eccentricity in orbital drilling of Al/CFRP stack materials. The good results were explained by avoiding the stationary tool centre (zero cutting velocity) compared to conventional drilling and reducing the axial forces by cutting a certain material volume with the peripheral cutting edges. Since discontinuous cutting is performed at the peripheral lands, smaller chips are generated even in metal machining, which results in better bore channel quality. DENKENA et al. [56] modelled the relationship of the undeformed chip thickness and explained the influence of the axial and tangential feed per tooth on process forces. The detailed kinematic and chip forming models of orbital drilling processes were explained independently by BRINKSMEIER et al. [21] and DENKENA et al. [57]. Accordingly the ratio between drilled and milled volume affects the bore quality and depends on the ratio between bore and tool diameter.

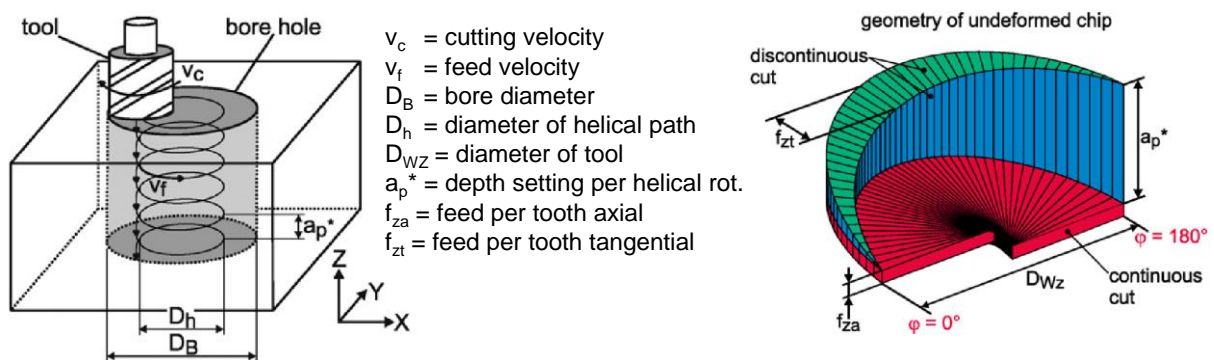


Figure 2.16: Orbital drilling kinematics and form of undeformed chip, according to [56]

A further adaptation of the original conventional drilling kinematics to tilted planetary drilling, also called wobble milling or tilted planetary milling, was proposed by BECKE [13] and TANAKA et al. [168, 214]. Figure 2.17 (left) shows the kinematics, where the axis of tool rotation is not parallel to the axis of planetary motion. The tilt angle and distance from tool tip to the centre of planetary motion determine the resulting bore diameter. According to TANAKA et al. [215] delamination and burrs in CFRP drilling were avoided, since the tool penetrates the CFRP layers with the inner cutting edges first and with advancing feed rate the outermost edges enlarge the drilled bore, as shown in Figure 2.17 (right). BECKE [13] presented several processing strategies and reported for 3-axis circular milling and 5-axis wobble milling a high

potential for damage reduction compared to conventional drilling. In a further strategy to the above mentioned ones, the rotating tool could introduce a bore with an axial feed process (drilling) and thereafter widen the bore with a tangential feed process (milling). Figure 2.18 shows a comparison of exemplary conventional and orbital drilling tools.

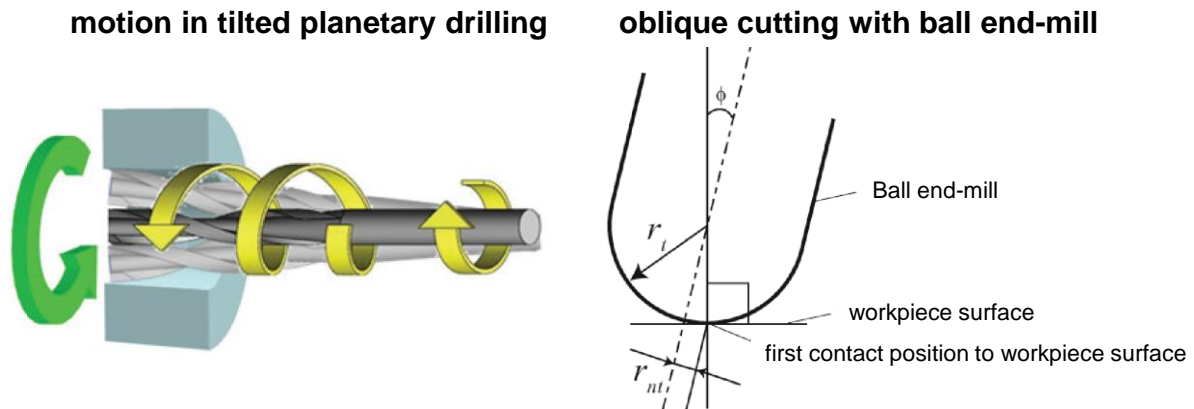


Figure 2.17: Tilted planetary drilling kinematics and contact conditions, according to [215]



Figure 2.18: Tool geometries for conventional drilling of CFRP in contrast to orbital and tilted planetary drilling, according to [13, 215]

Either for conducting orbital drilling (circular/helical milling) or for tilted planetary drilling (wobble milling) highly dynamic machine tools are necessary to generate bores not just in equal or better quality compared to conventional drilling but also in reasonable processing time. Furthermore the machine tools have to be precise, since the bore diameter (D_B) is not primarily given by the tool diameter but mainly by the NC control. In this way a regular decreasing bore diameter due to wear may be adjusted to a certain degree by the NC code and variable bore diameters can be created with one tool geometry. Additionally orbital drilling spindles exist, which realise the eccentric orbital motion with several servomotors or gears. Such prototypes were shown by LINDQVIST [149] or by OHTA et al. [168].

2.2 Bore quality in CFRP drilling

Quality control for drilling operations is established for metals, but full adaptation for FRPs has not been conducted yet. KÖNIG et al. [135] stated that the most commonly used quality criteria in metal machining, such as the characteristic values for detecting roughness, shape and dimensional accuracy, have to be supplemented with material typical parameters to describe the amount of delamination, fraying or uncut fibres. These latter mentioned effects describe the affection of the inhomogeneous materials by the machining operations. KÖNIG et al. [135] noted already in 1985 that standardisation of measurement techniques in FRP machining was not existing and even today no uniform quality measurement techniques exist. Various studies [15, 44, 61, 108, 110, 122, 135, 136, 158, 191, 225, 243, 268] confirm the occurrence of delamination, uncut fibres and fibre pull-outs at the bore entrance, exit or bore channel. The machining quality highly depends on the relative fibre orientation, as stated by GRASS [86]. According to ZEMANN et al. [264] the amount of damage, induced by a machining process depends on the workpiece material (fibre, matrix), the tool characteristics (geometry, wear state) and the process parameters (cutting speed and feed velocity). HAKE and ZEMANN [91] showed that even the position of the bore on CFRP surface with certain roving pattern influences the occurrence of delamination, due to varying fibre cutting angle during tool rotation. The following most common quality limiting factors in CFRP drilling are presented below and are used to structure the state of the art:

- Inappropriate bore channel form and roughness
- Bore entrance and exit damages (e.g. delamination)
- Insufficient mechanical strength
- Bore channel and subsurface damages (e.g. cracks)

2.2.1 Form and roughness

RAMULU et al. [180] stated that surface roughness and bore tolerances are closely related, since a smooth surface finish is necessary to maintain a fine tolerance. Measurements of the bore diameter and cylindricity have been transferred from metal machining to CFRP machining. Although inhomogeneous CFRP generates more irregular bore channel surfaces, the bore diameters for rivets or fasteners in structural components require being within tight tolerances. According to TOENSHOFF and DENKENA [220] in these components with high dimension and shape accuracy the utilisation of reamers may be necessary. It is a finishing process with small depths of cut and multiple edged tools. In this way tolerances of IT7 or even IT6 can be achieved with surface roughness of $R_z \sim 5 \mu\text{m}$. Either NC-controlled coordinate measurement devices or manual internal micrometre with two- or three-point-contact are commonly utilised for diameter measurements. GUEGAN [89] identified that in UD CFRP drilling roundness errors of the bores occur, due to material anisotropy and bending of the fibres by the fibre-cutting-edge interaction as well as fibre-peripheral-land interaction. It was found that this bending depends on the fibre cutting angle as well as cutting forces and generally results in smaller bore diameters compared to the tool diameters. Several authors [54, 60, 173] confirmed that the bore diameter in FRP is smaller than the tool diameter due to elastic deflection and spring-back effects. PIQUET et al. [173] illustrated that elastic deflection depending on the fibre cutting angle in drilling of UD CFRP may lead to non-circular bore holes, as shown in Figure 2.19.

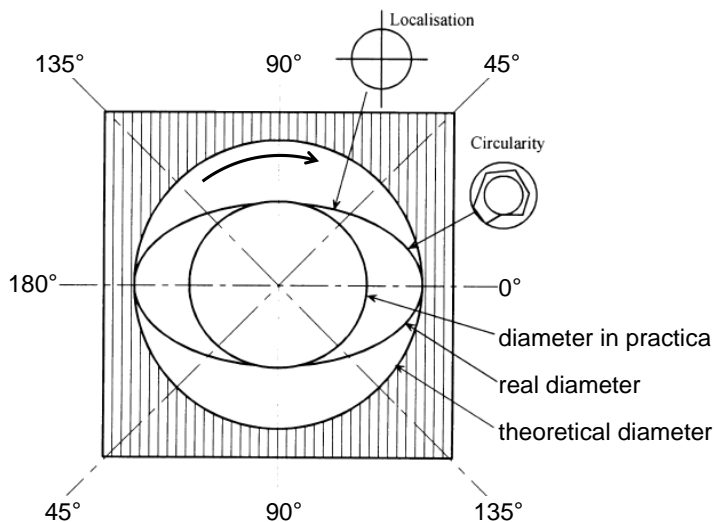


Figure 2.19: Influence of elastic deflection on bore diameter, according to [173]

Surface roughness measurements are commonly used to characterise machined surfaces. But average bore channel roughness is not suitable to describe the bore quality in FRPs, as shown by various investigations [63, 100, 135, 180, 181, 230, 241]. According to KÖNIG et al. [135], protruding uncut fibres may lead to incorrect roughness results or at least strong scattering of the measurement values. Furthermore, the results do not depict the actual surface quality since smeared particles cover the machined surface and cracks may be below the smeared surface. WANG et al. [239] even stated that inherent damages of the $\theta=135^\circ$ orientation, due to fibre/matrix interface shearing made accurate surface roughness measurements across the entire laminate impossible. RAMULU et al. [180] confirmed these difficulties with profile based description and identified that the two roughness parameters peak-to-valley height (R_y) and ten-point height (R_z) are slightly more appropriate than the average roughness (R_a) for describing topographical features in CFRP. Accordingly it was recommended to supplement quantitative profilometry with visual analysis of the surface morphology. Figure 2.20 shows a visual bore surface analysis presented by HENERICHS et al. [100] with partly smeared (even) surface and irregular regions, whose occurrence depends on the fibre orientation in each ply and the tool wear status.

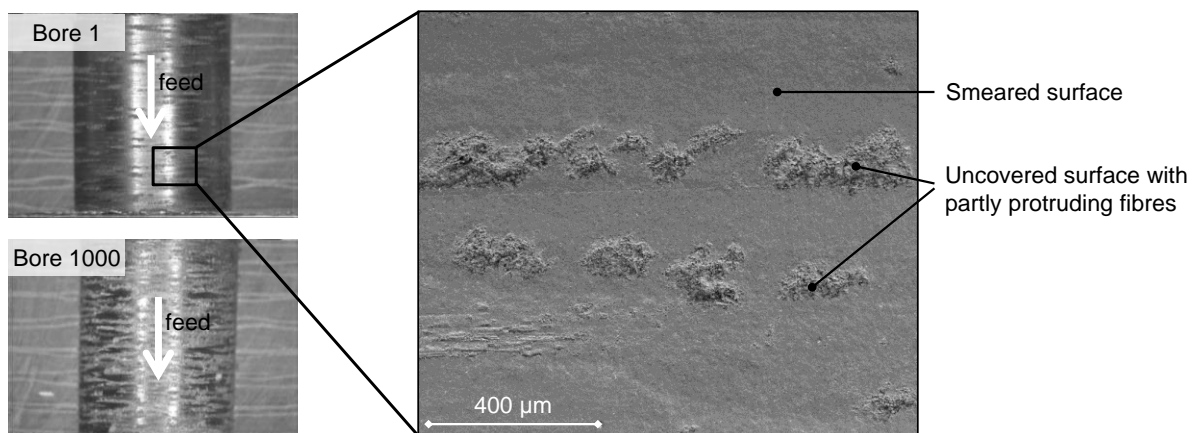


Figure 2.20: Visual bore channel analysis with microscope and SEM, according to [100]

According to GRASS [86], the fibre cutting angle influences the surface roughness, which is larger for $90^\circ < \theta < 180^\circ$ than for $0^\circ < \theta < 90^\circ$. The larger the feed rate and the cutting edge radius, the larger is the surface roughness, while the cutting speed has a limited influence.

2.2.2 Evaluation of bore entrance/exit damages

Damages at the bore entrance or exit side, introduced by the machining process, are the most common damages in machining of FRPs and probably the main critical damage. KÖNIG et al. [135] recognised that bore exit delamination is correlated to the feed force and feed rate. HOCHENG and DHARAN [109] identified that delamination occurs at both the bore entrance and exit and developed a delamination prediction model. To distinguish both mechanisms the delamination at the exit is called *push-out* and the one at the entrance *peel-up* delamination, as shown in Figure 2.21. *Push-out* delamination in CFRP drilling occurs due to the compressive thrust force on the uncut material under the drill. With progressing feed during a drilling operation the uncut thickness and amount of uncut plies becomes smaller and the resistance for deflection decreases. As soon as the interlaminar bonding strength is exceeded, delamination occurs just before the drill completely penetrated the material. *Peel-up* delamination occurs, as soon the cutting edges of the drill tend to pull the abraded material along the flute. Before the material is completely cut it undergoes a peeling force upwards, which tends to separate the upper laminate plies from the plies below. The plies below are loaded by the downward acting feed force in the tool centre. According to HOCHENG and DHARAN [109], *peel-up* delamination is a function of the tool geometry and tool/workpiece friction. The progressively more deeper the drill entered the material, the more difficult is the generation of peel-up delamination, since an increasing number of plies rather prevents bending. Based on different tool geometries HOCHENG and DHARAN [109] developed a model to predict the occurrence of *push-out* or *peel-up* delamination based on critical thrust and cutting forces.

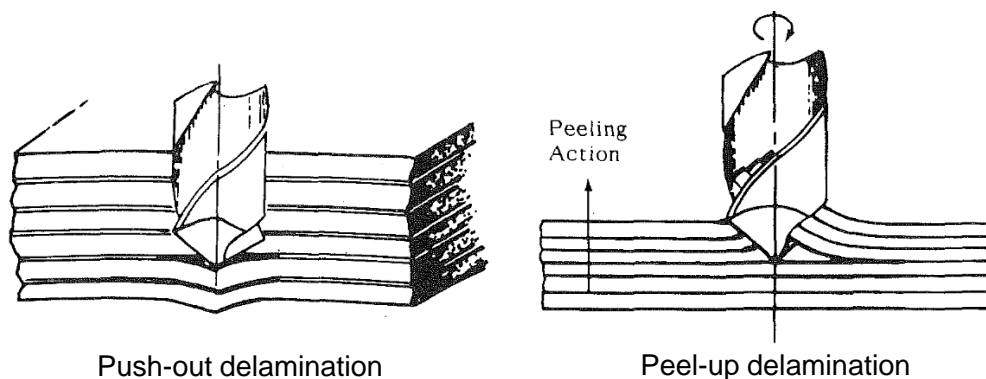


Figure 2.21: Drill bit showing push-out (left) and peel-up delamination, according to [109]

To reduce the risk of peel-up delamination, GUEGAN [89] recommended the use of small rake angle below 6° . For delamination-free drilling PIQUET et al. [173] suggested pre-drilling with a smaller diameter tool to avoid the negative effects of the chisel edge and enabling lubrication of the process. Furthermore better bore exit qualities were achieved with reduced feed rate but at the same time the tool wear and machining time increased. Backing plates at the bore exit side of the FRP component significantly reduce the risk for push-out delamination, but utilisation of these devices may be not possible in certain applications, due to limited space and accessibility.

Especially in the aviation industry with high safety standards delamination defects are undesirable, because it may be the starting point of a propagating crack (notch effect), as stated by BADER et al. [11] and BHATNAGAR et al. [14]. It is well known that bore exit delamination has a significantly negative effect on the fatigue life of the final structure, among

others analysed by PERSSON [170] in 1996. Operator independent and preferably automated visual inspection and assessment of delamination becomes more important with the increasing use of CFRP in industry. Analysing delamination, spalling and uncut fibres describe the bore quality more precisely. According to DENKENA and BIERMANN [60] different characterisation and measurement methods are known in literature to measure uncut fibres and damages around a bore. Nowadays optical measurement devices show accuracies in the range of one micro meter and a better reproducibility than tactile measurement devices, as stated by TIKAL [219]. Common measurement methods are 3D-microscopy [97, 107], digital image processing [53, 114, 173, 227] or ultrasonic C-Scan [8, 115, 161, 224]. Today tool geometries for CFRP machining are well adapted to generate a good bore quality and exhibit better wear resistance using optimised diamond coatings, which protect the cutting edge more efficiently [64, 98]. Nevertheless, some unidirectional CFRP materials, which are more difficult to machine than woven CFRP, still show massive delamination and uncut fibres using conventional drilling. These defects usually become worse with increasing tool wear and thrust force [44, 100, 110, 113], especially if a supporting glass fibre layer at the bore-exit side is absent. Referring to HOCHENG and TSAO [113, 114, 222, 224, 225] the critical thrust force leading to bore exit delamination mainly depends on the feed, the tool diameter and geometry as well as the ply thickness. The lower the critical thrust force, the smaller the process window to achieve a bore of sufficient quality, as stated by HOCHENG and TSAO [222].

The most common evaluation criterion for the bore exit quality in drilling CFRP is the delamination factor (F_d), proposed by CHEN [44] in 1997. The delamination factor F_d

$$F_d = \frac{D_{max}}{D}, \quad F_d \in [1; \infty] \quad (1)$$

is calculated by the ratio of the maximum diameter D_{max} in the damaged zone to the bore diameter D . The delamination factor represents a good approach to quickly assess the maximum extent of delamination at bore entrance and exit possessing a regular damage pattern, especially in GFRP or woven CFRP. Most researchers use this delamination factor due to the fast and easy determination of F_d . DAVIM and REIS [50, 51] considered in 2003 a delamination factor, calculating the ratio of D_{max} and the tool diameter d instead of the bore diameter D . They analysed the effect of different drill geometries on the magnitude of delamination around the bore. Due to elastic deformation and spring-back effects the bore diameter in FRP is smaller than the tool diameter, which was detected by several authors [54, 60, 173]. The same delamination factor including d is used by ARUL et al. [8] in 2006 studying the effect of axial vibration assisted drilling on the bore exit quality in woven glass fibre reinforced polymers (GFRP). HOCHENG and TSAO [115] use the reciprocal value (ratio of tool diameter d and D_{max}) to describe the influence of different tool geometries on critical thrust force at the onset of delamination. The effects are described mathematically as well as experimentally.

CAPELLO [27] investigates the effect of support structures underneath the work piece when drilling CFRP. The amount of delamination at the bore exit with and without backing was characterised by the delaminated area around the bore A_d and not just by the maximum damaged diameter D_{max} . The damaged area A_d around a bore is more difficult to assess but machining CFRP shows irregular defects like spalling, cracks and delamination, which are

hard to depict with only one diameter, as stated by DAVIM [53]. Figure 2.22 shows two bore exits schematically with the same delamination factor F_d but completely different magnitudes of the damaged area. While on the left hand side a single fibre roving is delaminated due to insufficient adhesion, the right hand side shows an intensive but rather uniform damage around the bore. It may be assumed that the right bore withstands less strain than the left one, analysed in detail by HENERICHS et al. [99] in 2014. This example shows that the delamination factor F_d alone is insufficient when the material generates irregular damages, especially in unidirectional CFRP material.

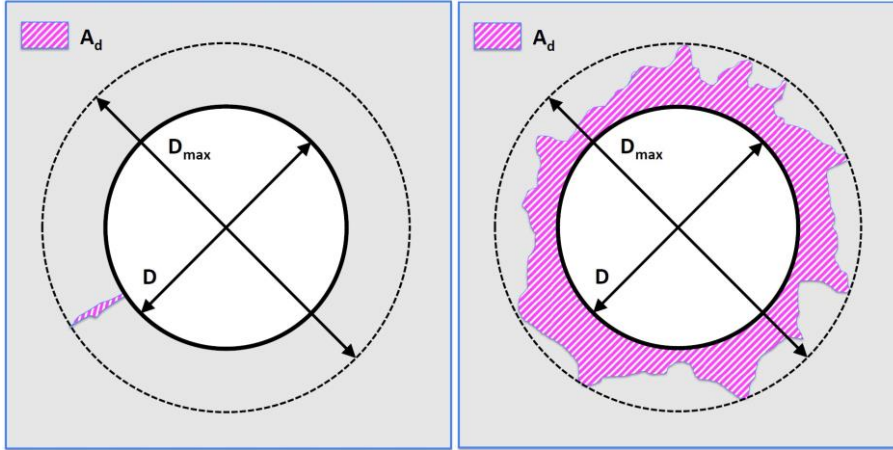


Figure 2.22: Example for identical delamination factor F_d , but a difference in the delaminated area A_d

Based on the initial delamination factor F_d according to (1) and the delaminated area A_d , DAVIM et al. [53] developed an adjusted delamination factor F_{da} .

$$F_{da} = F_d + \frac{A_d}{(A_{max} - A_0)} (F_d^2 - F_d), \quad F_{da} \in [1; \infty] \quad (2)$$

In this equation A_{max} is the area belonging to D_{max} and A_0 is the area belonging to the bore diameter D . As explained above, the area A_d is the damaged area around the bore, as shown in Figure 2.22. The fraction in equation (2) represents the percentage of the damaged area in the circular ring. If the delaminated area A_d is minimal as shown on the left hand side in Figure 2.22, the value of the adjusted delamination factor F_{da} tends to be equal to the delamination factor F_d in equation (1). For large and evenly distributed damages around the bore, see Figure 2.22 right hand side, the adjusted delamination factor (F_{da}) tends to be equal to F_d^2 . In general the first summand in (2) represents the crack-size contribution, and the second summand represents the contribution of the damaged area around the bore.

The adjusted delamination factor F_{da} in (2) still includes the delamination factor F_d , which is known to be insufficient when brittle fracture in UD CFRP generates irregular damages around the bore entry or exit. In 2012 TSAO et al. [227] have further developed a characteristic value, the equivalent delamination factor

$$F_{ed} = \frac{D_e}{D}, \quad F_d \in [1; \infty] \quad (3)$$

This factor depends on the maximum damaged diameter D_{max} and is calculated by the ratio of the equivalent delamination diameter D_e and the bore diameter D . The equivalent

delamination diameter D_e results, when both the damaged area A_d plus the bore area A_0 are formed to an ideal circle.

$$D_e = \sqrt{\frac{4(A_d + A_0)}{\pi}} \quad (4)$$

The equivalent delamination factor F_{ed} increases slower than the adjusted delamination factor F_{da} with increasing damaged area A_d . Figure 2.23 shows the influence of the damaged area A_d on the equivalent delamination diameter D_e and thus on F_{ed} for realistic examples.

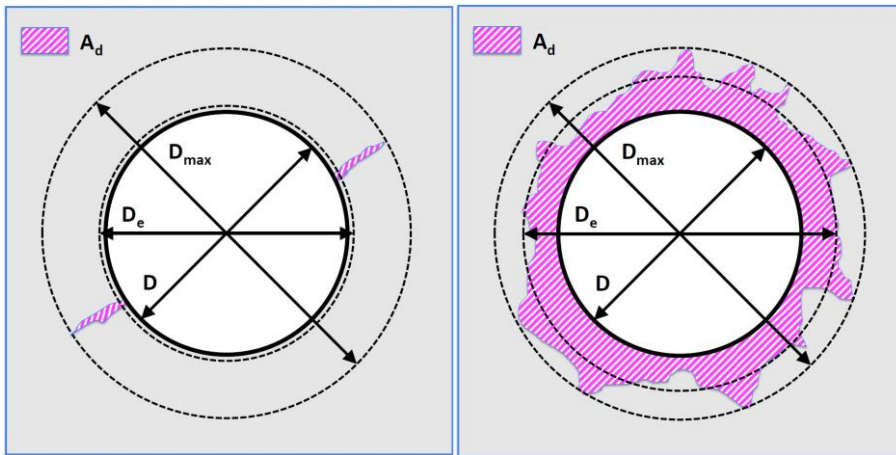


Figure 2.23: Example for identical delamination factor F_d , but small delaminated area A_d (left) and large delaminated area (right) and the resulting equivalent delamination diameter D_e

A more detailed approach of bore exit quality evaluation was presented by ZEMANN et al. [264], in which three separate damage effects, namely fraying, delamination and splintering were distinguished. Therefore two methods, a one dimensional maximum method (1D MM) and an extensive three dimensional damage analysis (3D DA) were proposed and compared. Figure 2.24 shows schematically the three types of damages at the edge of a bore. The 1D MM aims to be fast, being applicable at the shop floor and requires no expensive measuring equipment. Nonetheless the three above mentioned types of damages were distinguishable and the major damage identifiable. ZEMANN et al. [264] proposed a concept, in which the single damages were measured in length and put in relation to the tool diameter d . For each type of damage (fraying, delamination, splintering) separate indices

$$f_i = \frac{f_{max}}{d} = \frac{\text{maximum length of fraying in mm}}{\text{nominal tool diameter}}, \quad (5)$$

$$d_i = \frac{d_{max}}{d} = \frac{\text{maximum length of delamination in mm}}{\text{nominal tool diameter}}, \quad (6)$$

$$s_i = \frac{s_{max}}{d} = \frac{\text{maximum length of splintering in mm}}{\text{nominal tool diameter}}, \quad (7)$$

are calculated and averaged over the number of damages occurring. A total quality index

$$q_i = f_i + d_i + s_i \quad (8)$$

is calculated and enables standardised comparison of machining damages.

The proposed 3D DA method requires expensive measurement equipment but provides more detailed information. The measured fraying, delamination and splintering indices are

classified in a so called FI matrix, which give three separate damage indices, just like in the 3D DA. These indices enable for a fast overview of workpiece quality and damage distribution.

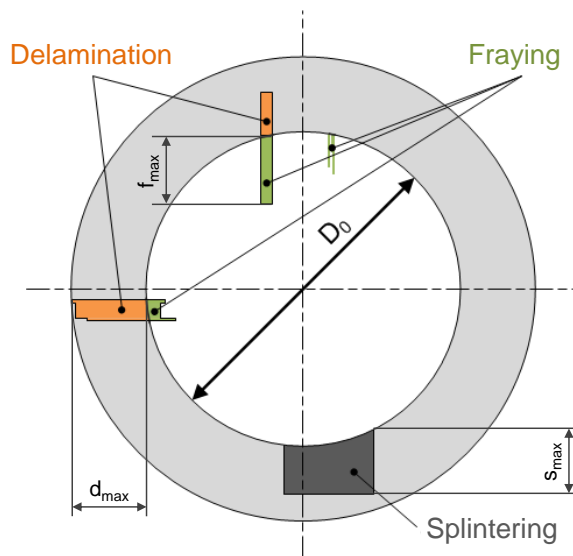


Figure 2.24: Bore edge damages introduced by a drilling operation, according to [264]

2.2.3 Bore channel and subsurface damages

According to KÖNIG and GRASS [136], fibre pull-out, fibre or bundle cracks and a thermally affected zone are typical damages along the bore channel in CFRP drilling. Most of the damages reach below the surface or are concealed by a layer of smeared particles. These damages are hard to detect by visual inspection and of special interest, because these failures are critical regarding material strength. Just very little research exists, focussing on the quality of the CFRP bore channel in contrast to the bore exit delamination. KEFERSTEIN [128] stated that either destructive or non-destructive methods exist to analyse the material regarding subsurface damages.

Exemplary non-destructive methods are ultrasonic C-Scan inspection, active lockin-thermography or X-ray computerised tomography (CT)/radiography. TSAO and HOCHENG [224] applied ultrasonic inspection and CT-techniques for evaluation of delamination damages introduced by drilling operations in CFRP. The resolution obtained from the images allowed for measurement of the delamination extension. Due to the heterogeneity of the material ultrasonic C-scan suffers from the large acoustic attenuation and scattering, which makes data interpretation difficult. Figure 2.25 shows a comparison of several non-destructive inspection methods. According to the measurement data by TSAO and HOCHENG [224], the ultrasonic C-scan generates poorer resolution compared to X-ray computerised tomography (CT). DURAO et al. [63] applied radiography and found out that it is only suitable for detection of delamination if a contrasting fluid (CH₂I₂, methylene iodide) is infused. The inherent contrast between epoxy matrix and carbon fibres is too low. Consequently, this method is inappropriate for damages without opening to the surface. HENERICHS et al. [100] presented an improved CT method based on diffraction X-ray. The advantage of this method is a higher contrast between fibres and matrix without contrasting fluid. It has been proven that damages along the bore channel can be detected non-

destructively by diffraction X-ray CT, but currently the method is very time-consuming and expensive. RIEGERT et al. [190] conducted ultrasonic, eddy-current and optically activated lockin-thermography for inspection of machined CFRP components, in which an ultrasound or thermal modulated wave respectively is induced in the specimen. This wave may be reflected by potential defects e.g. delamination, which affect the amplitude and phase of the temperature modulation on the surface. According to the measurement data, using phase images in combination with eddy-current activated lockin-thermography enables to detect small defects. But the resolution of the method certainly depends on the damage depth and the CFRP material properties. Generally, the above mentioned non-destructive methods may be appropriate for large delamination at the bore exit but for small damages e.g. cracks in the range of a few fibre diameters none of these methods is suitable.

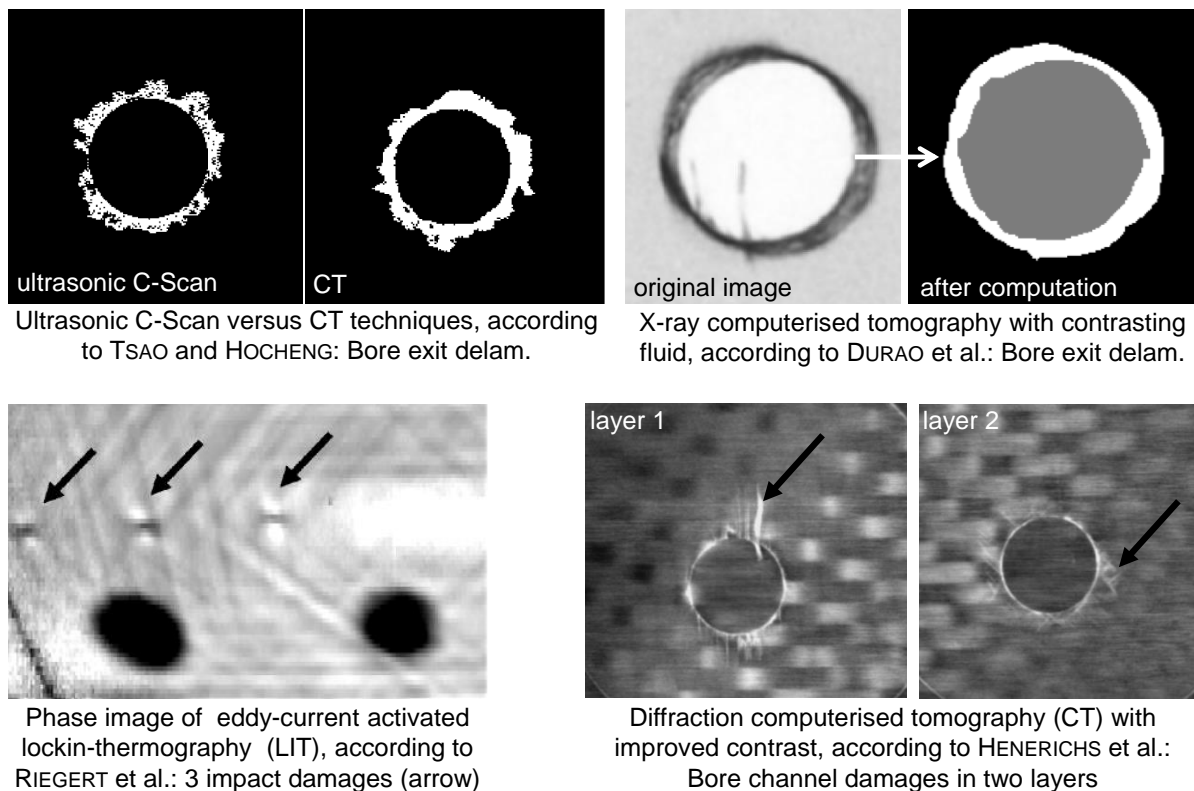


Figure 2.25: Comparison of ultrasonic C-Scan, X-ray computerised tomography/radiography, lockin-thermography and diffraction CT, according to [63, 100, 190, 224]

Micrographs of the machined edges as well as mechanical compression and tensile tests belong to the destructive processes. The state of the art of the latter mentioned mechanical tests will be explained in the following Chapter 2.2.4. Leastways in research and product development, micrographs are common methods to detect machining-induced damages below the surface. Therefore the samples are embedded, subsequently the top layers are ground and polished down to the desired depth. Afterwards microscopy of the micrographs below the surface enable detection of cracks and broken or bend fibres, as shown by HENERICHS et al. [100]. RENTSCH et al. [188], PECAT et al. [169] and BRINKSMEIER et al. [22] analysed the surface integrity in drilling of multilayer CFRP with diamond coated carbide drills. Figure 2.26 shows a comparison of the quality of the machined edges at $v_c=40$ m/min and $f=0.2$ mm/rot (Set 1) as well as $v_c=120$ m/min and $f=0.027$ mm/rot (Set 2) according to RENTSCH et al. [188]. At parameter Set 1, high axial forces and a low maximum process temperature of 112.9°C occurred. The fibres close to the bore edge were slightly bent in

cutting velocity direction. For parameter Set 2 with high cutting speed and low feed rate, small axial forces and high temperatures of 191.6°C occurred. This temperature is above the glass transition temperature of the matrix material ($T_g=180^\circ$). Especially for a fibre cutting angle of 90° , cracks below the bore channel surface were found up to depth of 50-100 μm . Accordingly the fibres crack in the machining process with high temperatures due to a reduced support capability of the matrix. According to WEINERT and KEMPMANN [246] a potential thermally affected zone along the bore channel may be detected by optical microscopy. Due to the poor heat conductivity of FRPs, thermal defects such as pyrolysis or decomposition of the polymer matrix concentrate right at the edge of the bore and may lead to exposed fibres. According to WEINERT and KEMPMANN [246] overheating of the peripheral zone is amplified by low feed rates, high cutting speeds and intensively worn tools.

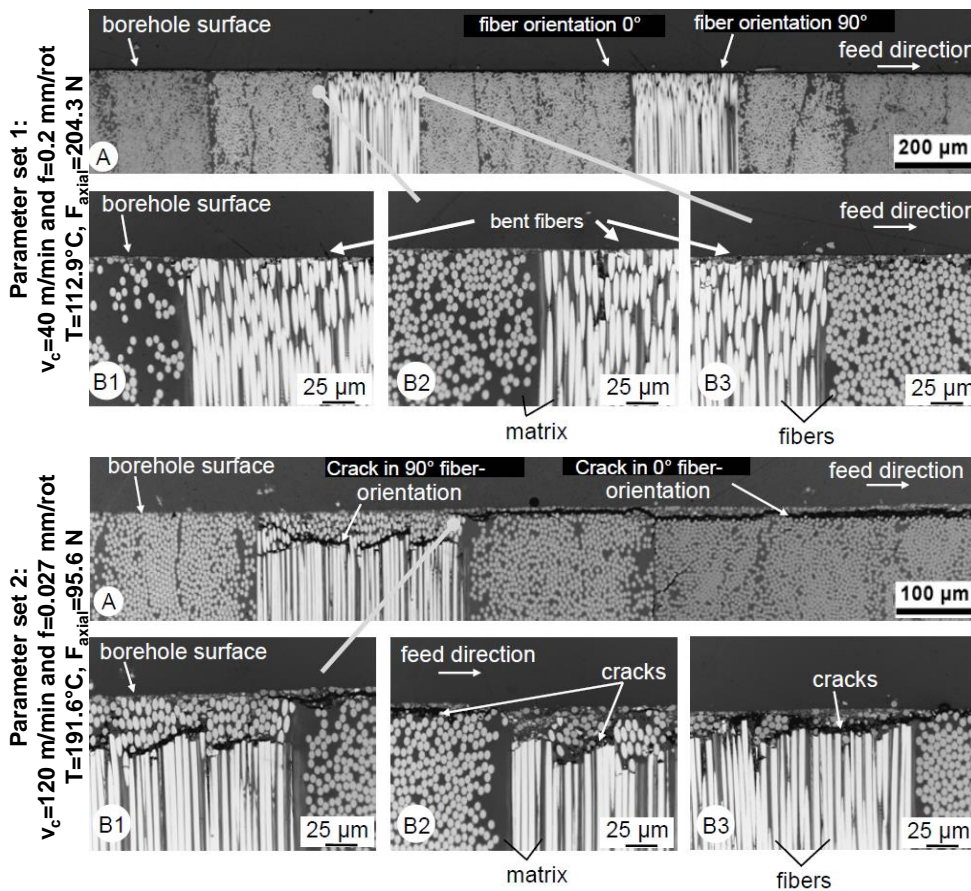


Figure 2.26: Micrographs of the subsurface structure of a borehole in multi-layered CFRP with parameter Set 1 and Set 2, according to RENTSCH et al. [188]

Additionally fundamental milling of unidirectional CFRP was presented by RENTSCH et al. [188] and PECAT et al. [169] focussing on the surface integrity. The same analyses were conducted by HENERICHS et al. [101, 230] in unidirectional CFRP turning. Correspondingly machining fibres under $\theta=0^\circ$ and $\theta=45^\circ$ generates smooth surfaces, the surface of $\theta=90^\circ$ shows frequently cracks reaching beneath the surface and in machining $\theta=135^\circ$ the fibres fail due to bending and generate a saw teeth profile, as shown in Figure 2.27.

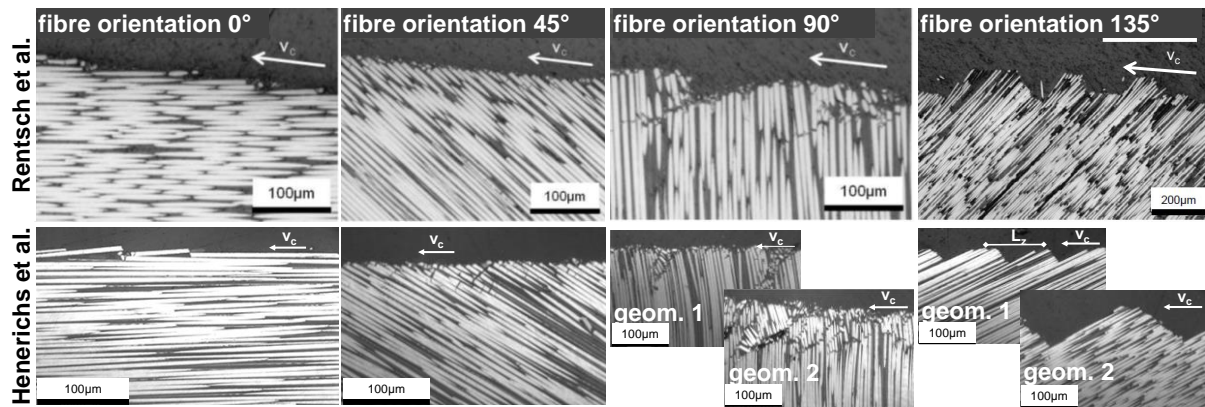


Figure 2.27: Micrographs of the subsurface structure of milled UD CFRP/epoxy, according to RENTSCH et al. [188] (top row) and of orthogonally cut UD CFRP/epoxy, according to HENERICHS and VOSS et al. [230] (bottom row)

2.2.4 Mechanical strength of bore

According to WITTEN [249] and KNOLL [133], the design of a bore for rivet joints should be done based on bearing stress failure to have defined structural and geometrical conditions. Accordingly the bearing stress in laminates depends on the laminate thickness as well as the structure, the distance of the bore to the edges of the component, the bore diameter and the clamping force. WITTEN [249] and KNOLL [133] identify the compressive strength of the bore channel and the notch resistance of the laminate as the assessment criteria of the mechanical strength of a bore. The compressive strength is a function of the fibre orientation, the shear strength of the matrix and the delamination resistance. Maximum force transmission in a bore is reached with a combination of 0° and $\pm 45^\circ$ fibre orientations in the laminate.

In aerospace industry commonly not the single bores but the rivet connections are mechanically evaluated in a geometrically defined tensile or shear test. These tests with rivets and machined CFRP plates do not allow for distinction, whether the rivet, the CFRP raw material or the drilling operation caused the potential failure of a test. Two exemplary tests of such rivet connections in lap shear and peeling tests are shown on the top-right in Figure 2.28. The test rig setup on the top-left in Figure 2.28 shows a pull-through test of the bore. With these tests HEIMBS et al. [95] analysed the testing speed influence, to investigate the potential strain rate effects on the failure behaviour. Compression, tension and shear load may be evaluated in the presented setups. Potential failure behaviours are shown on the bottom of Figure 2.28. But as mentioned above, the complexity of the total rivet connection does not enable for conclusions to the potentially introduced damages.

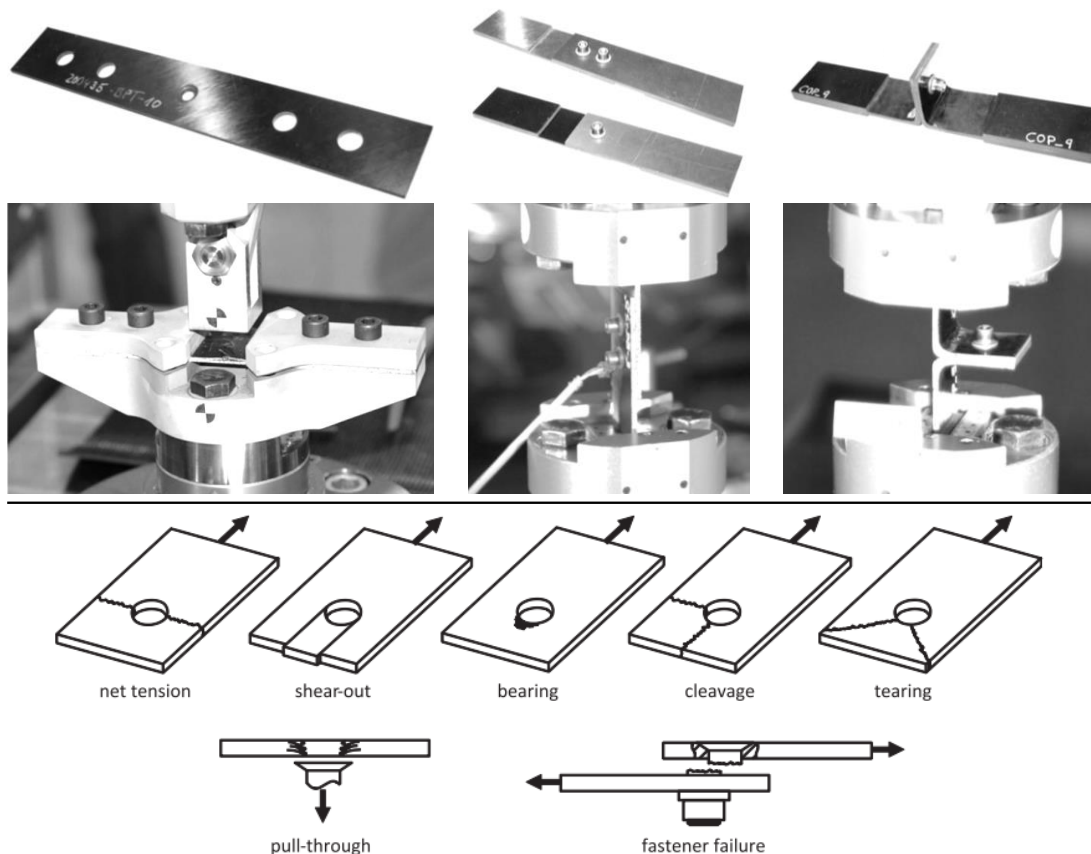


Figure 2.28: Test setups for bolt pull-through, single lap shear and coach peel tests as well as joint failure modes, according to [95]

In several publications [42, 82, 143, 148, 260] the potential alternative to drilling bores in the laminate by molding-in holes prior to the curing process have been evaluated. LANGELLA and DURANTE [143] evaluated the influence of drilled bores in CFRP compared to molded-in holes on the mechanical strength. The examinations of the mechanical strength of the bores were carried out by tensile tests (ASTM D 5766) at a speed of 1 mm/min. Subsequently the failure zones around the bores were evaluated. As expected, the drilled bores with fibre continuity interruption in the laminate and introduced damages by the drilling operation showed decreasing failure stresses, shown in Figure 2.29. The smaller the bore diameter, the larger the effect of the favourable fibre continuity in material with molded-in bores. According to GHASEMI NEJHAD et al. [82] as well as LIN and LEE [148] the bearing strength in drilled bores is reduced by 17% - 77%, which was attributed to fibre continuity, an increasing fibre volume fraction near the hole vicinity, and the absence of matrix micro-cracks induced by the drilling operation.

Analyses of drilled bores with ultrasonic C-scans, micrographs of the bore edges, static open hole compression/tension tests and dimensional measurements conducted by MEHTA et al. [161] suggested that the mechanical strength of rivet-holes is indeed influenced by the drilling-induced bore quality. These results were confirmed by HENERICHS et al. [99], who conducted mechanical strength tests of drilled bores in CFRP with six different test rigs on a static materials testing machine. PERSSON et al. [170] conducted fatigue tests under dynamic loading and found significantly lower strength (-8% to -10%) for worn tools, which generate bores with several defects in contrast to defect-free bores generated by orbital drilling.

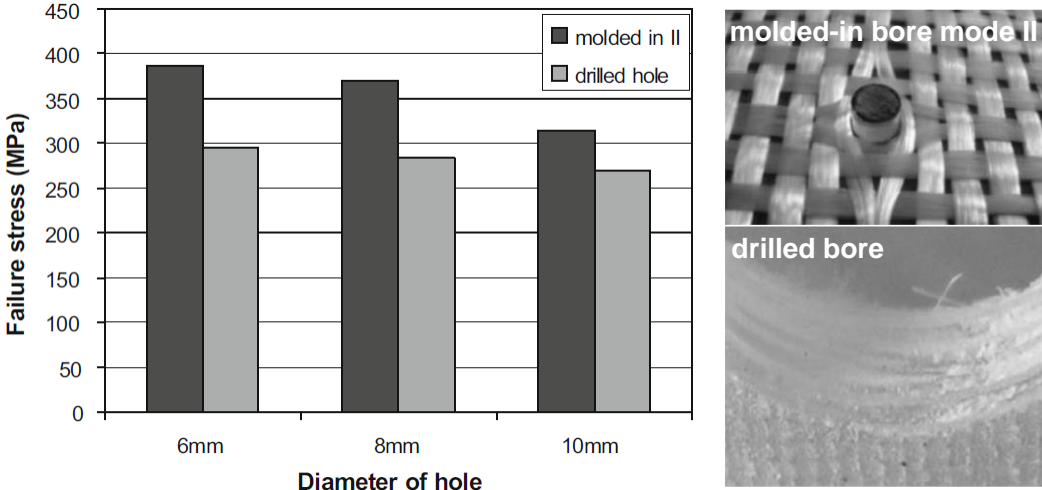


Figure 2.29: Comparison of mechanical strength between molded-in and drilled bore, according to [143]

2.3 Tool wear and microgeometry

The above described literature review in CFRP machining shows that intensive tool wear occurs compared to metal machining. It rapidly changes the initial tool micro-geometry and has a major effect on the machinability and introduced damages in CFRP. The fundamental experiments by KOPLEV et al. [137], RUMMENHÖLLER [193] and HENERICHS et al. [101, 102, 230] in Chapter 2.1.1 proved different wear intensity for variable fibre orientation θ . Maximum tool wear occurs along the flank face of the tool in machining UD CFRP with $30^\circ < \theta < 60^\circ$, according to HENERICHS et al. [102].

BOLDT and CHANANI [18] as well as TETI [218] show the possibility of increasing the bore quality and exhibit good wear resistance in CFRP drilling by optimising the tool geometry and process. Further improvements of wear resistance were achieved by using optimised diamond coatings protecting the cutting edge more efficiently, shown by HENERICHS et al. [98]. Despite these improvements, wear is unavoidable and in difficult to machine UD CFRP materials delamination and uncut fibres occur. These defects usually become worse with increasing tool wear and thrust force, presented by CHEN [44], HENERICHS et al. [100] and HOCHENG et al. [110, 113]. HOCHENG and TSAO [113, 114, 222, 224, 225] stated, the lower the critical thrust force the smaller the process window to achieve a bore of sufficient quality. This critical thrust force leading to bore exit delamination depends on the feed rate, the tool diameter and geometry as well as the ply thickness: The tool diameter and ply thickness are generally given by the CFRP component or its application. The feed rate should be as high as possible for high productivity. Consequently, the tool macro- and micro-geometry have to be adjusted to the needs of the CFRP material.

While the macro-geometry is well defined e.g. by the rake or clearance angle, description of the micro-geometry by robust and repeatable parameters in CFRP-machining is subject of current research. According to DENKENA and BIERMANN [60] the micro-geometry of a tool is defined as the transition between the rake face and the flank face of a cutting edge. Characterisation of the micro-geometry is usually conducted by analysing profile sections in various parts of the cutting edge. In CFRP machining, the workpiece quality highly depends on the current wear state of the rapidly wearing tool, shown amongst others by FARAZ et al. [72]. To determine the current wear state or the suitability of the tool to machine a CFRP component, a detailed definition of the tools micro-geometry is essential. According to the DIN6582 standard, originally composed for metal machining, the three following micro-geometries and combinations of those are common: Sharp edge, rounded edge and chamfered edge. In practise, ideal sharp cutting edges without radius or chamfer are not applicable for most machining operations due to insufficient stability against mechanical loads, shown by CORTES [49], BOUZAKIS et al. [19] and FRIEMUTH [80]. Due to the manufacturing process of the rake and flank faces, a certain rounded edge arises in the transition zone. The potential diamond coating represents an additional layer on top, usually with a thickness of 6-12.5 μm [98, 121, 244] leading to even larger cutting edge roundings. According to TSAO and HOCHENG [225], a sharp and wear resistant tool generates best bore exit quality in CFRP drilling. Consequently, tailored cutting edge geometries with additional rounding or chamfering to increase the stability, known from metal machining, are not applicable in CFRP machining. Breakage and breakouts of cutting edge corners are unusual

defects in CFRP drilling. However, in drilling with diamond coated carbide drills, break outs of the diamond layer due to insufficient coating adhesion may arise.

One of the most common evaluation criterion for the cutting edge acuity in drilling CFRP is the cutting edge radius r_β or cutting edge roundness, firstly mentioned by FISCHER [76] in 1897 for metal machining. In 1953 CHIEN [46] analysed the influence of the micro-geometry on the process forces and material surface and in 1960 ALBRECHT [1] introduced the ploughing mechanism in metal cutting. DENKENA and BIERMANN [60] pointed out that there is a rapidly increasing interest in this research field since the 1970s, due to advancements in automated production processes of tools and measurement devices. Several techniques have been developed to produce cutting edges with tailored rounding or chamfering [9, 24, 45, 49, 59, 94, 216, 221, 254]. Typically, the micro-geometry is measured to evaluate wear and tailored cutting edge conditioning. According to BASSETT [12] the tactile measurement methods show better repeatability than optical methods, while the optical methods are faster and determine cutting edge shape and topography in one measurement. The following optical measurement devices are listed by DENKENA and BIERMANN [60] to be commonly used for determination of tools micro-geometry: Digital micro-fringe projection, chromatic confocal scanning, focus detection methods and interferometry.

DENKENA et al. [25, 55] observed in 2002 that rounded cutting edges do not resemble a perfectly circular shape, consequently fitting a circle with r_β without specific fitting strategy leads to oversimplification. To date, no standards for fitting and measuring the cutting edge radius for different cutting edge shapes exist. Instead of fitting a radius DENKENA et al. [55] introduce four parameters characterising cutting edge rounding: Δr , φ , S_γ , S_α . This method is called *DetermineK* and is presented in Figure 2.30. In a first step, the method fits two linear interpolations to the unaffected part of the rake and the flank face of the two-dimensional tool profile and a bisecting line is implemented. The angle between those two best-fit lines represents the wedge angle of the cutting edge. Flattening of the tool profile is described with the parameter Δr , defined as minimum distance from the intersection of the two best-fit lines to the tool profile. The angle φ describes the shift of the cut point either to the rake- or flank-face relative to the bisecting line. The two parameters S_γ and S_α measure the length from the intersection to the separation point of the cutting edge rounding on the rake- and the flank-face, respectively. The asymmetry of the micro-geometry is defined by the K-Factor $K = S_\gamma / S_\alpha$ and the average cutting edge rounding $S = (S_\gamma / S_\alpha) / 2$.

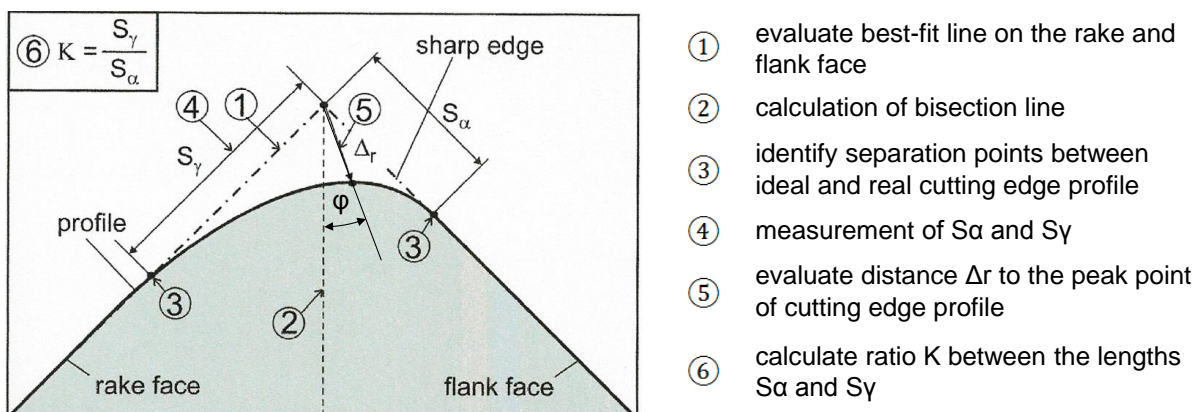


Figure 2.30 Concept of micro-geometry characterisation via *DetermineK* according to [25]

According to DENKENA and BIERMANN [60] *DetermineK* is a good method for describing asymmetric edge shapes (K, φ) and bluntness of a cutting edge (Δr), but it is unsuitable for cutting edges with curved rake or flank faces. HENERICHS [101] points out that the lengths from the separation points to the intersection of the two linear interpolations are intuitive and lead the measurement method to its huge popularity. A weakness of this method is the robustness, which depends on the amount and location of chosen points on the rake- or flank-face for the tangents-fit. Furthermore, a huge measuring uncertainty exists in separation point determination, because the cutting edge profile approaches the ideal geometry smoothly, explained by WYEN et al. [255].

At the CIRP general assembly in 2008 the results of a round robin tests were presented, in which cutting inserts prepared via brushing were measured with contact stylus method as reference. Afterwards five different measurement devices, three optical and two contact styluses, were used to evaluate the cutting edge radius. Deviations of up to 48% in evaluating the cutting edge radius r_β arise, when measuring at the same position with different measurement devices and operators. A main source of error identified is the algorithm used for calculation of micro-geometry parameters. The discrepancies in measurement were reduced by 29% to about 34%, by using *DetermineK* as standardised algorithm for the data generated with the different devices. It needs to be considered that the operator of *DetermineK* could manually modify the separation points leading to uncertainty in evaluation. WYEN et al. [253-255] developed an iterative algorithm to fit the micro-geometry more precisely. This approach contains straight line – circle – straight line, see Figure 2.31. Comparable to the *DetermineK* method the authors implemented two interpolations to the rake and flank face and adopt the bisecting line of the wedge angle $\beta/2$. The bisecting line was complemented by a vertical line $n_{\beta/2}$ at the intersection of $\beta/2$ and the tool profile; plotted with horizontal green line in Figure 2.31. The authors defined an ideal circle, called r_{ideal} , defined by three points as tangent to the linear interpolation at rake- and flank-face and $n_{\beta/2}$. This radius r_{ideal} represents the profile of an ideally rounded symmetric cutting edge. Starting from r_{ideal} a circle with minimum square error, called r_m , was fit to the tool profile; see black dotted and dashed line. WYEN et al. [254] evaluated the least square fit according to GAUSS as the appropriate method to fit a circle to the tool profile. Furthermore the possibility of an ellipse-fit was discussed; however the idea was discarded because of a lack of intuitiveness. According to DENKENA and BIERMANN [60] a drawback of WYENS' approach was the oversimplification of the micro-geometry to a single circular segment. But WYEN additionally described the asymmetry of the micro-geometry by two length dy and $d\alpha$. These values were defined as distances between the intersection of $n_{\beta/2}$ and the linear interpolation at rake- and flank-face in $\beta/2$ direction. In contrast to *DetermineK*, the value Δr in the WYEN approach described the distance from the rake and flank face intersection to the tool profile in the direction of $\beta/2$. WYENS' characteristic parameters were chosen in a way, requiring no customisation during evaluation. The parameters Δr , dy and $d\alpha$ reference points on the cutting edge profile, which could be measured with good repeatability and without approximation, in contrast to *DetermineK* by DENKENA et al. [59].

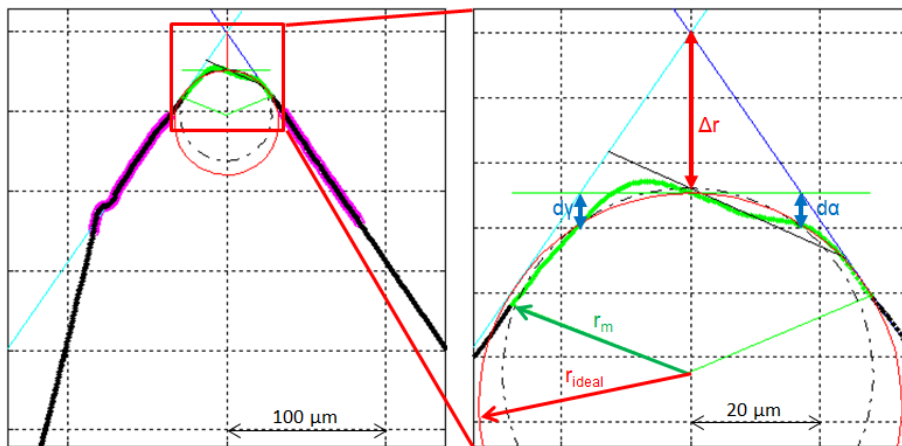


Figure 2.31: Characterisation of cutting edge micro-geometry, according to WYEN et al. [253]

Approaches optimised for tools with chamfered micro-geometry were described by HECKMANN [94] and CORTES [49]. These approaches implemented not just one circle-fit but one circle in each transition from rake- or flank-face respectively to the chamfer, presented in Figure 2.32. The wedge angle β as well as the bisecting line of the wedge angle $\beta/2$ was also evaluated in this approach. Additional parameters were the ridge width B_F and the chamfer pitch ψ . The chamfer pitch ψ described the asymmetry of the tool profile. Additionally CORTES [49] chose a sixth-order polynomial approach to determine various parameters. But according to WYEN [254] the description of the micro-geometry by polynomial approach might cause significant deviation from the actual cutting edge geometry and according to DENKENA and BIERMANN [60] the expressiveness is low.

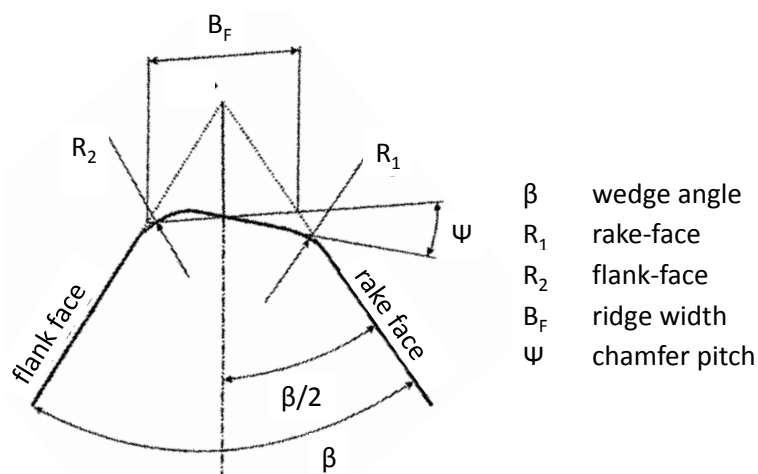


Figure 2.32 Characterisation of cutting edge micro-geometry according to Heckmann [94]

Further methods exist, which set the micro-geometry in relation to the uncut chip thickness h : For example CORTES [49] and XU [256] analysed the impact of the ratio $\lambda = r_\beta / h$ on the cutting performance. According to DENKENA and BIERMANN [60] a reliable statement about the impact of the above mentioned ratio on the cutting performance is limited, because it depends on the cutting edge determination. STORCH and ZAWADA-TOMKIEWICZ [210] analysed the minimum uncut chip thickness in relation to the cutting edge radius r_n . The findings were based on the determination of the incremental tangential and normal forces along the cutting edge rounding. These approaches based on plastic deformation and continuous chip formation, which do not apply in CFRP machining. But those approaches go in the right direction as they introduce the physics of cutting into the description of cutting edges and thus raise the right questions. It also reveals that dependent on cutting

mechanisms and thus on the material to be cut different approaches for determining the cutting edge geometry might be necessary.

All the above mentioned methods [49, 59, 60, 94, 210, 253-256] are optimised for metal machining with plastic deformation as chipping mechanism. In CFRP machining mostly brittle fractures occur. The tool micro-geometry in CFRP machining is not protected by a stagnation zone in front of the cutting edge, leading to massive abrasive wear and highly asymmetric cutting edge rounding, explained in detail by WANG et al. [244]. In 2009 FARAZ et al. [72] used the cutting edge radius r_β (CER) as tool wear criterion in drilling CFRP. The authors have statistically proven that the cutting edge radius correlates the workpiece delamination equally as the well-known flank wear (VB) criterion. The authors [72] pointed out that the measurement of the CER-based wear is easier and more accurate than the conventional measurement of VB not only at complex tool geometries but also at very little wear magnitudes. But as commonly explained amongst others by WYEN [254], the fitting of a cutting edge radius r_β without a robust fitting algorithm is highly operator dependent leading to inaccuracies.

HENERICHS et al. [101, 245] developed a *Cutting Edge Analyser (CEA)* approach for micro-geometry description adapted to the needs of CFRP machining, which is further developed in [232]. The CEA-approach is characterised by considering the cutting and feed direction and taking the typical wear geometry in CFRP into account. Wear in machining CFRP forms a waterfall-shape with $S_\gamma \ll S_\alpha$. A graphical user interface (GUI) has been developed for user-friendly evaluation of the micro-geometry. By implementing either the rake angle γ or the clearance angle α , the tool reference system indicates the relation between tool geometry and the cutting process, as shown in Figure 2.33 (left). In CFRP machining the utilisation of tools with positive rake and clearance angles is recommended, resulting in clearly defined contact points of the tool reference system with the tool rake and flank face, marked by blue crosses in Figure 2.33 (right). The distance from the origin of the tool reference system to the contact point in feed direction is defined as the length l_γ , where the material is forced to dive underneath the cutting edge. According to HENERICHS et al. [101, 232, 245] this length l_γ is of particular interest for CFRP machining, because it describes the zone where the material is mostly not conveyed along the rake face but compressed underneath the cutting edge. The corresponding length to l_γ being inclined to the flank face is called l_α .

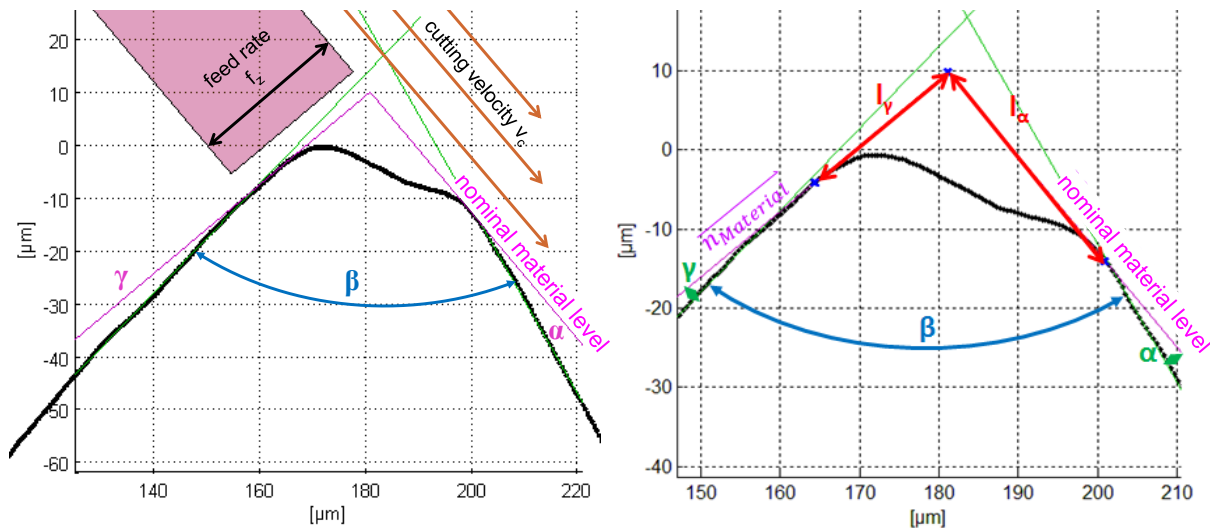


Figure 2.33: Consideration of cutting and feed direction in the CEA by HENERICHS et al. [101, 245]

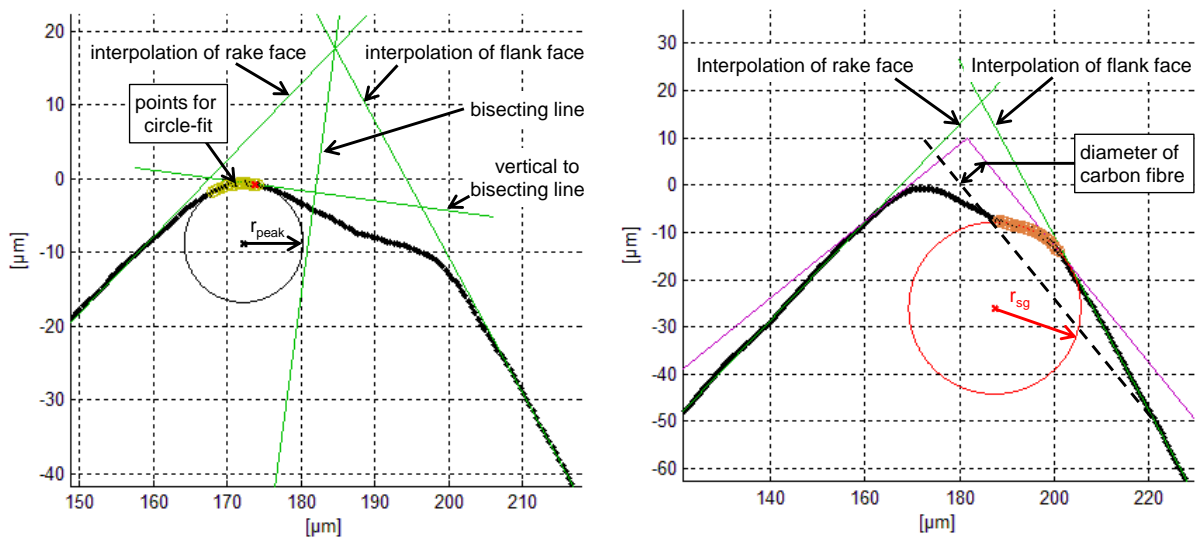


Figure 2.34: Radii fits in the CEA approach, according to HENERICHS et al. [101, 245]

Comparable to the approach by HECKMANN [94], HENERICHS et al. [101, 245] proposed a peak radius r_{peak} and a radius of surface generation r_{sg} in the CEA approach. The surface generation radius r_{sg} is shown in Figure 2.34 (right) and describes the tool profile at the transition from the negative to the positive clearance angle. In this zone high normal contact forces are exerted on the tool and damages can be introduced into the CFRP material. The radius r_{sg} is defined as a circular fit to the tool profile between the contact point and a width equal to the diameter of one carbon fibre ($\varnothing_{fibre}=6 \mu m$) in feed direction with negative clearance angle. According to HENERICHS et al. [101, 245], an infinitely large radius r_{sg} is desirable for good machining results. The peak radius r_{peak} is introduced, as presented in Figure 2.34 (left), which characterises the transition from the negative oriented part of the flank face to the rake face of the profile where material separation between workpiece and chips take place. A smaller peak radius represents a tool with better acuity, which is crucial for material separation with low feed- and cutting-forces. The asymmetry of the cutting edge profile is characterised in the CEA approach by the ratio of the enclosed areas between the cutting edge profile, the linear interpolation and the vertical to the bisecting line on the rake (A_v) and flank face (A_α), not marked but visible in Figure 2.34 (left). According to HENERICHS et al. [101, 245] this area approach for characterisation of asymmetry $K_{sym}=A_\alpha/A_v$ is more

robust than the K-Factor $K=S_v/S_\alpha$, proposed by DENKENA et al. [25, 55]. The CEA approach contains more micro-geometry parameters but l_γ , r_{sg} , r_{peak} and the clearance angle α had the largest effect on the machining quality. Consequently HENERICHS et al. [101, 245] proposed a quality criterion

$$Q_{krit} = w_1 \cdot v_1 \cdot l_\gamma + w_2 \cdot v_2 \cdot \frac{1}{\sqrt{r_{sg}}} + w_3 \cdot v_3 \cdot \frac{1}{1+\alpha} + w_4 \cdot v_4 \cdot r_{peak} \quad , \quad (9)$$

for diamond coated carbide tools, in which the v_i represent the scaling and w_i the weighting values. The weighting factors shall be adapted CFRP material specifically. In the presented drilling series in [101] the tools with micro-geometry quality values of $Q_{krit}>1$ showed extensive damage or delamination, whereas tools with $Q_{krit}<1$ generated bores of good quality.

2.4 Cutting edge treatment of diamond-coated tools for CFRP machining

Cutting edge preparation is an option to increase the machining quality as well as the tool lifetime not only in metal machining but also in drilling CFRP. According to DENKENA and BIERMANN [60] the following methods are common to generate a certain cutting edge micro-geometry, either as pre- or post-coating treatment:

- Abrasive jet machining (micro-blasting) [16],
- Abrasive brushing [58, 59],
- Drag-finishing,
- Magneto abrasive machining [185],
- Abrasive flow machining,
- Grinding,
- Electrical discharge machining (EDM) [262],
- Laser machining [9]

BASSETT et al. [12] stated that pre-coating processes aim to shape the cutting edges into consistent geometries by removing possible chipping and burrs and post-coating treatments aim to re-shape the cutting edges. Part of this thesis focuses on the post-coating treatment to improve the drilling quality of diamond coated carbide tools. Due to the abrasiveness of machining CFRP with high fibre content, diamond tools are increasingly used for high volume drilling operations in the aerospace industry. The hard and sliding-wear-resistant diamond protects the comparatively soft cutting edge from rapidly getting worn and rounded, among others presented by WANG et al. [244]. Although PCD tools possess a much thicker layer of diamond and nominal could stand the tool wear longer, at least for drilling operations, diamond coated carbide drills have become established due to currently higher geometry flexibility, as stated by HENERICHS et al. [98]. According to GILPIN [84], adjustments of the tools macro- and micro-geometry play a decisive role in drilling CFRP, where chip formation and transport have a huge influence on the machining quality. The diamond coating represents an extra layer on top of the grinded carbide tool, usually with a thickness in the range of 6-12.5 μm [98, 121, 244]. Assuming an average grind-able cutting edge radius of about 4 μm , depending on the carbide composition and the grinding process, a cutting edge radius after coating of 10-16.5 μm will arise. Most of the carbon fibres for the aerospace industry show diameters in the range of 5-7 μm . Consequently, the post-coating cutting edge radius is up to triple the size of the fibre diameter, resulting in rather blunt tools. According to extensive studies by TSAO and HOCHENG [225] and analyses by HENERICHS [101], tools should be as sharp as possible to reach acceptable machining quality with low forces. Despite coating companies use edge finishing techniques before the coating process to improve the cutting edge sharpness, experiments by HENERICHS et al. [98] and WANG et al. [244] showed that diamond coated carbide tools exhibit poor bore exit quality until the coating smoothens within the first bores. Hereinafter this effect will be designated as *run-in period*. The quantity of poor bores depends on the tool geometry, coating and CFRP material. No research has been found, focussing on post-coating cutting edge treatment of diamond coated drilling tools in CFRP machining.

2.5 Force modelling in orthogonal CFRP machining

Besides the experimental approaches presented in Chapter 2.1, an increasing number of analytical process force modelling approaches [14, 177, 195, 213, 242, 257, 258, 269, 270] were developed. But due to the high complexity of the inhomogeneous CFRP material no comprehensive mathematical model including tool wear is available to date. According to BECKE [13] analytical models base on basic mechanical considerations of the chip formation processes. Existing models of fundamental orthogonal cutting processes exhibit partially strong deviations and simplifications. It shows that approaches from force modelling in metal, such as the shear-plane model by MERCHANT or the USUI model are not or only conditionally transferable. In 1988 TAKEYAMA and IJIMA [213] developed a model, in which the CFRP material shears along a plane with the angle Φ , as shown in Figure 2.35 (A). BHATNAGAR et al. [14] upgrade this model by setting the angle of the shear plane equal to the angle θ of the fibre orientation. Fibre breakage due to axial tension was modelled as cutting mechanism. Subsequently, ZHANG et al. [242, 269, 270] published a new model with consideration of the cutting edge rounding by a simple radius. The spring-back effect of the fibres along the flank face was at least simplified taken into account, as shown in Figure 2.35 (B). Before, only ideal sharp cutting edges have been modelled without spring-back along the flank face.

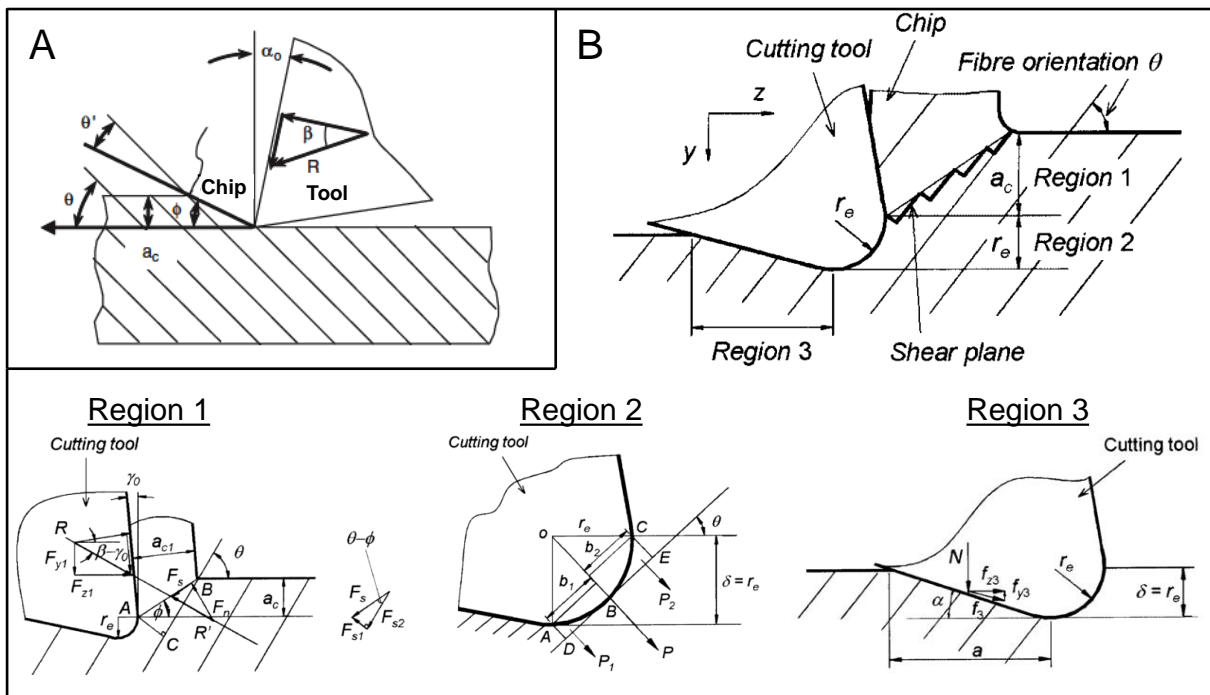


Figure 2.35: Force models of TAKEYAMA and IJIMA (A) and ZHANG et al. (B), according to [205, 269]

ZHANG et al. [269] divided the cutting edge profile into three separate areas: Rake face, cutting edge radius and flank face. A resulting force was assigned to each of these three areas, as shown in Figure 2.35 (B). The total cutting force and feed force were calculated by the sum of the single forces in each of the three areas. Shear, micro-cracking as well as fibre bending and fibre/matrix debonding are the cutting mechanisms, in which some ideas were adopted from metal modelling. This presented model was designed for a fibre orientation range of $0^\circ < \theta < 90^\circ$. In region 1 (rake face) the forces were calculated based on material shearing,

$$F_{y1} = \tau_1 h a_c \frac{\cos\phi \tan(\phi + \beta - \gamma_0) - \sin\phi}{\frac{\tau_1}{\tau_2} \cos(\theta - \phi) \sin\theta - \sin(\theta - \phi) \cos\theta} ,$$

$$F_{z1} = \tau_1 h a_c \frac{\sin\phi \tan(\phi + \beta - \gamma_0) + \cos\phi}{\frac{\tau_1}{\tau_2} \cos(\theta - \phi) \sin\theta - \sin(\theta - \phi) \cos\theta} ,$$
(10)

in which the angle of the shear plane needs to be evaluated. In region 2 (edge rounding) and region 3 (flank face) the forces were calculated based on contact mechanics with a cylinder or a wedge in elastic contact with a half-space respectively,

$$F_{y2} = K \frac{((\sin\theta)^2 + (\cos\theta)^2) r_e^2 \pi E^* h}{8 r_e} (\cos\theta - \mu \sin\theta) ,$$
(11)

$$F_{z2} = K \frac{((\sin\theta)^2 + (\cos\theta)^2) r_e^2 \pi E^* h}{8 r_e} (\cos\theta - \mu \sin\theta) ,$$

$$F_{y3} = \frac{1}{2} r_e E_3 h (1 - \mu \cos\alpha \sin\alpha) ,$$
(12)

$$F_{z3} = \frac{1}{2} r_e E_3 h \cos^2\alpha ,$$

in which E^* is the effective elastic modulus of the workpiece material perpendicular to the fibre axis, h is the thickness of the workpiece, r_e the nose radius and μ represents the friction coefficient. The coefficient K considers micro-cracking and pre-failure of the matrix material and needs to be evaluated by experiment for different CFRP materials. It was assumed that the spring-back height is equal to the cutting edge radius. The comparison of simulated and measured forces in orthogonal turning lead to maximum errors of 27% to 35% but according to ZHANG et al. [242, 269, 270] it predicts well the force trend due to variable process parameters such as rake angle variation, fibre-orientation and depth of cut. Although the authors also proposed chip formation mechanisms for $\theta > 90^\circ$ a model was not developed.

SAHRAIE JAHROMI and BAHR [195] complemented the above mentioned model of ZHANG et al. [242, 269, 270] by proposing an approach for fibre orientations ranging from $90^\circ < \theta \leq 180^\circ$ without the need for experimental parameter fitting. They used an energy method to analytically predict the process forces due to bending of the fibres and shear at the fibre-matrix interface. Therefore, defined representative volume elements (RVE) with a fibre segment surrounded by matrix material were considered, in which the complex interactions between the different RVEs were simplified, leading to significant deviations between predictions and measurements. Nevertheless, this model was an important contribution for analytical force prediction with consideration of multiphase, instead of equivalent homogeneous material.

QI et al. [177] developed an analytical microscale model for orthogonal cutting of CFRP with fibre orientations ranging from $0^\circ \leq \theta \leq \gamma + 90^\circ$, where γ is the rake angle of the tool. They adopted the subdivision of the cutting edge into three separate regions with each different deformation mechanisms from ZHANG et al. [242, 269, 270] and the consideration of representative volume elements (RVE) in combination with the minimum potential energy method (MPEM) from SAHRAIE JAHROMI and BAHR [195]. A critical concentrated force leading to fracture of the semi-infinite RVE due to compression and bending at the cutting edge

radius is calculated based on the failure criterion of exceeding the ultimate tensile strength of the fibre. Figure 2.36 (right) shows a single semi-infinite RVE under concentrated force (F_U) and with an elastic foundation (p_b).

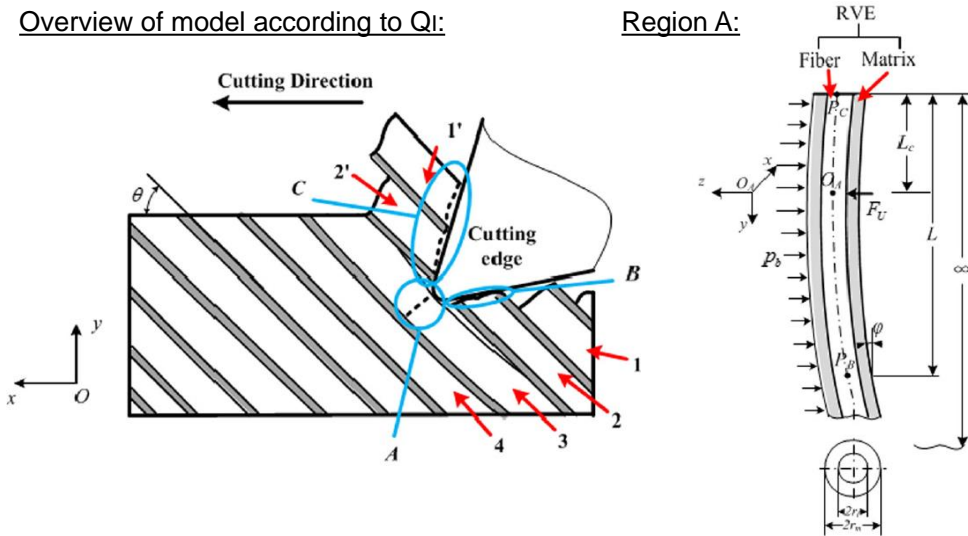


Figure 2.36: Overview of model scheme and single semi-infinite RVE under concentrated force (F_U) with elastic foundation (p_b), according to [177]

XU and ZHANG [257, 258] developed a further micro-mechanical force model for conventional and vibration assisted cutting. The interaction between tool nose and fibre was modelled as contact between two circular cylinders under normal load and friction. Exceeding the maximum tensile stress served as failure criterion in the contact area. The single semi-infinite fibres were backed on an elastic foundation (p_m , compression) and an equivalent modulus for fibre-matrix bonding (p_b , tension) was implemented, shown in Figure 2.37 (A). As soon the bonding strength is exceeded due to bending, a crack of the length h arises. Figure 2.37 (B) shows the deformation of a single fibre (blue) at different time steps and the red line represents the fibre-matrix debonding depth, according to the scale on the right. According to the authors, the debonding depth correlates to the subsurface damages, which could be found in the micrographs after machining. The simulation shows that utilisation of vibration results in lower forces and fewer damages, due to accelerated fibre fracture and reduced deflection. The diagram in Figure 2.37 (C) shows a certain correlation between simulated and measured forces, in which total deviations of more than 20% occur. XU and ZHANG [257, 258] drew the conclusion that the fibre orientation generally influence the subsurface damage depths and forces and $\theta=135^\circ$ is the most critical orientation regarding damages and forces.

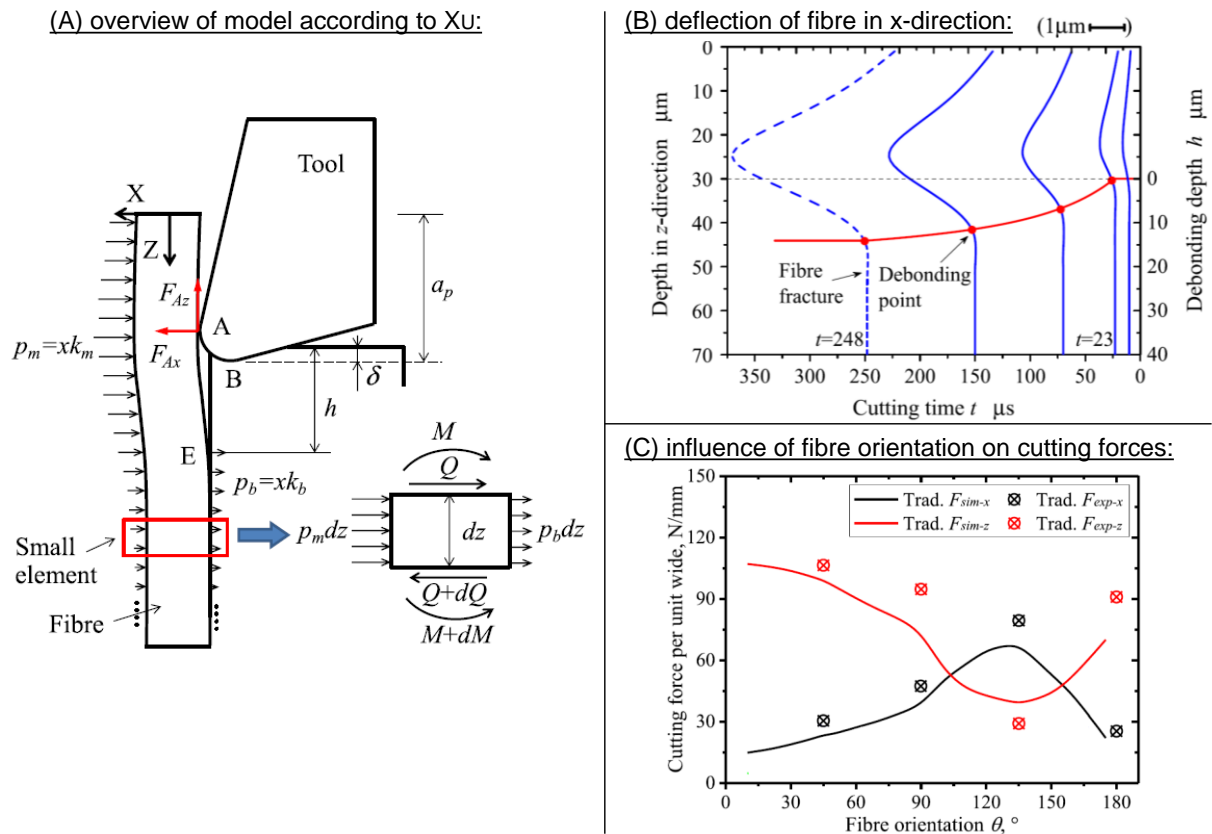


Figure 2.37: Fibre deformation model with exemplary deflection and fibre-matrix debonding depth with increasing feed path and time as well as simulated vs. measured force results, according to [257, 258]

According to SCHÜTTE [204], with increasing computing power the numerical approaches, such as finite element modelling (FEM) gain importance besides the analytical models. Some FEM approaches modelled orthogonal machining to predict the cutting forces or chip formation in general. These studies mostly included simplifications such as

- 2D approach,
- Macroscopic material model with continuous but anisotropic material properties,
- Pure linear elastic behaviour until critical stress level is reached wherein different stress levels are necessary to describe orthotropic material properties,
- And more...

AROLA and RAMULU [5] simulated the chip formation in CFRP with FEM in 1997, considering both the Tsai Hill and the maximum stress failure criterion. This quasi-static model is typical for the early FEM models of CFRP machining, which depict the composite material as an equivalent homogeneous material. This common simplification led to limitations of the model, making a separate fracture description of the fibre and matrix impossible. RAO et al. [183, 184] repealed this disadvantage of FEM approaches by modelling UD-CFRP and UD-GFRP composite materials as multiphase material with cohesive zones at the fibre-matrix interfaces, which allowed for debonding. This model was valid for fibre orientations of $0 \leq \theta \leq 90^\circ$ and enabled the prediction of damages and chip formation mechanisms. In [183] a standard ABAQUS FE code was used, while in [184] the calculations were conducted with an ABAQUS/Explicit FE code to overcome convergence difficulties. An advanced approach for interfacial modelling between fibres and matrix was presented by CALZADA et al. [26] with

continuum elements. These elements allowed for failure in both tension and compression and enabled for description of the fibre failure mode occurring during machining. While FE simulation of orthogonal cutting still needs simplifications, more complex simulations of real drilling processes to date need even stronger simplifications. CHAKLADAR et al. [41] presented a FEM simulation for analysis of delamination in drilling GFRP with different feed and speed combinations. The woven GFRP was modelled with an equivalent elastic macro-mechanical model and *Ansys Autodyn* served as solver environment. Despite several simplifications of the boundary conditions and the element shape functions, the calculated thrust forces were in good accordance (80-90%) of the experimental results. According to CHAKLADAR et al. [41] cutting action could not be predicted, because of the elastic material model approach; An elasto-plastic model would be essential to simulate chip formation and damages. Tool wear could not be simulated because the drilling tool was considered rigid.

In summary, numerical approaches e.g. FEM are currently suitable to visualise chip formation processes, but do not explain the correlation between cutting forces and key variables, such as fibre orientation, tool geometry or process parameters (feed, cutting speed). However, these relationships are precisely essential for effective optimisation of cutting processes in CFRP machining. Optimisation in FEM usually needs a lot of iterations, resulting in time consuming and costly calculations. Consequently, analytical force models revealing the cutting mechanisms are essential for efficient cutting process optimisation in CFRP machining. According to PWU [176] it is well known from metal machining that none of the existing models are universally accurate in predicting the material behaviour during machining, but nevertheless these works are still valuable for the progress of machining technology.

Friction Coefficients in Modelling of CFRP Machining

For realistic modelling of CFRP machining processes the understanding of friction and determination of friction coefficients is required. Due to the anisotropy, fundamental contact theories like the *Hertzian* are not valid for fibre reinforced polymers (FRPs), as stated by NING and LOVELL [167]. HWU and FAN [119, 120] were the first ones deriving a closed-form solution for a sliding contact between bodies and a plane with CFRP properties (elastic, anisotropic) by applying the STROH's formalism [211] for anisotropic elasticity. This approach was used by NING and LOVELL [167] to model sliding friction with FRPs: The authors analysed the influence of the fibre-volume fraction, -orientation, -material, matrix material and friction coefficient on the wear of the FRPs. According to their calculations the friction coefficient has a significant influence on the contact patch for transverse and normal sliding, relative to the fibre direction. While some of the early FEM analyses in FRPs [154, 155, 178] neglect friction effects, others [5, 6] use constant coefficients of friction of $\mu=0.3$ or $\mu=0.4$ at the flank face-material contact. These friction coefficients are based on measurements by SUNG and SUH [212], shown in Figure 2.38 (A), who tested various fibre orientations of graphite-epoxy FRP sliding against 52100 steel. A pin-on-ring apparatus was utilized to test with different speeds and varying fibre orientations relative to the sliding orientation. Normal orientation of the fibres to the sliding surface shows smaller frictional resistance than transverse orientation. NAYAK and BHATNAGAR [165] conducted pin-on-disk experiments with variable fibre orientations of GFRP sliding on HSS under a high normal load of 120 N to determine the directional friction coefficient, shown in Figure 2.38 (B). This high normal load is more similar to the machining conditions and promises for more accurate simulation

results of a machining operation. But this comparably high load is focused on a rather large area of 100 mm^2 resulting in a nominal contact pressure of just 1.2 MPa. It needs to be considered that the two studies [165, 212] use contrary definition of fibre orientation with respect to the sliding direction, shown in the boxes below the diagrams in Figure 2.38. Mismatching the results from SUNG and SUH the friction coefficient in Figure 2.38 (B) increased from $\mu=0.3$ at $\theta=0^\circ$ (transverse) to $\mu=0.88$ at $\theta=90^\circ$ (normal), which implies that the normal fibre orientation with respect to the sliding surface has higher frictional resistance. Considering this directional data, the cutting force in NAYAK and BHATNAGAR's [165] macro-mechanical model fits well, but the thrust force shows large variations compared to measurements and even a different trend arises.

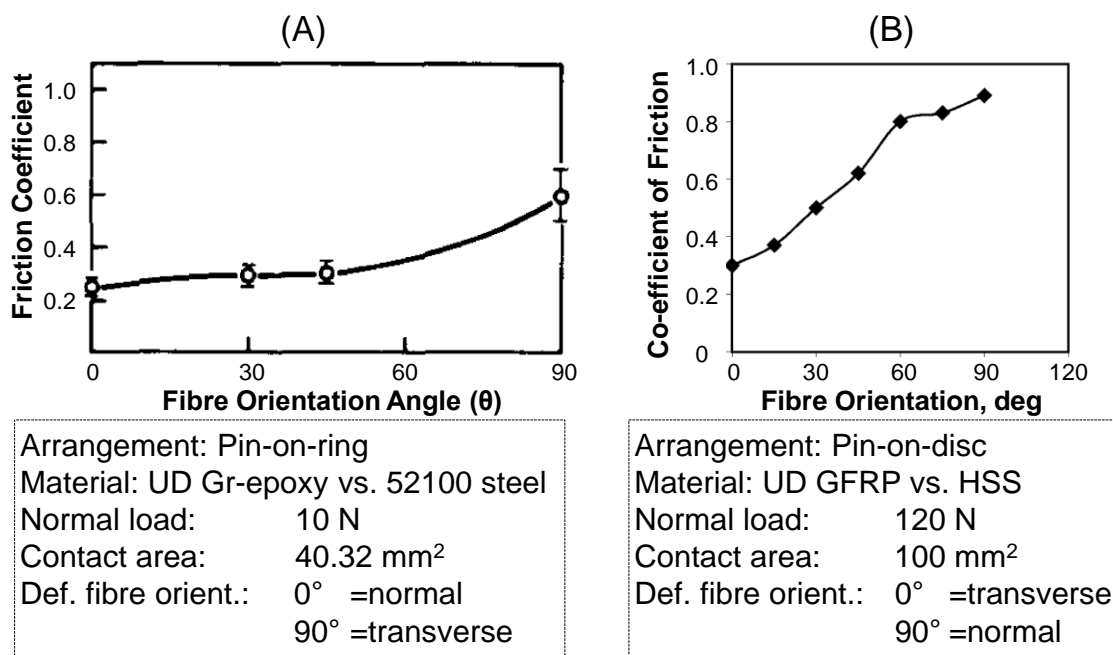


Figure 2.38: Friction coefficient according to SUNG and SUH (A) and NAYAK and BHATNAGAR (B)

In the past the friction coefficient between any material and FRP was determined by pin-on-disk, disk-on-disk or other similar closed tribometers, which allow for precise but limited adjustment of the boundary conditions. These setups enable for fast operation with good repeatability under lab conditions but show a multiple sliding contact along the same track, causing run-in effects. As pointed out by MONDELIN et al. [163] and PULS et al. [174], such closed tribometers neither reflect machining contact conditions nor use freshly generated surfaces for the sliding contact, as being typical for machining with continuous material flow along the tool faces. To date very few studies [43, 163, 237] exist, focusing on the determination of friction coefficient between CFRP and diamond under realistic cutting conditions:

- MONDELIN et al. [163] present the friction coefficient between monocrystalline diamond and CFRP depending on various contact pressures, sliding velocities (20 m/min and 40 m/min), CFRP layer orientations and consider the utilization of cutting fluid. The experimental friction coefficients for CFRP-Diamond are significantly smaller than any other value reported in literature and vary between 0.08 to 0.12 for dry and 0.06 to 0.07 for lubrication conditions. Due to the CFRP probe shape (sheet material) and unavailability of unidirectional material, the influence of fibre orientation has not been analysed.

- WANG et al. [237] determine the temperature influence on the friction coefficient between carbon/epoxy composites and monocrystalline diamond. The sliding speed over the unidirectional CFRP sheet material was just 0.5 m/min. The authors measure a coefficient of friction of $\mu=0.125$ for sliding in fibre orientation (0°) and $\mu=0.175$ for sliding perpendicular (90°). With increasing temperature the friction coefficient increases to $\mu=0.4$ at 125°C and drastically decreases when exceeding the glass transition temperature, due to changes in the properties of the epoxy resin.
- CHARDON et al. [43] analyse the influence of very high sliding velocities up to 800 m/min on the friction coefficient between polycrystalline diamond (PCD) and randomly structured CFRP. In general the friction coefficients with values between $\mu=0.05$ and $\mu=0.08$ are even lower than those obtained between monocrystalline diamond and CFRP in [163]. It needs to be considered that different CFRP materials were tested. For high speeds (>100 m/min) the influence of the sliding velocity on the friction coefficient is low.

3 Research approach

Subject of the research carried out in this thesis is the optimisation of rivet bore generation in carbon fibre reinforced polymers (CFRP) for the aerospace industry. Indeed, the proposed approaches are not only limited to the aviation industry but will be applicable in any field where CFRP has to be drilled. The thesis starts with an extensive literature and market review, shown in chapter 2 to evaluate the available technologies and identify needs for optimisation. The tool lifetime, limited by insufficient machining quality is identified as main research demand. To generate a sufficient machining quality in a certain CFRP material for a longer period of time, either an adaptation of the machining process strategy, the tool geometry, the tool coating or the process parameters may be conducted.

The main four topics, focussing on in this thesis are:

- development of an analytical **force model**
- powerful method for **evaluation of the bore entrance/exit quality**
- selective **cutting edge treatment** of drilling tools
- optimisation of **process strategy** in CFRP drilling

For efficient optimisation of rivet bore generation it is necessary to understand the chip formation processes, which are commonly investigated during fundamental orthogonal cutting experiments. Analytical force models, which are revealing the mechanics of chip formation, help to identify the correlation between the key variables influencing the machining quality and tool lifetime. The following key variables, which influence the chip formation, are unanimously reported:

- fibre orientation,
- fibre and matrix properties,
- rake and clearance angles,
- friction coefficient between tool and workpiece,
- cutting edge micro-geometry

Force Model under Consideration of Friction and Tool Wear

Current analytical force models in CFRP indeed include the first four of the above presented key variables. But no tool wear or detailed micro-geometry is reflected, except for the consideration of the simplified cutting edge radius. Among other simplifications this is the reason, why the existing models result in strong deviations of the absolute force values. It is evident that no model is universally accurate but the main mechanisms of CFRP machining should be represented and the simulation should match the course of force measurements.

Based on this demand identification, a focus of the micro-mechanical model proposed in this thesis will be on the consideration of the wear-induced change of tool micro-geometry on the chip formation, which has not been addressed in the existing models. This analytical force model adopts certain approaches from former force models and expands them to reveal mechanisms of cutting, which were found during several analyses of orthogonal cutting experiments. Wear of the cutting edge and micro-geometry changes are evaluated regularly during fundamental orthogonal cutting experiments. A further important sub-topic identified as main research demand is the evaluation of realistic friction coefficients, which are necessary for force simulation. Experiments with a cutting-process-tribometer developed

at IWF and variable fibre orientations are presented in this thesis. In contrast to standard pin-on-disk experiments, no run-in effects influence the measurement results of the friction coefficient and due to the setup, realistic cutting speeds, realistic normal forces and realistic surfaces which are covered with small fibre particles are considered.

The increasing number of publications in the field of analytical CFRP force modelling in recent time shows the necessity of such models and the demand for optimisation of CFRP machining processes. To date no comprehensive analytical model exists, describing the process forces in UD-CFRP machining as a function of the fibre orientation, the tool macro-geometry, the material and friction properties as well as the wear induced micro-geometry.

Evaluation of Bore Entrance/Exit Quality

It is well known that the tool lifetime in CFRP drilling is limited by insufficient machining quality. Delamination is one of the most critical damages in FRP occurring at the bore entrance and exit sides. Consequently, the bore quality evaluation techniques have to be adapted to the typical FRP-material characteristics. To date no uniform quality measurement technique exists. The most common method is the evaluation of the so called delamination factor F_d , which describes the ratio between the maximum damaged diameter to the bore diameter. Further adjusted factors exist, e.g. F_{da} and F_{ed} as being explained in chapter 2.2.2, which focus on spalling and delamination, when describing the damages being induced by a drilling operation in FRP. But practical experiences in CFRP prove that uncut fibres, which are neglected by these factors, occur at least as frequently as the delamination damages and are obstructive when inserting rivets. Consequently, to date the bore exit quality is assessed incompletely. This research gap is addressed in this thesis by proposing a comprehensive bore exit quality evaluation factor. The new damage criterion for bore entrance and exit quality evaluation takes the existing damage factors as well as the effect of uncut fibres at bore exits into account.

Cutting Edge Treatment of Drilling Tools

The two above described fundamentals – force model and bore quality evaluation factor – represent two different levers to increase the comprehension of chip formation processes in CFRP. Subsequently in this thesis, the advanced comprehension helps to find approaches for the optimisation of drilling processes. The first optimisation approach in this thesis for the rivet bore generation in CFRP aims for post-coating cutting edge treatment of CVD diamond coated carbide spiral drills. It addresses the effect found during drilling experiments by HENERICHS et al. [98] and WANG et al. [244], in which conventional diamond coated tools show a poor bore exit quality until the coating smoothens and partly wears within the first bores. The length of this run-in period depends on the tool geometry, coating surface and CFRP material. A certain roughness of the applied diamond coating surface and an increased cutting edge radius are identified as main reasons causing the run-in period. For optimised machining, it aims to generate diamond coated carbide drilling tools, which produce damage-free bores from the first bore on. Approaches exist, adjusting the rake, flank or tip angle as well as using web thinning or multifaceted tools to optimise drilling in CFRP, as presented in chapter 2.1.3. But no research in CFRP machining exists, focussing on post-coating cutting edge treatment of diamond coated drilling tools, as being expound in 2.4. It promises to produce ideal sharp cutting edges from the first bore on, if it is possible not to damage the diamond coating during post-processing. Chapter 2.4 presents, that no research is found taking purposefully advantage of the different wear rates of the tool substrate

material and the diamond coating, theoretically resulting in ideally sharp cutting edges and leading to very long lasting tool lifetimes. Hereinafter this effect is referred to as *self-sharpening effect*.

Optimisation of Process Strategy: Orbital Drilling vs Conventional Drilling

The second optimisation approach for the rivet bore generation in CFRP aims for a different machining process strategy, named *orbital drilling*. It promises a better machining quality in CFRP by avoiding the unfavourable region on the tool centre with zero cutting velocity. By means of the increased CFRP machining comprehension in the context of this thesis, orbital drilling tool geometries are developed, which result in drastically increased bore quality. Significantly less bore exit damages e.g. delamination or uncut fibres and less bore channel damages e.g. fibre cracks, pull-out or bending occur in orbital drilling. Although single approaches exist presenting the advantages of orbital drilling, no study shows a direct comparison to conventional drilling process with the same boundary conditions. The presented comparison takes detailed quality analyses, force measurements and the processing time into account.

4 Fundamental orthogonal cutting experiments

Orthogonal cutting experiments serve to increase the fundamental knowledge about machining properties and chip formation processes in CFRP machining. As presented in Chapter 2.1, several authors conducted cutting experiments in CFRP with simplified machining conditions, e.g. planing and shaping. In collaboration with HENERICHS [101] further free orthogonal cutting experiments were conducted on a turning test rig, which allows for realistic cutting speeds and continuous, infinite cutting. A cutting speed variation from approximately 20 m/min to 500 m/min is possible in these experiments as well as a fibre orientation variation in the ring-shaped CFRP. Parts of these experiments were presented by HENERICHS [101] in 2015 and in several publications [62, 96, 102, 230]. The thesis and publications [62, 96, 101, 102, 230] showed the influence of tool geometry and fibre orientation on the process forces in orthogonal cutting as well as on the chip formation mechanisms.

The present thesis aims to extend the discovered mechanisms in free orthogonal cutting by introducing an analytical force model, which takes the observed effects during machining, the occurring damages in the CFRP, tool wear and friction along the cutting edge into account. To improve clarity of this thesis, individual observations that have already been shown in [101] but are necessary for the force model will be explained again briefly.

4.1 Free orthogonal cutting test rig setup

The orthogonal cutting experiments are carried out on an *Okuma LB15_{II}-M* lathe. It has been arranged to allow machining CFRP in an orthogonal face turning operation at a constant fibre orientation θ . The setting angle is $\kappa=90^\circ$ and the inclination angle $\lambda=0^\circ$. Cutting velocities in a range of 20-500 m/min in an infinite, non-interrupted cut are possible. The setup and specifications of the lathe are shown in Figure 4.1.

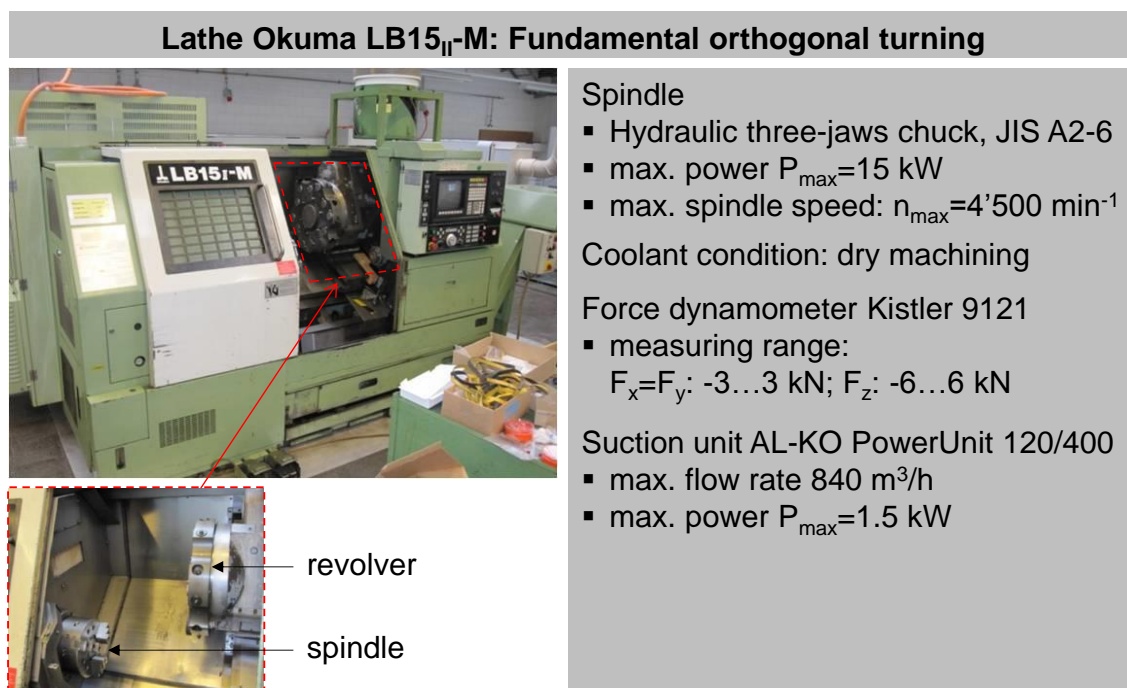


Figure 4.1: Specifications of the lathe *Okuma LB15_{II}-M* used for orthogonal cutting tests

Due to good accessibility, the setup enables for high-speed camera recordings of the tool in contact with the material. Figure 4.2 (A) shows exemplary manufacturing of the unidirectional semi-circular shaped CFRP laminate with constant fibre orientation of $\theta=45^\circ$. By means of waterjet machining three segments of 120° each are cut out and are assembled to a ring. In Figure 4.2 (C) the CFRP segments with an outer diameter of approximately $d_{\text{out}}=195$ mm and width of approximately $w_t=5$ mm are presented clamped in the chuck of the lathe.

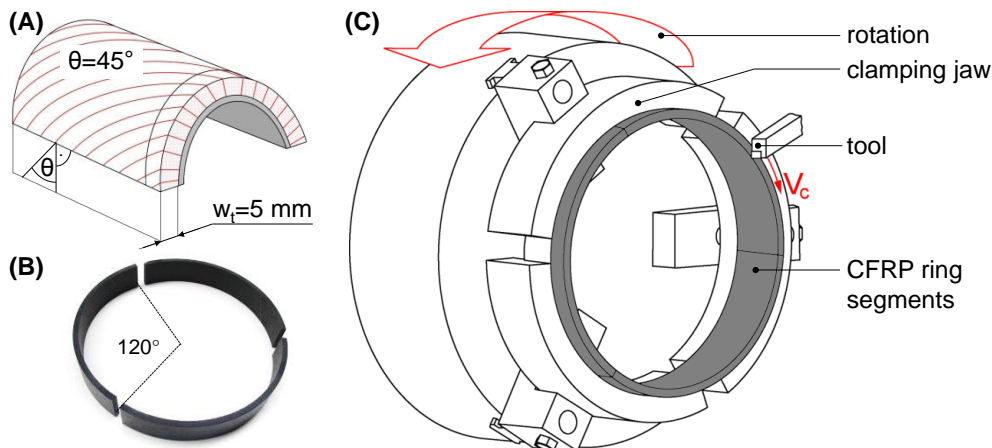


Figure 4.2: CFRP raw material with indicated UD fiber orientation by red lines (A); CFRP segments prior to machining (B); CFRP workpieces clamped into machine tool (C)

Machining experiments are analysed by force measurements with a *Kistler*[®] three axes dynamometer 9121 mounted to the tool and high speed camera recordings with a *Vision Research Phantom V12*. The sensitivity of the dynamometer for the x- and y-axes are 7.9 pC/N, and for the z-Axis 3.8 pC/N. Load amplifiers and data acquisition card prepare and digitise the signals that are ultimately saved for analysis by means of a *LabView* program. Several further analyses are performed subsequently to the experiments, e.g. roughness measurements and micrographs of the machined surfaces as well as tool wear analyses.

The designation of the unidirectional CFRP workpiece material utilized in the experiments is M21/34%/UD194/IMA-12K, which is common in the aerospace industry. According to the specifications it contains 66% (by weight) intermediate modulus (IM) carbon fibres and impact-modified matrix material HexPly[®] M21 (epoxy-based) from *Hexcel*[®]. One roving contains each 12000 single fibres. The material is well known to be difficult to machine. Both, the high fibre content as well as the high toughness of the fibre and matrix system cause extensive tool wear. Drilling operations of this material result in serious delamination due to the unidirectional configuration and the difficult cutting characteristics of the fibre. The material properties of the CFRP with epoxy-based matrix material are presented in Table 4.1. Six fibre orientations are tested: $\theta=0^\circ, 30^\circ, 60^\circ, 90^\circ, 120^\circ, 150^\circ$.

Table 4.1. Physical and mechanical properties of the unidirectional CFRP material

Physical properties	fibre	weave/UD	fibre Mass [g/m ²]	fibre volume [%]	laminate density [g/cm ³]	glass trans. temp. [°C]
	IMA	UD	194	59.2	1.58	195
Mech. properties	tensile	tensile strength [MPa]	tensile modulus [GPa]	compression	compr. strength [MPa]	compr. modulus [GPa]
	method EN6032	3050	178	method EN2561 B	1500	146

Uncoated carbide tools of the grade H13A (K20) of the company *Sandvik*[®] with insert geometry “CCMW 09 T3 04” are utilised. In total eight different tool geometries with varying rake and clearance angles are tested in the experimental series. As shown in Table 4.2, the rake angle γ is adapted from 0° to 30° , the clearance angle α varies from 7° to 21° and the mean initial cutting edge radius is $r=5 \mu\text{m}$. The different macro geometries are created by grinding from the initial geometry $\gamma=0^\circ$ and $\alpha=7^\circ$, as exemplarily shown in the microscope image in Figure 4.3 (C).

Table 4.2: Cutting inserts geometries

tool description	C	E	H	I	J	L	M	N
rake angle γ	0°	10°	10°	10°	20°	20°	20°	30°
clearance angle α	14°	7°	14°	21°	7°	14°	21°	7°

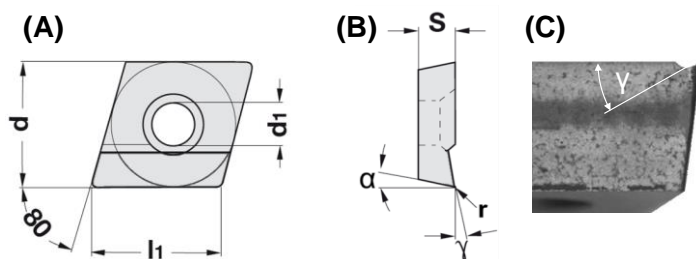


Figure 4.3: Schematic cutting tool top view (a) and side view (b); Microscope image with ground rake angle γ

Except for the rake angle γ , the clearance angle α and the varying fibre orientation, the machining conditions are constant, as shown in Table 4.3. Based on these parameters the removed material per millimetre cutting edge is $V_w=1241 \text{ mm}^3/\text{mm}$ and the specific removal rate $Q_w=2700 \text{ mm}^3/\text{mm}/\text{min}$. Due to a constant feed f_z in the presented experiments, the actual feed travel l_f is linearly correlated to the cutting length l_c of a certain tool with $l_c = l_f/f_z \cdot \pi \cdot (d_{out} - w_t)$, in which d_{out} represents the outer diameter of the CFRP ring segments and w_t the wall thickness of the workpiece. Table 4.4 shows this correlation for a workpiece with an outer diameter of 195 mm for each analysing step. At these analysing steps, some of the orthogonal cutting experiments were repeatedly interrupted to measure the actual cutting edge wear. The cumulated cycle time of one orthogonal turning experiment with a total feed travel of 2 mm is approximately 26.5 seconds.

Table 4.3: Machining parameters of orthogonal turning tests and chip root experiments

$\gamma ; \alpha$ [deg]	v_c [m/min]	f_z [mm/rev]	a_e [mm]	Θ [deg]	Q_w [mm ³ /mm/min]	V_w [mm ³ /mm]
0, 10, 20, 30; 7, 14, 21	90	0.03	5	0, 30, 60, 90, 120, 150	2700	1241

Table 4.4: Analysing steps for tool wear analysis

analysing step	#1	#2	#3	#4	#5	#6	#7
feed travel l_f [mm]	0	0.25	0.5	0.75	1	1.5	2.0
cutting length l_c [m]	0	5	10	15	20	30	40
time [s]	0	3.31	6.62	9.93	13.24	19.87	26.49

4.2 Results of cutting experiments with focus on forces and wear

In correspondence with the fundamental experiments by RUMMENHÖLLER [193] or WANG et al. [240] the process forces in the conducted experiments increase with progressing length in material contact, due to abrasive tool wear. Figure 4.4 shows an exemplary force plot of the tool geometry H ($\alpha=14^\circ$; $\gamma=10^\circ$) during machining material with $\theta=0^\circ$. It shows a digressively increasing feed force and slightly increasing cutting forces. Due to the orthogonal cutting conditions the passive force is zero. The force magnitude and amount of force increase in the various experiments depends on the chip formation mechanisms, tool geometry and extend of tool wear. To enable comparability, the forces are evaluated at the end of the experiments at 2 mm feed travel length, marked by a red cross in Figure 4.4.

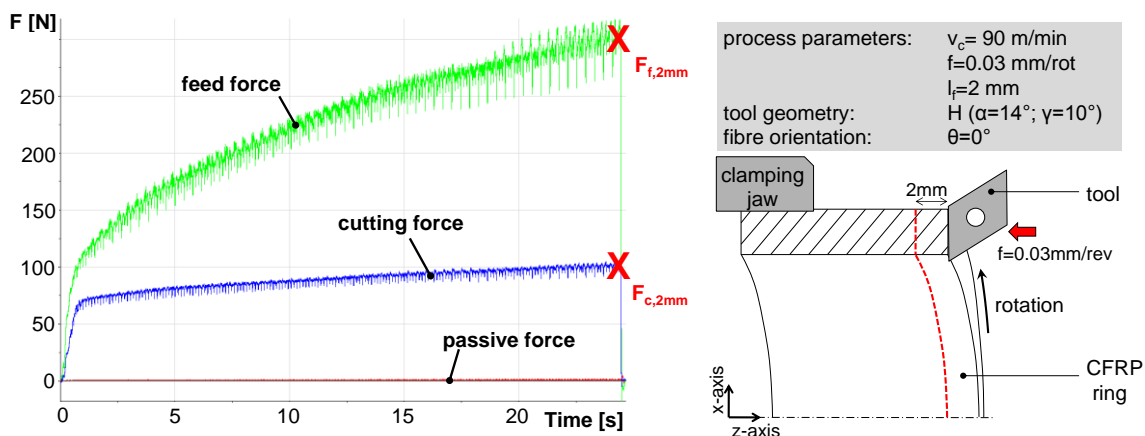


Figure 4.4: Exemplary force plot of orthogonal cutting process and test-rig setup

Figure 4.5 and Figure 4.6 show the feed forces and cutting forces at the above explained evaluation position of 2 mm feed travel length or cutting length of $l_c=40$ m respectively. The unidirectional fibre orientation of $\theta=120^\circ$ does not lead to evaluable results in this test rig setup, due to crack initiation in fibre orientation and insufficient stability of the workpiece material. The fibre orientation θ and the clearance angle α have a significantly larger influence on the process forces compared to the rake angle γ . Maximum feed forces $F_{f,2mm}$ occur in cutting fibre orientations close to $\theta=30^\circ$ in combination with small clearance angles and maximum cutting forces $F_{c,2mm}$ close to $\theta=60^\circ$. Lowest process forces appear, when machining contrary to the fibre orientation at $\theta=150^\circ$.

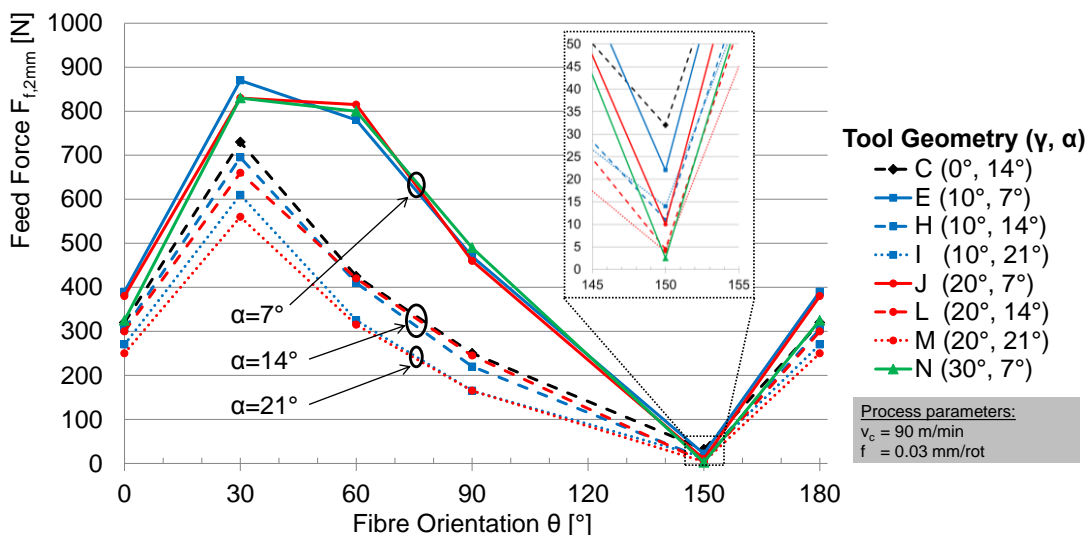


Figure 4.5: Feed forces $F_{f,2mm}$ at 2 mm feed path ($l_c=40$ m); $v_c=90$ m/min, $f=0.03$ mm

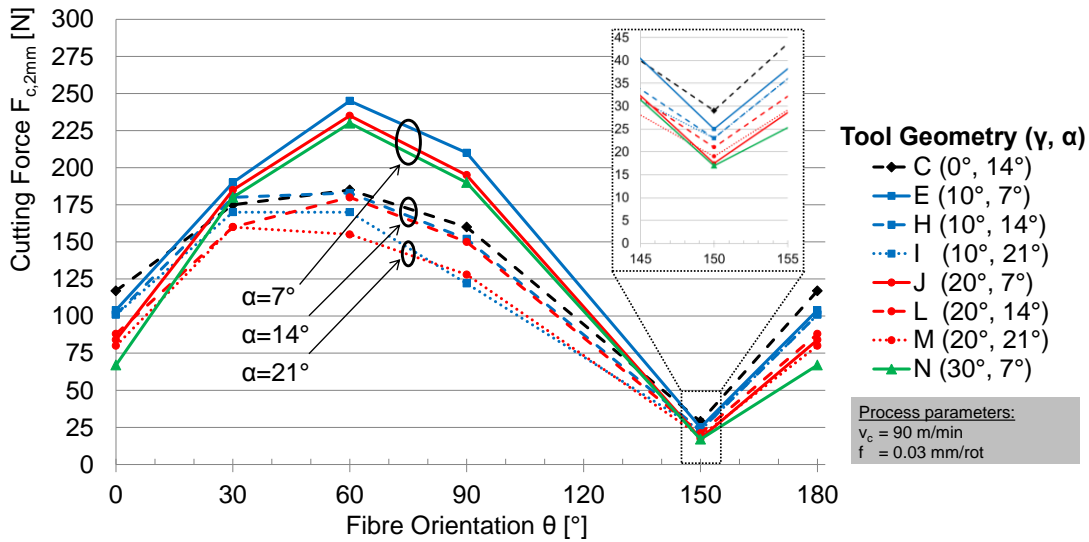


Figure 4.6: Cutting forces $F_{c,2mm}$ at 2 mm feed path ($l_c=40$ m); $v_c=90$ m/min, $f=0.03$ mm

To show the tool wear influence on the forces, the same evaluation for 0.5 mm feed path or a cutting length of $l_c=10$ m respectively, is presented in Figure 4.7 and Figure 4.8. Depending on the tool geometry, the cutting forces decrease for fibre orientations larger than 30° or 60° . This is divergent to the results by WANG et al. [240] and ZHANG et al. [270], who showed maximum cutting force values in orthogonal cutting of $\theta=90^\circ$. Comparing these results it needs to be considered that different CFRP material was tested, the cutting speed of 90 m/min in the presented setup is significantly higher than the 1-4 m/min in [240, 270] and carbide tools are applied in contrast to PCD tools. In accordance with evaluations in [101, 230], this cutting force decrease for fibre orientations larger than 30° - 60° is due to subsurface damages, which are detected in micrographs parallel to the cutting velocity direction. Figure 4.9 shows an overview of the micrographs at various fibre orientations, which show an association of the subsurface damages and the cutting forces.

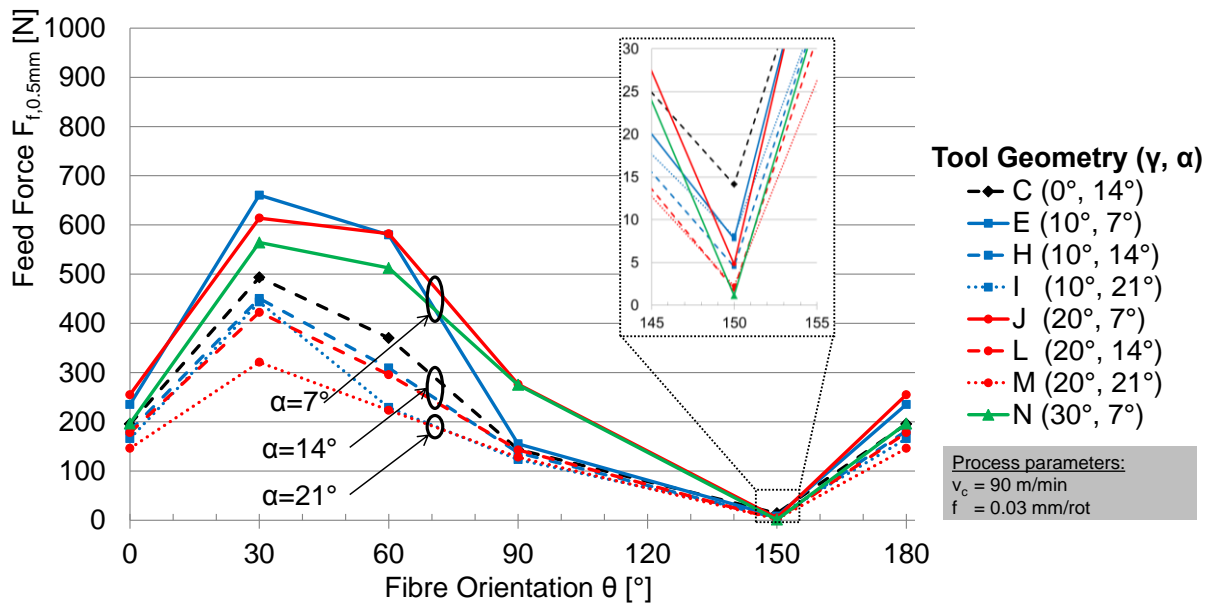


Figure 4.7: Feed forces $F_{f,0.5mm}$ at 0.5 mm feed path ($l_c=10$ m); $v_c=90$ m/min, $f=0.03$ mm

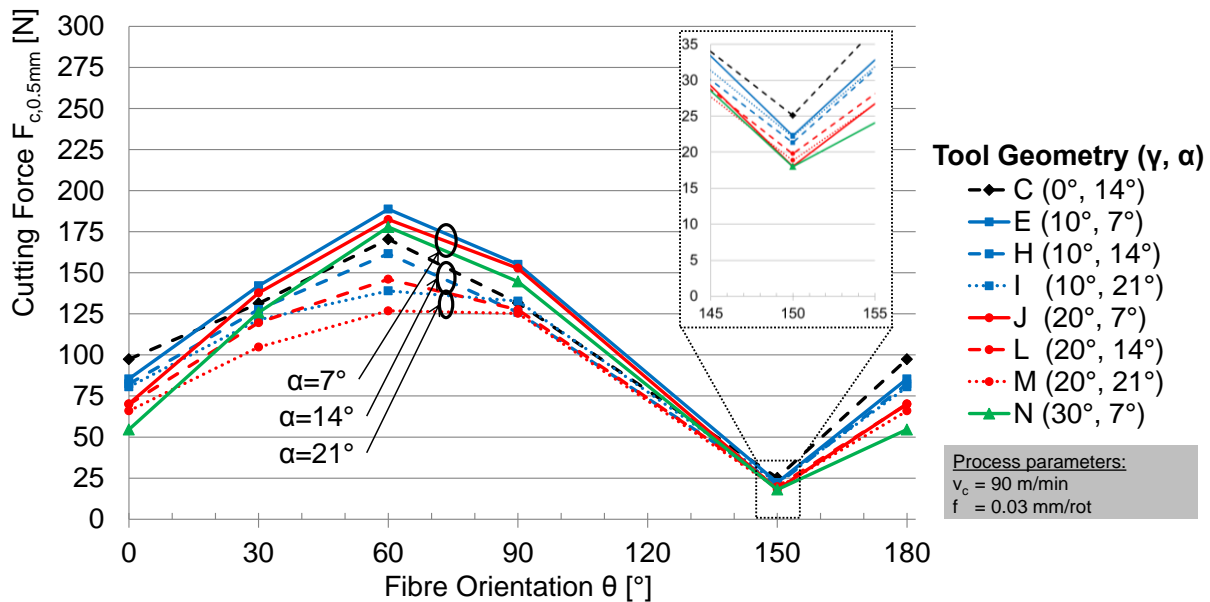


Figure 4.8: Cutting forces $F_{c,0.5mm}$ at 0.5 mm feed path ($l_c=10$ m); $v_c=90$ m/min, $f=0.03$ mm

For fibre orientations $\theta=0^\circ$ and $\theta=30^\circ$ no significant subsurface damages occur. In total very few fibres are broken beneath the surface and the top layer is covered with compressed abrasion material. In the $\theta=60^\circ$ material, machined with tools of $\alpha=21^\circ$ and $\alpha=14^\circ$ (not presented) cracks run periodically across the fibre direction up to depth of $80\ \mu\text{m}$. About 50% of the fibres are broken at least once. For $\theta=90^\circ$ material even more cracks appear. While tools with small flank angle ($\alpha=7^\circ$) generate cracks in 50% of the fibres, for $\alpha=21^\circ$ every fibre is broken multiple times up to depths of $90\ \mu\text{m}$. The damages correspond to the force measurements, with a force decrease for fibre orientations $\theta>30^\circ$ in combination with large flank angle ($\alpha=21^\circ$) and with a decrease for $\theta>60^\circ$ for smaller flank angle ($\alpha=7^\circ$). The presented subsurface damages weaken the material, resulting in reduced cutting forces.

According to current findings, these cracks occur due to bending of the fibres by the cutting edge and exceeding the bending strength. For larger fibre orientations, the fibres are steeper relative to the cutting velocity direction and the necessary deflection for diving beneath the cutting edge is larger. One possible explanation for the flank angle influence is the higher compression force of the material underneath the tools with low flank angle ($\alpha=7^\circ$), counteracting crack propagation. For further explanations and SEM microscopy analyses of the CFRP surface, please consider the dissertation by HENERICHS [101].

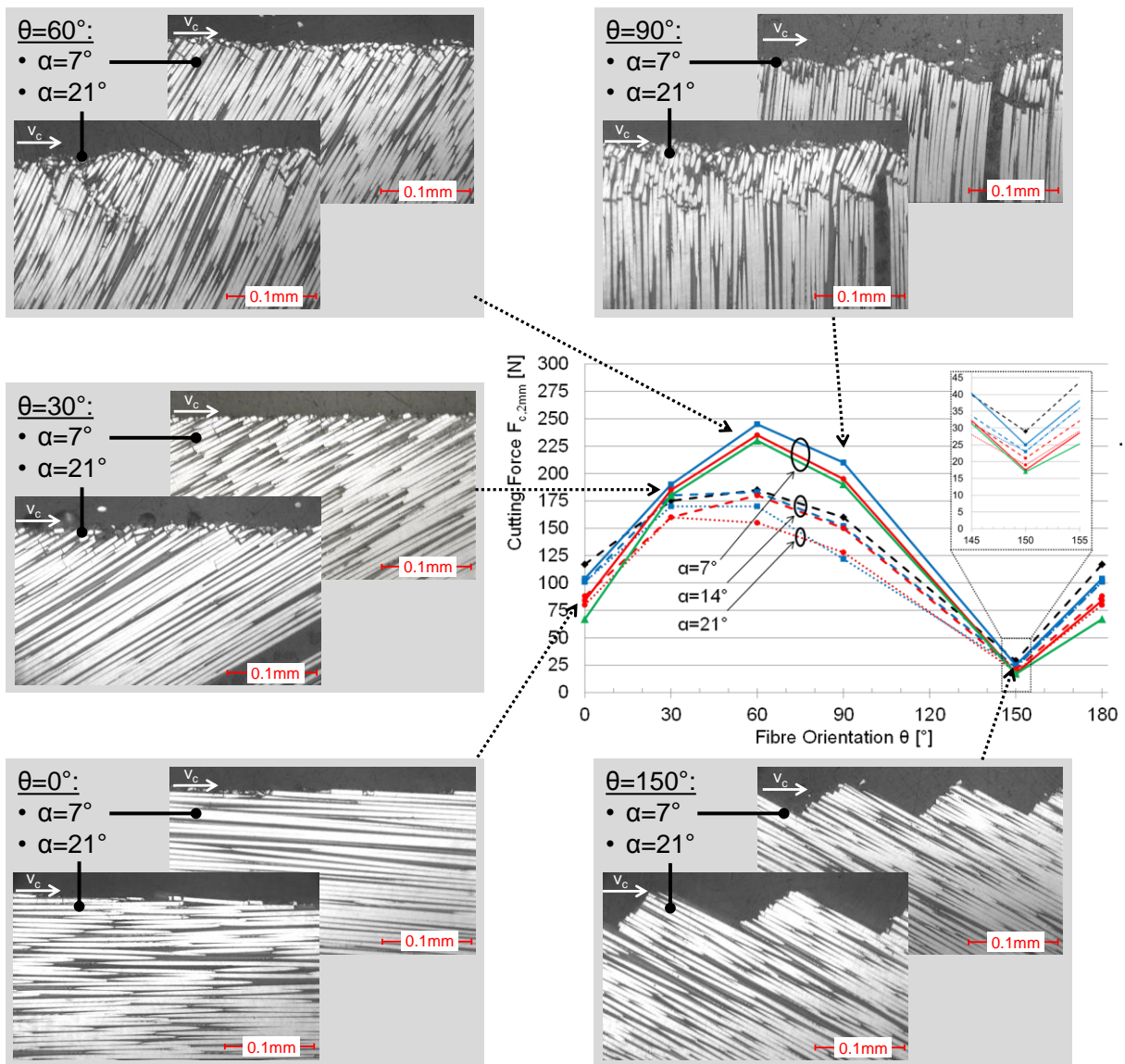


Figure 4.9: Micrographs parallel to cutting velocity direction for two tool geometries M ($\gamma=20^\circ$, $\alpha=21^\circ$) and J ($\gamma=20^\circ$, $\alpha=7^\circ$) at each fibre orientation; $v_c=90$ m/min, $f=0.03$ mm

The tool geometries M ($\gamma=20^\circ$ and $\alpha=21^\circ$) and J ($\gamma=20^\circ$ and $\alpha=7^\circ$) with variable clearance angle are exemplarily chosen to show the effect of tool wear with progressing feed travel and cutting length on the process forces. The diagrams in Figure 4.10 demonstrate that the feed forces from cutting lengths $l_c=5$ m to $l_c=40$ m at $\theta=30^\circ$ increase by a maximum of 75%-100%, while at $\theta=90^\circ$ the feed forces increase only by 42% for tool geometry M but by even 190% for tool geometry J. In general the tools with smaller clearance angle have an increased contact area along the flank face, thus show more abrasive tool wear and the forces grow significantly faster. At fibre orientations of $\theta=0^\circ$ and $90^\circ \leq \theta < 180^\circ$, where just little spring back of the fibres occurs along the flank face, the initial feed and cutting forces of the hardly worn tools are very similar, independent on the tools macro geometry. These observations lead to the assumption that the process forces are mainly influenced by the actual state of tool wear. As presented by HENERICHS et al. [101] maximum tool wear occurs for fibre orientations $\theta=30^\circ$ and $\theta=60^\circ$, where the fibres comb along the cutting edge. Consequently, analytic force modelling without consideration of tool wear is inadequate.

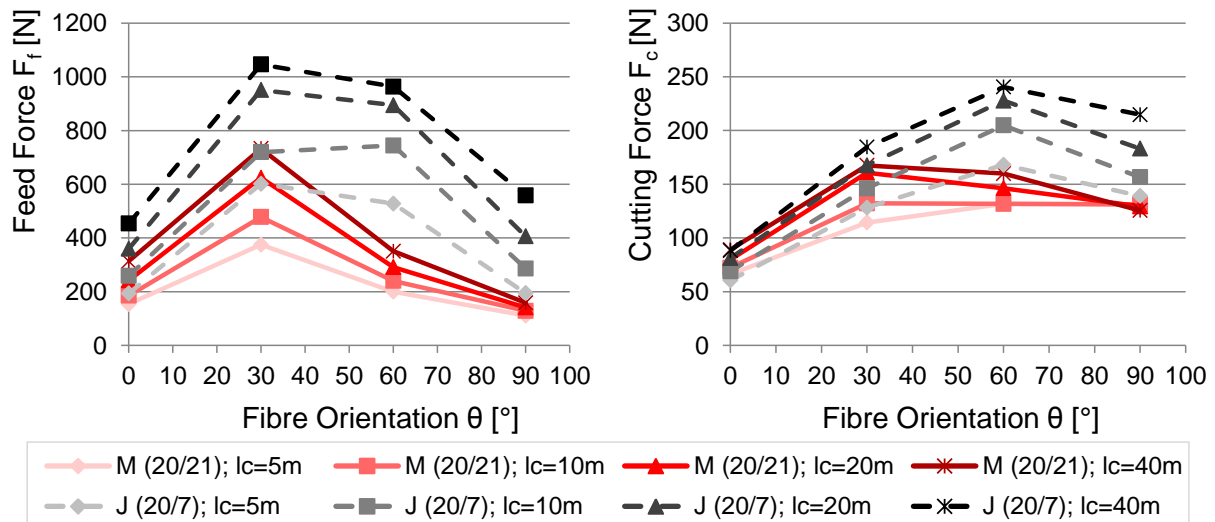


Figure 4.10: Force increase caused by tool wear with increasing cutting length $l_c=5\text{m}-40\text{m}$ of tool geometry M ($\gamma=20^\circ$, $\alpha=21^\circ$) and J ($\gamma=20^\circ$, $\alpha=7^\circ$); $v_c=90\text{ m/min}$, $f=0.03\text{ mm}$

The various cutting edge micro-geometries are evaluated by means of the CEA-approach, proposed by HENERICHS et al. [101]. This method provides a large number of micro-geometry parameters, of which five meaningful ones are chosen to describe the actual wear state. In accordance with ZHANG et al. [269] the cutting edge is subdivided into three separate regions, namely the *chipping region 1* along the rake face, the *pressing region 2* along the cutting edge rounding and the *bouncing region 3* at the flank face, as shown in Figure 4.11 (left). The analysis of several worn CFRP tools shows that the operative part of cutting edges can sufficiently be described by the simplification «straight-line – ellipse – straight-line», as being presented in Figure 4.11 (right). Region 1 is bounded by the nominal material level ahead of the cutting tool (1) and the most forward point in cutting velocity direction (2). The straight line may be described by an arising rake angle γ^* . Region 2 is described by an ellipse between the most forward points in cutting velocity (2) and feed direction (3) respectively, in which the semi-major axes correspond to the length l_α and l_γ as proposed by HENERICHS et al. [101]. Ultimately, region 3 is bound by point (3) and the profile separation point (4) between the new and the worn profile. The distance in feed direction between (3) and (4) corresponds to the bouncing back height b_c and the friction length in cutting velocity direction is described by the arising angle α^* . This proposed wear description will subsequently be considered in the suggested analytical force model. Therefore several experiments and tool measurements are considered, as being shown in the overview in Figure 4.12.

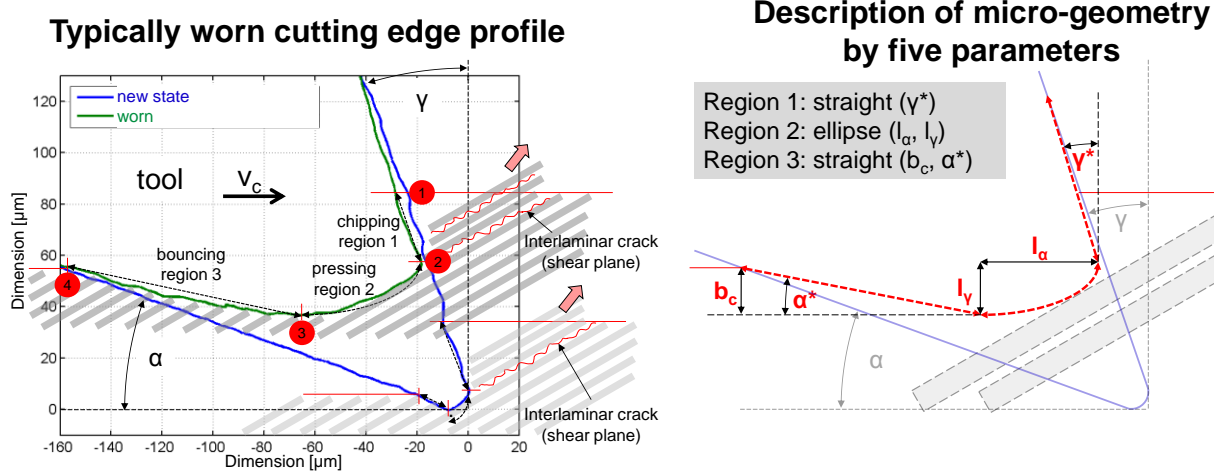


Figure 4.11: Exemplary worn cutting edge profile of tool geometry M ($\gamma=20^\circ$, $\alpha=21^\circ$) in $\theta=30^\circ$ material ($v_c=90$ m/min, $f=0.03$ mm) and evaluation of actual micro-geometry with 5 parameters

Figure 4.12 shows a comparison between worn tool profiles (green), which machined unidirectional CFRP with various fibre orientations and new state profiles (blue). The total cutting length of the worn profiles is $l_c=40$ m. Obviously the occurring cutting edge micro-geometry and worn volume depend on the fibre orientation, but also on the cutting edge macro-geometry.

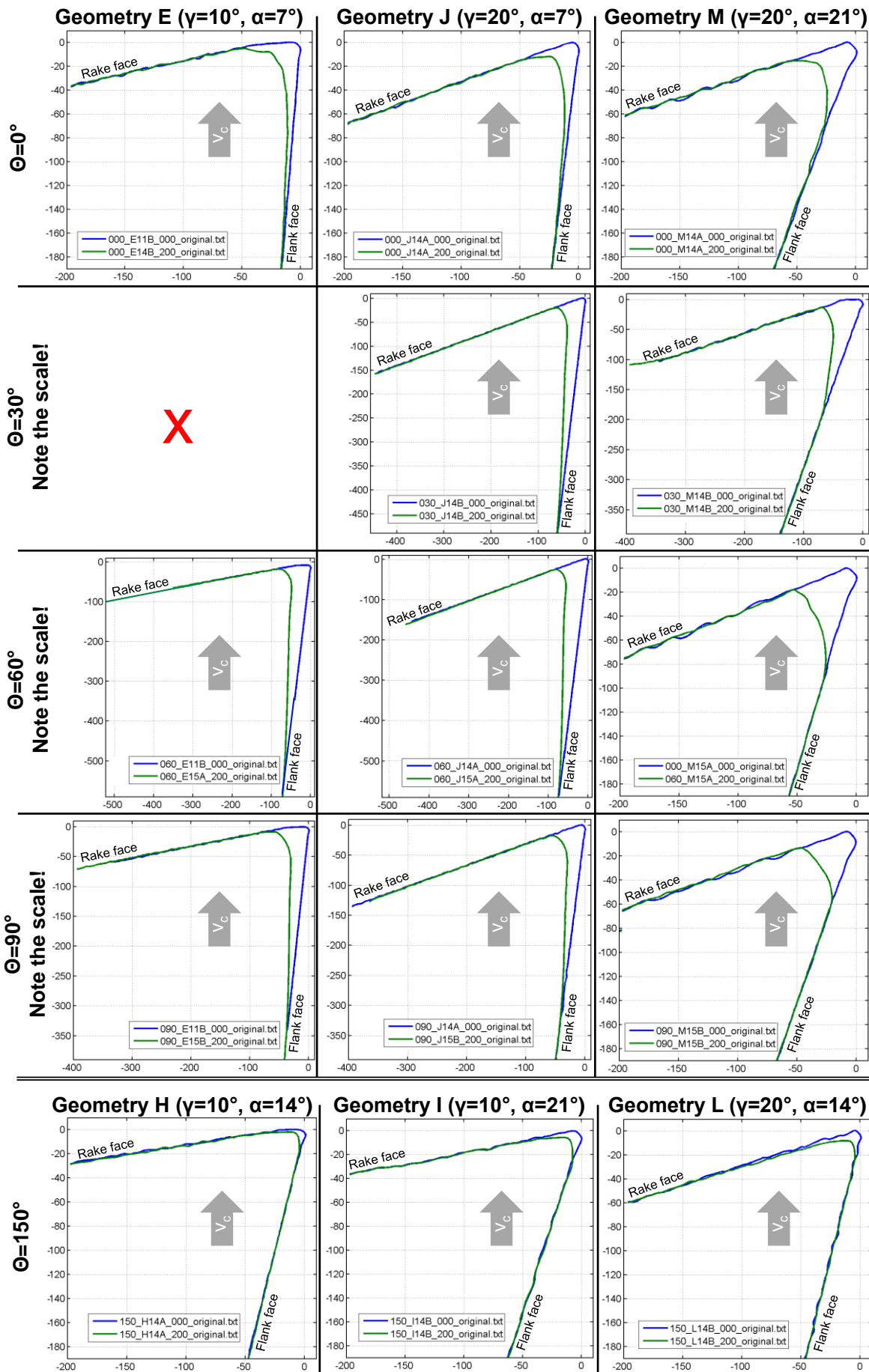


Figure 4.12: New (blue) and worn tool profiles in micrometres at $l_c=40$ m (green) after machining $\theta=0^\circ, 30^\circ, 60^\circ, 90^\circ, 150^\circ$; $v_c=90$ m/min, $f=0.03$ mm

The trend of increasing tool wear with cutting length is exemplarily shown in Figure 4.13 for the tool geometry M ($\gamma=20^\circ$, $\alpha=21^\circ$) and a fibre orientation of $\theta=30^\circ$. For this regular tool wear evaluation, the orthogonal cutting process is periodically interrupted and imprints of the actual cutting edge are created using the *IWF-Wunder method*, which was published by HENERICHS et al. [97]. Subsequently the imprints are poured with epoxy, analysed with an infinite focus microscope and evaluated by means of the matlab programm Cutting Edge Analyser (CEA), also proposed by HENERICHS [101]. The corresponding micro-geometry values l_α and l_γ as well as b_c , α^* and γ^* are plotted in the two diagrams on the right in in Figure 4.13. It is well known, that mainly abrasive wear occurs in CFRP machining with carbide tools, which is proportional to the cutting length. This leads to increasing l_α and l_γ values as well as digressively decreasing α^* and γ^* values. The trend of the five wear parameters depends mainly on the machined fibre orientation and fibre properties as well as the original tool macro-geometry and tool material. Indeed the cutting speed and feed rate have not been evaluated in these experiments but most likely these will also have an influence on the actual micro-geometry. It has been found that the measurement of the bouncing height b_c along the flank face by means of epoxy-imprints is error prone. However, during 3D-measurement of the original carbide tool at a cutting length of $l_c=40\text{m}$, the relevant point on the flank face is optically identifiable by abrasion marks. Therefore the actual bouncing height at a certain cutting length, which is increasing digressively, is approximated by means of the following square-root function

$$b_c = b_{c,40m} \cdot \sqrt{\frac{l_c}{40m}}, \quad (13)$$

where $b_{c,40m}$ is the measured bouncing height at a cutting length of $l_c=40\text{m}$. The detailed micro-geometry evaluation is presented in the table in A.1 in the appendix.

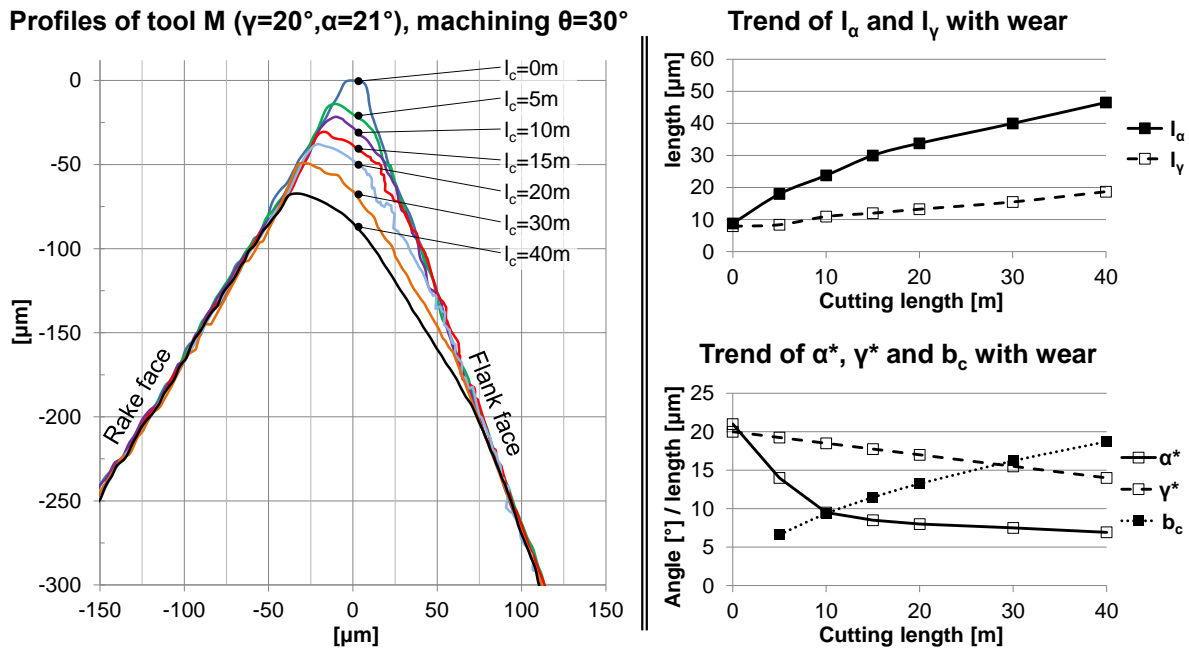


Figure 4.13: Tool wear and micro-geometry trend with increasing cutting length presented at the example M ($\gamma=20^\circ$, $\alpha=21^\circ$) in $\theta=30^\circ$ material; $v_c=90\text{ m/min}$, $f=0.03\text{ mm}$

4.3 Evaluation of the friction coefficient

To address the lack of friction coefficient between CVD diamond and CFRP under realistic cutting conditions, an open cutting-process-tribometer (CP-T) is applied, which enables for friction measurements close to the machining process. This CP-T is based on an orthogonal cutting process with a spring pre-loaded pin sliding downstream, but close to the process, on the freshly generated material surface. The process enables testing of various fibre orientations, relative to the sliding direction. With experiments in titanium, presented by SMOLENICKI et al. [206], the CP-T setup showed its capability and it is adapted to determine the friction coefficient between heterogeneous CFRP material and CVD diamond. Part of this research is published at the International Conference on Precision Engineering (ICPE) in Hamamatsu, Japan in 2016 [235] and at CIRP Conference on Composite Materials Parts Manufacturing (CCMPM) in Karlsruhe, Germany in 2017 [236].

The experimental study aims to determine the friction coefficient between a CVD diamond coating and a unidirectional CFRP surface. Therefore an open CP-T in combination with an orthogonal cutting process is applied. The experimental setup for the turning tests is carried out on an *Okuma* LB15-II lathe. It has the same arrangement of workpiece material as presented in Figure 4.2, to allow machining CFRP in an orthogonal turning operation at constant fibre orientation θ . The outer diameter of the CFRP ring-shaped material in Figure 4.14 is $d_{out}=195\text{-}200$ mm.

The machining conditions are constant during one experiment. But within the experimental series variable tool geometries, fibre orientations, feed rates and cutting velocities are tested, presented in Table 4.5. All experiments are conducted under dry cutting conditions. A new diamond coated pin is used for each separate experiment. One CP-T experiment is completed as soon a feed travel of $l_f=2$ mm is incrementally machined, which takes about 67 rotations at a feed rate $f=0.03$ mm.

Table 4.5: Machining parameters of orthogonal turning tests

$\gamma ; \alpha$ [deg]	v_c [m/min]	f [mm]	a_e [mm]	θ [deg]
0, 20; 7, 14	60, 90	0.03, 0.06, 0.1	5	0, 30, 60, 90, 120, 150

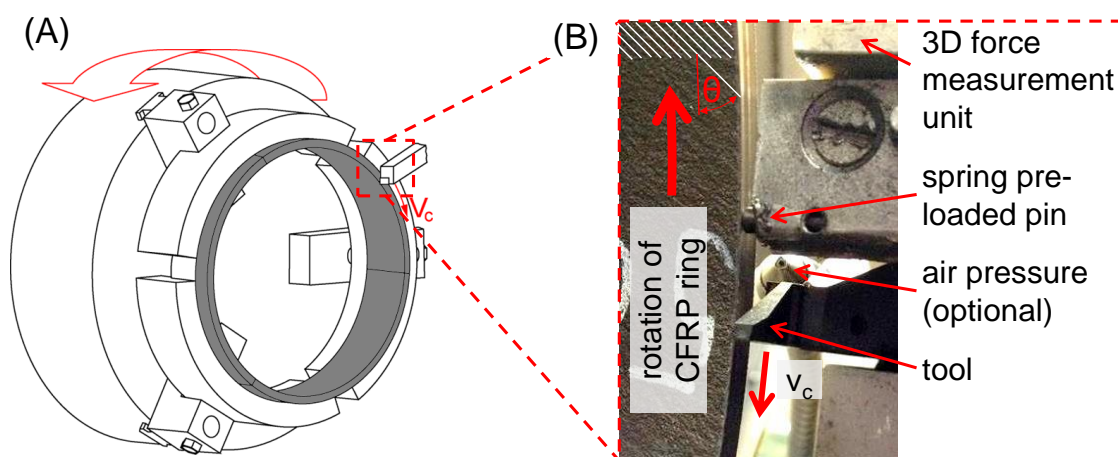


Figure 4.14: Schematic illustration of ring-shaped workpieces clamped into machine tool (A) and detailed view of contact conditions during machining (B); published in [235, 236]

Conventional carbide cutting inserts of the grade MG12 (*Ceratizit*) with nano-crystalline CVD diamond coating of 8^{+2} μm thickness are utilized. Three different tool geometries with varying rake and clearance angles are generated by grinding: RA with $\gamma=0^\circ$ and $\alpha=14^\circ$; RB with $\gamma=20^\circ$ and $\alpha=14^\circ$; RC with $\gamma=20^\circ$ and $\alpha=7^\circ$. The cutting edge radius of the CVD-coated tools is approximately 18 μm .

Carbide pins of the same grade (MG12) and with the same CVD-coating (Diamond Nano Plus 8+2 μm) as the cutting inserts are generated to slide on the freshly generated CFRP surface. The diameter of the cylindrical pins, which are marked red in Figure 4.15, is 3 mm and the overall length is 17 mm. One side of the pin, which slides on the CFRP surface, has a spherical shape of 3 mm radius.

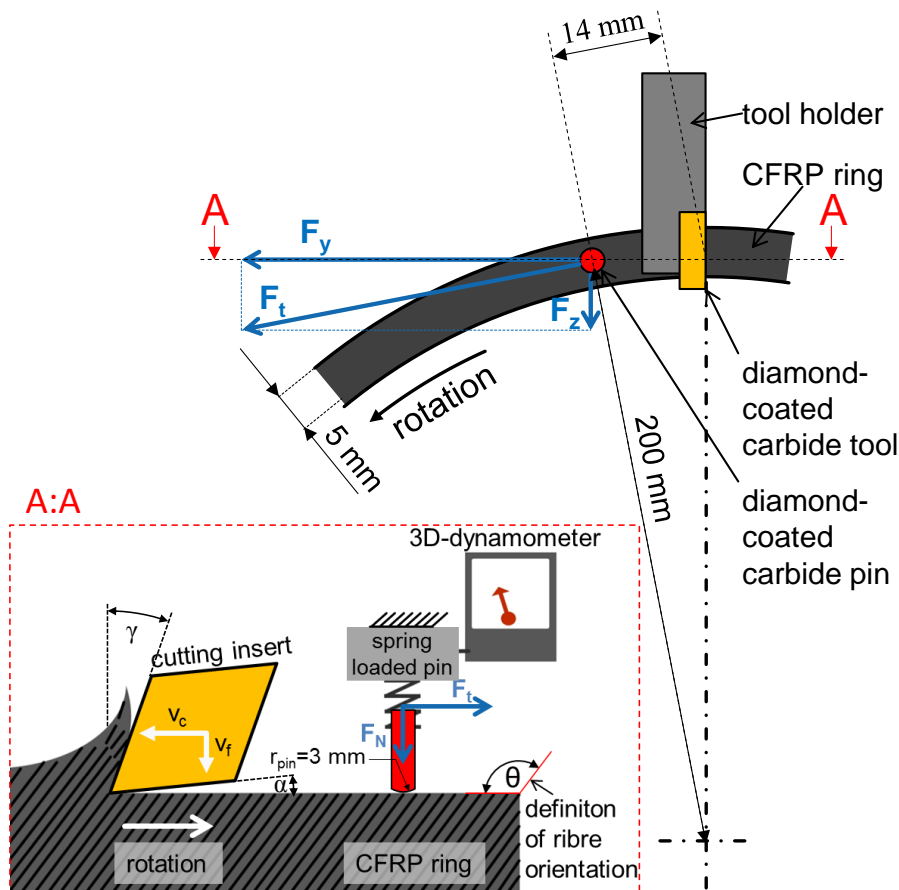


Figure 4.15: Scheme and geometrical conditions of the cutting-process-tribometer (CP-T); published in [235, 236]

To ensure contact conditions between CFRP surface and the CVD diamond coated pin being as similar to the cutting process as possible, the pin is situated only 14 mm behind the cutting edge. In this way, the cutting velocity of the infinite, non-interrupted cut and sliding velocity correspond (adjustable: 20-500 m/min). At an exemplary cutting speed of $v_c=100$ m/min, the time interval from the cutting edge to the pin is 8.4 ms. This leads to the assumption that the temperature at the CFRP surface at sliding position is still similar to the temperature during CFRP cutting. Furthermore high-speed camera images proof the existence of some loose CFRP and matrix particles floating close to the CFRP surface at pin position. These particles are forced underneath the cutting edge during the machining process instead of being evacuated along the rake face of the tool. The normal load between pin and CFRP surface is set to the actual forces occurring in the orthogonal cutting process, measured during separate experiments and showing a range of 50 N - 200 N. These settings

promise to measure the coefficient of friction at the pin under similar conditions (speed, temperature, normal load, existence of loose particles) as prevail along the tool flank face during machining.

The setup enables evaluation of variable fibre orientations θ by changing the direction of laminate in the semi-circular shaped raw material in Figure 4.2. In this way the results of SUNG et al. [212] and NAYAK and BHATNAGAR [165] may be verified, which were presented in the state of the art in 2.5 and suggest a strong dependency of the friction coefficient on the fibre orientation θ .

Friction forces and normal load on the pin are measured with a 3D-dynamometer 9047C by Kistler. According to the geometrical conditions, shown in Figure 4.15, the friction force F_t is calculated as the resulting force composed by F_y and F_z

$$F_t = \sqrt{F_y^2 + F_z^2} \quad (14)$$

The apparent friction coefficient μ_{app} is provided by the ratio between friction force F_t and the normal force F_N , measured as average value in the stable machining zone. According to MONDELIN et al. [163], who referred to the analytical solution developed by LAFAYE et al. [141, 142], this apparent friction coefficient μ_{app}

$$\mu_{app} = \frac{F_c}{F_N} = \mu_{adh} + \mu_{def} , \quad (15)$$

represents a superposition of adhesion and plastic deformation effects, as illustrated in Figure 4.16.

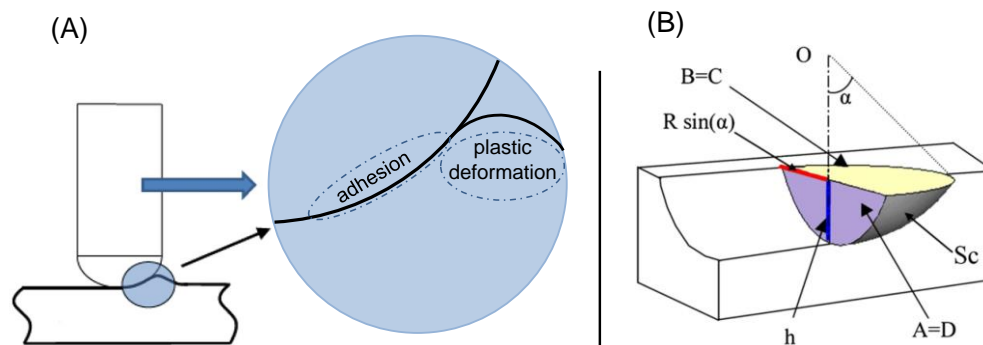


Figure 4.16: Illustration of plastic deformation and adhesion in friction tests, according to [163]

4.3.1 Results and discussion

Figure 4.17 shows the influence of a variable fibre cutting angle on the apparent friction coefficient. In contrast to experiments with closed tribometers [165, 212] (pin-on-disk, etc.) and steel sliding on CFRP/epoxy, presented in Figure 2.38 in the state of the art, in the experiments with the introduced setup the fibre orientation has a lower influence. The measurement values, shown in Figure 4.17 range between $\mu_{app}=0.107$ and $\mu_{app}=0.146$ and are slightly larger compared to the measurements by MONDELIN et al. [163] with monocrystalline diamond ($0.08 < \mu_{app} < 0.12$). Maximum values appear for $\theta=0^\circ=180^\circ$ (parallel) and $\theta=90^\circ$ (normal), while $\theta=30^\circ$ and $\theta=150^\circ$ generate somewhat smaller values ($\mu_{app}=0.119$). Each tested fibre orientation is averaged at least on three measurements. In contradiction to the results of SUNG and SUH [212] and NAYAK and BHATNAGAR [165] the

pronounced effect of fibre orientation on the friction coefficient cannot be confirmed. According to analyses by MATSUNAGA et al. [159], pronounced effects of fibre orientation on the friction coefficient are somewhat suppressed for higher contact pressures as they occur in cutting. Based on measurements of the pin-track width on the CFRP surface, a contact area of 0.27 - 2.14 mm² occurs in these experiments, depending on the normal load and fibre orientation, which results in average contact pressures of 90 - 530 MPa. Furthermore the presence of loose CFRP and matrix particles, partly covering the freshly generated CFRP surface, changes the friction process from mainly sliding to rolling and reduce the influence of fibre orientation in the sliding contact.

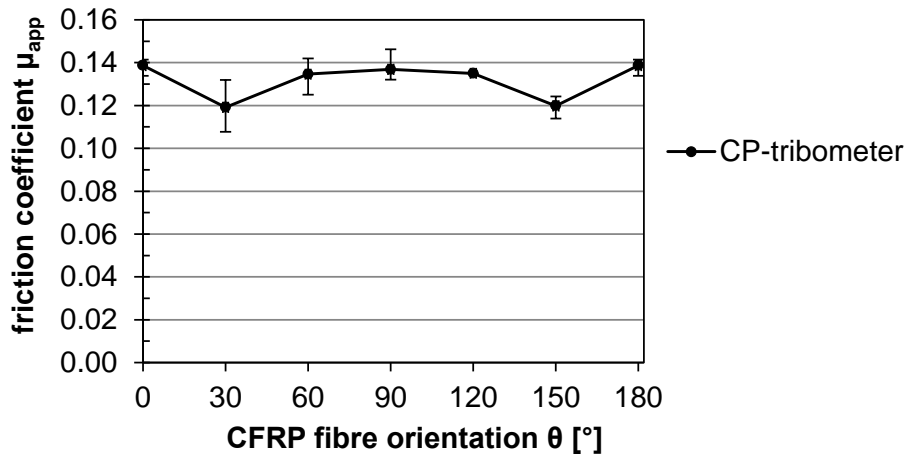


Figure 4.17: Influence of fibre cutting angle θ on the apparent friction coefficient, measured with the cutting-process-tribometer; published in [235, 236]

The apparent friction coefficient plotted over the normal pin pre-load in Figure 4.18, does not show an explicit trend with increasing load. Superimposing ambient scattering effects prevent an explicit conclusion about the influence of the normal load on the apparent friction coefficient. These observations that the pin pre-load has no significant influence are in accordance with results reported by MONDELIN et al. [163]. Accordingly, contact pressure does not significantly influence the apparent friction coefficient between CFRP and diamond.

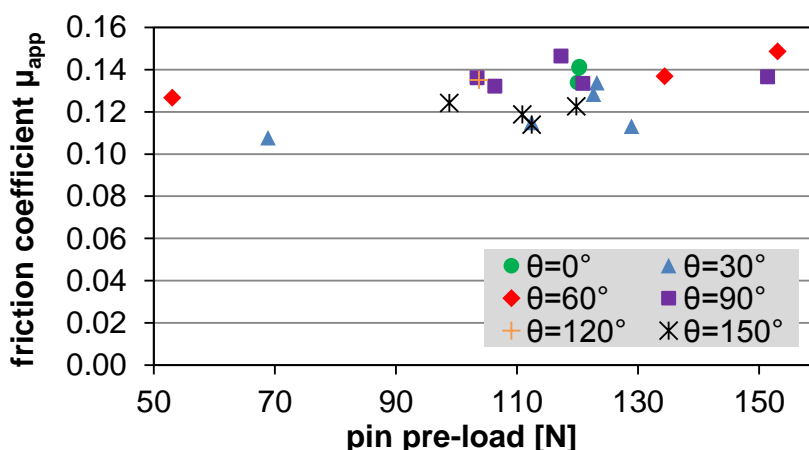


Figure 4.18: Influence of pin pre-load on the apparent friction coefficient, measured with the cutting-process-tribometer; published in [235, 236]

The results with the CP-tribometer are compared with pin-on-disk (POD) tribometer experiments at room temperature, shown in Figure 4.19. It needs to be considered that in the POD-experiments one different friction partner is tested: CFRP pins of the same material as

in the CP-experiments are tested on a steel plate, instead on CVD diamond as in the CP-experiments. The CFRP probes are generated by cutting out elements of the machined workpieces and applying them to pins in a way that the machined surface rests even on the steel plate during the tests. Dimensions of the nominal contact area between CFRP and steel are about $7.5 \times 5 \text{ mm}^2$. The diagram in the grey box in Figure 4.19 shows a section of an exemplary measuring plot of the friction coefficient over time with an increasing run-in behaviour. But depending on the probes, also measuring plots with a certain decreasing trend occur. The total measuring time per experiment is five minutes and the friction coefficients are evaluated as average value in the stable region of the signal. A comparison of the apparent friction coefficients, evaluated with the two different methods is shown in the diagram on the left side in Figure 4.19. The frictional resistance in the POD-experiments is generally higher than in the CP-experiments and shows an increased influence of the fibre orientation. But consider that a direct comparison of the absolute numerical values for μ_{app} is not possible, because of different friction partners in test (CVD diamond/CFRP vs. CFRP/steel). Furthermore, the normal load of approximately $F_N=10 \text{ N}$ and relative velocity of 15 m/min in the POD-experiments differentiates from the CP-experiments. Nevertheless the friction coefficient evaluated with POD-experiments matches the trend of experiments by NAYAK and BHATNAGAR [165] with a maximum at $\theta=90^\circ$ and a minimum at $\theta=0^\circ$, even though the absolute values differentiate due to dissimilar tested material; GFRP instead of CFRP.

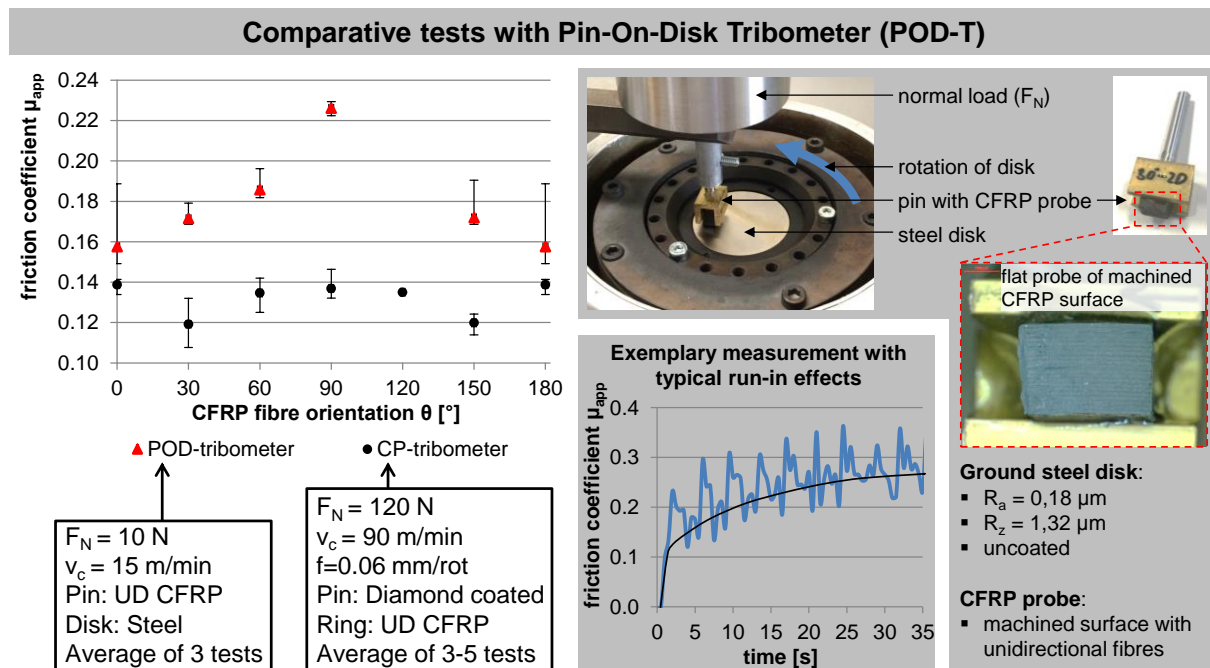


Figure 4.19: Comparison of CP-tribometer results (CVD diamond/CFRP) with pin-on-disk experiments (CFRP/steel)

It is known from fundamental orthogonal cutting experiments that fibre orientations of $\theta=150^\circ$ lead to saw tooth like surface topography, shown in Figure 4.20 (left). Subsequently it is focused on this specific fibre orientation. It is also known from HENERICHS [101] that the feed rate and at least slightly the rake angle γ influence the generated tooth size L_z for $\theta=150^\circ$. Since the surface roughness value R_a is not sufficient to describe machined CFRP topographies, in this case μ_{app} is compared to R_z (av. of peak-to-valley distance) and R_p (maximum peak height) in the diagrams in Figure 4.20. The larger L_z , the higher the roughness and thus the apparent friction coefficient tends to be larger, as shown in Figure

4.20 (right). In accordance with MONDELIN et al. [163], this effect may be due to a larger amount of plastic deformation at the pin, as illustrated in Figure 4.16. The influence of the tool geometry on the CFRP topography is much weaker for the other tested fibre orientations $\theta \neq 150^\circ$ and thus has no significant influence on μ_{app} .

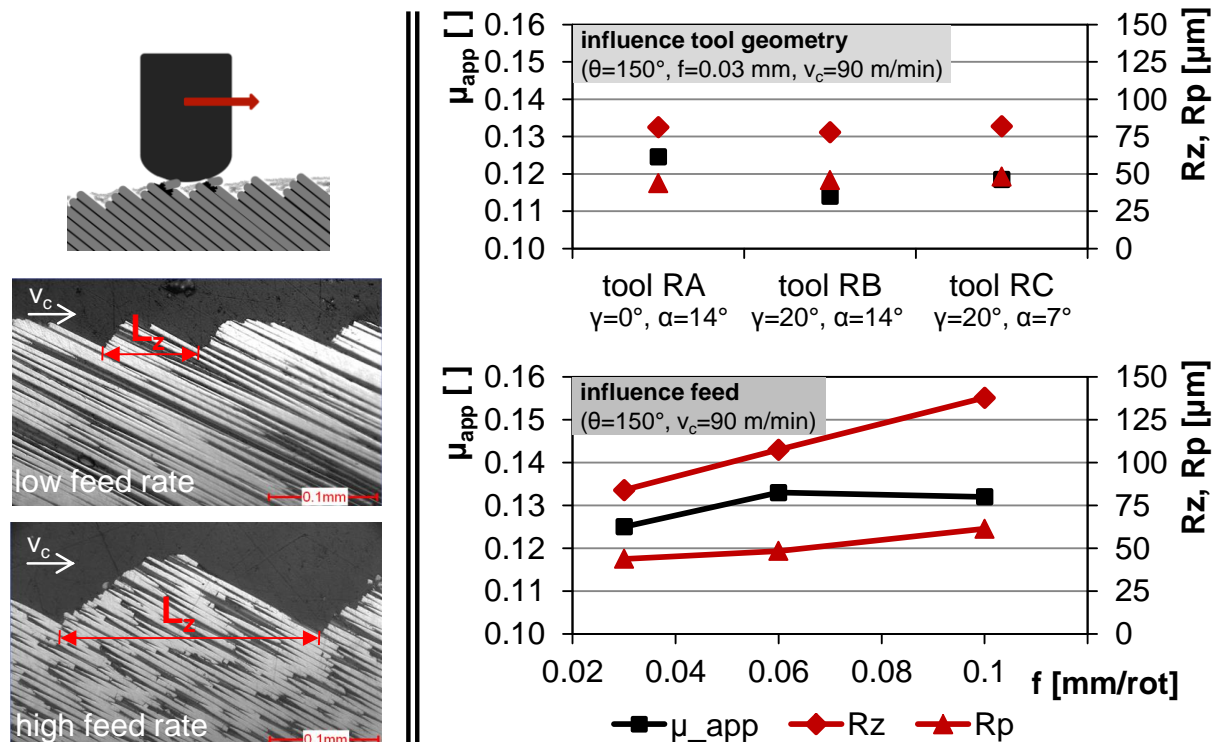


Figure 4.20: Influence of tool geometry and feed rate on roughness and friction coefficient for $\theta = 150^\circ$ with CP-tribometer; $v_c=90$ m/min; published in [235, 236]

4.3.2 Conclusion of friction evaluation

The results of MONDELIN et al. [163], WANG et al. [237] and CHARDON et al [43] are confirmed by these presented tribometer experiments close to the machining process: Obviously the apparent friction coefficient between CFRP and diamond is lower than any other reported friction coefficient in CFRP literature. In the experiments the range of the apparent friction coefficient is $0.107 \leq \mu_{app} \leq 0.146$.

The cutting process tribometer setup with CFRP ring segments has been newly developed to enable evaluation of the CFRP fibre orientation on the friction coefficient. The results show only a very weak dependency of the CFRP fibre orientation, compared to the aforementioned publications with closed tribometers and steel and CFRP as friction partners. Laminates with parallel ($\theta = 0^\circ$) and perpendicular orientation ($\theta = 90^\circ$) of the carbon fibres relative to the cutting velocity result in similar average values of $\mu_{app} = 0.14$, whereas orientations of $\theta = 30^\circ$ and $\theta = 150^\circ$ show slightly lower average values of $\mu_{app} = 0.12$. This effect, in contrast to closed tribometers, might be due to the following reasons:

- High, machining-like stresses at workpiece-pin contact suppress the effects of fibre orientation
- Loose CFRP and fibre particles from the machining operation cover the freshly generated surface and result rather in rolling than in sliding effects

No significant influence of the load on the apparent friction coefficient has been shown by the experiments with variable pin pre-load. The particular case of CFRP material with a fibre orientation of $\theta = 150^\circ$ shows a saw teeth topography on the machined surface depending on the tool rake angle and feed rate: The larger the feed, the larger the saw teeth which is proportional to the roughness. The smallest feed rate ($f=0.03\text{mm/rot}$) results in the lowest frictional resistance when sliding with a pin over such a topography.

The experiments show in general that the utilized tribometer setup close to an orthogonal cutting operation is suitable for machining of inhomogeneous CFRP material.

5 Analytical force model

With a varying fibre orientation, different chip formation mechanisms occur, such as bending, buckling, compression or shear. Four groups with similar chip formation mechanisms are identified, dividing the fibre orientation range from $0^\circ \leq \theta < 180^\circ$ into four specific intervals. These intervals are shown in Figure 5.1 by rows, presenting in the first column a schematic drawing of the cutting conditions at the cutting edge, which is subdivided into three regions, as suggested by ZHANG et al. [269]. Accordingly, the forces F_z in cutting and F_y in feed direction are separately calculated for each of the three regions and subsequently are determined for the whole machining process by superposing the force components in all three regions

$$\begin{aligned} F_z &= F_{R1_z} + F_{R2_z} + F_{R3_z} , \\ F_y &= F_{R1_y} + F_{R2_y} + F_{R3_y} . \end{aligned} \quad (16)$$

The following columns in Figure 5.1 describe the general load conditions of the UD CFRP workpiece in each region of the cutting edge during machining. The intervals I ($\theta = 0^\circ$) and III ($\theta = 90^\circ$) mark the orientations in which the fibres are cut exactly in axial direction or perpendicular, whereas the intervals II ($15^\circ < \theta < 75^\circ$) and IV ($105^\circ + \gamma < \theta < 165^\circ$) represent the transitions in between. It may be noted that each of these intervals has an angular gap of 15° to the adjacent interval. The cutting mechanisms of the adjacent sub-models mix in these angular gap regions, which might result in singularities and poles during calculation. To obtain the overall forces for the whole range of fibre orientations ($0^\circ \leq \theta < 180^\circ$) with the proposed force model, it is recommended to interpolate between two adjacent models in the angular gaps. Every sub-model is explained in detail in the following Chapters 5.1 to 5.4.

In former publications about analytical force modelling of orthogonal cutting in CFRP [195, 213, 242, 269, 270] tool wear is not considered or only simplified taken into account by considering the cutting edge radius. But the tool wear analysis in Paragraph 4.2 shows a significantly different micro-geometry from a radius shape for uncoated carbide tools. Consequently, these models show significant deviations from the measured forces.

In the proposed model a database is imported, filled with the actual cutting edge micro-geometry, which has been measured during extensive experiments with different tool geometries and fibre orientations. The force model is deliberately separated from the actual tool micro-geometry, to be valid for various tool materials and tool wear characteristics, as presented in Figure 5.2. The five micro-geometry parameters proposed above are evaluated in extensive experiments for $\theta = 0^\circ, 30^\circ, 60^\circ, 90^\circ$ with the three tool geometries E ($\gamma=10^\circ, \alpha=7^\circ$), J ($\gamma=20^\circ, \alpha=7^\circ$) and M ($\gamma=20^\circ, \alpha=21^\circ$), while for $\theta = 150^\circ$ the geometries H ($\gamma=10^\circ, \alpha=14^\circ$), I ($\gamma=10^\circ, \alpha=21^\circ$) and L ($\gamma=20^\circ, \alpha=14^\circ$) are tested. The table in the appendix A.1 shows the detailed data corresponding to the tool profiles in Figure 4.12. A function could be fitted into this data, however currently the required wear values are selected if necessary by interpolating in the look-up table. It will be explained in detail in the following chapters how the micro-geometry values are considered in the proposed force model and how the cutting edge shape affects the forces. Further input variables to the model are the material properties, the fibre orientation, the process parameters and the friction coefficient, summarised as 'Boundary Conditions'.

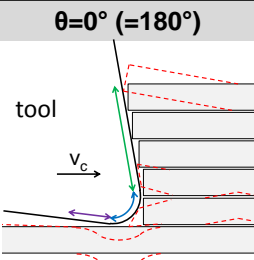
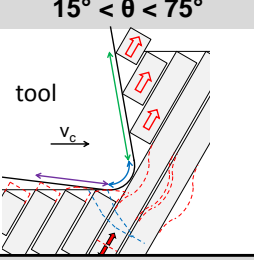
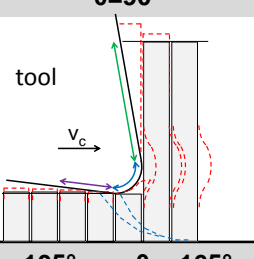
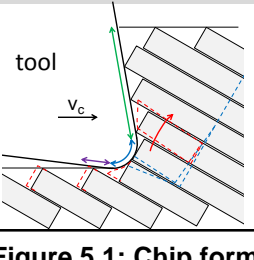
	Region 1	Region 2	Region 3
$\theta=0^\circ$ (=180°)	 <ul style="list-style-type: none"> •compr. in fibre direction •lateral force on fibres due to γ → buckling and bending, depending on γ → peeling of matrix 	<ul style="list-style-type: none"> •compr. in fibre direction •lateral force on fibres due to γ •peeling of matrix → interlaminar crack 	<ul style="list-style-type: none"> •bouncing back (low intensity) •friction between tool/CFRP
$15^\circ < \theta < 75^\circ$	 <ul style="list-style-type: none"> •compr. on fibres •shear in matrix → shear plane 	<ul style="list-style-type: none"> •initial fibre separation due to bending •shear in matrix •bending of fibres and ploughing under cutting edge •possibly secondary breakage of fibres 	<ul style="list-style-type: none"> •bouncing back (high intensity) •friction between tool/CFRP
$\theta=90^\circ$	 <ul style="list-style-type: none"> •shear force on fibres and compr. perpend. to fibre axis •shear force and compr. on matrix 	<ul style="list-style-type: none"> •compr. perpend. to fibre axis •shear force and compr. on matrix •bending of initially broken fibres and ploughing under cutting edge 	<ul style="list-style-type: none"> •bouncing back (medium intensity) •friction between tool/CFRP
$105^\circ + \gamma < \theta < 165^\circ$	 <ul style="list-style-type: none"> •compr. on fibres (buckling) •bending of fibres •peeling of matrix 	<ul style="list-style-type: none"> •compression of fibres → buckling •bending of fibres •peeling of matrix → interlaminar crack 	<ul style="list-style-type: none"> •bouncing back (very low intensity)

Figure 5.1: Chip formation mechanisms clustered into four fibre orientation intervals

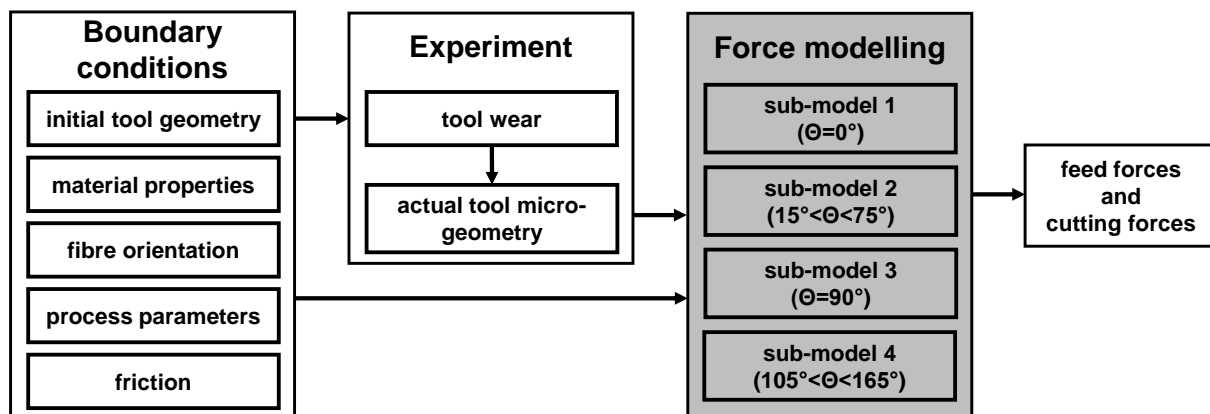


Figure 5.2: Breakdown of the process force modelling with boundary conditions and experimental tool wear parameters as input variables

5.1 Sub-model $\theta=0^\circ(=180^\circ)$

In this chapter the approach of the sub-model $\theta = 0^\circ$ is explained in detail and exemplary simulation results are presented. Figure 5.3 shows the contact conditions of a worn cutting edge during machining $\theta = 0^\circ$ UD CFRP. According to the wear characterisation proposed in chapter 4.2, the cutting edge is divided into three regions, which are geometrically described by the five micro-geometry parameters l_α , l_γ , γ^* , a^* , b_c as well as the feed rate per revolution. For each of the three regions an appropriate modeling approach is defined.

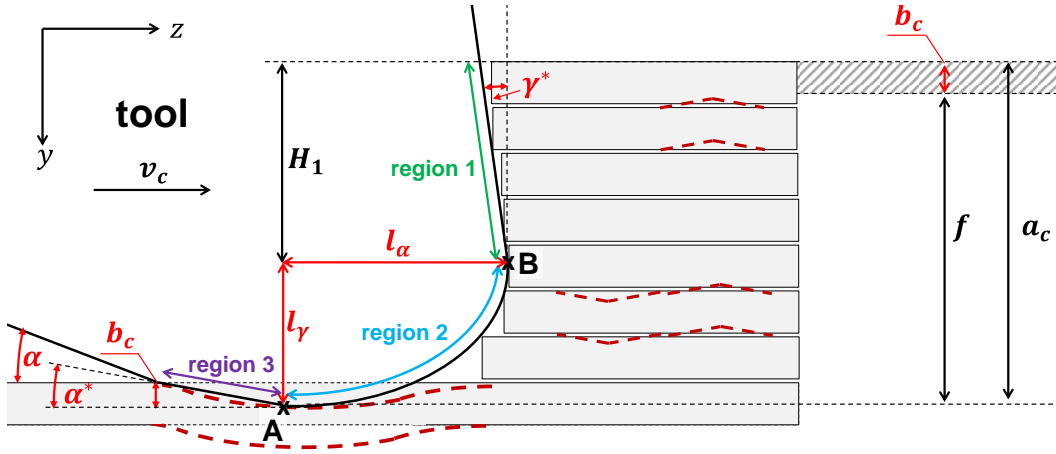


Figure 5.3: Schematic representation of the contact conditions for $\theta = 0^\circ(= 180^\circ)$

Due to the experimental setup in a turning process, a layer-wise removal of the CFRP material is implemented. Consequently, the machined surface is re-processed after one spindle rotation. An elastic spring-back effect of the CFRP material occurs in contact region 3, resulting in a difference between the programmed and the actual chip thickness. This difference corresponds to the recovered height \tilde{b}_c of the previous rotation, drawn in Figure 5.3. Thus, the average cutting depth is

$$a_c = f + \tilde{b}_c \quad (17)$$

In this force model it is simplified that the spring-back height of the previous spindle rotation \tilde{b}_c is equal to the current spring-back height b_c . Under this assumption, the height of region 1 is

$$H_1 = a_c - l_\gamma = f + b_c - l_\gamma \quad (18)$$

5.1.1 Modelling

Modelling of region 1:

Based on the state of the art and the fundamental machining experiments it is assumed that the fibres being in contact with the rake face fail by lateral *micro-buckling* due to the axial compression at a specific load. This specific load is defined as the *micro-buckling* strength σ_{mb} of the fibres being embedded in the matrix material. As soon as the strength is exceeded the fibres fail by lateral *micro-buckling* and the separated fibre-ends as well as matrix particles are evacuated along the rake face of the tool by the cutting motion. According to MAYER et al. [160] the term *micro-buckling* describes a coordinated structural failure in

unidirectional fibre composites, in which simultaneous buckling of large portions of adjacent fibres occur, due to axial load. However, this phenomenon with wavy buckling of the fibres, which may occur over large areas should not be confused with *kinking*, which is a highly localized fibre buckling, explained by NAIK and KUMAR [164]. The modelling approach by XU and REIFSNIDER [259] is applied to calculate the material-specific compression strength of the CFRP. The authors use a micro-mechanical beam-on-elastic-foundation model with an representative volume element (RVE). The RVE is an infinite plate of the thickness $b = \sqrt{\pi} \cdot r_f$ with an embedded fibre of the width b , shown in Figure 5.4. It is assumed that the fibre is buckled in a wavelength of L under the force P_{mb} .

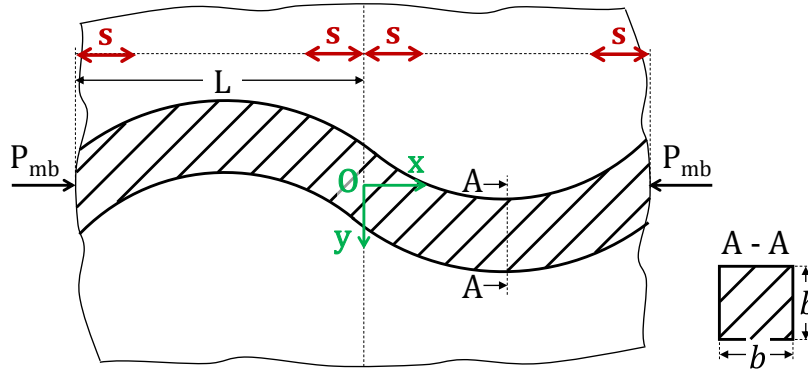


Figure 5.4: RVE-model to evaluate fibre *micro-buckling*, according to XU and REIFSNIDER [259]

According to the model [259], the compression strength is exceeded and the fibre fails as soon as a critical compressive force P_{mb_cr} is applied. XU and REIFSNIDER [259] evaluate this compressive force by determining a function for the fiber transverse displacement. Therefore the approach of the total potential energy Π is used. Applied to the RVE in Figure 5.4, the total potential energy is

$$\Pi = \int_0^L \left[\frac{E_{f1} I_f}{2} \left(\frac{d^2 \omega}{dx^2} \right)^2 + \frac{k}{2} \omega^2 - \frac{P_{mb}}{2} \left(\frac{d\omega}{dx} \right)^2 + \frac{1}{2} \tau b^2 \frac{d\omega}{dx} \right] dx, \quad (19)$$

in which E_{f1} , I_f , ω , k and τ are the axial *Young's* modulus of the fibres, the moment of inertia, the transverse deflection of the fibre, the normalized stiffness of the elastic foundation and the interfacial shear strain of the matrix. The four terms in brackets in this equation represent the bending energy in the carbon fibre, the work through passive force in the elastic foundation, the work through external compression force and the work by shear stresses in the boundary region. For the interfacial shear strain an ultimate shear strength τ_c is defined according to STEIF [208], above which local matrix slippage would occur. As long as the ultimate shear strength τ_c is not reached or exceeded, a linear elastic relationship between the fibre deflection ω and the corresponding shear stresses τ can be calculated by

$$\tau = \frac{d\omega}{dx} G_m \quad \text{if} \quad \left| G_m \frac{d\omega}{dx} \right| < \tau_c \quad (20)$$

$$\tau = \tau_c \quad \text{if} \quad \left| G_m \frac{d\omega}{dx} \right| > \tau_c, \quad (21)$$

in which the constant of proportionality G_m represents the shear modulus of the matrix material. If buckling of the carbon fibres occurs, due to instability during compressive loading, strong locally varying shear stresses at the fibre/matrix interface appear. This may lead to local exceeding of the ultimate shear strength τ_c , which would result in regional matrix

sliding. In the approach by XU and REIFSNIDER [259] it is assumed that the matrix slippage occurs at the nodes in a distance of L and with a width of $2s$, as presented in Figure 5.4. Accordingly the slippage regions are $[0, s]$ and $[L - s, L]$. Consequently, the adjusted total potential energy considering matrix slippage is

$$\begin{aligned} \Pi = & \int_0^L \left[\frac{E_{f1} I_f}{2} \left(\frac{d^2 \omega}{dx^2} \right)^2 + \frac{k}{2} \omega^2 - \frac{P_{mb}}{2} \left(\frac{d\omega}{dx} \right)^2 \right] dx + \\ & + \int_0^s \frac{1}{2} \tau_c b^2 \frac{d\omega}{dx} dx + \int_{L-s}^L \frac{1}{2} \tau_c b^2 \frac{d\omega}{dx} dx + \int_s^{L-s} \frac{1}{2} G_m b^2 \left(\frac{d\omega}{dx} \right)^2 dx \end{aligned} \quad (22)$$

By using a variational method for the minimum potential energy, exemplarily explained in publications by GAWEHN [81] or KNOTHE [134], it is possible to evaluate a function for the fibre transverse displacement. Based on this, XU and REIFSNIDER [259] calculate the critical compressive force

$$P_{mb_cr} = E_{f1} I_f \frac{\pi^2}{L^2} + G_m b^2 + \frac{kL^2}{\pi^2} - \frac{2G_m b^2 s}{L} - \frac{G_m b^2}{2\pi} \sin\left(\frac{2\pi s}{L}\right). \quad (23)$$

Thus the compressive strength of the composite, in which fibres are partially slipped, can be calculated by

$$\sigma_{mb} = \frac{E_{f1} V_f + E_m (1 - V_f)}{E_{f1}} \cdot \left(E_{f1} \frac{r_f^2 \pi^3}{12L^2} + G_m + \frac{kL^2}{\pi^3 r_f^2} - \frac{2G_m s}{L} - \frac{G_m}{2\pi} \sin\left(\frac{2\pi s}{L}\right) \right), \quad (24)$$

in which the parameters E_m , r_f and V_f stand for the matrix modulus of elasticity, the radius of the carbon fibre and the volume fraction of the fibres in the CFRP. According to XU and REIFSNIDER [259] the fibre-buckling wavelength L may be determined by using equation (23) and applying a minimum buckling load condition without slippage, which results in

$$L = \pi \cdot \sqrt[4]{\frac{E_{f1} I_f}{k}}. \quad (25)$$

To derive the normalized stiffness of the elastic foundation, XU and REIFSNIDER [259] solve a boundary value problem in combination with an elastic foundation modelling approach, which leads to

$$k = \eta \frac{\pi E_{c2} b}{(1 + \nu_{c12})} \quad \text{mit } 1 \leq \eta \leq 2, \quad (26)$$

where E_{c2} and ν_{c12} are the modulus of elasticity transverse to the fibre axis and the corresponding *Poisson's* ratio. The value η describes the interfacial fibre-matrix bonding properties. In case of a both-sided embedded fibre the value is $\eta = 2$; for a one-sided embedding $\eta = 1$. Combining equations (24), (25) and (26) under consideration of the general equations (46) and $E_m = G_m 2(1 + \nu_m)$ gives a general equation for the compressive strength, depending on ξ and η

$$\sigma_{mb} = G_m \left(V_f + \frac{E_m}{E_{f1}} (1 - V_f) \right) \cdot \left(2(1 + \nu_m) \sqrt{\frac{\pi \sqrt{\pi} \eta r_f}{3 \frac{E_m}{E_{f1}} \left(V_f \frac{E_m}{E_{f1}} + 1 - V_f \right) (1 + V_f \nu_f + \nu_m (1 - V_f))}} + 1 - \xi - \frac{\sin(\pi \xi)}{2\pi} \right). \quad (27)$$

ξ describes the share of matrix slippage in relation to the wavelength L with $\xi = 2s/L$ and ν_f and ν_m are the *Poisson's* ratios of the fiber and the matrix. The exact values of ξ und η have to be evaluated experimentally. Referring to the experimental study by NAIK and KUMAR [164], the values of $\xi = 0.02$ und $\eta = 1.98$ fit well for carbon/epoxy composites and are adopted in this thesis. Based on Equation (27), the force at fibre failure is calculated by multiplying the maximum compressive strength with the projected contact area in region 1.

$$P_{mb_1max} = A_{mb_1} \cdot \sigma_{mb} = b \cdot H_1 \cdot \sigma_{mb}, \quad (28)$$

where A_{mb_1} is the projected area defined by the width of the workpiece b and the height H_1 , marked green in Figure 5.5.

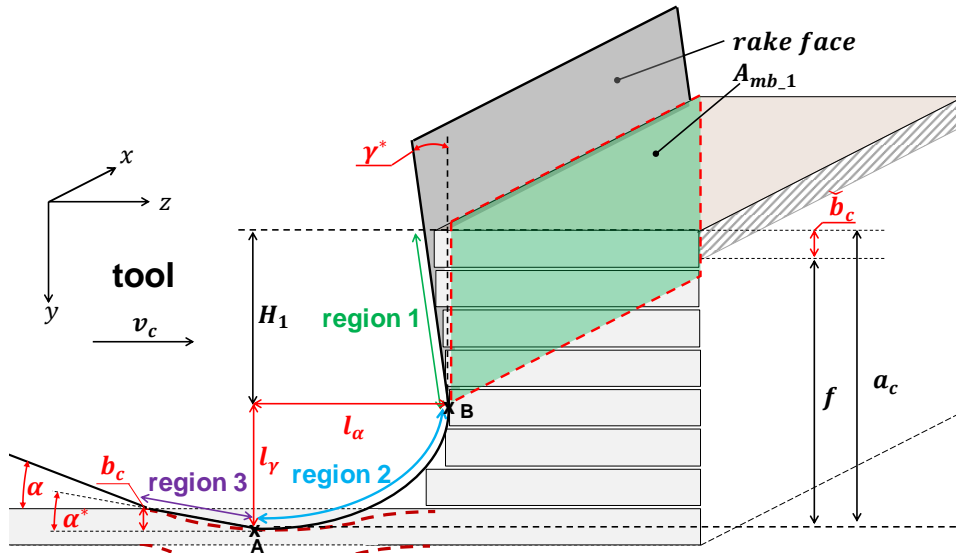


Figure 5.5: Schematic representation of the contact area A_{comp_1}

To calculate the average force by *micro-buckling*, which acts on the tool, two effects need to be considered. First, it is assumed that the axial force on the tool by *micro-buckling* increases linearly, as presented in Figure 5.6. Second, the fibre failure by *micro-buckling* occurs in a certain distance to the tool/fibre contact point. Consequently, immediately after fibre fracture the tool is locally out of contact with the remaining fibre-ends, which are still attached to the workpiece. To calculate the average resulting force \bar{P}_{mb_1} on the tool, a correction factor K_f is defined, which is $K_f = 0.5$ in case of continuous tool/fibre contact and $K_f < 0.5$ in case of fibre breakage in a certain distance to the tool. For the experiments in this thesis values of $K_f = 0.33$ proved to be suitable.

$$\bar{P}_{mb_1} = K_f \cdot P_{mb_1max} \quad (29)$$

Friction between the tool and workpiece along the rake face is considered by means of the *Coulomb* friction model with the friction coefficient μ , which is evaluated experimentally in chapter 4.3, and the adjusted rake angle γ^*

$$\bar{P}_{mb_{1f}} = \mu \cdot \bar{P}_{mb_{1}} \cdot \cos \gamma^* \quad (30)$$

Based on the equations (29) and (30), a vectorial decomposition of the resulting force gives the components in feed and cutting velocity direction for the interval I ($\theta = 0^\circ$) in region 1.

$$\begin{aligned} F_{I1_{R1_z}} &= \bar{P}_{mb_{1}}(1 + \mu \cos \gamma^* \sin \gamma^*) = K_f A_{mb_{1}} \sigma_{mb}(1 + \mu \cos \gamma^* \sin \gamma^*) \\ F_{I1_{R1_y}} &= \bar{P}_{mb_{1}} \mu (\cos \gamma^*)^2 = K_f A_{mb_{1}} \sigma_{mb} \mu (\cos \gamma^*)^2 \end{aligned} \quad (31)$$

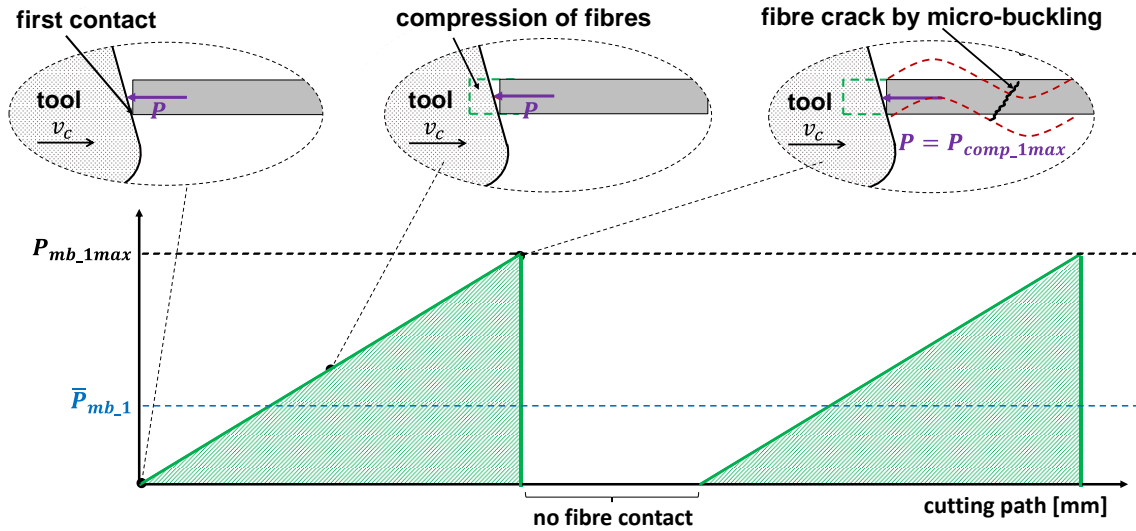


Figure 5.6: Linearly increasing forces over the cutting path by micro-buckling in region 1

Modelling of Region 2:

The region 2 of the cutting edge in the sub-model $\theta = 0^\circ$ is divided into two sub-regions (2.1 and 2.2), due to the superposition of two occurring effects, namely axial compression and pressing transverse to the fibre axes, presented in Figure 5.7. In reality a smooth transition between these two effects appears along the elliptical cutting edge rounding. For complexity reduction the point C defines a digital transition from *micro-buckling* to *pressing*, in which the proportion of both effects in region 2 might be set by the sub-region heights $H_{2.2}$ and $H_{2.1}$. In this case $H_{2.2}$ is the fitting variable for the $\theta = 0^\circ$ model, with $H_{2.1} = l_\gamma - H_{2.2}$. The force components in each sub-region are separately calculated and in the end vectorial added under the assumption of superposition.

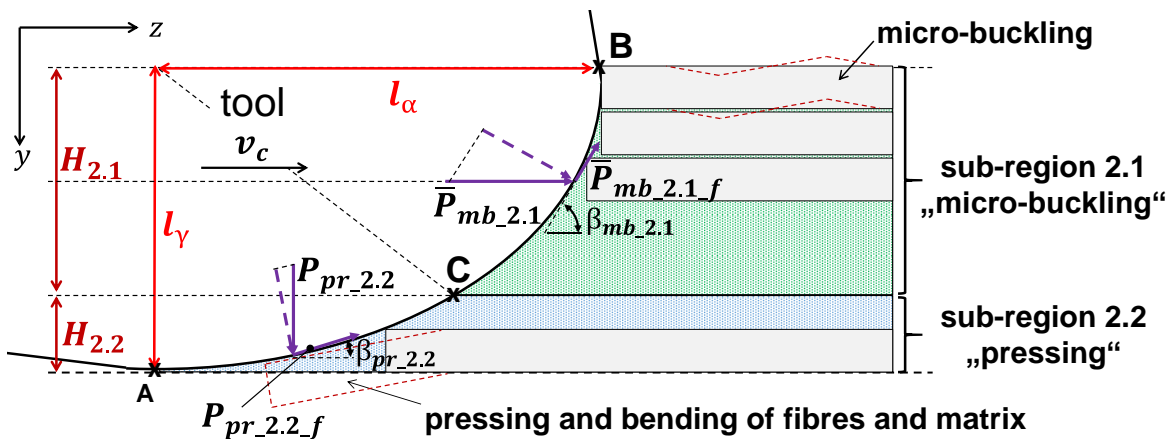


Figure 5.7: Schematic representation of the contact conditions for $\theta = 0^\circ$ in region 2

The load situation in sub-region 2.1 with mainly axial compression of the fibres is similar to the situation in region 1, which has been explained above. The derived compressive strength in equation (27) is applied and in combination with the projected contact area $A_{mb,2.1} = b \cdot H_{2.1}$ as well as the correction factor $K_f = 0.33$ the average force due to *micro-buckling* in sub-region 2.1 is

$$\bar{P}_{mb,2.1} = K_f \cdot A_{mb,2.1} \cdot \sigma_{mb} = K_f \cdot b \cdot H_{2.1} \cdot \sigma_{mb} . \quad (32)$$

Coulomb friction between the tool and workpiece along the *micro-buckling* region is considered in the middle of the sub-region 2.1 with the friction coefficient μ and the tangential angle $\beta_{mb,2.1}$ in this position of the elliptical cutting edge. Consequently the force components, due to *micro-buckling* in sub-region 2.1 are

$$\begin{aligned} F_{I1,R2.1,z} &= \bar{P}_{mb,2.1} (1 + \mu \cos \beta_{mb,2.1} \sin \beta_{mb,2.1}) \\ &= K_f A_{mb,2.1} \sigma_{mb} (1 + \mu \cos \beta_{mb,2.1} \sin \beta_{mb,2.1}) \end{aligned} \quad (33)$$

$$F_{I1,R2.1,y} = -\bar{P}_{mb,2.1} \mu (\cos \beta_{mb,2.1})^2 = -K_f A_{mb,2.1} \sigma_{mb} \mu (\cos \beta_{mb,2.1})^2$$

In the second sub-region 2.2 mainly pressing of the CFRP material occurs transverse to the fibre axis (in feed direction). As suggested by ZHANG et al. [267, 269], the forces in this region of the tool are modelled with indentation mechanics of a circular cylinder in contact with a half-space. A schematic representation of this ideal contact situation is shown on the left in Figure 5.8 with a cylinder of a radius R . This approach is based on elastic deformation conditions and according to ZHANG et al. [267, 269] the pressing force on the cylinder may be calculated by

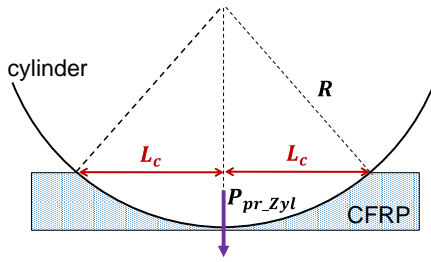
$$P_{pr,Zyl} = \frac{L_c^2 \pi E_{c2} b}{4R} , \quad (34)$$

where E_{c2} , b and L_c are the *Young's* modulus of the composite material, the width of the workpiece and the half projected contact length of the indented cylinder. The schematic representation in Figure 5.8 (right) shows the contact condition in sub-region 2.1. The half projected contact length is calculated depending on the tool micro-geometry and the fitting variable $H_{2.2}$

$$L_c = \frac{l_\alpha}{l_\gamma} \sqrt{l_\gamma^2 - H_{2.2}^2} . \quad (35)$$

To apply equation (34) on the contact situation in sub-region 2.2 the ellipse segment AC is simplified by a segment of a circle with the approximated radius R^* , shown on the right in Figure 5.8. For this purpose a regression analysis is performed based on the least squares method using the software *Matlab*. The necessary input parameters are the coordinates of the two points on the ellipse A and C, and the semiaxes l_α and l_γ .

Indentation of circular cylinder in half-space



Indentation transferred to sub-region 2.2

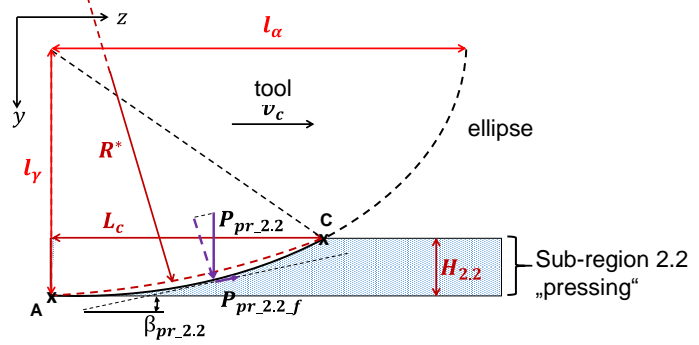


Figure 5.8: Schematic representation of a circular cylinder in contact with a half-space (left) and transferred to the contact conditions for $\theta = 0^\circ$ in sub-region 2.2

Furthermore equation (34) has to be divided by factor 2, due to considering only half of the cylinder being in contact with the half-space. Consequently, the pressing force in sub-region 2.2 is calculated by

$$P_{pr.2.2} = \frac{L_c^2 \cdot \pi \cdot E_{c2} \cdot b}{8 \cdot R^*}, \quad (36)$$

Comparable to sub-region 2.1, Coulomb friction between the tool and workpiece along the pressing region is considered in the middle of the sub-region 2.2 with the friction coefficient μ and the tangential angle $\beta_{pr.2.2}$ in this position of the elliptical cutting edge. Consequently, the force components due to *pressing* in sub-region 2.2 are

$$\begin{aligned} F_{I1_R2.2_z} &= \mu P_{pr.2.2} (\cos \beta_{pr.2.2})^2, \\ F_{I1_R2.2_y} &= P_{pr.2.2} (1 - \mu \cos \beta_{pr.2.2} \sin \beta_{pr.2.2}). \end{aligned} \quad (37)$$

Finally, the total resulting forces in cutting velocity and feed direction of region 2 in the fibre orientation interval I ($\theta = 0^\circ$) yield by superposition of microbuckling and pressing to

$$\begin{aligned} F_{I1_R2_z} &= F_{I1_R2.1_z} + F_{I1_R2.2_z} \\ &= K_f A_{mb.2.1} \sigma_{mb} (1 + \mu \cos \beta_{mb.2.1} \sin \beta_{mb.2.1}) + \mu \frac{L_c^2 \pi E_{c2} b}{8 R^*} (\cos \beta_{pr.2.2})^2 \\ F_{I1_R2_y} &= F_{I1_R2.1_y} + F_{I1_R2.2_y} \\ &= -K_f A_{mb.2.1} \sigma_{mb} \mu (\cos \beta_{mb.2.1})^2 + \frac{L_c^2 \pi E_{c2} b}{8 R^*} (1 - \mu \cos \beta_{pr.2.2} \sin \beta_{pr.2.2}) \end{aligned} \quad (38)$$

Modelling of Region 3:

In region 3 it is assumed that the composite material, which is pressed below the cutting edge in region 2, springs back with a height of b_c and is in contact with the flank face of the tool over a projected friction length L_{pf} . A geometric description of the expected load situation is shown in Figure 5.9. L_{pf} can easily be calculated, since the two micro-geometry wear parameters α^* and b_c are assumed to be given in this force model by a look-up table, derived from the experimental results, as shown in Figure 5.2.

$$L_{pf} = \frac{b_c}{\tan \alpha^*}, \quad (39)$$

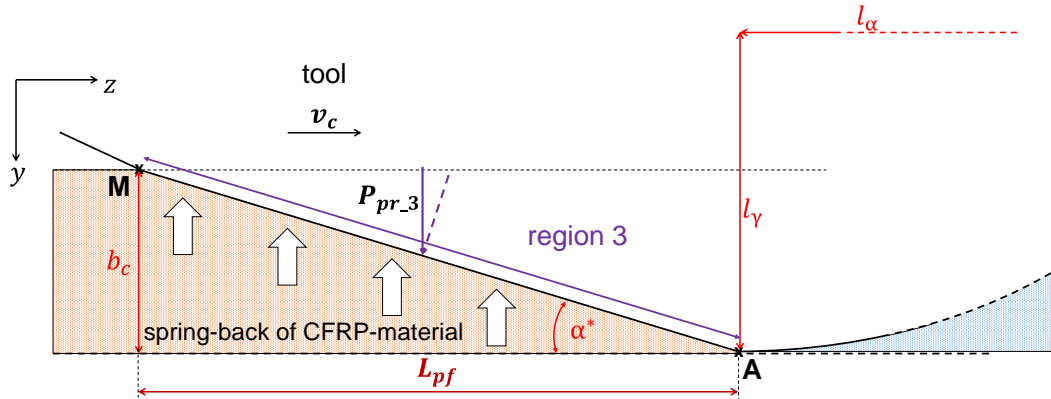


Figure 5.9: Schematic representation of the contact conditions for $\theta = 0^\circ$ in region 3

This load situation in region 3 is similar to the pressing sub-region 2.2, and in accordance with ZHANG et al. [267, 269] approximated by a wedge in contact with a half-space. According to JOHNSON [124], the force on the tool in feed direction may be calculated by

$$P_{pr.3} = \frac{b \cdot L_{pf} \cdot E_{c3} \cdot \tan \alpha^*}{2} = \frac{b \cdot b_c \cdot E_{c3}}{2}, \quad (40)$$

in which E_{c3} is the *Young's* modulus of the composite material in region 3. It is assumed in accordance with XU and REIFSNIDER [259] and ZHANG et al. [269] that the value of E_{c3} is smaller than the original *Young's* modulus, due to process-related material pre-damages during passing below the cutting edge. The variable E_{c3} is a fitting parameter of the force model in the interval I ($\theta = 0^\circ$). Additionally *Coulomb* friction between the tool and workpiece along the flank face is considered in the middle of region 3 with the friction coefficient μ and the adjusted flank angle α^* . Thus, the force components due to flank face contact in region 3 are

$$F_{I1_R3_z} = \mu \frac{b \cdot b_c \cdot E_{c3}}{2} (\cos \alpha^*)^2, \quad (41)$$

$$F_{I1_R3_y} = \frac{b \cdot b_c \cdot E_{c3}}{2} (1 + \mu \cos \alpha^* \sin \alpha^*).$$

Based on the modelling explained above, the total thrust and cutting forces for the fibre orientation interval I ($\theta = 0^\circ$) are determined by superposing the force components in z and in y direction [(31), (38), (41)] in all three regions

$$F_{I1_z} = F_{I1_R1_z} + F_{I1_R2_z} + F_{I1_R3_z},$$

$$F_{I1_y} = F_{I1_R1_y} + F_{I1_R2_y} + F_{I1_R3_y}. \quad (42)$$

5.1.2 Results of sub-model $\theta=0^\circ$

Appendix A.3 shows the main input variables for the sub-model $\theta=0^\circ$ including material properties separately for each component, process parameters and the fitting variables. A detailed description of the CFRP composite used with the label "M21/34%/UD194/IMA-12k" and the associated material properties can be found in section 4.1. In case, specific

properties are not given in the material datasheet, comparable values from literature have been used. According to a study by SCHOSSIG et al. [201] who analysed the strain rate influence on the tensile strength in short glass fibre reinforced thermoplastics a positive strain rate influence could be found. Especially for strain rates larger than 20 s^{-1} , which equals a loading speed of 138 m/min , a much stronger increase occurs in [201] due to a transition from isothermal to adiabatic material behavior. Since the values in the datasheet are usually evaluated according to standards (e.g. DIN EN ISO 14129) at very low strain rates, these values have to be adjusted to higher strain rates in case of machining operations with $v_c = 90 \text{ m/min}$. No data is found in literature for the specific application. Therefore a correction factor $K_{\sigma_{Tf}} > 1$ is introduced as fitting variable. The effective value of $K_{\sigma_{Tf}}$ is determined by parameter fitting to the experiments. Applied to the force model, these factors are multiplied with the corresponding material property from the datasheet $\sigma_{Tf\text{real}} = K_{\sigma_{Tf}} \cdot \sigma_{Tf0}$. According to ROOS and MAILE [192], polymers generally show a stronger dependence on the strain rate, e.g. compared to metals. This applies both to the strength and stiffness for the characteristic values. Referring to FRENZ [79] and KEUERLEBER [129] it can generally be assumed that the elongation at break decreases with increasing strain rate and the modulus of elasticity increases. Due to a lack of description of the strain rate dependency for the specific polymer material, a correction factor K_{Em} is utilised and also fitted to the experiments. It is applied in the force model by multiplying with the value from the datasheet: $E_{m\text{real}} = K_{Em} \cdot E_{m,0}$. The shear strength S_m of the matrix material and the corresponding shear modulus G_m are chosen in consistency with the force model by QI [177]. According to the cutting process friction evaluation, presented in chapter 4.3, the friction coefficient is almost constant for the whole range of fibre orientations and set to $\mu=0.12$. Besides the values in the Appendix A.3, the actual micro-geometry of the tools, represented by the five wear parameters l_α , l_γ , γ^* , α^* , l_γ is imported by means of the look-up table, shown in the appendix A.1.

Figure 5.10 shows the simulated results of the cutting and thrust forces over the cutting length in comparison to the experiments, which were presented in detail in sections 4.1 and 4.2 exemplarily for the tool geometry E ($10^\circ/7^\circ$). While the solid lines represent the total simulated force in cutting velocity or feed direction, the dashed lines show the corresponding force components in each of the three regions of the cutting edge. Basically, the results are in good agreement to the experiments and describe the force increase due to wear. The average deviation between simulation and experiment for Tool E ($10^\circ/7^\circ$) is 5% for the cutting forces and 6.5% for the thrust forces over a cutting length of 40 m, while the maximum deviation for this example is about 20%. Similar to the tool geometry E ($10^\circ/7^\circ$), in the appendix A.4 the results for a second Tool J ($20^\circ/7^\circ$) and a third Tool M ($20^\circ/21^\circ$) are additionally shown.

In the relatively new state of the cutting edge at $l_c=5 \text{ m}$, the largest share of the cutting force arises in region 1 and region 2, where *micro-buckling* of the fibres occurs. The results show that the cutting forces in region 1 and region 2 are inversely proportional with increasing cutting length. This is caused by a decrease of height of region 1 (H_1) with wear according to equation (18), whereas l_γ increases. The total feed force is almost exclusively generated in regions 2 and 3 of the cutting edge. The feed force in region 2 is proportional to the asymmetric cutting edge rounding (ratio of $\frac{l_\alpha}{l_\gamma}$) and in region 3 to the contact length between tool and material. Furthermore it is striking that the force increase in either direction ($F_{11,z}$ and

$F_{11,y}$) is mainly due to the force increase in region 3. Consequently, the force model is very sensitive to the spring-back height and the arising clearance angle α^* . Deviations in the force model, such as a too strong/weak force increase, which e.g. is slightly visible in the feed force simulation of Tool J ($20^\circ/7^\circ$) in the appendix A.4, are most likely due to deviations of the micro-geometry input parameters. In this presented example, the four micro-geometry input parameters l_α , l_γ , γ^* , α^* have been measured regularly, whereas the trend of the spring-back height b_c was approximated with a universal root function in (13), as explained in 4.2. This simplified function neglects the influence of tool geometry, fibre orientation, and material properties on the spring-back height. The conspicuous sensitivity of the model with respect to the actual cutting edge micro-geometry is consistent to experiments [102], which prove that a change in geometry has a major influence on the forces. Aside from the sensitivity to the wear input parameters the force sub-model I for $\theta = 0^\circ$ reflects the measurement data well.

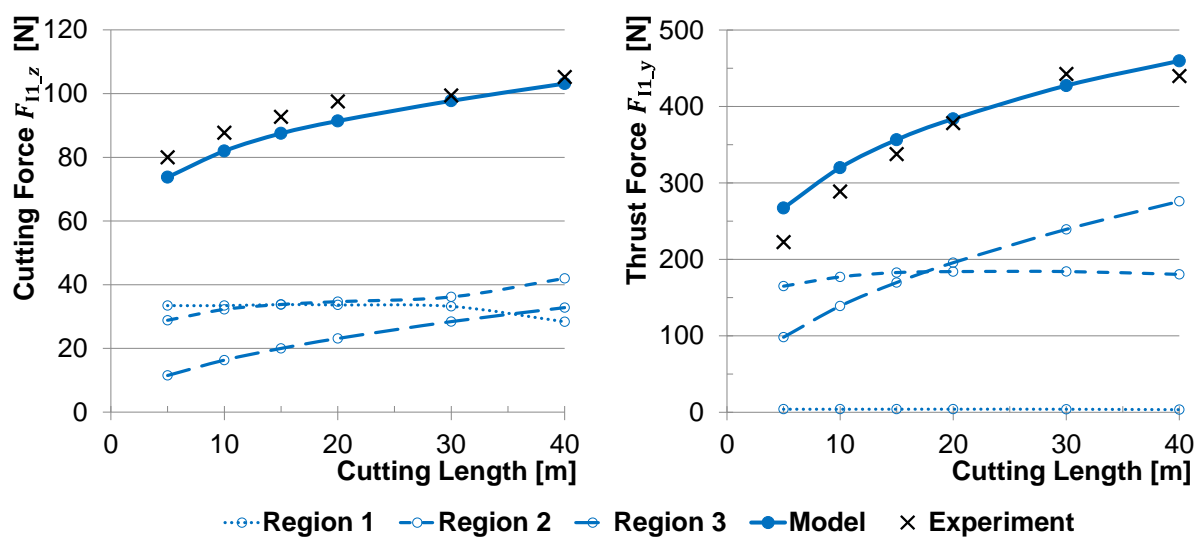


Figure 5.10: Comparison of cutting and thrust forces between model and experiment for the Tool E ($10^\circ/7^\circ$) in $\theta = 0^\circ = 180^\circ$ material; $v_c=90$ m/min and $f=0.03$ mm/rot

5.2 Sub-model $15^\circ \leq \theta \leq 75^\circ$

The contact conditions of a tool during orthogonal cutting of CFRP with exemplary $\theta = 45^\circ$ fibre orientation are presented in Figure 5.11. Analogous to the interval I ($\theta = 0^\circ$) in section 5.1, the contact area between tool and CFRP is divided into three regions and the micro-geometry is described by the same five micro-geometry parameters l_α , l_γ , γ^* , α^* as well as b_c . The relationship of the parameters H_1 , a_{cut} and \hat{b}_c has already been explained in (17) and (18) on page 78 and is still valid.

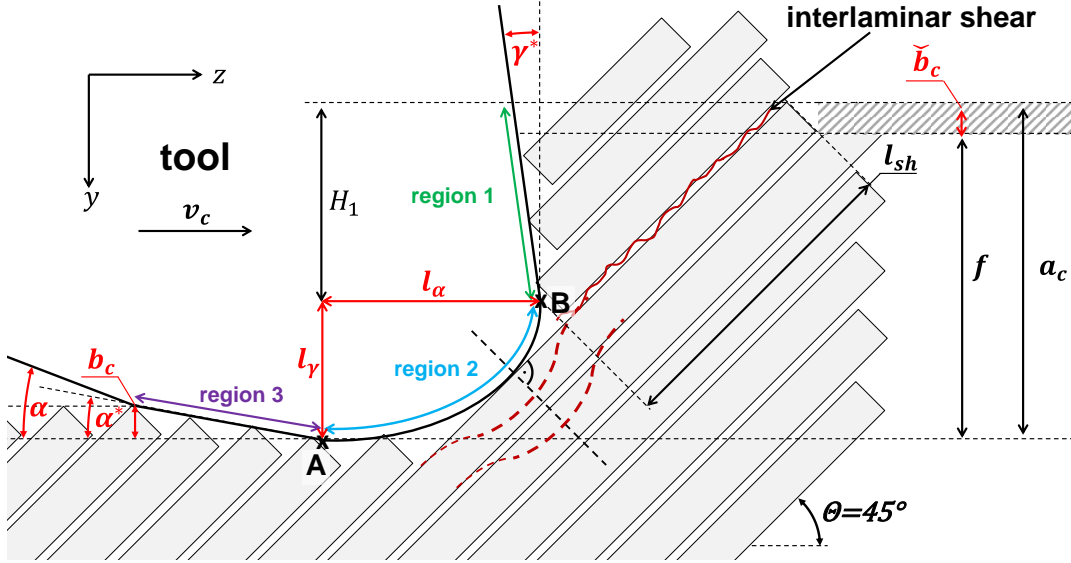


Figure 5.11: Schematic representation of the contact conditions for $15^\circ \leq \theta \leq 75^\circ$

5.2.1 Modelling

Modelling of region 1:

The first contact between tool and fibres in the fibre orientation interval II ($15^\circ \leq \theta \leq 75^\circ$) occurs in region 2 of the tool. It is assumed that the fibres are locally cut due to a bending and compression load in the first contact point. After this initial cut the upper fibre-end is still in contact with the next fibres in feed direction and touches the tool along the rake face in region 1. With progressing cutting motion of the tool and the actual rake angle γ^* a relative motion between the individual fibre layers occurs, stressing the interlaminar matrix in shear. According to ZHANG et al. [269], an interlaminar shear crack is induced, due to the lower shear strength of the matrix material. Corresponding to BHATNAGAR et al. [14] the angle of this so called shear plane is assumed to be equal to the fibre orientation angle θ for the chosen interval ($15^\circ \leq \theta \leq 75^\circ$). After initiation of the interlaminar shear crack, the cut CFRP fibres and matrix particles are no longer in contact with the workpiece and may be evacuated along the rake face. The subsequent force components on the tool by chip evacuation are neglected in the presented force model. Consistent with ZHANG et al. [269] the force component on the tool in region 1 due to shear is calculated by multiplying the interlaminar shear strength of the matrix τ_c with the area of the shear plane

$$P_{sh} = \tau_c \cdot l_{sh} \cdot b = \tau_c \cdot \frac{H_1}{\sin \theta} \cdot b , \quad (43)$$

where l_{sh} describes the length of the shear crack and b the width of the workpiece in x -direction. The Coulomb friction model is applied in the fibre-tool contact analogous to the consideration of friction in the interval I ($\theta = 0^\circ$). After a vectorial decomposition of the total force by shear and friction in region 1, the corresponding cutting and feed forces are

$$\begin{aligned} F_{I2,R1,z} &= \tau_c \cdot \frac{H_1}{\sin \theta} \cdot b (\cos \theta + \mu \cos(\theta - \gamma^*) \sin \gamma^*) , \\ F_{I2,R1,y} &= \tau_c \cdot \frac{H_1}{\sin \theta} \cdot b (-\sin \theta + \mu \cos(\theta - \gamma^*) \cos \gamma^*) . \end{aligned} \quad (44)$$

Modelling of region 2:

The carbon fibres in contact with the tool in region 2 are stressed by compression perpendicular to the fibre axis, due to the relative cutting motion between the tool and the workpiece. This load situation results in local bending of the fibre until the outer edge fails by exceeding the maximum tensile strength, as being proposed by Qi et al. [177]. This research team applied a micro-mechanical model with a beam on elastic foundation under a concentrated load. The detached upper fibre-ends are subsequently stressed in region 1 as described above. At the same time the lower part of the initially cut fibre is still attached to the remaining workpiece material and it is bend/pushed underneath the cutting edge by the progressing cutting motion of the tool. Due to an elastic deformation, the fibres spring back by a certain amount in region 3 of the cutting edge.

Figure 5.12 shows the mentioned cutting conditions in region 2 in detail. Obviously the first contact point K moves up along the elliptical cutting edge rounding, when machining material with larger fibre orientation θ . The position of K depends on the fibre orientation and the two semi-axes of the ellipse l_α and l_γ . While the force component for the initial fibre crack is theoretically almost similar for all fibre orientations in this interval II ($15^\circ \leq \theta \leq 75^\circ$), the additional force component by subsequent bending of the lower part of the initially cut fibres in region 2 increases with θ . Consequently, the theoretical maximum feed and cutting forces are expected to occur during machining CFRP with $\theta = 90^\circ$. Notwithstanding this, the analysis of orthogonal turning experiments, presented in detail by HENERICHS [101] and at least partially in section 4.2, shows a deviation from this theory with maximum cutting and feed forces arise for fibre orientations of $\theta = 30^\circ$ and $\theta = 60^\circ$. Micrographs prove the existence of sub-surface cracks for $\theta \geq 60^\circ$. These cracks are assumed to occur during bending of the lower part of the initially cut fibres in region 2. For larger fibre orientations (e.g. $\theta \geq 60^\circ$), where the contact point K is located in the upper part of the ellipse and the fibre has to be bend all the way down to pass the lowest point A of the cutting edge, it is more likely that the bending strength is exceeded and additional cracks are introduced. Based on these findings the force model in region 2 considers the following two effects:

- 1.) Initial cut of the fibres due to bending and compression in the first contact point K
- 2.) Further bending of the lower part of the initially cut fibres with potential further cracks

To model the forces between cutting edge and fibre, arising during the first effect, the micro-mechanical approach of Qi et al. [177] is applied. The authors defined a representative volume element (RVE) with a carbon fibre embedded in a layer of matrix material, shown in Figure 5.12. This RVE with infinite axial length in one direction is back supported by an elastic foundation (p_p, k_{cush}) and stressed by a concentrated force at the contact point in K . By means of the elastic foundation with a certain stiffness k_{cush} , the passive force p_p is considered.

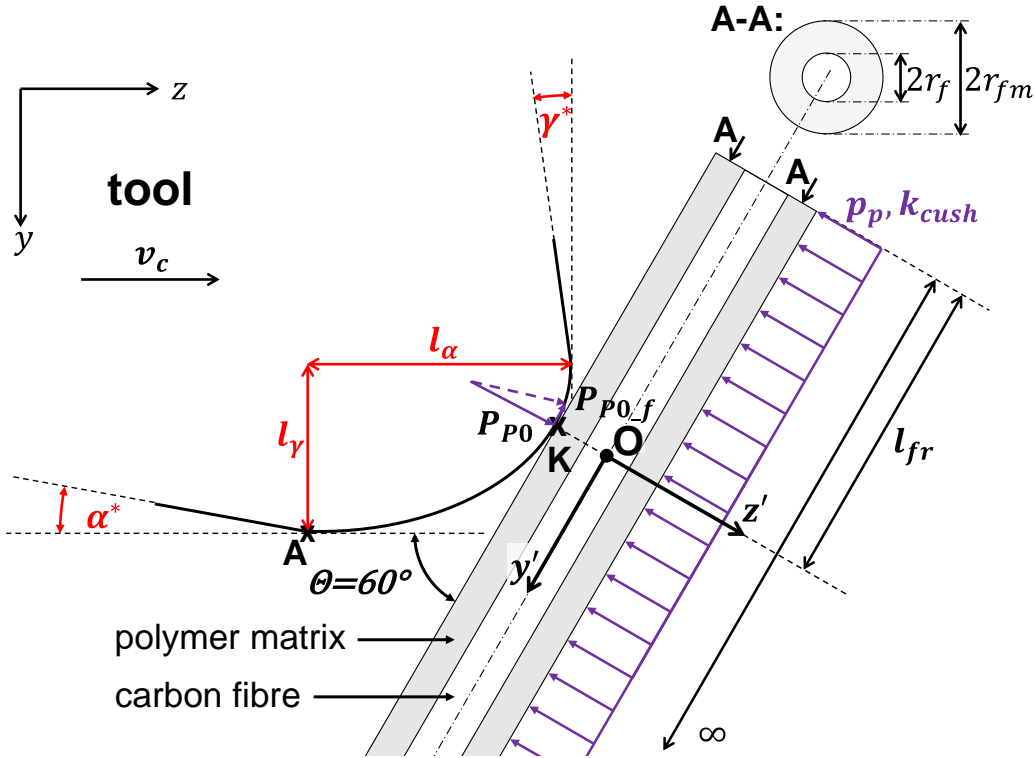


Figure 5.12: Schematic representation of the contact conditions for $\theta = 60^\circ$ in region 2

Analogue to the sub-model $\theta = 0^\circ$ (interval I), firstly a function for the fibre transverse displacement is determined by means of a total potential energy Π approach. It is assumed that the carbon fibre is exclusively loaded in bending and the surrounding matrix-material in shear. Applied to these boundary conditions the total potential energy is

$$\begin{aligned} \Pi = & \frac{1}{2} \int_{-l_{fr}}^{\infty} E_{f2} I_f \left(\frac{d^2 \omega}{dy'^2} \right)^2 dy' + \frac{1}{2} A_m G_m \left(\frac{r_{fm}}{r_f} \right)^2 \int_{-l_{fr}}^{\infty} \left(\frac{d\omega}{dy'} \right)^2 dy' - P_{P0} \omega |_{y'=0} \\ & + \frac{E_{c2}}{k_{cush}} \int_{-l_{fr}}^{\infty} \omega^2 dy' , \end{aligned} \quad (45)$$

in which the four summands describe the bending energy of the fibre, the shear energy in the matrix, the energy due to external load and the energy by passive force from the elastic foundation. The following Table 5.1 gives an overview of the variables and material properties in (45) and its meaning.

Table 5.1: Overview of variables in (45) and its meaning

Variable	Description	Variable	Description
E_{f2}	Young's Modulus of fibre (transv.)	r_{fm}	radius of RVE
E_{c2}	Young's Modulus of CFRP (transv.)	r_f	radius of fibre
I_f	moment of inertia of fiber	P_{P0}	concentrated force
A_m	cross-sectional area of matrix	k_{cush}	stiffness of elastic foundation
G_m	shear modulus of matrix	l_{fr}	fibre length from origin to free end
ω	fibre transverse displacement	p_{passiv}	passive force

According to KRESS [140], the *Young's* modulus of a composites material transversal to the fibre direction may be calculated by the separate *Young's* modules of each component as well as the volume fibre fraction

$$E_{c2} = \frac{E_{f2}E_m}{E_mV_f + E_{f2}(1 - V_f)} . \quad (46)$$

Furthermore, the cross sectional area of the idealised matrix layer surrounding the fibre and the radius of the RVE are calculated according to QI et al. [177] by

$$A_m = \frac{\pi r_f^2(1 - V_f)}{V_f} \quad \text{and} \quad (47)$$

$$r_{fm} = \sqrt{\frac{1}{V_f}} r_f . \quad (48)$$

The fourth summand in (45) is based on the WINKLER's [248] elastic foundation model, in which the variation of the passive force along y' can be expressed by

$$dp_p(y') = -\frac{E_{c2}}{H} \omega(y) 2r_{fm} dy' . \quad (49)$$

The variable H describes the cushion thickness and may be expressed with a dimensionless cushion factor k_{cush}

$$H = 2 \cdot k_{cush} \cdot r_{fm} . \quad (50)$$

After integration of (49) and substituting H by equation (50), the energy by passive force from the elastic foundation results in the fourth term in equation (45). In the proposed y'/z' -coordinate system in Figure 5.12, the origin O is defined as the intersection of the fibre axis and the vertical extension of the contact point K . Accordingly, a transverse displacement of the RVE is defined in positive z' direction. The variable l_{fr} describes the distance from the contact point K to the free end of the fibre and depends on the fibre orientation as well as the tool wear. Analogue to the sub-model $\theta = 0^\circ$ (interval I), the transverse displacement of the RVE is determined with the variational method of GAWEHN [81], resulting in the following differential equation

$$E_{f2}I_f \left(\frac{d^4 \omega}{dy'^4} \right) - A_m G_m \left(\frac{r_{fm}}{r_f} \right)^2 \left(\frac{d^2 \omega}{dy'^2} \right) + \frac{2E_{c2}}{k_{cush}} \omega = 0 . \quad (51)$$

Detailed descriptions for the solution of differential equations in form of $E_f I_f \omega^{(4)} - N \omega^{(2)} + Q \omega = 0$ can be found in the book of HETÉNYI [103]. For this specific application the following general approach is selected

$$\omega(y') = e^{-\hat{\alpha}y'} (\check{C}_1 \cos(\hat{\beta}y') + \check{C}_2 \sin(\hat{\beta}y')) + e^{\hat{\alpha}y'} (\check{C}_3 \cos(\hat{\beta}y') + \check{C}_4 \sin(\hat{\beta}y')) , \quad (52)$$

with the following four substitution variables

$$\hat{\alpha} = \sqrt{\sqrt{\frac{Q}{4E_{f2}I_f}} + \frac{N}{4E_{f2}I_f}} ; \quad \hat{\beta} = \sqrt{\sqrt{\frac{Q}{4E_{f2}I_f}} - \frac{N}{4E_{f2}I_f}} ; \quad N = A_m G_m \left(\frac{r_{fm}}{r_f} \right)^2 ; \quad Q = \frac{2E_{c2}}{k_{cush}} . \quad (53)$$

By means of suitable boundary conditions the four coefficients \check{C}_1 , \check{C}_2 , \check{C}_3 and \check{C}_4 can be evaluated. Due to a generally very small cutting depth a_c in relation to the material thickness, the RVE is assumed to have an infinite fibre expansion in positive y' direction. Furthermore the deflection of the fibre ω decreases with increasing distance from the contact point. Consequently, according to HETÉNYI [103] the condition $\lim_{y' \rightarrow \infty} \omega(y') = 0$ applies and in combination with (52) is $\check{C}_3 = \check{C}_4 = 0$. The description of the RVE as a one-side elastically supported infinite cantilever beam results in the simplified approach

$$\omega(y') = e^{-\hat{\alpha}y'} (\check{C}_1 \cos(\hat{\beta}y') + \check{C}_2 \sin(\hat{\beta}y')). \quad (54)$$

Due to the asymmetric load on the RVE, the transverse deflection function of the RVE is determined in two independent steps. In the first step the RVE is artificially extended on the originally free end in negative y' direction, resulting in a both sided infinite beam, see Figure 5.13 (left). The boundary conditions for this first step are

$$\left. \left(\frac{d\omega}{dy'} \right) \right|_{y'=0} = 0, \quad (\text{symmetry in the origin}) \quad (55)$$

$$P_Q = -E_{f2} I_f \left. \left(\frac{d^3 \omega}{dy'^3} \right) \right|_{y'=0} = -\frac{P_{P0}}{2}. \quad (\text{lateral force in the origin}) \quad (56)$$

Under these conditions the deflection function of the both sided infinite beam (step 1) is

$$\omega_{s1}(y') = e^{-\hat{\alpha}|y'|} (\check{C}_1 \cos(\hat{\beta}|y'|) + \check{C}_2 \sin(\hat{\beta}|y'|)) \quad (57)$$

with the two constants $\check{C}_1 = \frac{P_{P0}}{4E_{f2} I_f \hat{\alpha} (\hat{\alpha}^2 + \hat{\beta}^2)}$ and $\check{C}_2 = \frac{P_{P0}}{4E_{f2} I_f \hat{\beta} (\hat{\alpha}^2 + \hat{\beta}^2)}$. In order to determine the deflection function of the original RVE with a free end, the force and torque are evaluated at the position P ($y' = -l_{fr}$) of the infinite beam and are inversely considered, as shown in Figure 5.13 (right).

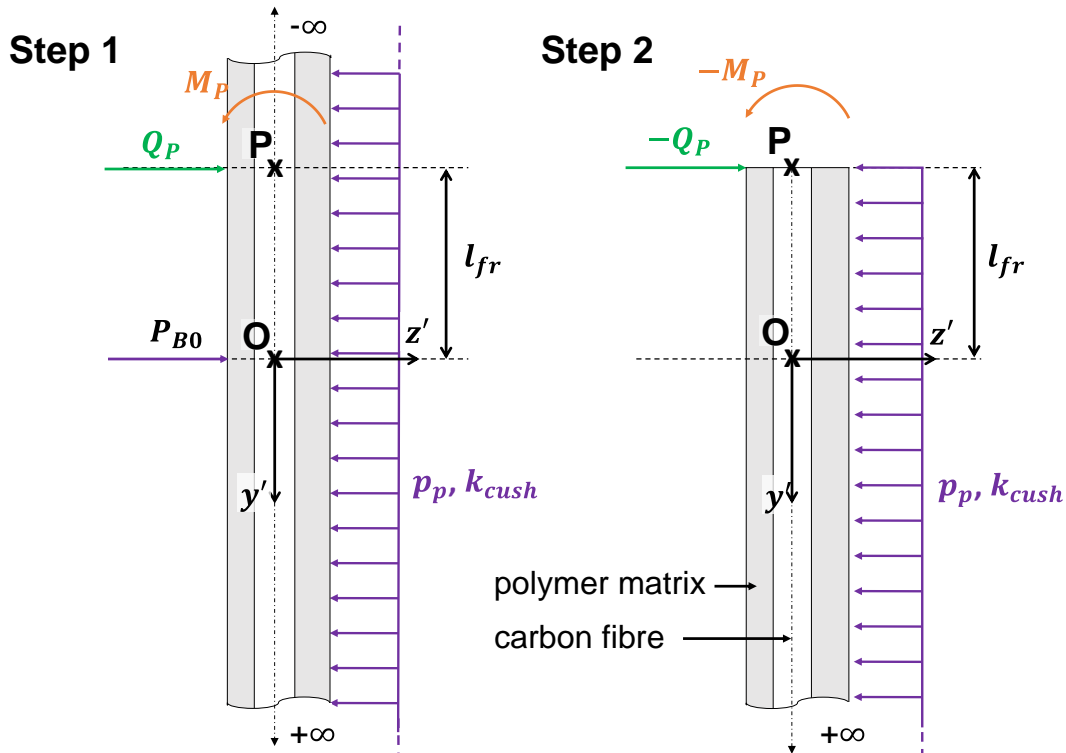


Figure 5.13: Incremental determination of the deflection function of the RVE in two steps

Therefore, the same general approach is applied for step 2

$$\omega_{s2}(y') = e^{-\hat{\alpha}y'} (\check{C}_5 \cos(\hat{\beta}y') + \check{C}_6 \sin(\hat{\beta}y')), \quad (58)$$

in which the the two constants \check{C}_5 and \check{C}_6 are evaluated by means of the two following boundary conditions, as explained above

$$-E_{f2}I_f \left. \frac{d^2\omega_{s1}}{dy'^2} \right|_{y'=-t_c} = -M_P \quad \text{and} \quad -E_{f2}I_f \left. \frac{d^3\omega_{s1}}{dy'^3} \right|_{y'=-t_c} = -Q_P . \quad (59)$$

By combining the equations (57) and (58), the deflection function of a one-side elastically supported infinite cantilever beam can be expressed coincidentally with Qi et al. [177]

$$\omega(y') = e^{-\hat{\alpha}|y'|} (\check{C}_1 \cos(\hat{\beta}|y'|) + \check{C}_2 \sin(\hat{\beta}|y'|)) + e^{-\hat{\alpha}y'} (\check{C}_5 \cos(\hat{\beta}y') + \check{C}_6 \sin(\hat{\beta}y')) . \quad (60)$$

Subsequently the force for the initial fibre separation in the contact point can be calculated. Therefore it is assume consistently with Qi et al. [177] that due to the bending of the fibre compression stresses occur in the contact point K , whereas tension stresses arise on the opposite side. Fiber failure occurs precisely when the induced tension on the opposite side of the contact point exceeds the tensile strength σ_{T_f} of the fibre

$$E_{f2}r_f \left. \frac{d^2\omega}{dy'^2} \right|_{y'=0} - \sigma_{T_f} = 0 . \quad (61)$$

This failure criterion leads to a critical bending force P_{P0_cr} for the initial fibre separation in K

$$P_{P0_cr} = \frac{4 \cdot \hat{\alpha} \cdot \hat{\beta} \cdot I_f \cdot \sigma_{T_f} \cdot e^{2\hat{\alpha}l_{fr}}}{r_f (\hat{\beta} e^{2\hat{\alpha}l_{fr}} - \hat{\beta} \cos(2\hat{\beta}l_{fr}) + \hat{\beta} \sin(2\hat{\beta}l_{fr}))} . \quad (62)$$

P_{P0_cr} is the maximum force on the tool during one fibre failure. To evaluate the average force during CFRP machining for this initial fibre separation in K , a linear force increase is assumed and it is averaged over the workpiece width b . Thus \bar{P}_{P0} can be described as

$$\bar{P}_{P0} = \frac{1}{2} P_{P0_cr} = \frac{1}{2r_f} \frac{4 \cdot \hat{\alpha} \cdot \hat{\beta} \cdot I_f \cdot \sigma_{T_f} \cdot e^{2\hat{\alpha}l_{fr}}}{\hat{\beta} e^{2\hat{\alpha}l_{fr}} - \hat{\beta} \cos(2\hat{\beta}l_{fr}) + \hat{\beta} \sin(2\hat{\beta}l_{fr})} , \quad (63)$$

where ω_0 describes the deflection at fibre fracture. Friction between the cutting edge and the carbon fibre in the contact point K is considered by means of the above presented *Coulomb friction* (μ), since the cutting edge slides along the fibre with progressing cutting motion until it fails. The resulting total force is decomposed vectorially into the feed and cutting force components

$$F_{I2_R2.1_z} = \bar{P}_{P0} (\sin \theta + \mu \cos \theta) \left(\frac{\omega_0 \cdot b \cdot V_f}{\pi \cdot r_f^2} \right) , \quad (64)$$

$$F_{I2_R2.1_y} = \bar{P}_{P0} (\cos \theta - \mu \sin \theta) \left(\frac{\omega_0 \cdot b \cdot V_f}{\pi \cdot r_f^2} \right) .$$

Subsequently a second effect is modelled, which is mentioned above as *step 2 "further bending of the lower part of the initially cut fibres with potential further cracks"*. Therefore, the lower fibre fragment is modelled as one-sided infinite cantilever beam on an elastic

foundation and stressed by a concentrated force at the free end. Theoretically, this fibre must be bent until it passes below the cutting edge in A . The corresponding distance in y direction depends on the micro-geometry (elliptical shape) and the fibre orientation. The geometric context is explained in detail later in this paragraph. For further calculations it is assumed that the y -component of the initial contact point K is equal to the y -component of the contact point K_{B01} at initial fibre separation. A schematic representation of the contact conditions immediately after the initial fibre separation is shown in Figure 5.14. With progressing cutting motion of the tool in z -direction, the lower fibre end is bending in positive z' -direction. According to the bending beam theory, the deflection of the fibre is assumed to be perpendicular to the initial fibre axis, marked by the dot-and-dashed line in Figure 5.14 and named r_B . A potential real bending path is indicated with r_{real} . For the assumption of a one-sided infinite cantilever beam, r_{real} is identical to r_B .

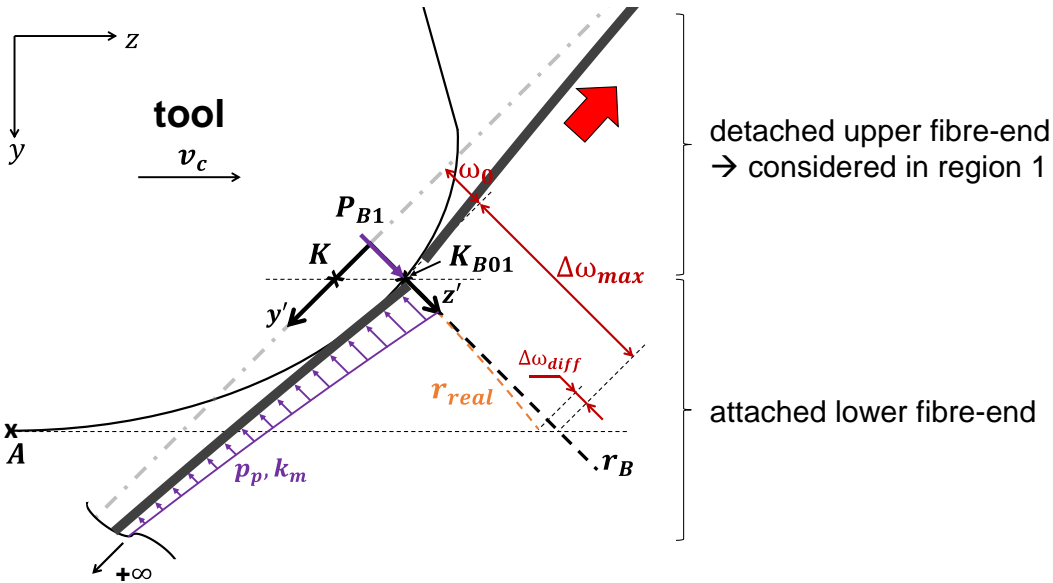


Figure 5.14: Schematic representation of the contact conditions for $\theta = 45^\circ$ in region 2 after initial fibre separation in K_{B0}

The maximum further deflection $\Delta\omega_{max}$ of the lower fibre end relative to the initial fibre separation state (ω_0) to pass below the tool can be derived by the contact point K_{B01} in combination with the elliptical cutting edge, see Figure 5.15. According to HETÉNYI [103], the general formulation of the displacement function $\omega(y')$ for a one-sided infinite cantilever beam on an elastic foundation with a force acting on the free end is

$$\omega(y') = \frac{2P_{B1}\lambda}{k_m} e^{(-\lambda y')} \cos(\lambda y') , \quad (65)$$

with $\lambda = \sqrt[4]{\frac{k_m}{4E_{f2}I_f}}$, in which the parameter k_m describes the WINKLER constant [248] of the elastic foundation. According to ZHANG et al. [269] who adjusted the approach from BIOT [17], the WINKLER constant k_m of the foundation is approximated by means of the mechanical material properties

$$k_m = \frac{0.95E_m}{(1 - \nu_m^2)} \left(\frac{(2r_f)^4 E_m}{E_{f2}I_f(1 - \nu_m^2)} \right)^{0.108} , \quad (66)$$

It is in a range of $k_m=14.958$ MPa for the given material. The deflection ω_0 at initial fibre separation is known by the deflection function in (60) of the still intact fibre. Based on this deflection, the actual force P_{B1} on the one-sided infinite cantilever beam can be calculated with (65). It needs to be considered that the forces for the initial fibre separation P_{B0_cr} (62) and P_{B1} are not identical, due to the different shape of the deflection function. With increasing deflection it is incrementally checked in the model whether potential further cracks occur until reaching the maximum required displacement $\omega_{max} = \omega_0 + \Delta\omega_{max}$. In each iteration step the value as well as the location of the maximum curvature of the displacement function is evaluated. The failure criterion for a further fibre crack is defined, just like in the initial fibre separation case, by exceeding the tensile strength σ_{t_f} . The correlation between the curvature ω of the fibre and σ_{t_f} is according to HETÉNYI [103]

$$-E_f r_f \left. \frac{d^2 \omega}{dy'^2} \right|_{y=0} = \sigma_{t_f} . \quad (67)$$

As soon the maximum tensile strength is exceeded, it is assumed that the fibre fails at the location of maximum curvature, shown by a flash symbol in Figure 5.15. This crack position differs from the current tool/fibre contact point K_{B1} . The deflection in relation to ω_0 of the one-sided infinite fibre at failure is called $\Delta\omega_{cr1}$ and the force on the tool at failure is P_{B1_cr} . It needs to be considered that the point of force initiation K_{B1} is shifted in axial direction by y'_{sh} during bending and the distance from K_{B1} to the fibre crack is y'_c . Applying the linear correlation proposed by HETÉNYI [103], the average bending-induced force for displacing the fibre by $\Delta\omega_{cr1}$ is calculated by

$$\bar{P}_{B1} = \frac{P_{B1_cr} - P_{B1}}{2} = \frac{1}{2} \frac{k_m}{2\lambda} (\Delta\omega_{cr1}) . \quad (68)$$

This force acts on the tool in the middle between the two positions K_{B01} and K_{B1} of the cutting edge, shown in the detailed view on the right in Figure 5.15. The tangential angle in this position (z_i is the actual z-value) is calculated by means of the general elliptic equation

$$\beta_{i,m} = \arctan\left(\frac{-l_y z_i}{l_\alpha \cdot \sqrt{l_\alpha^2 - z_i^2}}\right) . \quad (69)$$

Subsequently, the bending force components in the cutting speed and feed direction under consideration of *Coulomb* friction for one universal bending induced crack are calculated by

$$\begin{aligned} \bar{P}_{Bi_z} &= \bar{P}_{B1} \cdot (\sin \theta + \cos(\theta - \beta_{i,m}) \cdot \mu \cdot \cos \beta_{i,m}) \quad \text{and} \\ \bar{P}_{Bi_y} &= \bar{P}_{B1} \cdot (\cos \theta - \cos(\theta - \beta_{i,m}) \cdot \mu \cdot \sin \beta_{i,m}) . \end{aligned} \quad (70)$$

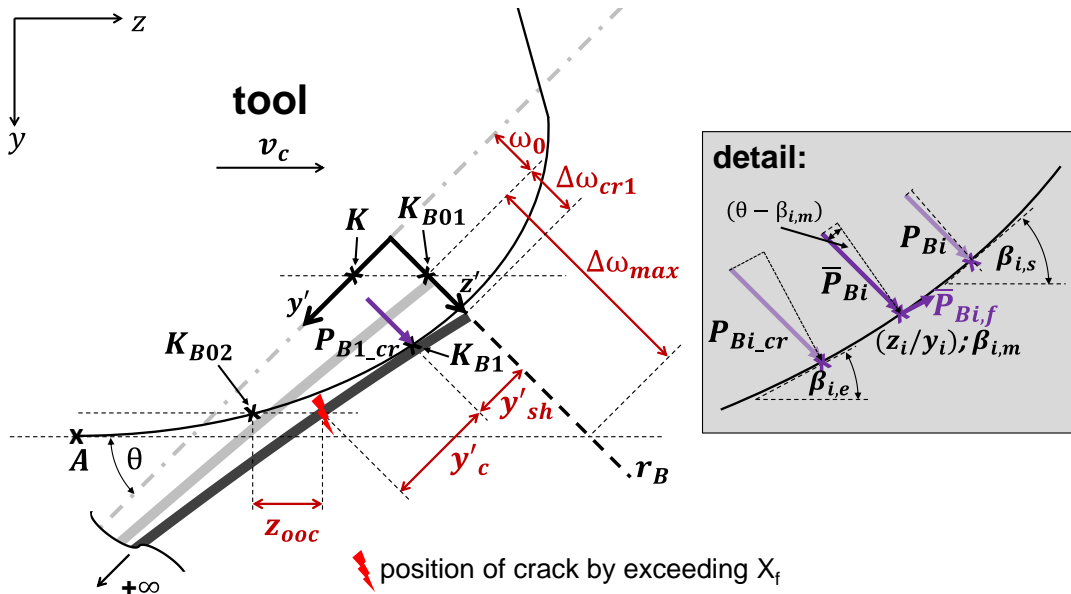


Figure 5.15: Schematic representation of the contact conditions for $\theta = 45^\circ$ in region 2 at first fibre crack, due to bending of one-sided infinite beam

To account for a potential second bending-fracture, the new initial deflection is calculated by means of (65) at the position $y' = y'_c$. Generally, due to a differing initial fibre deflection $\omega_0 \neq \omega_1 \neq \omega_i$ the deflection at fibre crack is also dissimilar $\omega_{cr1} \neq \omega_{cr2} \neq \omega_{cri}$. Based on this bending induced crack-theory, the fibre would be out of contact after the first crack for a cutting distance of $z = z_{00c}$, as shown in Figure 5.15 and touch the tool in K_{B02} . In these intermediate intervals it is assumed that no further bending-induced force is applied to the tool but the broken fibre and matrix fragments are pressed along the cutting edge. The associated pressing force $\bar{P}_{pr,i}$ is calculated by means of the mechanical approach of a cylinder in contact with a half-space, as already explained in section 5.1 with (36).

The above described approach of potentially multiple bending and pressing segments is repeated consistently until the fibre is either bent down to the lowest point A of the tool without a further crack or the potential next crack appears below the tool. Regardless of how many bending induced fibre cracks occur, a periodic load is induced by a single fibre, moving along the cutting edge rounding from the first contact in K to the lowest point in A . This periodic load is characterised by a specific number of bending and pressing portions, schematically shown in Figure 5.16. The representation shows an exemplary differentiation of two bending-induced cracks, two pressing intervals and one residual fibre bending (ω_3). The number of pressing and bending force components does not necessarily be identical and depends on the actual contact situation. According to their definition, the sum of all bending and pressing displacements ($\Delta\omega_i, \Delta d_j$) is equal to the maximum further deflection $\Delta\omega_{max}$, subsequent to the initial fibre separation.

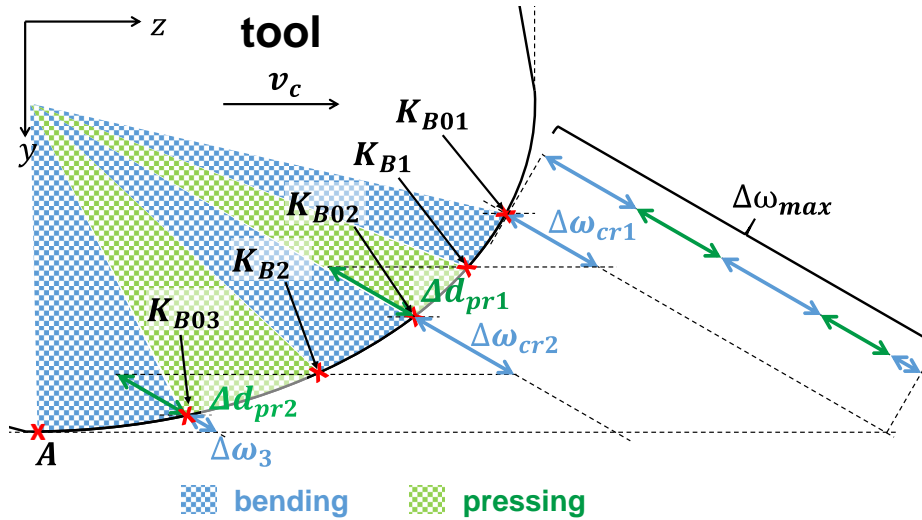


Figure 5.16: Schematic representation of the contact conditions for $\theta = 60^\circ$ in region 2 with 2 bending induced cracks, 2 pressing and 1 residual bending segment

To calculate the resulting force on the tool, which is loaded simultaneously by bending and pressing of several fibres, a weighting of the individual force components is performed. Therefore, the number of fibres being in contact with the tool in each bending and pressing portion is considered by the respective bending displacement lengths ($\Delta\omega_i$) as well as the pressing lengths (Δd_j) in y' -direction. After a vectorial decomposition in y - and z -direction and with consideration of the initial fibre separation (64), the total forces in region 2 are

$$\begin{aligned}
 F_{I2_R2_z} &= F_{I2_R2.1_z} + F_{I2_R2.2_z} \\
 &= \bar{P}_{P0}(\sin \theta + \mu \cos \theta) \left(\frac{\omega_0 \cdot b \cdot V_f}{\pi \cdot r_f^2} \right) + \sum_1^{n_B} \bar{P}_{Bi_z} \frac{\Delta\omega_i \cdot b \cdot V_f}{\pi \cdot r_f^2} + \sum_1^{n_{Pr}} \bar{P}_{Prj_z} \frac{\Delta d_j \cdot b \cdot V_f}{\pi \cdot r_f^2} ,
 \end{aligned} \tag{71}$$

$$\begin{aligned}
 F_{I2_R2_y} &= F_{I2_R2.1_y} + F_{I2_R2.2_y} \\
 &= \bar{P}_{P0}(\cos \theta - \mu \sin \theta) \left(\frac{\omega_0 \cdot b \cdot V_f}{\pi \cdot r_f^2} \right) + \sum_1^{n_B} \bar{P}_{Bi_y} \frac{\Delta\omega_i \cdot b \cdot V_f}{r_f^2 \pi} + \sum_1^{n_{Pr}} \bar{P}_{Prj_y} \frac{\Delta d_j \cdot b \cdot V_f}{r_f^2 \pi} ,
 \end{aligned}$$

in which n_B , n_{Pr} describe the total number of bending and pressing segments respectively. The indices i and j are used for numbering of the individual components in the bending and pressing segments.

Modelling of region 3:

The cutting-process-tribometer experiments, presented in Chapter 4.3, with pressing and friction effects along an indenter are similar to the contact conditions occurring in region 3 of the cutting edge. These experimental results prove that the pressing and friction forces are independent on the fibre orientation. Consequently, it is feasible to model the process in region 3 with spring-back of the material and friction along the flank face of the tool analogous to the approach of sub-model $\theta = 0^\circ$. The equations have already been derived and explained in section 5.1. Accordingly, the pressing force in region 3 of the interval II ($15^\circ \leq \theta \leq 75^\circ$) is proportional to the bouncing height b_c and the adjusted *Young's* modulus

$$P_{pr.3} = \frac{b \cdot L_{pf} \cdot E_{c3} \cdot \tan \alpha^*}{2} = \frac{b \cdot b_c \cdot E_{c3}}{2} . \quad (72)$$

Thus, the force components in z - and y -direction due to flank face contact in region 3 are

$$\begin{aligned} F_{I2_R3_z} &= \mu \frac{b \cdot b_c \cdot E_{c3}}{2} (\cos \alpha^*)^2 , \\ F_{I2_R3_y} &= \frac{b \cdot b_c \cdot E_{c3}}{2} (1 + \mu \cos \alpha^* \sin \alpha^*) . \end{aligned} \quad (73)$$

The total thrust and cutting forces for the second fibre orientation interval ($15^\circ \leq \theta \leq 75^\circ$) are determined by superposing the force components in z - and in y -direction [(44), (71), (73)] in all three regions

$$\begin{aligned} F_{I2_z} &= F_{I2_R1_z} + F_{I2_R2_z} + F_{I2_R3_z} \\ F_{I2_y} &= F_{I2_R1_y} + F_{I2_R2_y} + F_{I2_R3_y} \end{aligned} \quad (74)$$

5.2.2 Results of sub-model $15^\circ \leq \theta \leq 75^\circ$

Due to a lack of description of the strain rate dependency for the tensile strength σ_{Tf} of the CFRP fibres, a correction factor $K_{\sigma_{Tf}}$ is utilised and also fitted to the experiments. It is applied in the force model by multiplying with the value from the datasheet: $\sigma_{Tf} = \sigma_{Tf0} \cdot K_{\sigma_{Tf}}$. Basing on the same material properties, process parameters and fitting variables, which are shown in the table in the Appendix A.3, the simulation results for an exemplary Tool E ($10^\circ/7^\circ$) and the fibre orientation $\theta = 30^\circ$ are presented in Figure 5.17. Further results of different geometries Tool J ($20^\circ/7^\circ$) and Tool M ($20^\circ/21^\circ$) and a further exemplary fibre orientation of $\theta = 60^\circ$ are presented in the Appendix A.5 and A.6.

Focusing firstly on the cutting forces, these increase over the cutting length by tool wear and the simulation results are in good agreement with the measurements. The average deviation between simulation and experiment for Tool E ($10^\circ/7^\circ$) is 5%. According to the simulation results with separate consideration of the three cutting edge regions, the main share of the total cutting forces is generated in region 2 in the relatively new state of $l_c = 5m$. Only with increasing tool wear, the share of cutting forces in region 3 increases continuously, exceeding region 2 after $l_c = 20m$ of cutting length. This is due to the effect of maximum wear occurring in Region 3 during $\theta = 30^\circ$ and $\theta = 60^\circ$ machining, where generally mainly thrust force is transferred, but due to consideration of friction a not negligible portion of cutting force arises. The cutting force share of region 1, where the already cut fibres are transported along the rake face by inducing interlaminar shear in the matrix, is almost constant and on a relatively low level of 13 N. Comparing these results to a tool with larger clearance angle like Tool M ($20^\circ/21^\circ$), shown in the Appendix A.5, confirm the expectations of a smaller share of region 3, resulting in generally smaller cutting and thrust forces. The increase of the rake angle from 10° to 20° has an overall negligible influence on the total forces, due to the specific chip formation mechanisms in the interval II ($15^\circ \leq \theta \leq 75^\circ$).

Analysing the thrust forces for Tool E ($10^\circ/7^\circ$) shows an average deviation between simulation and experiment of 9% over a cutting length of 40 m, while the maximum deviation for this example is about 16.7%. Due to the positive rake angle in region 1, the associated thrust force portion is even negative and analogue to the cutting forces on a very low level.

The modelled chip formation mechanisms along the cutting edge rounding in region 2 result in a similar magnitude for the cutting as well as the thrust forces in region 2 for $\theta = 30^\circ$ but contrary to the cutting forces this only accounts for 10-20% of the total thrust forces. This is because by far the largest share of the total thrust force originates in region 3, where maximum tool wear and thus the main force increase occurs. As soon the fibres are oriented steeper, exemplarily shown with $\theta = 60^\circ$ and Tool E in the Appendix A.6, the first contact point on the elliptical cutting edge rounding moves upwards and the resulting force in region 2 is oriented more in cutting speed than in feed direction. Consequently, the magnitude of cutting forces in region 2 is larger compared to the magnitude of thrust forces.

The deviation of the shape of the thrust force increase between simulation and reality is most likely due to deviations of the micro-geometry input parameters, as already being explained in 5.1.

Generally, these results validate the findings from 5.1 that the forces originating in region 3 are proportional to the tool/material contact area along the flank face and thus to the tool wear. The forces in region 2 depend on the contact condition and initiation of cracks in the carbon fibres and thus are proportional to the asymmetric cutting edge rounding (ratio of $\frac{l_\alpha}{l_\gamma}$).

For this interval II ($15^\circ \leq \theta \leq 75^\circ$) the influence of region 1 on the forces is negligible.

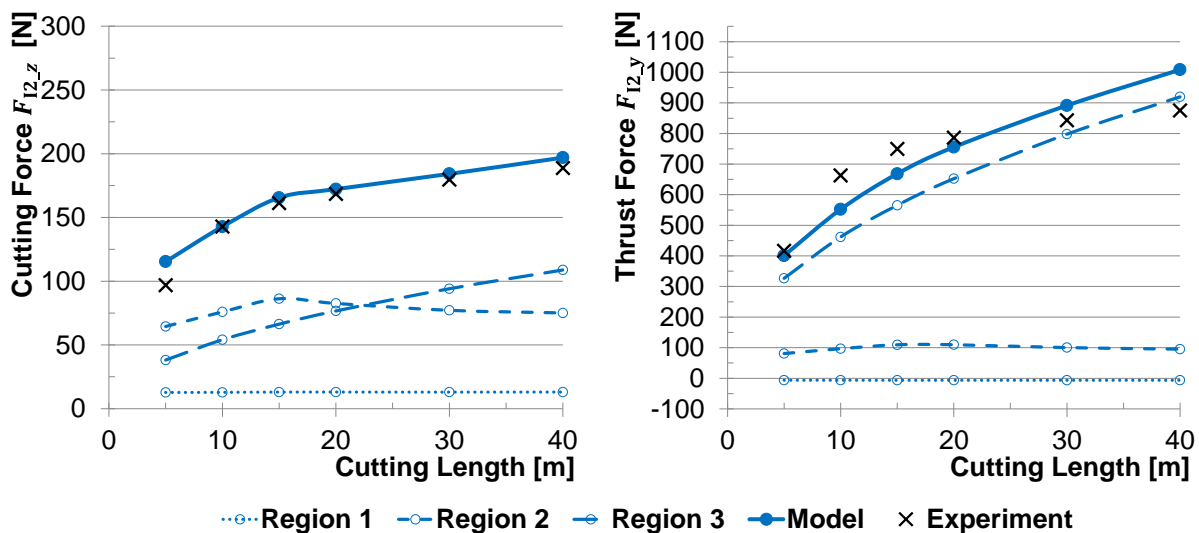


Figure 5.17: Comparison of cutting and thrust forces between model and experiment for the Tool E ($10^\circ/7^\circ$) in $\theta = 30^\circ$ material; $v_c=90$ m/min and $f=0.03$ mm/rot

5.3 Sub-model $\theta=90^\circ$

The contact conditions of a tool during orthogonal cutting of CFRP with exemplary $\theta = 90^\circ$ fibre orientation are presented in Figure 5.18. The chip formation mechanisms start theoretically at a first tool/fibre contact in the most forward point B of the cutting edge in cutting speed direction. Based on the analysis results of the fundamental experiments it is assumed that the tool loads the vertically oriented fibre in bending until it fails by exceeding the tensile strength. Subsequently, the lower end of the cut fibre is further bend until it passes the lowest point A of the cutting edge, which may result in an interlaminar crack. The micro-geometry of the cutting edge is described by the same five micro-geometry parameters

l_α , l_γ , γ^* , α^* and b_c as in the sub-models before. This fibre orientation of $\theta = 90^\circ$ represents a limit case, where the largest number of fibres have to be cut per specific cutting length, generally leading to the highest cutting forces in test. The relationship of the parameters H_1 , a_{cut} and \hat{b}_c has already been explained in (17) and (18) on page 78 and is still valid.

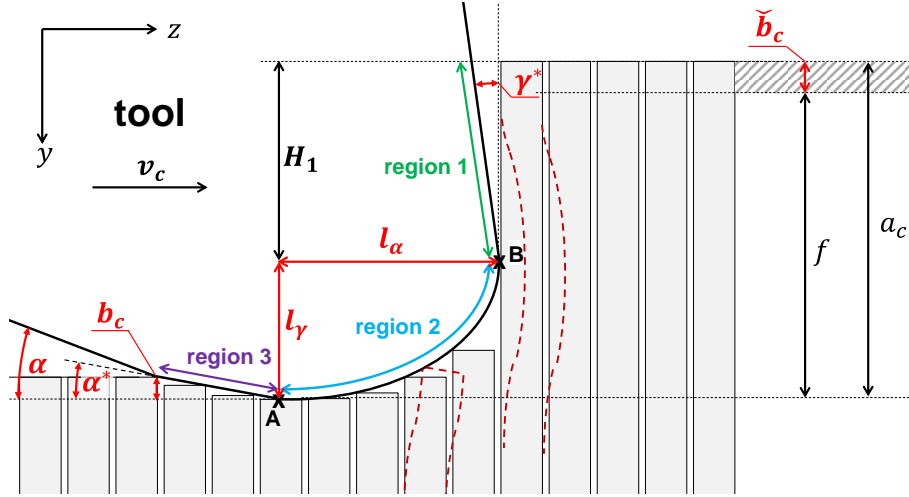


Figure 5.18: Schematic representation of the contact conditions for $\theta = 90^\circ$

5.3.1 Modelling

Modelling of region 1:

Starting from the foremost point B in cutting direction of the tool, the carbon fibres are loaded in the model transverse to the axis of the carbon fibre. This bend fibre is supported by the residual material behind. Because point B describes the transition from region 1 to region 2, the fibre bending extends to both regions. However, since in region 2 an overlap of several effects occurs, the initial fibre bending for both regions is described at this point. In order to describe the forces on the tool, the modelling approach of XU and ZHANG [257] is applied, which bases on the bending beam theory in combination with the elastic foundation model, presented by WINKLER [248]. Figure 5.19 shows a schematic representation of a single carbon fibre, loaded with a concentrated force in B . For consistent description of the fibre deformation, a coordinate system y''/z'' is introduced with the origin in the fibre end A . Assuming an elastic correlation between the fibre deformation and the force intensity of the foundation on the fibre, the Winkler approach with the above explained stiffness constant k_m may be applied. This constant is determined by means of the approximation by BIOT [17] based on the material characteristics, which is presented in Equation (66). Comparable to the modelling approach in 5.2, the fibre in front of the cutting edge is bend until it fails in the contact point B and the upper part of the cut fibre is evacuated along the rake face of the tool. The lower part of the initially cut fibre is still attached to the workpiece and with progressing cutting motion it is further bend. According to the approach of XU and ZHANG [257] this bending introduces a relative motion between the lower part of the initially separated fibre and the next still intact fibre. This results in an interlaminar crack, starting in B parallel to the fibres in feed direction y'' and described in Figure 5.19 by Section 2 and Figure 2.37. The vertical length of this crack is described by the length h^* and C represents the bottom of the crack. To determine the point C as a function of the actual deflection of the

still intact bending beam, a critical deflection $\omega_{z''_{cr}}$ is defined. This deflection describes the length, which the matrix is able to withstand without failure. As long as this critical value is not exceeded, the matrix-fibre connection remains intact between the adjacent carbon fibres. Hence, the point C defines the location at which the critical deflection is not yet achieved. With progressing deflection of the still uncut carbon fibre immediately upstream of the cutting edge, peeling stress occurs in the crack ground, resulting in an increasing vertical crack length h^* and a shifting of C in positive y'' direction. The additional support of the carbon fibre in the case of an intact fibre-matrix connection counteracts the fibre deflection and is described by means of a second *Winkler* constant k_b supporting the elastic foundation (k_m), according to XU and ZHANG [257]. This area of the carbon fibre, with intact fibre-matrix connection is described in Figure 5.19 by Section 3.

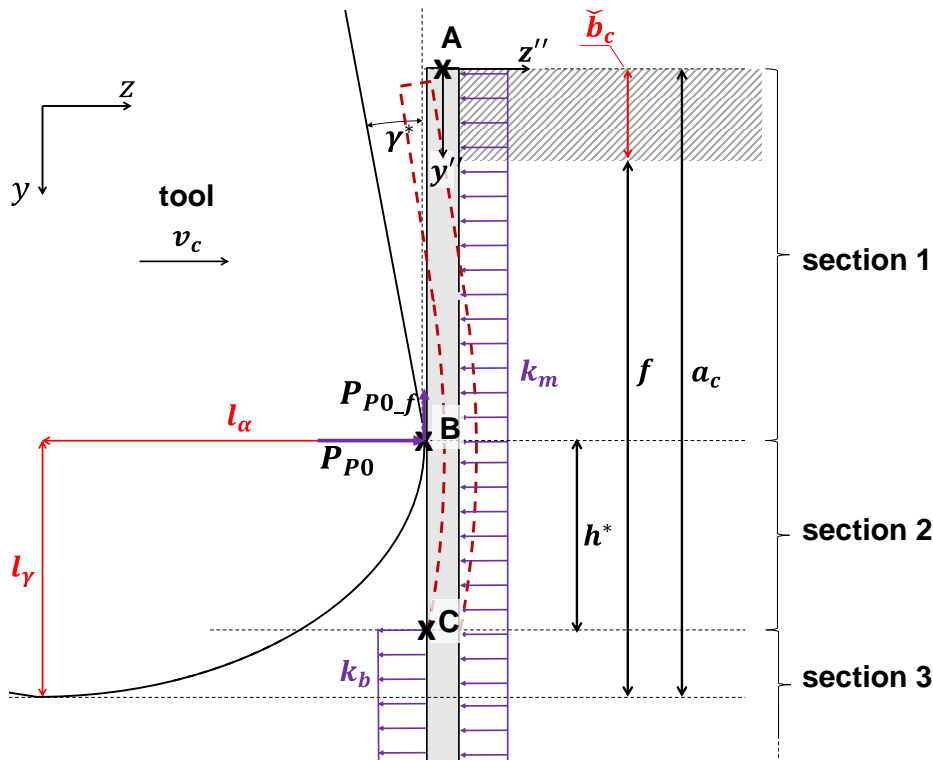


Figure 5.19: Schematic representation of the contact conditions for $\theta = 90^\circ$

It is necessary to determine the deflection function of the carbon fibre immediately upstream of the cutting edge to evaluate the process forces. Due to the above explained change of the load situation along the carbon fibre, the deflection function is subdivided into three sections, shown in Figure 5.19. By defining boundary and transition conditions, the three separate sections are combined. The definition of the three sections with respect to the y''/z'' coordinate system is as follows:

- section 1: $0 \leq y'' < a_c - l_\gamma$
- section 2: $a_c - l_\gamma \leq y'' \leq a_c - l_\gamma + h^*$
- section 3: $y'' > a_c - l_\gamma + h^*$

In these definitions a_c is the effective cutting depth of the orthogonal machining operation explained in (17) and l_γ describes the micro-geometrical value of the elliptical cutting edge rounding. According to the approach by XU and ZHANG [257], the differential equation of the bending beam on elastic foundation may be expressed by

$$E_{f2}I_f \frac{d^4\omega}{dy^4} + k_i\omega = 0 \quad , \quad (75)$$

in which k_i is place holder for the winkler constant, which is $k_i = k_m$ for $y'' \leq a_c - l_\gamma + h^*$ and $k_i = k_m + k_b$ for $y'' > a_c - l_\gamma + h^*$. According to XU and ZHANG [257], the general solution of the differential equation can be formulated by

$$\omega(y'') = e^{\lambda y''} (C_1 \cos(\lambda y'') + C_2 \sin(\lambda y'')) + e^{-\lambda y''} (C_3 \cos(\lambda y'') + C_4 \sin(\lambda y''))$$

$$\text{with } \lambda = \sqrt[4]{\frac{k_i}{4E_{f2}I_f}} \quad . \quad (76)$$

Using the mathematic correlations $\cosh(\lambda y) = \frac{(e^{\lambda y} + e^{-\lambda y})}{2}$ and $\sinh(\lambda y) = \frac{(e^{\lambda y} - e^{-\lambda y})}{2}$, the equation (76) can be written for each section as

$$\omega_1(y'') = B_1 F_1 \lambda_m y'' + B_2 (F_2 \lambda_m y'' + F_4 \lambda_m y'') + B_3 (F_2 \lambda_m y'' - F_4 \lambda_m y'') + B_4 F_3 \lambda_m y''$$

$$\text{for } 0 \leq y < a_c - l_\gamma \quad (77)$$

$$\omega_2(y'') = B_5 F_1 \lambda_m y'' + B_6 (F_2 \lambda_m y'' + F_4 \lambda_m y'') + B_7 (F_2 \lambda_m y'' - F_4 \lambda_m y'') + B_8 F_3 \lambda_m y''$$

$$\text{for } a_c - l_\gamma \leq y \leq a_c - l_\gamma + h^* \quad (78)$$

$$\omega_3(y'') = C_1 (F_1 \lambda_{mb} y'' + F_2 \lambda_{mb} y'' - F_4 \lambda_{mb} y'') +$$

$$+ C_2 (F_2 \lambda_{mb} y'' + F_3 \lambda_{mb} y'' + F_4 \lambda_{mb} y'') +$$

$$+ C_3 (F_1 \lambda_{mb} y'' - F_2 \lambda_{mb} y'' + F_4 \lambda_{mb} y'') +$$

$$+ C_4 (F_2 \lambda_{mb} y'' - F_3 \lambda_{mb} y'' + F_4 \lambda_{mb} y'')$$

$$\text{for } y > a_c - l_\gamma + h^* \quad (79)$$

in which λ_m , λ_{mb} as well as F_1 , F_2 , F_3 and F_4 are substitution variables

$$\lambda_m = \sqrt[4]{\frac{k_m}{4E_{f2}I_f}} \quad \text{and} \quad \lambda_{mb} = \sqrt[4]{\frac{(k_m + k_b)}{4E_{f2}I_f}}$$

$$F_1 = \cosh(\lambda y) \cos(\lambda y) \quad \text{and} \quad F_2 = \frac{\cosh(\lambda y) \sin(\lambda y) + \sinh(\lambda y) \cos(\lambda y)}{2} \quad (80)$$

$$F_3 = \sinh(\lambda y) \sin(\lambda y) \quad \text{and} \quad F_4 = \frac{\cosh(\lambda y) \sin(\lambda y) - \sinh(\lambda y) \cos(\lambda y)}{2}$$

According to the general mechanical approach, the torque M_i and the transverse force Q_i of a section i ($i=1,2,3$) can be calculated depending on y''

$$M_i = -E_{f2}I_f \frac{d^2\omega_i}{dy''^2} \quad \text{and} \quad Q_i = -E_{f2}I_f \frac{d^3\omega_i}{dy''^3} \quad . \quad (81)$$

The gradient of the deflection function can be calculated by $g_i = \frac{d\omega_i}{dy''}$. To evaluate the deflection function of the carbon fibre, the still unknown coefficients B_1 , B_2 , B_3 , B_4 , B_5 , B_6 , B_7 , B_8 , C_1 , C_2 , C_3 , C_4 in the Equations (77), (78) and (79) and the length of the interlamiar crack h^* have to be evaluated. Therefore, the following boundary and transition conditions are defined in accordance to the approach of XU and ZHANG [257]

section 3 ($y'' \geq a_c - l_\gamma + h^*$)

$$\omega_3|_{y'' \rightarrow \infty} = 0 \quad (82)$$

in point A ($y'' = 0$)

$$M_1|_{y''=0} = 0 \quad (83)$$

$$Q_1|_{y''=0} = 0 \quad (84)$$

in point B ($y'' = a_c - l_\gamma$)

$$\omega_2|_{y''=a_c-l_\gamma} = v_c t \quad (85)$$

$$\omega_1|_{y''=a_c-l_\gamma} = \omega_2|_{y''=a_c-l_\gamma} \quad (86)$$

$$g_1|_{y''=a_c-l_\gamma} = g_2|_{y''=a_c-l_\gamma} \quad (87)$$

$$M_1|_{y''=a_c-l_\gamma} = M_2|_{y''=a_c-l_\gamma} \quad (88)$$

in point C ($y'' = a_c - l_\gamma + h^*$)

$$\omega_3|_{y''=a_c-l_\gamma+h^*} = \omega_{Z''_{cr}} \quad (89)$$

$$\omega_2|_{y''=a_c-l_\gamma+h^*} = \omega_3|_{y''=a_c-l_\gamma+h^*} \quad (90)$$

$$g_2|_{y''=a_c-l_\gamma+h^*} = g_3|_{y''=a_c-l_\gamma+h^*} \quad (91)$$

$$M_2|_{y''=a_c-l_\gamma+h^*} = M_3|_{y''=a_c-l_\gamma+h^*} \quad (92)$$

$$Q_2|_{y''=a_c-l_\gamma+h^*} = Q_3|_{y''=a_c-l_\gamma+h^*} \quad (93)$$

Analogous to the explanations in 5.2, due to modelling of a semi-infinite bending beam, the deflection in large distance ($y'' \rightarrow \infty$) from the concentrated force on the beam in *B* is zero (82) and thus the constants C_1 , C_2 are zero. According to the mechanical definition of a free-end, Equations (83) and (84) describe the torque and force being zero in *A*. In the Equation (85), v_c represents the cutting speed and t the time from the first tool/fibre contact. Furthermore, at the transition of section 1 to section 2, the deflection (86), the gradient (87) and the torque (88) of both adjacent deflection functions needs to be equal. The Equation in (89) describes the above defined critical deflection $\omega_{Z''_{cr}}$ in *C*. It needs to be considered that the distance between *B* and *C* is not constant but increases during progressing bending of the fibre. Finally, the Equations (90)-(93) take into account that the deflection function must be continuous in *C*.

The above described equation system is solved in the *Matlab* model by means of a gradually symbolic calculation method resulting in a final equation in form of $f(h^*, t) = 0$. Since this equation cannot be solved analytically, the numerical approach *fminsearchbnd* is applied. Therefore, gradually increasing time steps are pretended and the according vertical crack length is evaluated. After the 12 unknown coefficients and the parameter h^* are determined for a specific time t , the corresponding deflection function can be assembled by combining the three sections ω_1 , ω_2 and ω_3 . According to XU and ZHANG [257] the corresponding force on the tool can be calculated

$$\begin{aligned}
P_{B0} &= \int_{a_c-l_\gamma}^B k_m \omega_1 d\mathbf{y}'' + \int_{a_c-l_\gamma+h^*}^C k_m \omega_2 d\mathbf{y}'' + \int_C^\infty (k_m + k_b) \omega_3 d\mathbf{y}'' \\
&= \int_0^{a_c-l_\gamma} k_m \omega_1 d\mathbf{y}'' + \int_{a_c-l_\gamma}^{a_c-l_\gamma+h^*} k_m \omega_2 d\mathbf{y}'' + \int_{a_c-l_\gamma+h^*}^\infty (k_m + k_b) \omega_3 d\mathbf{y}'' .
\end{aligned} \tag{94}$$

In $\theta = 90^\circ$ orientation, the fibre is transversely stressed in B by a high compressive force. This tool/fibre contact in B is modelled as a contact between two perpendicular cylinders, shown in Figure 5.20.

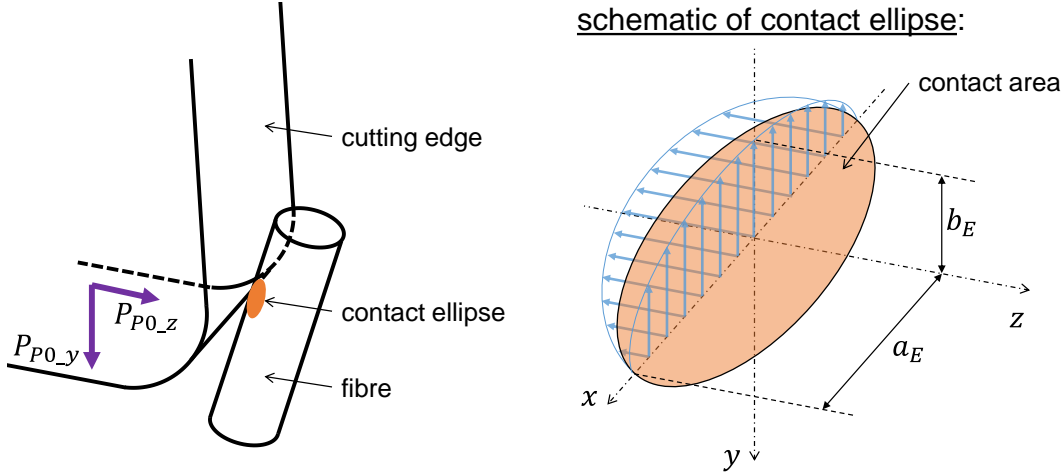


Figure 5.20: Contact area between carbon fibre and cutting edge, in accordance to XU and ZHANG [257, 258]

In contrast to the interval II ($15^\circ \leq \theta \leq 75^\circ$), the fibres are loaded perpendicular to the fibre axis and the cutting edge most likely does not slide along the fibre but stays in contact in point B . Due to the increasing load in the contact area during cutting, an increasing compressive stress is induced. Corresponding to XU and ZHANG [257], the exceeding of the compressive strength of a fibre σ_{Pr_cr} in B is modelled as the failure mechanism. The relationship between the force P_{P0} and the induced compressive stress in this contact situation is described by YOUNG and BUDYNAS [261]. Accordingly, the induced compressive stress σ_{Pr} can be calculated

$$\begin{aligned}
\sigma_{Pr} &= 0.579 n_c \sqrt[3]{\frac{P_{P0}}{K^2 \xi^2}} , \\
\text{with } \xi &= \frac{(1 - \nu_1^2)}{E_1} + \frac{(1 - \nu_2^2)}{E_2} \quad \text{and} \quad K = \frac{D_1 D_2}{D_1 + D_2} \quad \text{and} \quad \zeta = \frac{D_1}{D_2} .
\end{aligned} \tag{95}$$

In which the two parameter D_1 and D_2 are the diameter of the carbon fibre ($D_1 = 2r_f$) and the diameter of cutting edge in the contact point B . The latter diameter can be approximated from the mathematical ellipse equation at the point B of the tool by

$$D_2 = \frac{2l_\gamma^2}{l_\alpha} . \tag{96}$$

The other parameters ν_1 , ν_2 , E_1 and E_2 represent the respective *Poisson's ratio* and the *Young's modulus* of elasticity of the cylinders. To evaluate n_c , the tables in the Appendix A.9

and A.10 are utilised, according to PILKEY [172]. This table also gives the characteristic numbers n_a and n_b , which are necessary to evaluate the semi axes (a_E , b_E) of the resulting contact ellipse between the tool and the carbon fibre

$$\begin{aligned} a_E &= 0.909n_a \sqrt[3]{P_{P0}K\xi} , \\ b_E &= 0.909n_b \sqrt[3]{P_{P0}K\xi} \end{aligned} \quad (97)$$

Now all necessary equations for force determination on the tool until fibre failure in the contact point B have been presented. In summary, the procedure for force calculation in the model is as follows: The time t is incrementally increased ($t_{n+1} = t_n + \Delta t$) and in each time step the equations (77) to (79) are solved and the value of h^* is evaluated. Subsequently, the coefficients $B_1 - B_8$ and $C_1 - C_4$ are determined. Afterwards, the actual force on the tool is evaluated by Equation (94) and the compressive stress by Equation (95). A comparison of the evaluated stress and the compressive strength of the carbon fibre shows whether the fibre bends or fails at the actual increment t_n . If the fibre withstands the load, the compressive stress is evaluated for the next time-increment and the failure criterion is tested. The force at fibre failure P_{P0_cr} is the maximum transferable load, which is averaged under the assumption of a linear force increase by

$$\bar{P}_{P0} = \frac{P_{P0_cr}}{2} . \quad (98)$$

Subsequently, the bending force components in the cutting speed and feed direction under consideration of *Coulomb* friction for one universal bending induced crack are calculated by

$$\begin{aligned} F_{I3_R1_z} &= \bar{P}_{P0} \quad \text{and} \\ F_{I3_R1_y} &= -\mu \cdot \bar{P}_{P0} . \end{aligned} \quad (99)$$

Modelling of region 2:

After fibre failure in the first contact point B by exceeding the compressive strength, the upper part of the cut fibre is evacuated along the rake face of the tool. The lower part of the cut fibre is still attached to the workpiece and with compressive cutting motion it is bend. Analogous to the sub-model $15^\circ < \theta < 75^\circ$, bending is modelled perpendicular to the initial fibre axis. The corresponding deflection direction is indicated by r_B in Figure 5.21.

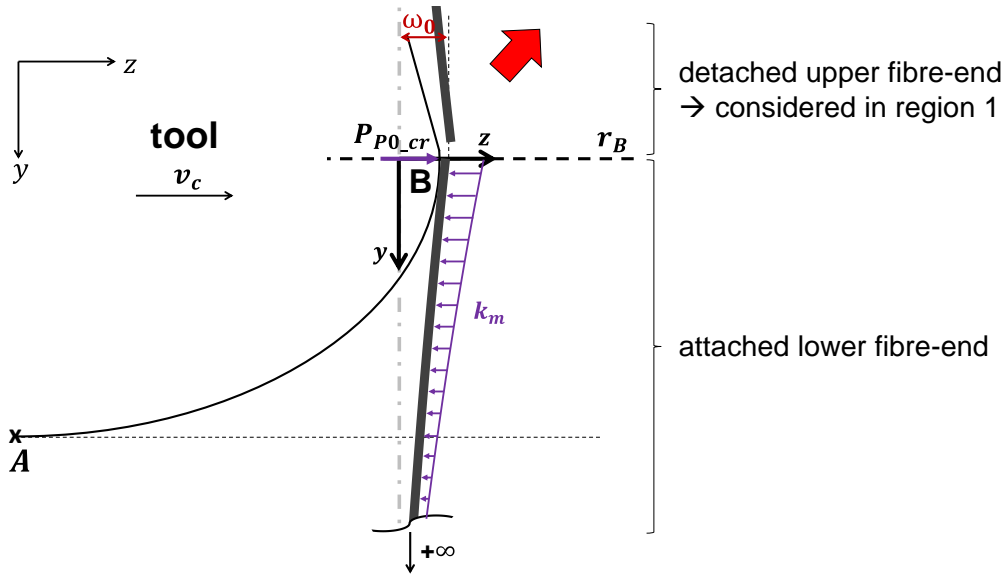


Figure 5.21: Schematic representation of the contact conditions for $\theta = 90^\circ$ at fibre failure in B

In order to describe the deflection function of the carbon fibre on the elastic foundation, the approach proposed by HETÉNYI [103] is applied analogously to the explanations in chapter 5.2. With increasing deflection of the lower fibre-end, the tensile stress at the edge of the carbon fibre increases. Due to the correlation between deflection and maximum tensile strength, shown in Equation (67), the maximum stresses occur at the location of the maximum curvature. The fibre fails in this location, as soon the maximum tensile strength is exceeded. Due to the elliptical cutting edge rounding, this additional crack position becomes the prospective contact point as soon the tool moves in cutting direction by the appropriate length. Analogous to the explanations for the sub-model $15^\circ < \theta < 75^\circ$ in Paragraph 5.2, between the tool/fibre contact before the crack and when touching in the new contact point at crack position, pressing of the resulting fibre and matrix particles is considered, as shown in Equations (36) and (71). Analogously it needs to be considered, that the crack position of the fibre could be below the cutting edge and in this case no further bending would occur. It is assumed for each averaged bending and pressing portion that the resulting force acts in the middle of each segment. Depending on the number of fibre cracks, a certain number of ultimately resulting averaged bending and pressing forces, divided into cutting and feed direction, exist: $\bar{P}_{Bi,y}$ and $\bar{P}_{Bi,z}$ according to (70) as well as $\bar{P}_{Prj,y}$ and $\bar{P}_{Prj,z}$ according to (37), in which i is the number of bending and j the number of pressing portions. For evaluation of the average resulting force on the cutting edge in region 2, a weighting of the individual force components is performed, as presented in 5.2 in Equation (71). The resulting total force in region 2 can be divided into the following feed and cutting force components

$$\begin{aligned}
 F_{I3_R2_z} &= \sum_1^{n_B} \bar{P}_{Bi,z} \frac{\Delta\omega_i \cdot b \cdot V_f}{r_f^2 \pi} + \sum_1^{n_{Pr}} \bar{P}_{Prj,z} \frac{\Delta d_j \cdot b \cdot V_f}{r_f^2 \pi} \\
 F_{I3_R2_y} &= \sum_1^{n_B} \bar{P}_{Bi,y} \frac{\Delta\omega_i \cdot b \cdot V_f}{r_f^2 \pi} + \sum_1^{n_{Pr}} \bar{P}_{Prj,y} \frac{\Delta d_j \cdot b \cdot V_f}{r_f^2 \pi}
 \end{aligned} \tag{100}$$

Modelling of region 3:

The forces in region 3 are modelled analogous to the approach of sub-model $\theta = 0^\circ$ and $15^\circ \leq \theta \leq 75^\circ$. Accordingly, the pressing force in region 3 of the interval III ($\theta = 90^\circ$) is

$$P_{pr_3} = \frac{b \cdot L_{pf} \cdot E_{c3} \cdot \tan \alpha^*}{2} = \frac{b \cdot b_c \cdot E_{c3}}{2} \quad (101)$$

Thus, the force components in z- and y-direction due to flank face contact in region 3 are

$$\begin{aligned} F_{I3_R3_z} &= P_{pr_3} \cdot \mu \frac{b \cdot b_c \cdot E_{c3}}{2} (\cos \alpha^*)^2 \\ F_{I3_R3_y} &= P_{pr_3} \frac{b \cdot b_c \cdot E_{c3}}{2} (1 + \mu \cos \alpha^* \sin \alpha^*) \end{aligned} \quad (102)$$

The total thrust and cutting forces for $\theta = 90^\circ$ are determined by superposing the force components in z and in y direction [(99), (100), (102)] in all three regions

$$\begin{aligned} F_{I3_z} &= F_{I3_R1_z} + F_{I3_R2_z} + F_{I3_R3_z} \\ F_{I3_y} &= F_{I3_R1_y} + F_{I3_R2_y} + F_{I3_R3_y} \end{aligned} \quad (103)$$

5.3.2 Results of sub-model $\theta=90^\circ$

An overview of the material data, process parameters and fitting variables used for the $\theta = 90^\circ$ model is given in the appendix A.3. While the first *winkler*-constant k_m of the CFRP material is calculated by means of the above presented approximation (66), the second *winkler*-constant k_b describing the stiffness of the interlaminar matrix compound is adopted from XU and ZHANG [257]. The critical deflection $\omega_{Z''_{cr}}$ in C is a fitting variable in the model. As explained above the fibre/matrix connection fails and an interlaminar crack is initiated, as soon the fibre deflection exceeds $\omega_{Z''_{cr}}$. Another fitting variable is the compressive strength σ_{Pr_cr} of the carbon fibre, which depends on the strain rate. Fitting of the $\theta = 90^\circ$ model to the measurement data, results for optimum correlation in the two values $\omega_{Z''_{cr}} = 0.26 \mu\text{m}$ and $X_{Pr_cr} = 8500 \text{ MPa}$.

The two diagrams in Figure 5.22 show the simulated forces (solid lines) compared to the measured data for the geometry of Tool E ($10^\circ/7^\circ$) in $\theta = 90^\circ$. Additional results for two further tool geometries are presented in the Appendix A.7. Generally the average deviation of the cutting forces is slightly larger (11.9% for Tool E), than the average deviation of the thrust forces (7.8% for Tool E). It is striking that the total thrust force is almost exclusively generated from the force component in region 3. The thrust forces due to fibre separation and bending in regions 1 and 2 are apparently negligible. This is due to the fact that the corresponding resulting forces are almost directly oriented in cutting speed direction (perpendicular to the fibre axis). This is confirmed by the cutting forces in the diagram on the left in Figure 5.22 with fibre separation and bending (region 1 and 2) having a significant share on the total cutting force. In the relatively new state ($l_c = 5 \text{ m}$) this two mentioned mechanisms in regions 1 and 2 have together a large share of 78.5% on the total cutting force. With increasing wear or cutting length respectively, the portions on the total cutting force generated by the initial separation (region 1) and by elastic spring back (region 3) are

increasing, whereas the portion generated in region 2 is decreasing. The latter effect of decreasing bending force can be observed with all tested tool geometries in $\theta = 90^\circ$ (Appendix A.7) and it is due to an increasing interlaminar crack length h^* with wear. The other two portions initial separation (region 1) and elastic spring back (region 3) increase proportional to the increasing cutting edge rounding (l_α and l_γ values) and the increasing contact area on the flank face (b_c and α^*).

At this point, reference is also made to the outlier Tool M ($20^\circ/21^\circ$) with a large average deviation (66.8%) of the simulated thrust force, presented in the Appendix A.7. This is due to the very small and hardly measurable spring back height of values below $b_c = 2\mu\text{m}$ for this tool with an large initial clearance angle of $\alpha = 21^\circ$. In future such errors can be avoided, as soon the tool micro-geometry can also be modelled instead of being measured.

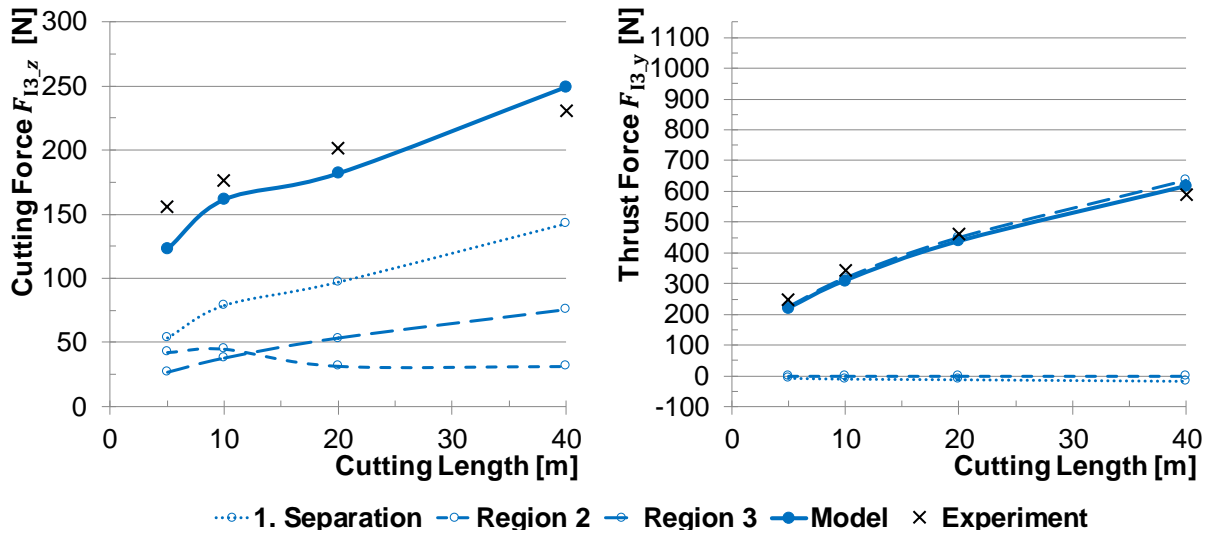


Figure 5.22: Comparison of cutting and thrust forces between model and experiment for the Tool E ($10^\circ/7^\circ$) in $\theta = 90^\circ$ material; $v_c=90$ m/min and $f=0.03$ mm/rot

5.4 Sub-model $105^\circ + \gamma \leq \theta < 165^\circ$

In this chapter the approach for the fibre orientation interval IV ($105^\circ + \gamma \leq \theta < 165^\circ$) is explained in detail, where γ is the rake angle of the tool. The rake angle is considered in the validity range of this sub-model, since the chip formation depends on the relative angle between rake face of the tool and the fibre axis. Figure 5.23 shows the contact conditions of a worn cutting edge during machining $\theta = 150^\circ$ UD CFRP material. Tool wear for fibre orientations in the range of $\theta = 150^\circ$ is in general much weaker, compared to the other fibre orientations, as shown in the detailed tool wear analysis, exemplarily presented in Figure 4.13. No obvious flank face wear occurs. Consequently, spring back or friction along the flank face (region 3) is not considered ($b_c = \tilde{b}_c = 0$) in this sub-model, resulting in $f = a_{cut}$. The micro-geometry in region 1 and region 2 is described by the before proposed micro-geometry parameters l_α , l_γ and γ^* . The chip formation mechanisms are local axial compression (buckling) of the fibres in region 2, introduction of an interlaminar crack in fibre direction due to peeling (bending) of the fibres in contact with the rake face (region 1) as well as failure of the bend fibre bundle due to exceeding the flexural strength. In this way a saw teeth topography is mapped on the material surface. In the proposed model, the scattering

angular deviation ε of a bending crack initiation perfectly transverse to the fibre orientation is neglected; the crack is assumed to be transverse.

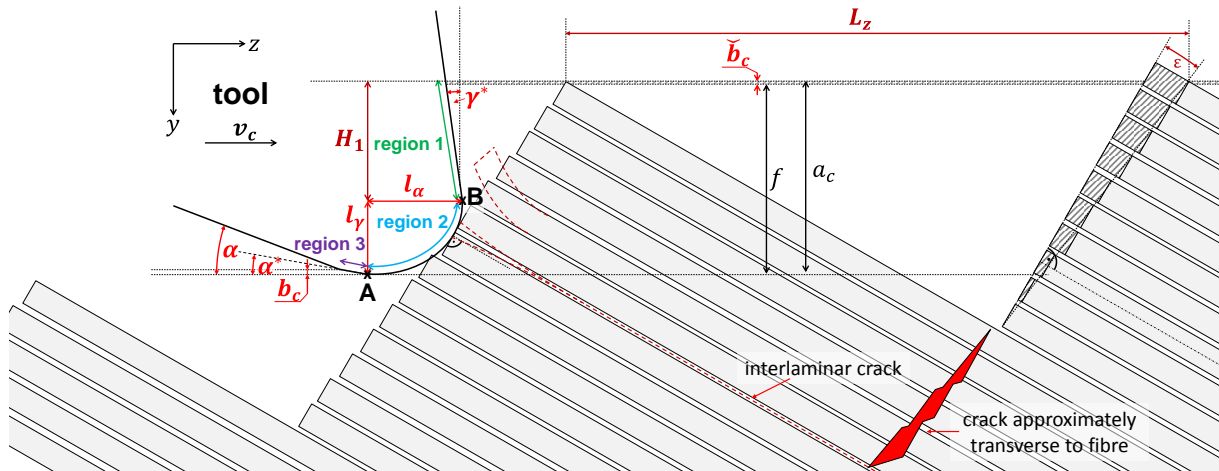


Figure 5.23: Schematic representation of the contact conditions for $\theta = 150^\circ$ with saw tooth topography on surface

5.4.1 Modelling

Modelling of region 1:

Figure 5.24 shows the explicit cutting conditions in region 1 (rake face) of the tool during machining of $\theta = 150^\circ$ UD material. The checkered area in the background represents the saw teeth topography. Starting from the foremost point B in cutting direction of the tool, one fibre gets first in contact with the rake face (*region 1*). This single fibre in point B is modelled, being surrounded by matrix material (RVE) and placed on an elastic foundation, which is caused by the supporting fibres behind. The amount of the elastic foundation factor $k_{m,0}$ (first saw teeth) and $k_{m,1}$ (second saw teeth) depends on the number of supporting fibres, which is influenced by the feed rate f , the fibre orientation θ and the position of the contact point B , described by l_γ .

$$k_{m,0} = \hat{k} \frac{H_{1.1}}{2 \cdot r_f} = \hat{k} \cdot \frac{(f - l_\gamma) / \cos(180^\circ - \theta)}{2 \cdot r_f},$$

$$k_{m,1} = \hat{k} \frac{H_{1.2}}{2 \cdot r_f} = \hat{k} \cdot \frac{\frac{f - l_\gamma}{\cos(180^\circ - \theta)} + L_z \cdot \sin(180^\circ - \theta)}{2 \cdot r_f} \quad (104)$$

In these equations \hat{k} represents the normalized elastic foundation factor for a single fibre and in the considered range it is assumed to be linearly correlated to the number of supporting fibres behind. The fraction in (104) represents the number of fibres per saw teeth. The foundation factor \hat{k} is a fitting variable and in general much lower compared to the foundation factors in the before presented sub-models, where the load on the fibre is directed inside the workpiece material with multiple supporting fibres layers, instead of pointing to the material surface with just a few supporting layers.

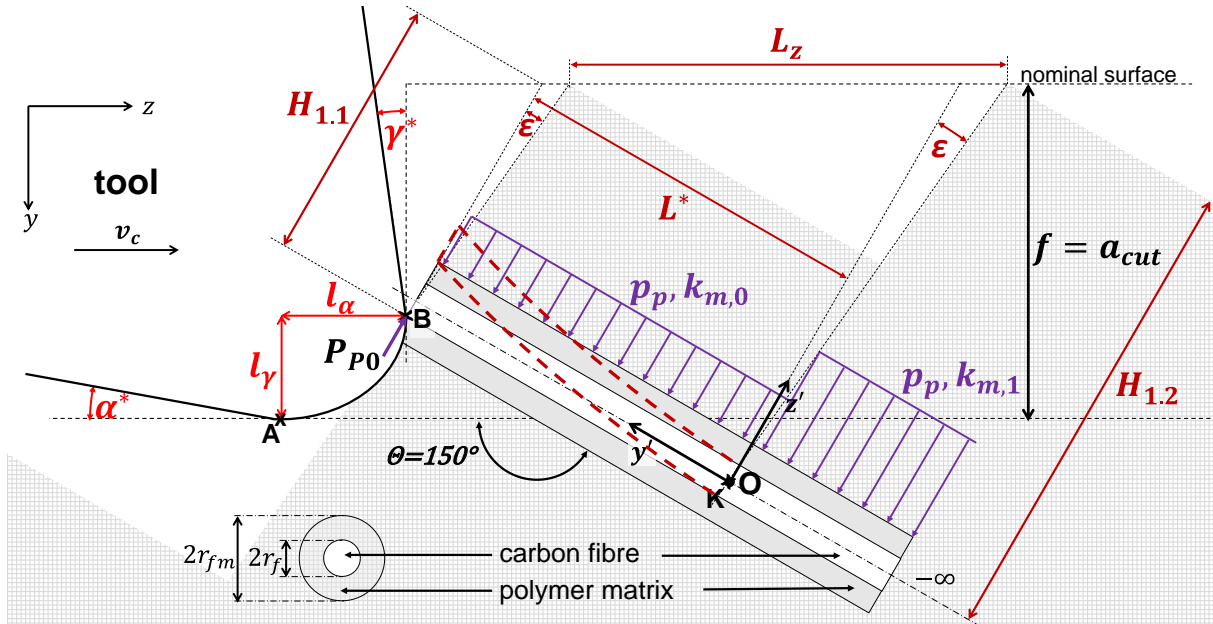


Figure 5.24: Schematic representation of the contact conditions for $\theta = 150^\circ$ in region 1

With progressing cutting motion the fibre in contact with *region 1* of the tool is bend and slides along the rake face. Analogue to the sub-models for the interval I ($\theta = 0^\circ$) and interval II ($15^\circ \leq \theta < 75^\circ$), firstly a function for the fibre transverse displacement is determined by means of a total potential energy Π approach. It is assumed that the carbon fibre in contact with region 1 is exclusively loaded in bending and the surrounding matrix-material in shear. Applied to these boundary conditions the total potential energy is

$$\Pi = \frac{1}{2} \int_0^{L^*} E_{f2} I_f \left(\frac{d^2 \omega}{dy'^2} \right)^2 dy' + \frac{1}{2} A_m G_m \left(\frac{r_{fm}}{r_f} \right)^2 \int_0^{L^*} \left(\frac{d\omega}{dy'} \right)^2 dy' - P_{P0} \omega |_{y'=L^*} + \left[k_{m,0} \int_0^{L^*} \omega dy' \right], \quad (105)$$

in which the four summands describe the bending energy of the fibre, the shear energy in the matrix, the energy due to external load and the energy by passive force from the elastic foundation. A_m and r_m are calculated as explained in 5.2 by (47) and (48). The fourth summand in (105) (square brackets) is based on the WINKLER's [248] elastic foundation model.

The origin O in the proposed y'/z' -coordinate system in Figure 5.24 is defined as being in a distance of L^* from the free end. This variable L^* describes the distance from the contact point B to the expected fibre bundle crack position ($y' = 0$). According to analyses in the thesis of HENERICHS [101], L^* has a rather constant periodicity for machining with one tool-material combination and depends on L_z , f and the fibre orientation θ . HENERICHS [101] analysed the chip formation mechanisms for $\theta = 150^\circ$ in detail based on micrographs, high speed camera analyses and SEM images. Figure 5.25 shows a comparison of the influence of different tool geometries on the saw teeth size. According to the analyses the bend fibres break at L^* due to the effect of notches and reduced back-support by behind fibres by the saw teeth topography.

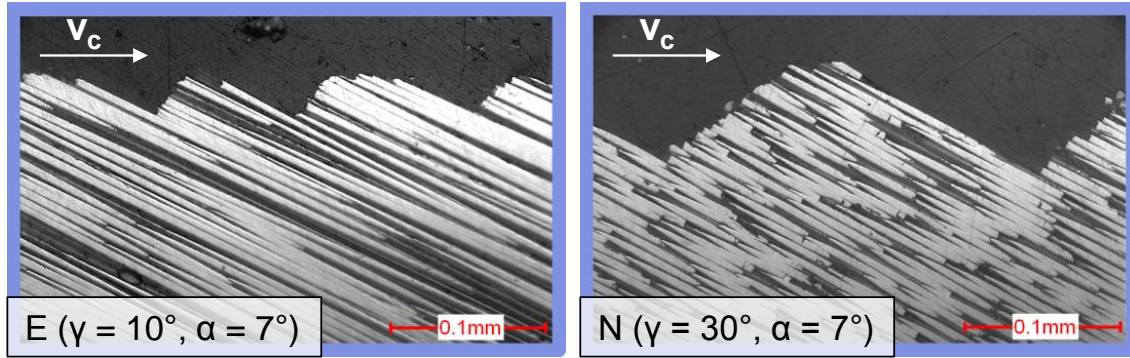


Figure 5.25: Micrographs of UD CFRP surface perpendicular to cutting velocity for Tool E ($\gamma = 10^\circ$, $\alpha = 7^\circ$) (left) and Tool N ($\gamma = 30^\circ$, $\alpha = 7^\circ$) (right) in $\theta = 150^\circ$ material; $v_c=90$ m/min and $f=0.03$ mm/rot, according to HENERICHS [101]

Based on these analyses the influence of the tool rake angle, flank angle as well as the cutting speed and feed on the saw tooth size L_z have been described for $\theta = 150^\circ$. The correlation function by HENERICHS [101]

$$L_z = 0,0447 \cdot e^{0,00545 \cdot v_c} + 0,0441 \cdot e^{28,9325 \cdot f} + 0,0028 \cdot \gamma - 0,0002 \cdot \alpha - 0,083 \quad (106)$$

proved to be valid, in which the feed rate and the rake angle have the largest influence on L_z . The following equation gives the geometrical correlation between L^* and L_z

$$L^* = \cos(180^\circ - \theta) \cdot L_z \quad , \quad (107)$$

under neglect of the slight tilting ε of the saw teeth. Consequently, one value of L^* can be determined for a certain tool geometry, fibre orientation and process parameter combination.

In this model the transverse displacement of the RVE is defined in positive z' direction. The differential equation for the transverse displacement is calculated by means of the RITZ method applied to the total potential energy in (105) with the basis function

$$\omega = a_1 y'^2 + a_2 y'^3 \quad , \quad (108)$$

which has already been chosen by XU et al. [258] to describe a bending beam of similar shape. By means of this RITZ method the variables a_1 and a_2 are determined in a way that the potential energy in (105) is minimal. Therefore, the basis function and its differentiations are inserted in the potential energy equation (105) and this term is first differentiated with respect to a_1 and then to a_2 to find the minimum. For the failure criterion at crack initiation it is necessary to describe the curvature c_{cur} of the fibre. The exact solution of the curvature c_{cur} of the bending beam

$$c_{cur} = -\frac{M(y')}{EI} = \frac{\omega''(y')}{\left(1 + (\omega'(y'))^2\right)^{\frac{3}{2}}} = \frac{2a_1 + 6a_2 y'}{\left(1 + (2a_1 y' + 3a_2 y'^2)^2\right)^{\frac{3}{2}}} \quad (109)$$

is applied. Fibre failure occurs precisely when the induced tension at the edge of the carbon fibre in the point of maximum curvature $c_{cur,max}|_{y'=0}$ exceeds the tensile strength σ_{T_f} of the fibre

$$E_{f1} \cdot r_f \cdot c_{cur,max}|_{y'=0} - \sigma_{T_f} = 0 \quad . \quad (110)$$

For the given boundary conditions, the maximum curvature occurs exactly at $y' = 0$, shown in Figure 5.26, while the bending force P_{P_0} acts on the fibre in $y' = L_0$. This figure shows an exemplary deflection function and curvature for one tool-, fibre orientation- and process-parameter-combination at fibre failure. It is assumed in the analytical force model that the residual fibres of the bend fibre bundle fail concurrent, as soon the first fibre in contact with the cutting edge fails.

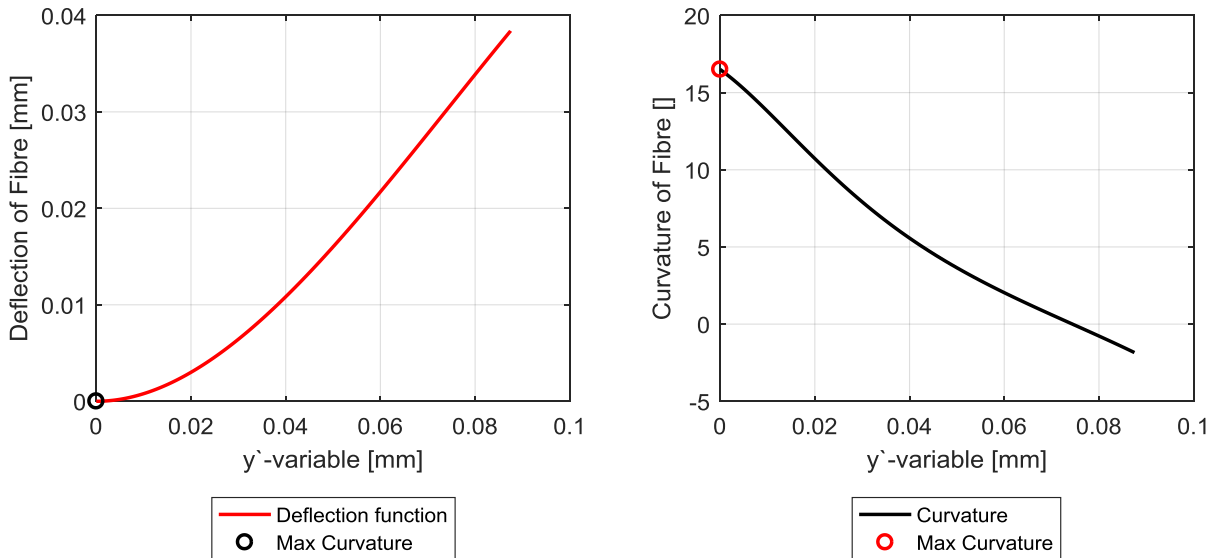


Figure 5.26: Exemplary deflection function and curvature for the Tool E ($10^\circ/7^\circ$) in $\theta = 150^\circ$ material; $v_c=90$ m/min and $f=0.03$ mm/rot

This failure criterion leads to a critical bending force $P_{P_0,cr}$ for crack initiation. Although the equation (110) cannot be solved mathematically for $P_{P_0,cr}$, this value can be determined numerically in Matlab. Therefore the iterative approach, shown in Figure 5.27 is applied. In doing so the bending force is incrementally increased, starting from P_{P_0} close to zero until the critical tension $\sigma_{T,f}$ at the edge of the loaded fibre is exceeded.

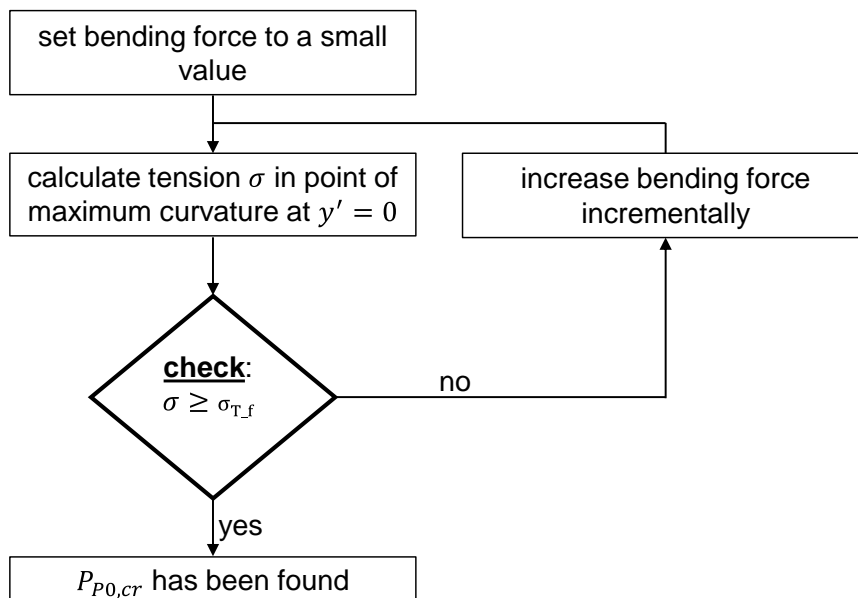


Figure 5.27: Schematic representation of iterative approach to calculate the force $P_{P_0,cr}$

P_{P0_cr} is the maximum force on the tool during fibre failure. To evaluate the average force during machining process until crack initiation in K , a linear force increase is assumed the same way as in the before mentioned sub-models. Thus \bar{P}_{P0} can be described as

$$\bar{P}_{P0} = \frac{1}{2} P_{P0_cr} . \quad (111)$$

Due to the saw teeth topography of the UD CFRP material surface, a local point of the cutting edge is discontinuously in contact with the material. The contacting share K_c during cutting motion from one tooth to the next one under consideration of the fibre deflection ($\omega_0 = z' |_{y'=L_0; P=P_{P0_cr}}$) at crack initiation is calculated by

$$K_c = \frac{\omega_0 \cdot (\sin(180^\circ - \theta) + \cos(180^\circ - \theta) \cdot \tan \gamma)}{L_z} . \quad (112)$$

Subsequently, the total forces on the tool are calculated by averaging over the workpiece width b under consideration of the RVE diameter ($2 \cdot r_{fm}$). Furthermore, friction between the cutting edge and the carbon fibre is considered by means of *Coulomb friction* (μ), since the fibre slides along the rake face with progressing cutting motion until it fails. The resulting total force is decomposed vectorially into the feed and cutting force components

$$\begin{aligned} F_{I2_R2.1_z} &= (\bar{P}_{P0} \cdot [\mu \cos(\theta - \gamma - 90^\circ) \cdot \sin(\gamma) + \cos(\theta - 90^\circ)]) \cdot K_c \cdot \frac{b}{2 \cdot r_{fm}} , \\ F_{I2_R2.1_y} &= (\bar{P}_{P0} \cdot [\mu \cos(\theta - \gamma - 90^\circ) \cdot \cos(\gamma) - \sin(\theta - 90^\circ)]) \cdot K_c \cdot \frac{b}{2 \cdot r_{fm}} . \end{aligned} \quad (113)$$

Modelling of region 2:

The UD fibres being in contact with the cutting edge rounding are mostly loaded in compression. Thus the predominant fibre failure mechanism in region 2 is micro-buckling. Figure 5.28 shows the idealised contact conditions for a slightly worn cutting edge in contact with material with $\theta = 150^\circ$. According to the detailed derivation in 5.1, the load in region 2 of the tool may be calculated by

$$\bar{P}_{mb} = 0.5 \cdot b \cdot H_2 \cdot \sigma_{mb} , \quad (114)$$

in which σ_{mb} is evaluated with equation (27) and H_2 is geometrically given by

$$H_2 = l_\alpha \cdot \sin(180^\circ - \theta) + l_\gamma \cdot \cos(180^\circ - \theta) . \quad (115)$$

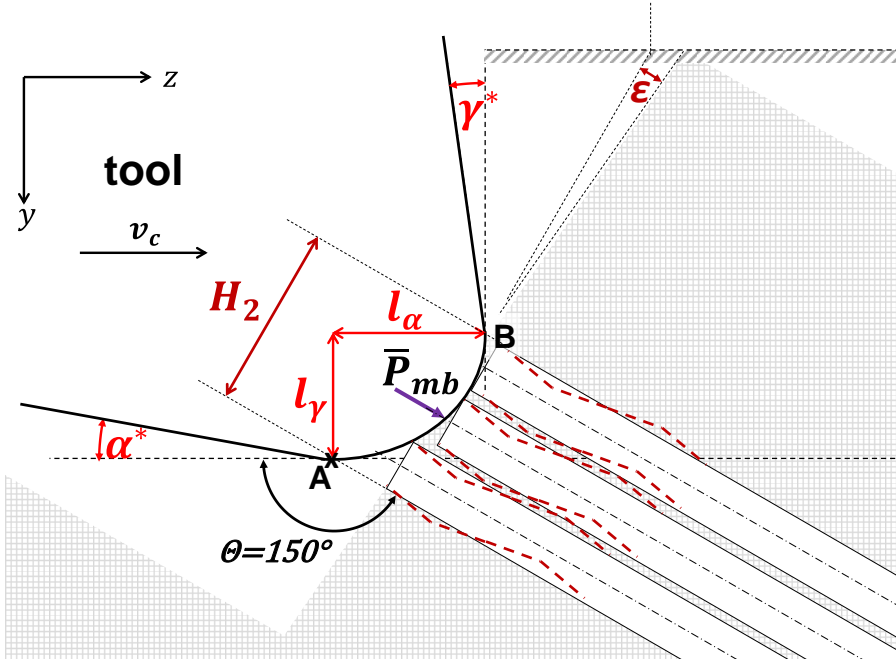


Figure 5.28: Schematic representation of the contact conditions for $\theta = 150^\circ$ in region 2

Based on the equation (114) and (115), a vectorial decomposition of the resulting force gives the components in feed and cutting velocity direction for the interval IV ($105^\circ + \gamma \leq \theta < 165^\circ$) in region 2.

$$\begin{aligned} F_{I4_R2_z} &= \bar{P}_{mb} \cos(180^\circ - \theta) = 0.5 \cdot b \cdot H_2 \cdot \sigma_{mb} \cdot \cos(180^\circ - \theta) \\ F_{I4_R2_y} &= \bar{P}_{mb} \sin(180^\circ - \theta) = 0.5 \cdot b \cdot H_2 \cdot \sigma_{mb} \cdot \sin(180^\circ - \theta) \end{aligned} \quad (116)$$

Modelling of region 3:

The detailed tool wear analysis, exemplarily presented in Figure 4.13, shows very little tool wear along the flank face when machining fibre orientations in the interval IV ($105^\circ + \gamma \leq \theta < 165^\circ$). This is because the flank face rather faces away from the fibre axes. Consequently, contact effects in region 3 of the cutting edge are neglected for force modelling in this sub-model. Thus, the total thrust and cutting forces for the fibre orientation interval IV ($105^\circ \leq \theta < 165^\circ$) are determined by superposing the force components in z- and in y-direction [(113), (116)] in the first two regions

$$\begin{aligned} F_{I4_z} &= F_{I4_R1_z} + F_{I4_R2_z} \\ F_{I4_y} &= F_{I4_R1_y} + F_{I4_R2_y} \end{aligned} \quad (117)$$

5.4.2 Results of sub-model $105^\circ + \gamma \leq \theta < 165^\circ$

An overview of the material data, process parameters and fitting variables used for the $105^\circ + \gamma \leq \theta < 165^\circ$ model is given in the appendix A.3. The normalised *winkler*-constant \hat{k} is a fitting variable, describing the supporting effect to the RVE by the behind CFRP material. Other fitting variables are the strain rate dependent material properties $\sigma_{T,f}$, E_m and the RVE dimensions, which were chosen the same way as in the before described sub-models. Fitting of this sub-model to the experimental data is rather difficult, because only limited experimental data is available for one fibre orientation of $\theta = 150^\circ$. As explained in detail in the thesis of HENERICHS [101], scheduled experiments with deviating fibre orientations, such as $\theta = 120^\circ$ failed with the fundamental experiment setup. Consequently, micro-geometrical tool wear data as well as CFRP surface topography data is only available for $\theta = 150^\circ$. Therefore, a further analysis is carried out by means of micrographs of drilled bores in UD CFRP material to validate the existence of the saw teeth topography for a certain fibre orientation range. It has been made use of the fact that during the drilling process, each fibre orientation occurs twice during one rotation of the tool. Figure 5.29 (left) shows an exemplary micrograph of a section of the bore edge with apparent saw teeth. For several bores the saw teeth distribution over the fibre cutting angle has been measured and evaluated to a total distribution in the diagram in Figure 5.29. Generally saw teeth are identified from $\theta = 119^\circ$ to $\theta = 170^\circ$ with a maximum probability for the range of $145^\circ < \theta < 153^\circ$. Obviously, despite the support effect of fiber layers below or above this analysed layer, saw teeth occur. Although these surface topography data of drilling operations cannot be directly compared with the fundamental turning operations, it gives an indication. Based on this analysis, in the validity range of the sub-model $105^\circ + \gamma \leq \theta < 165^\circ$ it is highly probable that saw teeth occur. No conclusions can be drawn about the size L_z of the saw teeth.

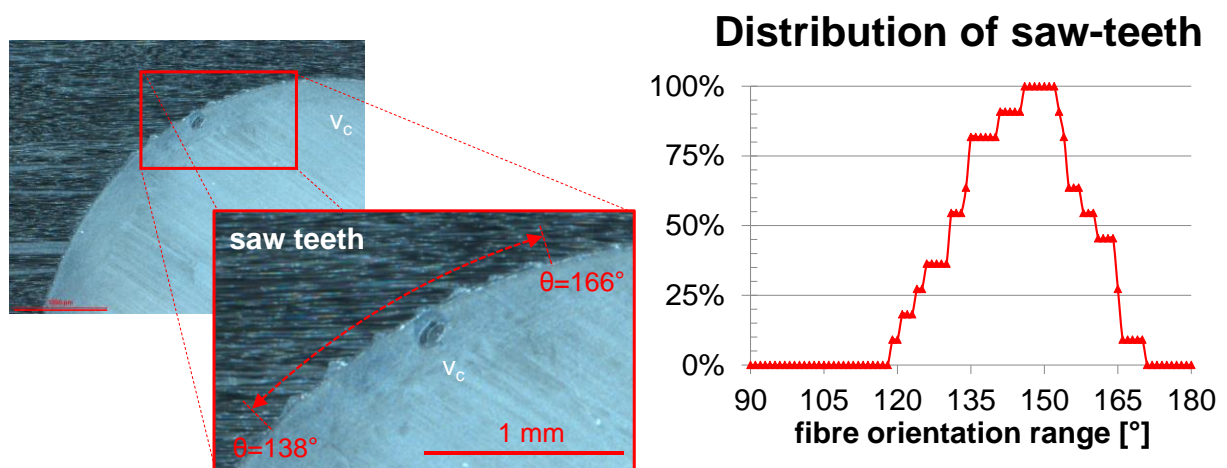


Figure 5.29: Exemplary micrograph of bore and analysis of saw-teeth distribution of several bores ($\varnothing=6.35$ mm) in UD CFRP material

The two diagrams in Figure 5.30 show the simulated forces (solid lines) compared to the measured data for the geometry of Tool H ($10^\circ/14^\circ$) in $\theta = 150^\circ$ material. Additional results for two further tool geometries are presented in the Appendix A.8. The feed and thrust forces are generally of the right magnitude, which is on a much lower level compared to the other fibre orientations. Despite the fact that there is few experimental data to fit the model, the force profile is represented well both for the feed force and the cutting force. The rather small absolute force increase, compared to $0^\circ \leq \theta < 90^\circ$ is due to the small change of

micro-geometry (tool wear). It is striking that the thrust force generated in region 1 of the tool is negative, due to the positive rake angle and the orientation of the fibres. It can thus be understood that the tool is pulled into the workpiece by the force in this region 1. In combination with the thrust forces generated by micro-buckling this leads to an in total slightly positive thrust force.

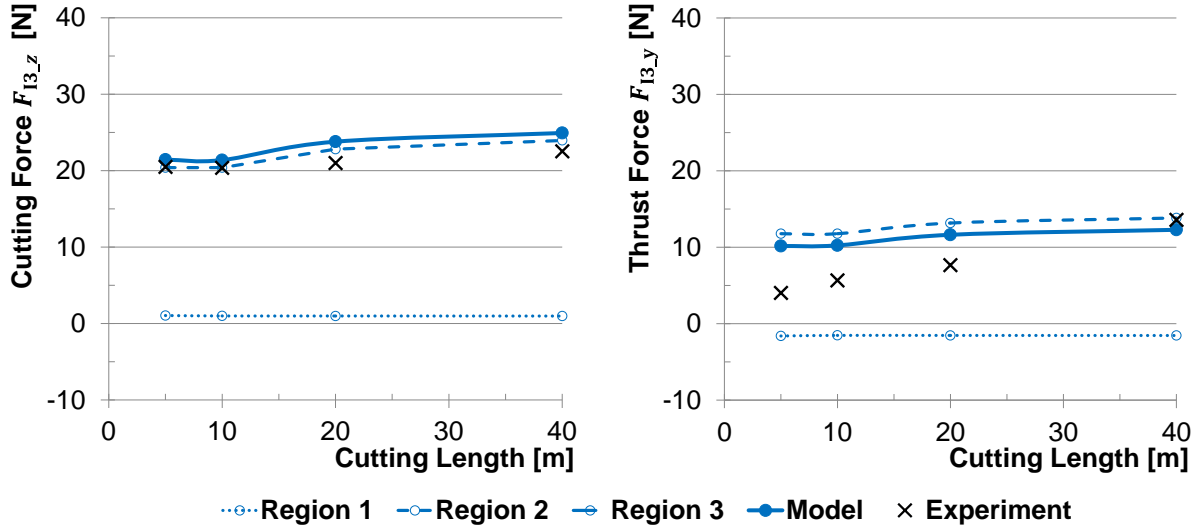


Figure 5.30: Comparison of cutting and thrust forces between model and experiment for the Tool H ($10^\circ/14^\circ$) in $\theta = 150^\circ$ material; $v_c=90$ m/min and $f=0.03$ mm/rot

5.5 Interconnecting sub-models to overall force model

Combining the separately presented sub-models $\theta = 0^\circ$, $15^\circ \leq \theta \leq 75^\circ$, $\theta = 90^\circ$ and $105^\circ + \gamma \leq \theta \leq 165^\circ$ and additionally linearly interpolating in the fibre-orientation-gaps in between gives a total force model for CFRP machining. The exemplary results for a fibre orientation range from $\theta=0^\circ$ to $\theta=90^\circ$ are presented in Figure 5.31 and from $\theta=90^\circ$ to $\theta=180^\circ$ in Figure 5.32. Two different wear states at $l_c=5$ m and at a more intensively worn state $l_c=40$ m are presented. The linear interpolations in between the sub-models are marked by black dashed lines. The gaps between the sub-models are necessary because the modelling approach of sub-model 2 shows mathematic poles at the edges and sub-model 4 is only valid for CFRP surfaces with saw teeth topography, as being explained in the corresponding paragraphs 5.2 and 5.4. In most cases, the interpolations represent a smooth transition between two adjacent sub-models. The only conspicuous exception for the first three force sub-models is the cutting force of Tool E at $l_c=40$ m with an uneven change in slope. In general the simulations with the overall force model are in fairly good correlation to the measured forces. These results prove that the limitation of sub-model 2 to a range of $15^\circ \leq \theta \leq 75^\circ$ and sub-model 4 to a range of $105^\circ + \gamma \leq \theta \leq 165^\circ$ is a suitable choice.

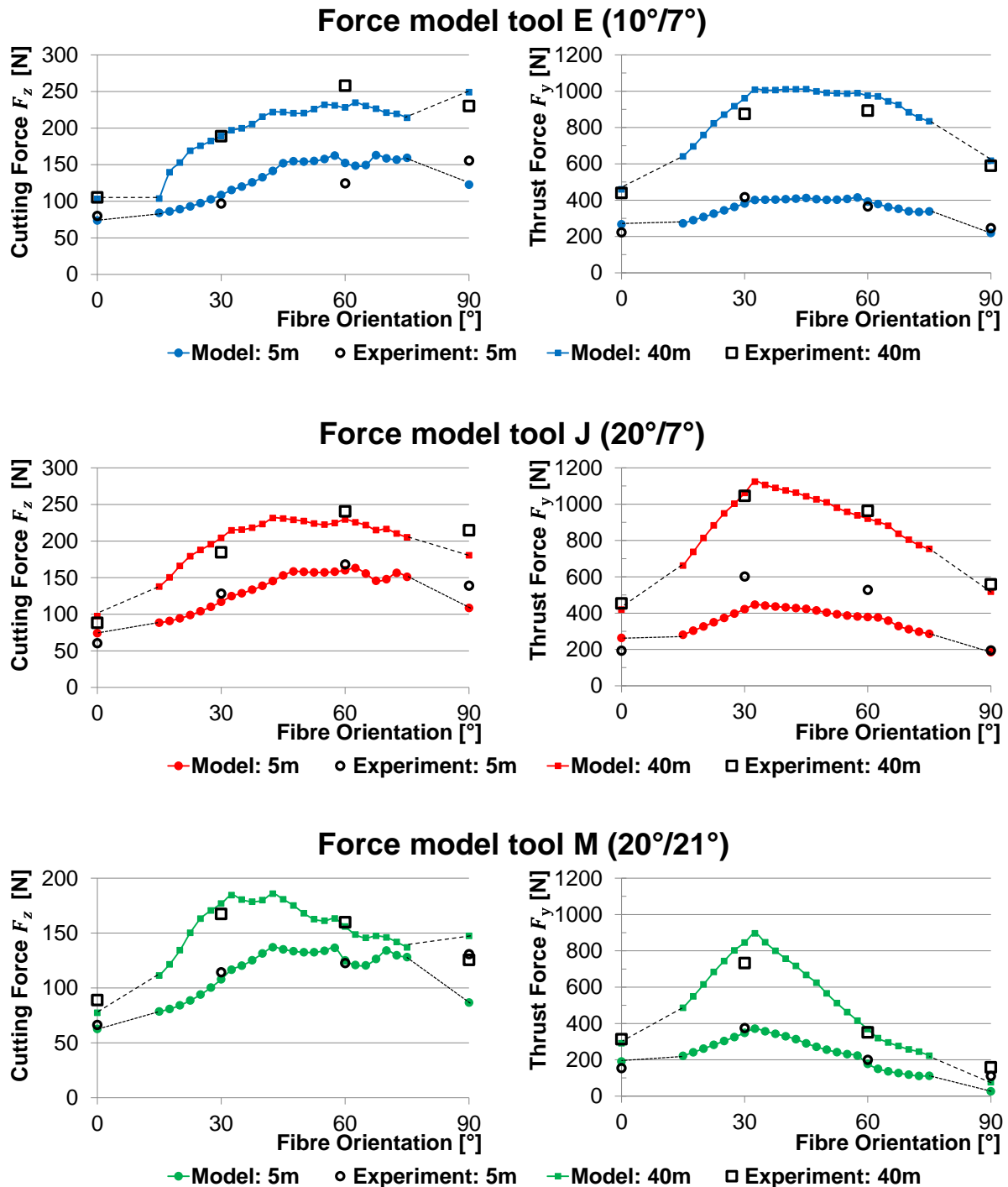


Figure 5.31: Total CFRP machining force model, applied to three different tool geometries for each model over a fibre orientation range of $0^\circ \leq \theta \leq 90^\circ$.

In the case of the sub-model 4 ($105^\circ + \gamma \leq \theta \leq 165^\circ$), shown in Figure 5.32, it needs to be considered that slightly different tool geometries are compared in this diagram: Tool E (10°/7°) and Tool J (20°/7°) for $\theta=90^\circ/180^\circ$ as well as Tool H (10°/14°), Tool I (10°/21°) and Tool L (20°/14°) for $105^\circ + \gamma \leq \theta \leq 165^\circ$. However, since the flank angle has only a slight influence in sub-model 4, this comparison is acceptable. Furthermore, it needs to be considered that the presented simulation of sub-model 4 bases on the tool wear data at $\theta=150^\circ$ (Appendix A.1), because only one interpolation point is available due to failed workpiece material at $\theta=120^\circ$. This missing tool wear parameters at different fibre orientations are expected to be the main reason for potential deviations in the transition

areas of this sub-model. The partly sharp transitions between the adjacent sub-models in Figure 5.32 are also due to changed chip formation mechanisms: It is expected that at these transitions at the margins of sub-model 4 ($105^\circ + \gamma \leq \theta \leq 165^\circ$) no saw teeth are mapped into the CFRP surface. These effects would result in increasing forces because bending of the fibre bundles along the rake face (region 1) would be more difficult due to larger elastic foundation effects.

In summary, the overall model considers the actually occurring effects and depicts the experimental measured forces very well.

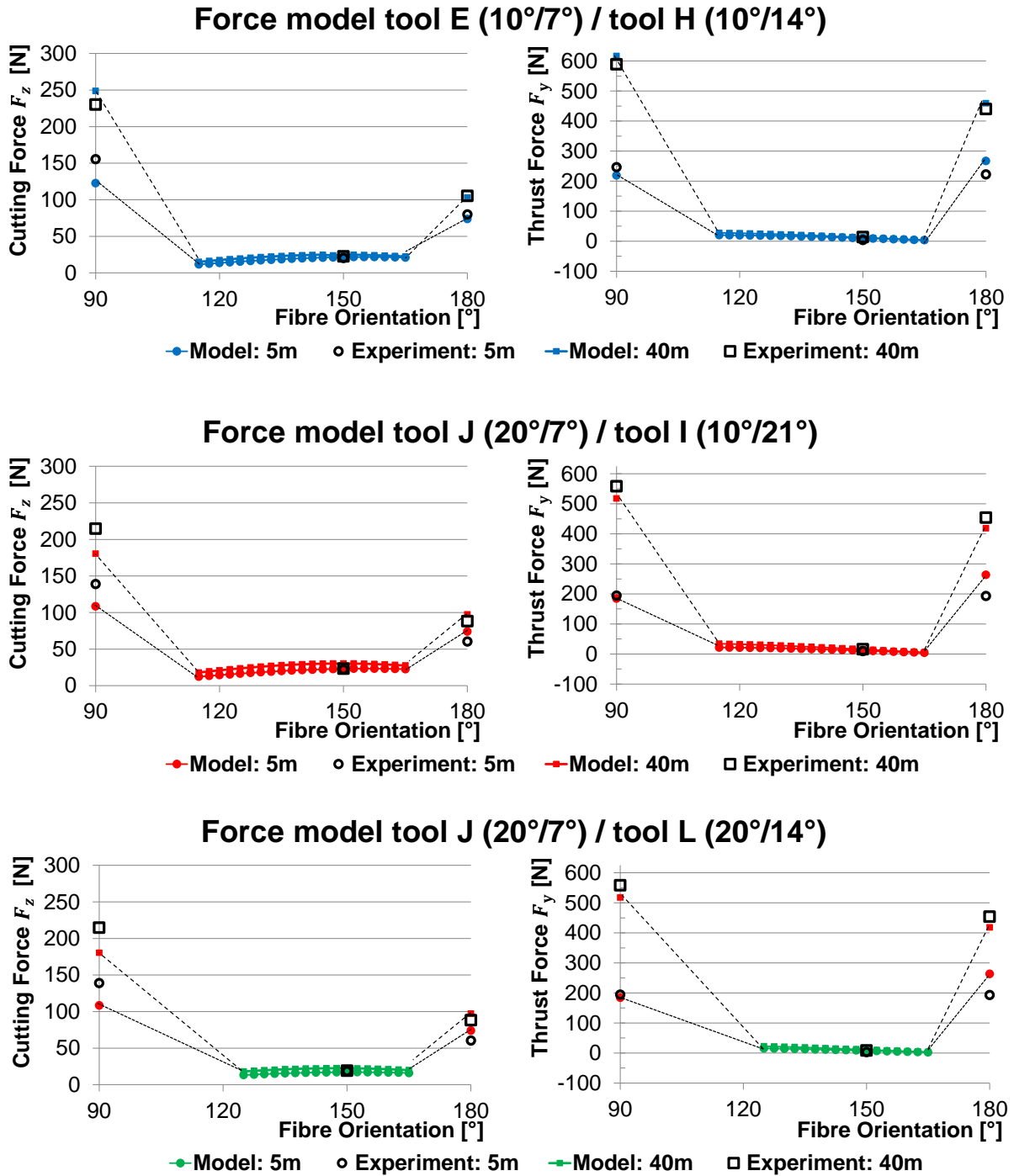


Figure 5.32: Total CFRP machining force model, applied to two different tool geometries for each model over a fibre orientation range of $90^\circ \leq \theta \leq 180^\circ$.

5.6 Conclusion and transferability of model to drilling operation

In the proposed analytical force model the main influencing parameters «fibre orientation», «material properties», «tool geometry» and «tool wear» as well as «feed rate» are considered. In contrast to existing models, the fibre orientation range from $0^\circ \leq \theta \leq 180^\circ$ is subdivided into four separate models, since distinct cutting mechanisms occur depending on the fibre orientation. The following intervals with each similar cutting mechanisms have been identified:

- $\theta = 0^\circ$
- $15^\circ \leq \theta \leq 75^\circ$
- $\theta = 90^\circ$
- $105^\circ + \gamma \leq \theta \leq 165^\circ$

For each of these intervals a separate micro-mechanical force model is developed, considering the respective cutting mechanisms. The modelling methods are based on fundamental approaches by ZHANG et al. [242, 269, 270], QI et al. [177], XU and ZHANG [257, 258] as well as XU and REIFSNIDER [259]. One of the features adopted is the subdivision of the cutting edges into three regions, as being initially proposed in the approach of ZHANG et al. [242, 269, 270]. Finally, the resulting force on the tool is calculated by superposing the individual forces in each region.

In interval I ($\theta = 0^\circ$), the fibres in contact with the rake face and in the upper part of the cutting edge rounding are stressed axially in compression, resulting in so called *micro-buckling*. This effect is modelled according to the approach of XU and REIFSNIDER [259]. In the lower part of the cutting edge rounding and along the flank face, the material is compressed. This load situation is modelled according to the approach of ZHANG et al. [242, 269, 270] by means of contact mechanical equations representing a cylinder and wedge in contact with half-space. The modelling approach for region 3 (flank face), where spring-back effects occur is the same for the first three sub-models.

For fibre orientations in the interval II ($15^\circ \leq \theta \leq 75^\circ$), the first contact between fibres and the cutting edge is in region 2 (cutting edge rounding). The forces acting on the cutting edge by fibre bending in region 2 are determined by means of the beam theory in combination with an elastic foundation according to the approach of QI et al. [177]. The initial fibre separation is introduced by exceeding the tensile strength at the outer edge of the carbon fibre. Furthermore, it is considered that the lower part of the initially separated fibre is bent in cutting direction and potential further fractures occur. The upper part of the initially separated fibre is evacuated along the rake face by introducing interlaminar shear cracks. This effect is modelled in accordance with previous modelling approaches by ZHANG et al. [242, 269, 270], QI et al. [177] as well as results from experiments by RUMMENHÖLLER [193], SHEIKH-AHMAD [205], TAKEYAMA and IJIMA [213].

In interval III with a fibre orientation of $\theta = 90^\circ$, the carbon fibers are stressed locally in transverse direction to the fibre axis so that the fibre fails by exceeding the compressive strength. This effect is modelled in accordance to XU and ZHANG [257, 258] with a half-infinite bending beam on elastic foundation. Analogous to the modelling approach for $15^\circ \leq \theta \leq 75^\circ$, it is considered that the lower parts of the initially separated fibres, which are still attached to the workpiece, are bent further and potential further fractures occur.

In the fibre orientation interval IV ($105^\circ + \gamma \leq \theta \leq 165^\circ$), where the fibres are directed towards the rake face of the tool, two main effects are considered: Firstly, bending of the fibres in contact with the rake face and simultaneously introducing an interlaminar crack until spontaneously the bending strength of a fibre bundle is exceeded. This effect results in a saw-teeth topography of the machined CFRP surface and is modelled in accordance with Xu and Zhang [258]. Secondly, compression of single fibres in axial direction by the cutting edge rounding, which is modelled by so called *micro-buckling*.

As mentioned in the corresponding paragraphs 5.1 to 5.4, some fitting variables are necessary for the model. Table 5.2 shows an overview of these variables, sorted by sub-Model and region where it is applied. Most of the variables are necessary due to a lack of information on the strain rate dependency of the material properties $K_{\sigma_{Tf}}$, $\sigma_{Pr_{cr}}$, K_{Em} . Others describe geometrically the transition from *micro-buckling* to pressing at the cutting edge rounding in region 2 ($H_{2.2}$) or the effect of fibres being out of contact with the cutting edge after micro-buckling (K_f). The cushion factor of the elastic foundation (k_{cush}) is fitted to the measurement results as well as the critical deflection ($\omega_{Z''_{cr}}$) at which interlaminar fibre/matrix cracks occur in the $\theta = 90^\circ$ model. In sub-Model four, a linear correlation between the size of the saw teeth and the support of the elastic foundation is assumed, modelled by the normalised elastic foundation factor (\hat{k}). Finally, the *Young's* modulus (E_{c3}) of the pre-damaged CFRP material being in contact in region 3 of the cutting edge is adjusted to the measurement data. A detailed overview of the optimum fitting values and data from literature is presented in the appendix A.3.

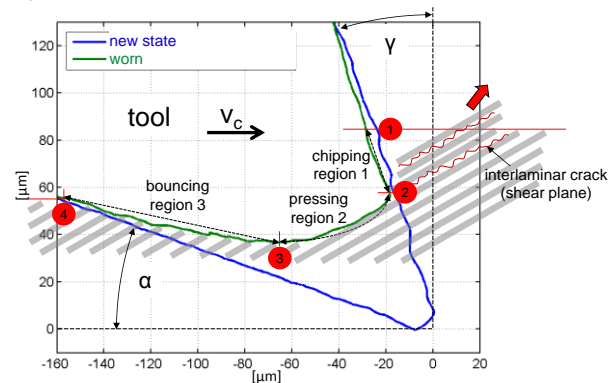
Table 5.2: Fitting variables for force model, ordered by sub-models

	$\theta=0^\circ$	$15^\circ \leq \theta \leq 75^\circ$	$\theta=90^\circ$	$105^\circ + \gamma \leq \theta \leq 165^\circ$
region 1	- correction factor micro-buckling (K_f)	/	/	- WINKLER'S elastic foundation factor \hat{k}
region 2	- height sub-region 2.2 ($H_{2.2}$) - correction factor micro-buckling (K_f)	- dimensionless cushion factor (k_{cush}) for elastic foundation	- critical deflection ($\omega_{Z''_{cr}}$) for interlaminar fibre/matrix crack	/
region 3	- <i>Young's</i> Modulus of predamaged CFRP (E_{c3})	- <i>Young's</i> Modulus of predamaged CFRP (E_{c3})	- <i>Young's</i> Modulus of predamaged CFRP (E_{c3})	/
general	- factor tensile strength of fibre ($K_{\sigma_{Tf}}$) [influence strain rate] - compr. strength of fibre ($\sigma_{Pr_{cr}}$) [influence strain rate] - factor <i>Young's</i> modulus matrix (K_{Em}) [influence strain rate]			

It was found that the simulated forces with the overall force model are in fairly good correlation to the measured forces, with outliers occurring naturally. It is well known from the further advanced force modelling in metal machining that none of the existing models is universally accurate in predicting the forces; but nevertheless these works are valuable for the optimisation of machining processes and the prediction of material behaviour. The resulting data from the proposed force model gives information regarding the origin of the process forces along the cutting edge, subdivided into region 1 to region 3. Furthermore, the model enables to show causality correlations. In these respects, the model is superior to experimental measurements, which cannot give such information easily.

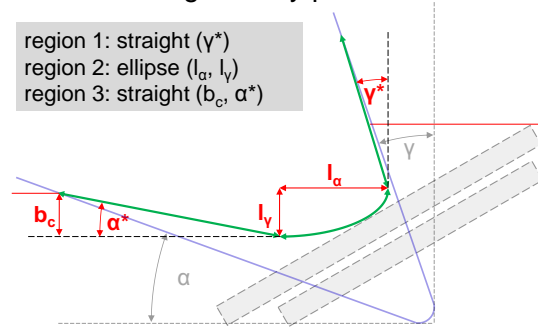
Furthermore, the proposed analytical force model for CFRP machining is characterised by considering tool wear in an absolutely new way by five elementary wear parameters. Applied to an orthogonal cutting operation, the results confirm that the model is significantly more accurate compared to existing models which only consider tool wear in form of a single cutting edge radius. The approach is practicable, since «straight-line – ellipse – straight-line» is intuitive and mathematically still handle-able. Figure 5.33 shows that the tool wear characterisation by the five micro-geometry parameters l_α , l_γ , γ^* , α^* , b_c is even transferable to diamond-coated cutting edges in CFRP machining. As long no local break-outs of the coating occur, the intensively worn diamond-coated cutting edges are characterised by a large region 3, due to a small adjusted clearance angle α^* in combination with b_c . The size of region 1 depends on the feed rate and the size of l_α as well as l_γ become very small. Consequently, the cutting edge rounding (region 2) has a lower influence on the total forces. However, the proposed force model is still valid for diamond-coated tools because the different boundary conditions compared to uncoated tools are considered in the simulation by means of the adjusted micro-geometry. In order to prevail the proposed micro-geometry description by regular measurements, a tool wear model has to be developed in future so that wear measurements are no longer necessary.

Typical tool wear of uncoated tool

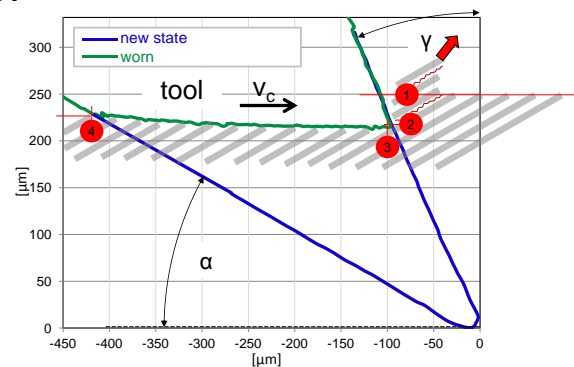


micro-geometry parameters

region 1: straight (γ^*)
 region 2: ellipse (l_α , l_γ)
 region 3: straight (b_c , α^*)



Typical tool wear of diamond-coated tool



micro-geometry parameters

region 1: straight (γ^*)
 region 2: ellipse (l_α , l_γ)
 region 3: straight (b_c , α^*)

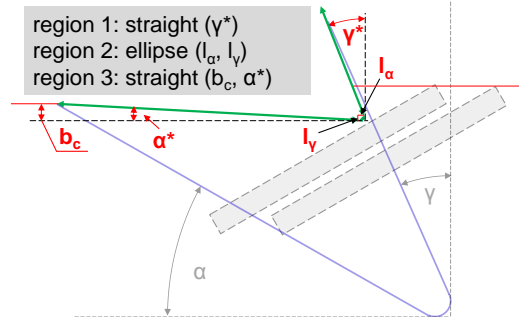


Figure 5.33: Transfer of five proposed *micro-geometry* wear parameters to diamond-coated tool

It is conceived that in future this fundamental force model for orthogonal machining of constant fibre orientations can be adapted for drilling operations. The conditions at a cutting edge in drilling differ from turning of UD-CFRP material by constantly changing fibre orientations in a range of $0^\circ \leq \theta \leq 180^\circ$ with certain tool setting and inclination angles, dissimilar cutting speeds as well as cutting paths along the cutting edge and adverse chip transport in the chip flute of a drill.

The constantly changing fibre orientations at a specific position of the cutting edge can be considered with this approach by incrementally calculating the forces for the currently aligned fibre orientation. The consideration of the setting and inclination angles will make additional experimental approaches necessary, comparable to the ones presented by SCHÜTTE [204]. A dissimilar cutting speed, which is maximum at the cutting edge corner and decreases to zero in the direction of the drill centre, influences the strain rate dependent material properties. Consequently, the correction factors of the material properties, which are implemented as fitting variables $K_{\sigma_{Tf}}$, $\sigma_{Pr_{cr}}$, K_{Em} in the model, have to be adjusted. For higher strain rates in the outer part of the cutting edge, these factors are expected to have higher values. Consistent to the cutting speed, the cutting path of a certain position of a cutting edge decreases linearly from the corner to the centre of the drill. According to SHEIKH-AHMAD [205] the dominant form of tool wear in CFRP cutting is gradual soft abrasion, erosion and micro-fractures, which mechanically remove micro-particles. It leads to edge rounding during relative motion of the material along the cutting edge and depends linearly on the bulk hardness. Accordingly, the wear at a certain position of the cutting edge primarily depends on the relative cutting length in material contact. Therefore, a variable cutting path may be considered in the proposed force model for drilling by means of the actual cutting edge *micro-geometry*. It is expected that l_{α} , l_{γ} and b_c generally increase, while α^* and γ^* decrease in direction of the cutting edge corner (maximum cutting path). Besides the dissimilar cutting paths, also the unfavourable chip transport in the flute of the drill will be considered by adversely adjusted *micro-geometry* wear parameters.

Drilling experiments with diamond-coated cutting tools, which are presented in detail in paragraph 7, partially show additional wear effects at the cutting edge corner to the ones mentioned by SHEIKH-AHMAD [205] (Soft abrasion, erosion and micro-fractures). Although the expected gradually increasing wear occurs at the chisel edge and partly along the main cutting edge, sometimes certain effects stabilise the diamond coating in the area of the cutting edge corner, shown exemplarily in red in Figure 5.34. This observation has not been discussed in the research community so far. Analyses suggest that there is a supporting effect of the three contacting surfaces: Rake face, primary flank face and peripheral flank face. The occurrence of this effect depends on the tool geometry and the tested CFRP material. In future when transferring the model, this effect should be further investigated. Consequently, the tool wear in the cutting edge corner region of a drilling tool may be different and need to be modelled with separate *micro-geometry* parameters.

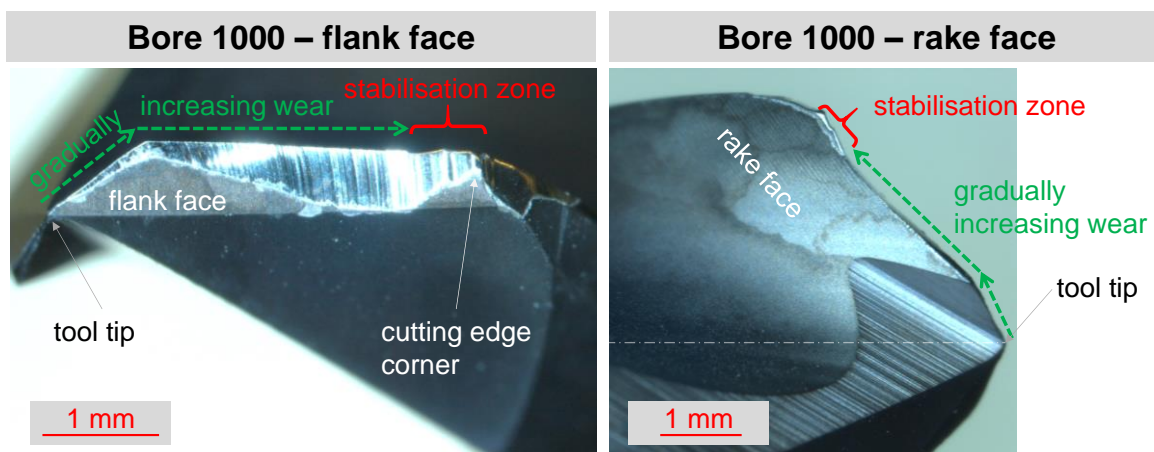


Figure 5.34: Heavily worn diamond-coated drilling tool after 1000 bores in 8 mm thick UD-CFRP with exceptional wear effect.

6 New approach for bore exit evaluation

When describing bore exit damages the common delamination factors F_d , F_{da} and F_{ed} presented by CHEN [44], DAVIM et al. [53] and TSAO et al. [227] focus on cracks, spalling and delamination at bore edges, as stated in Chapter 2.2. But when evaluating the damages being induced by a drilling operation in FRP, protruding uncut fibres should also be considered. These damages protruding inside the bore are obstructive when inserting rivets. Overall, the optimum damage criterion should consider all damages which influence the statement, whether a bore is suitable for the subsequent riveting operation. A new damage criterion is presented, which takes the existing factors as well as the effect of uncut fibres at bore exits into account. Part of this research is published in the CIRP Journal of Manufacturing Science and Technology [234].

6.1 Key parameters of the approach

The proposed damage value Q_d combines a comprehensive set of five characteristic parameters describing the overall bore entrance or exit quality non-destructively. The first two parameters F_{nd} and F_{A_d} consider cracks, spalling and delamination in the vicinity of a drill hole and the following three parameters $F_{L,95\%}$, F_n and $F_{A_{cov}}$ describe the scale and amount of uncut fibres inside a bore:

$$Q_d = K[w_1 F_{nd} + w_2 F_{A_d} + w_3 F_{L,95\%} + w_4 F_n + w_5 F_{A_{cov}}] \quad (118)$$

The impact of each damage-parameter F_i on Q_d is considered by a certain weighting factor w_i . It needs to be considered that the sum of all w_i must be equal to 1. K represents the scaling factor for the whole damage value. Proper selection of these constant parameters will be explained later on.

The first two damage parameters are generally based on former approaches and these are common factors to describe cracks, spalling and delamination in the vicinity of the bore. The first one is called normalised delamination factor F_{nd} , which considers the general delamination factor F_d . This factor takes the maximum extend of cracks in the vicinity of the bore (D_{max}) into account and it can be expressed as follows:

$$F_{nd} = \frac{F_d - 1}{F_d} = \frac{D_{max} - D}{D_{max}} \quad (119)$$

The second parameter F_{A_d} analyses the damaged area around a bore. It is calculated as the ratio of the damaged area A_d to the ring-shaped area between D_{max} and D :

$$F_{A_d} = \frac{A_d}{(A_{max} - A_0)} \quad (120)$$

The weighted bilinear combination of the first two parameters F_{nd} and F_{A_d} allows the distinction between a single delaminated fibre vs. a rather uniform large damage around the bore. This combination reduces the sensitivity to a significantly scattering maximum diameter in the damage zone D_{max} in unidirectional CFRP material, because F_{nd} shows a positive and F_{A_d} a negative correlation to D_{max} .

The three following summands of equation (118) describe the extent of uncut fibres when drilling CFRP. The first of these parameters $F_{L,95\%}$ represents the relative circumferential length at 95% of the bore radius ($D_{95\%}$) being punctured by fibres:

$$F_{L,95\%} = \frac{L_{95\%} - L_{f,95\%}}{L_{95\%}} \quad (121)$$

Experiments show that at $D_{95\%}$ the covered circumferential length $F_{L,95\%}$ is unaffected by fraying fibres at the bore edge. $L_{95\%}$ represents the circumferential length of a circle with the diameter $D_{95\%}$ and $L_{f,95\%}$ represents the uncovered circumferential length at $D_{95\%}$. Thus the numerator in (121) represents the length at $D_{95\%}$ being covered with protruding uncut fibres.

The fourth parameter F_n describes the number of uncut fibre bundles, which plays a decisive role on the reparability of drilled bores:

$$F_n = \tanh\left(\frac{n_{uncut}}{15}\right) \quad (122)$$

Scaling of F_n between 0 and 1 is achieved using a hyperbolic tangent term. F_n can be calculated by the adapted hyperbolic tangent in (122) and is plotted in Figure 6.1 on the right. Based on various experiments in unidirectional CFRP material, the influence of the number of uncut fibre-bundles on the bore quality is declining, especially for more than 10 to 15 uncut fibre bundles. Hence a linear gradient of 1/15 has been chosen for the asymptote of the hyperbolic tangent. It needs to be considered that this equation (122) might be diameter dependent especially for extremely different bore diameters to the ones used in this study. Due to limited availability of tools this influence has not been analysed.

The fifth parameter $F_{A_{cov}}$ represents the covered relative bore area by uncut fibres. It is calculated by the ratio of the covered bore area ($A_0 - A_{free}$) to the complete bore area (A_0) and is directly influenced by the width and length of the uncut fibre bundles:

$$F_{A_{cov}} = \frac{A_0 - A_{free}}{A_0} \quad [0; 1] \quad (123)$$

Figure 6.1 shows two realistic and completely different bore exits in CFRP: On the left side a bore with many but narrow uncut fibre bundles and on the right hand side a bore with a single but wide uncut fibre bundle. The three described parameters $F_{L_{cov_circ,95\%}}$, $F_{n_{uncut}}$ and $F_{A_{cov}}$ help to evaluate the characteristics of the uncut fibres.



Figure 6.1: Bore exit in CFRP (\varnothing 6.35 mm) with numerous fine (left) and single wide uncut fibre bundle (middle) and plotted hyperbolic tangent for F_n (right); published in [234]

All influencing parameters to the damage value Q_d are clearly depicted and a schematic illustration of the damage, considered by each factor, is shown on the right in Table 6.1. A uniform range of value between 0 and 1 of each parameter allows simple adjustment of each impact to the bore quality valuation by the weighting factors (w_i). The selection of potential weighting factors is explained during the experimental demonstration of this approach in Chapter 6.2. In general, two alternative distributions of the weighting factors will be discussed: Equal distribution for damages inside the bore (50%) and in the vicinity of the bore (50%) as well as adaptation of the weighting factors to the thrust force. A good comparison of different results requires constant weighting factors within one test series.

Table 6.1: Overview of influencing parameters and factors to the damage value Q_d

	Parameter	Equation	Range of value	Description	Illustration
Vicinity of the bore	F_{nd}	$\frac{F_d - 1}{F_d}$	[0; 1]	normalised delamination factor	
	F_{A_d}	$\frac{A_d}{(A_{max} - A_0)}$	[0; 1]	relative damage area	
Inside of the bore	$F_{L,95\%}$	$\frac{L_{95\%} - L_{f,95\%}}{L_{95\%}}$	[0; 1]	covered relative circumference	
	F_n	$\tanh\left(\frac{(n_{uncut})^{1.0}}{15}\right)$	[0; 1]	$\tanh()$ of amount of uncut fibre bundles (\approx linear increase up to 15 uncut fibres)	
	$F_{A_{cov}}$	$\frac{A_0 - A_{free}}{A_0}$	[0; 1]	covered relative bore area	

6.2 Demonstration of analysing procedure

To demonstrate the applicability of the above proposed quality parameters and damage value Q_d , the quality analysis of an exemplary drilling series is presented below. It enables to explain the determination of the weighting factors and highlights the advantages of the new quality parameters compared to the existing ones in literature.

The exemplarily analysed drilling series of a total of 1000 bores is implemented in unidirectional CFRP material AS4/3501-6 with dimension of 230 x 230 x 8 mm³, resulting in a total feed path of 8 m for the CFRP spiral drilling tool. The material consists of 68 unidirectional layers with a symmetric arrangement of $-45^\circ/0^\circ/+45^\circ/+90^\circ$. Physical and mechanical properties of the material are shown in Table 6.2. The CFRP plate does not have

a supporting glass fibre layer nor back-up plates at the drill exit side of the CFRP plate. In aerospace industry AS4/3501-6 material is used for general purpose structural applications, according to the datasheet [105]. Spiral drills, optimised for CFRP machining, with diameter 6.35 mm are used for the machining experiments. The tools are made of tungsten carbide MG12 and are coated with a Nano-crystalline diamond coating of 8^{+2} μm thickness. The cutting speed for the drilling series is 90 m/min and the feed rate 0.06 mm/rev. Microscope pictures of the tool tip and the corresponding tool wear are presented in Figure 6.6.

Table 6.2: Properties of AS4/3501-6 unidirectional CFRP material [105]

Physical properties	fiber	weave/UD	fiber mass	fiber volume	laminate density	glass trans. temp.
Unit	/	/	g/m^2	%	g/cm^3	$^{\circ}\text{C}$
	AS4	UD	150	62	1.59	177
Mechanical properties	tensile	tensile strength	tensile modulus	compression	compr. strength	compr. modulus
Unit	method	MPa	GPa	method	MPa	GPa
	ASTM D3039	2137	141	ASTM Mod. D695	1723.7	128

It is hard to estimate the difference in bore exit quality solely based on optical microscope images; compare for example bores 600, 800 and 1000 in the first column in Figure 6.5. Consequently, a detailed analysis of the drilling series is performed using 3D data from an *Alicona* infinite focus microscope. The workflow including drilling, microscopy analyses, conversion of the raw data and evaluation is shown schematically in the following Figure 6.2. Periodically, all 200 bores the bore exit quality is analysed; No significant damages occur at the bore entrance side. For the 3D measurement of the bore exit a lens with 5x magnification is chosen and the estimated vertical and lateral resolutions are set to 4 μm and 8 μm respectively. Due to the small field of vision an image field of 4 by 5 pictures and an overall size of 10 mm by 10 mm is stitched to detect all damages at the bore exit ($D = 6.35$ mm). With the Software *IF-Measure Suite 4.2* the 3D data in form of a scatter plot with X, Y and Z coordinates of the work piece is converted with a compression factor of 16 and exported into a text file. The grid spacing of the text file in X and Y plane is 56 μm . A user independent *Matlab*® graphical user interface (GUI) helps to analyse and graphically present the results of the damage value Q_d presented above.

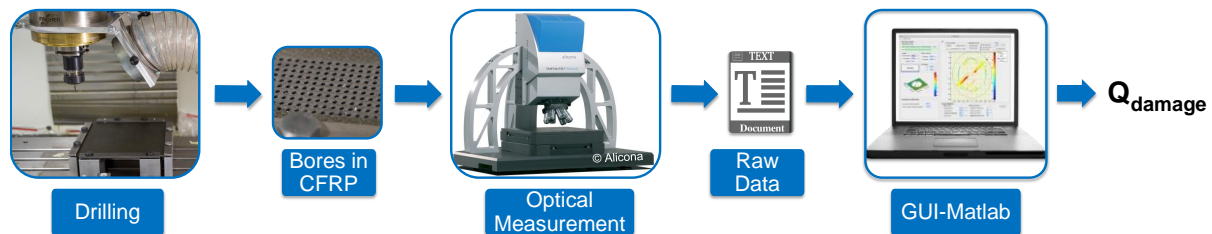


Figure 6.2: Workflow for the presented results including drilling and analysing processes; published in [234]

To detect delaminated and spalled areas in the vicinity of each bore, the X, Y and Z coordinates of the 3D data are automatically analysed. A measuring point is defined as damaged, as soon the z-deviation is larger than 150% of the maximum surface roughness in the four red circles in the unaffected part of the CFRP surface, see Figure 6.3 on the left hand side. Both, positive and negative deviation of the z-value from the limit leads to the

classification “damaged”. The value of 150% is based on several empirical experiments. Single outliers are deleted using a filter algorithm. The right picture in Figure 6.3 shows the result of the *Matlab*® tool with the colour coded damaged area of the work piece including uncut fibres. A rhombus marks the outermost delaminated point and a square marks the outermost spalled point. The inner green circle represents the bore diameter D and the outer circle represents the maximum diameter in the damage zone D_{max} . The damaged area A_d is determined by adding up the damaged parts outside the bore diameter D and the covered area A_{cov} inside the bore is determined by adding up the area of uncut fibre bundles inside the bore diameter D .

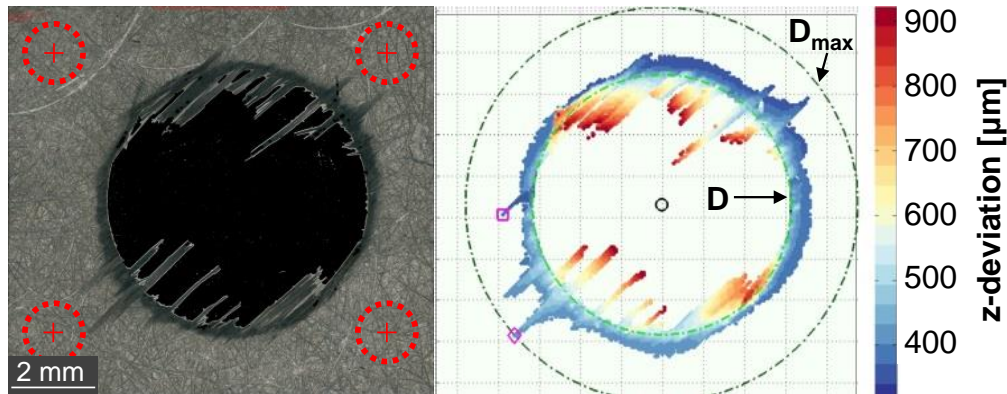


Figure 6.3: Delamination analysis by means of a *Matlab*® tool based on 3D microscopy; published in [234]

To calculate the proposed parameters describing the scale and amount of uncut fibres $F_{L,95\%}$ and F_n the 3D data is cropped to $D_{95\%}$ to trim fraying effects at the bore edge, shown on the left in Figure 6.4. The relative covered circumferential length $F_{L,95\%}$ is calculated by adding up the covered length marked with pink coloured asterisked points in proportion to the uncovered length. A cluster analysis algorithm DBSCAN by ESTER [68] is used to detect and count coherent uncut fibres within the cropped circle of $D_{95\%}$. To be recognised as single uncut fibre bundles, the adjacent fibres must not be connected with each other, as explained in detail by ESTER [68]. These detected single fibre bundles are plotted with separate colours on the right hand side in Figure 6.4. Besides the recognition of uncut fibres, the length and angle of each fibre bundle relative to the unidirectional fibre direction of the outermost layer is calculated and plotted in the pictures as additional information but not utilized for the bore exit quality value Q_d .

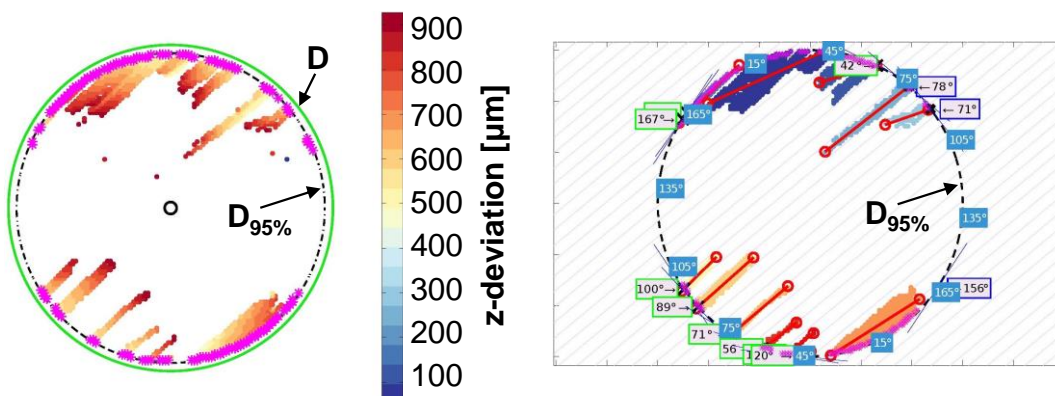


Figure 6.4: Uncut fibre analysis by means of a *Matlab*® tool based on 3D microscopy; published in [234]

6.3 Analysing results

To specify the proposed damage value Q_d , different drilling series are carried out in CFRP and the bore exits are analysed at regular intervals. The following Figure 6.5 shows the microscope pictures of the bore exits and the corresponding analyses based on the 3D-data regarding damages around the bore and uncut fibres for one drilling series. The microscope pictures in the first column in Figure 6.5 show a decreasing bore exit quality with increasing number of bores, expressed by more uncut fibres and increasing delamination.

In the second column in Figure 6.5 the z-level of the damaged material is presented color-coded in which the bluish colours show low z-values (e.g. spalling) and the yellow and red colours show high z-values (e.g. delamination). In contrast to the first 600 bores, where D_{max} depends on single delaminated fibres and the damaged area A_d is rather small, after 600 bores the damaged area becomes larger uniformly around the bore. D_{max} remains in the same range as it is for the first 400 bores. The pictures in columns three and four of Figure 6.5 show the analysed bores concerning scale and amount of uncut fibres. Obviously the covered circumferential length as well as the number of uncut fibres is increasing with tool wear. The detailed and automated analysis of the corresponding factors Q_d , F_d , F_{da} and F_{eq} is presented in Figure 6.7 and Figure 6.8.

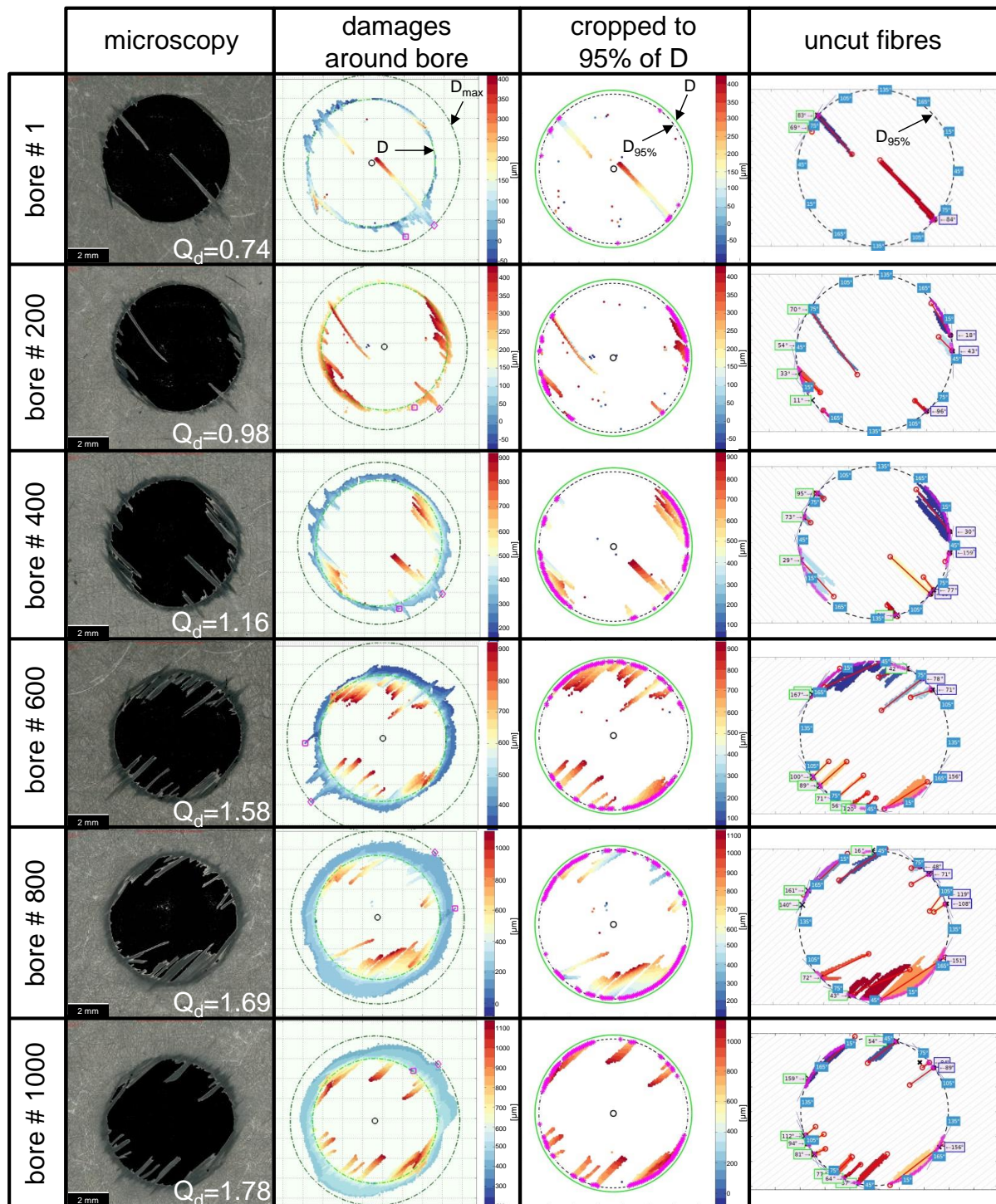


Figure 6.5: Regular bore exit microscope images and processed 3D-data of drilling series; published in [234]

The continuously increasing wear of the tool having executed the bores in Figure 6.5 is shown in Figure 6.6. Already at the 200th bore the carbide is revealed over a length of 50-75% of the main cutting edge. With bore number 600 the coating at the chisel edge of the drilling tool starts to wear, indicated by the shiny cutting edge. At bores number 1, 600 and 1000 the profiles of the main cutting edge at $d_{80\%}=0.8 d$ marked with coloured bars in the left of Figure 6.6 are plotted and compared with each other in the diagram on the right of Figure 6.6. With cumulative number of bores, the width VB of wear marks at $d_{80\%}$ of the main cutting edge increases linearly from 490 μm at 600 bores to 713 μm at 1000 bores. As expected, the tool wear appears mainly on the flank face of the tool.

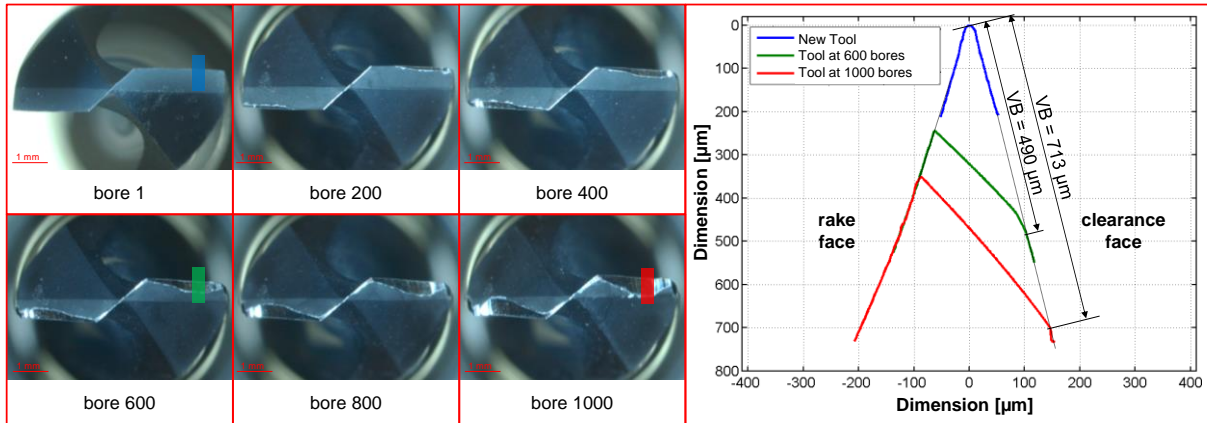


Figure 6.6: Drilling tool points (left) and profiles of main cutting edge at $d_{80\%} = 0.8 d$ (right); published in [234]

The five proposed parameters influencing the damage value Q_d are plotted separately with lines in the graph in Figure 6.7. The solid lines display the parameters influenced by the damaged area around the bore and the dashed lines represent parameters affected by uncut fibres. The associated damage value Q_d at each analysing step is plotted with grey bars belonging to the scale on the right hand side. Weighting factors used for equation (118) in this drilling test are listed in the table in Figure 6.7 and are based on an equal distribution: The sum of the weighting factors (w_1, w_2) for damages in the vicinity of the bore is 0.5 as well as the summation for the inside weighting factors (w_3, w_4, w_5). The overall scaling factor K has been set to 5.00.

As explained above, the solely consideration of the conventional delamination factor F_d and the normalised corresponding factor F_{nd} are insufficient in unidirectional CFRP material. The solid black line in Figure 6.7 represents the normalised delamination factor F_{nd} showing a rather random scattering function in a range of 0.25 to 0.35 depending on the diameter D_{max} . For this drilling series in unidirectional CFRP F_{nd} solely does not show any correlation between the linear tool wear in Figure 6.6 nor the thrust force increase and it represents the bore exit quality in the presented drilling series insufficiently.

The factor $F_{A,d}$ considering the damaged area remains 0.1 for the first 200 bores and increases afterwards steadily representing increasing tool wear and decreasing bore quality, with an exception of the outlier at bore 600. At the 600th bore Figure 6.5 and Figure 6.7 show the largest amount for D_{max} in this drilling series, simultaneously causing a large A_{max} . The influence of the ring area $A_{max}-A_0$ in equation (120) outweighs the damaged area (A_d) by far. In the presented approach of Q_d both damage-terms F_{nd} and $F_{A,d}$ are combined in a bilinear form with weighting factors (w_1 and w_2), as written in (118) representing the decreasing quality in the vicinity of the bore sufficiently.

The covered relative circumferential length $F_{L,95\%}$ grows in a decreasing manner, starting at a small value of 0.03 at the first bore to 0.47 at the 800th bore. The 1000th bore shows a better bore quality again, with a covered relative circumferential length of 0.38. The function of $F_{L,95\%}$ is very similar to the function of the parameter describing the covered relative area inside the bore $F_{A,cov}$, but the covered area increases much slower with tool wear than $F_{L,95\%}$. The value $F_{A,cov}$ remains in a range of 0.04 – 0.19 and is mainly depending on the length and width of the uncut fibre bundles. The presented unidirectional CFRP material machined with

the drill in Figure 6.6 shows many uncut fibres, especially when the tool wear increases. As well as the two parameters F_{A_cov} and $F_{L,95\%}$, the parameter F_n grows in a decreasing manner, starting from 0.21 for the first bore to a maximum of 0.72. It needs to be considered that the two proposed parameters $F_{L,95\%}$ and F_n strongly depend on the chosen cropping factor of the actual bore diameter.

The five parameters described above with their function over the number of bores shown in Figure 6.7 lead to a damage value Q_d subsequent to equation (118). Based on the presented uniformly distributed weighting factors shown in Figure 6.7, Q_d increases almost linearly from 0.74 at the first bore to 1.8 for the 1000th bore. The error bars show the bore quality scattering effect in unidirectional CFRP material for the three consecutive bores being analysed at each analysing step regularly every 200 bores. A quality value variation for Q_d between ± 0.05 and ± 0.3 within three consecutive bores can be observed in this unidirectional CFRP material.

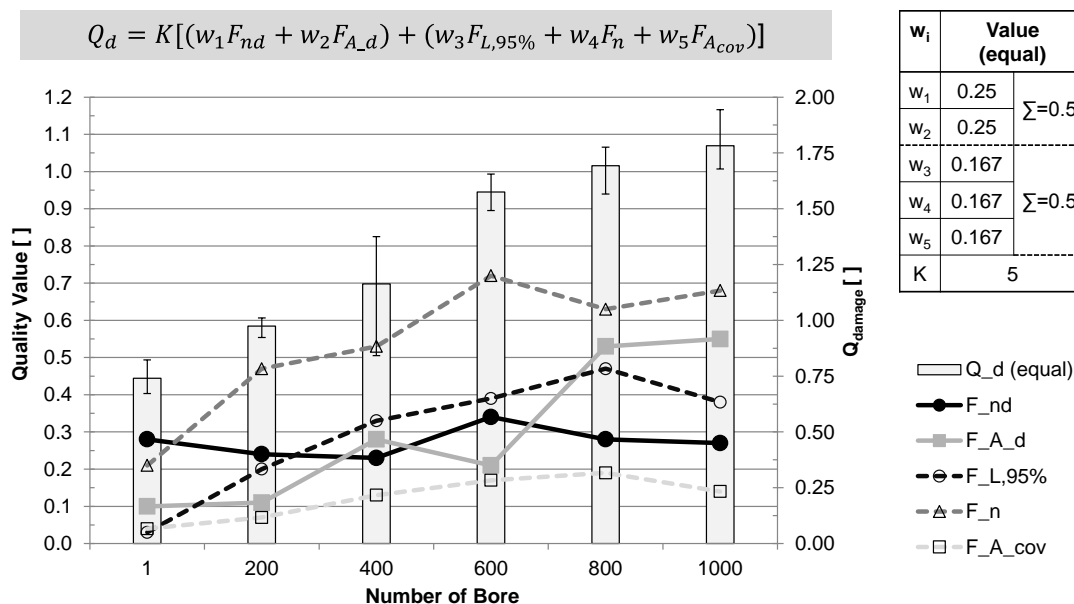


Figure 6.7: Q_d (grey bars) for a bore series of 6.35 mm in UD-CFRP together with the individual constituents of damage description F_{nd} , F_{A_d} , $F_{L,95\%}$, F_n , F_{A_cov} (lines); published in [234]

Former publications e.g. by HOCHENG and TSAO [113] show a direct correlation of thrust force increase due to tool wear and the amount of damages and delamination around a bore. To assess the reliability and accuracy of the damage value Q_d , its function with number of bores is compared with the thrust force, see grey bars and green dot-and-dashed line in Figure 6.8. The proposed value Q_d based on uniformly distributed weighting factors matches the associated thrust force quite good represented by a correlation coefficient R^2 of 0.95.

Another possibility to set the weighting factors of the damage value (w_1 - w_5) is the ordinary least square method based on the thrust force development over the number of bores: Using this method to set the weighting factors, a correlation coefficient between the thrust force and the damage value Q_d of $R_2=0.99$ is possible for this drilling series. The corresponding weighting factors are shown in the right column in the table in Figure 6.8. Obviously the emphasis is on the damage areas F_{A_d} and F_{A_cov} representing a total of 80% of the weighting factors. In this example the influence of the number of uncut fibres F_n is very small, when fitting the damage value to the thrust force, expressed by a weighting factor $w_4=0.01$. Besides Q_d the three delamination factors F_d , F_{da} , F_{ed} presented by CHEN [44], DAVIM et al.

[53] and TSAO et al. [227] are also plotted in Figure 6.8. Especially the factors F_d and F_{da} do not show a good correlation between the thrust force increase nor the tool wear in Figure 6.6; R^2 is just 0.19 and 0.76 respectively. These factors are very sensitive to single cracks or far delaminating fibres leading to rather random scattering maximum diameters in the damaged zone D_{max} , which appears for example at the 600th bore in Figure 6.5. The equivalent delamination factor F_{ed} does not respond as sensitive on varying D_{max} as the other two delamination factors, because the calculation is based on a more robust area A_d instead of a length D_{max} . F_{ed} shows a similar development and correlation coefficient of 0.93 as Q_d with decreasing quality for the first 800 bores but in general on a much weaker scale. Ultimately the three delamination factors F_d , F_{da} , F_{ed} fade out the damages inside and right at the edge of a bore.

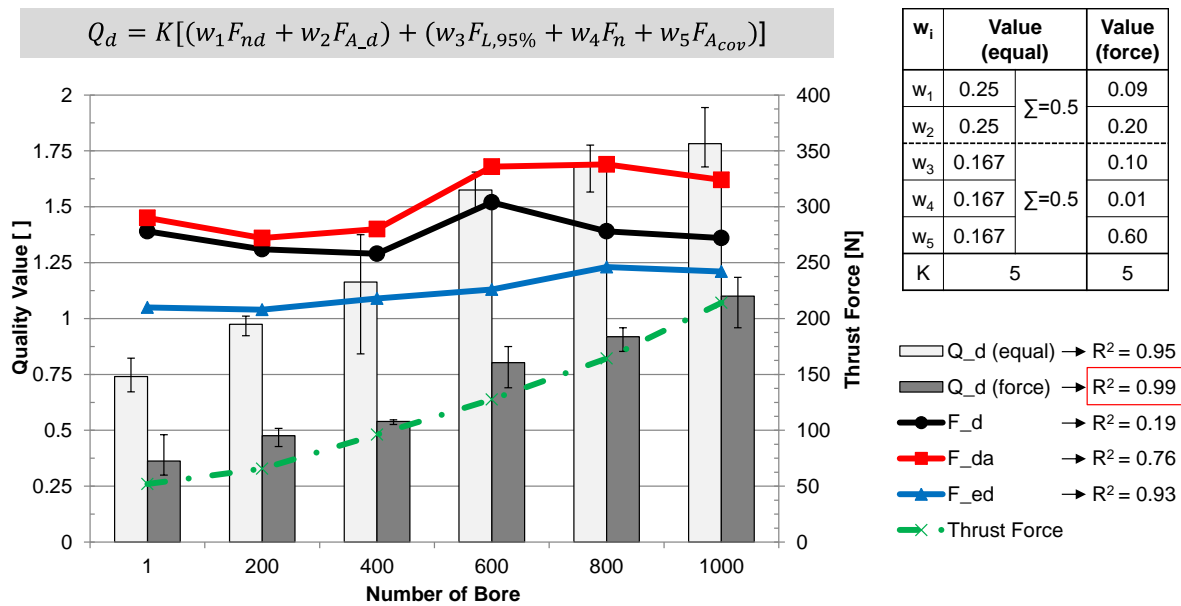


Figure 6.8: Comparison between existing factors F_d , F_{da} , F_{ed} and Q_d and the thrust force for bore series in 6.35 mm UD-CFRP; Q_d (equal) considers an equal distribution of the weighting factors inside and outside the bore whereas in Q_d (force) the weighting factors are fitted to the thrust force measurements by ordinary least square method, see the table on the top right; This data is published in [234]

An additional evaluation of the bore exit quality by mechanical strength tests corresponds to the bore exit quality approach shown above. Therefore in a test setup the bore channel is charged from the bore exit side with a conical expansion device, according to HENERICHS et al. [99]. In this case a diamond-coated conical pin with 100° cone angle is used to expand the bore hole, while the force and displacement of the pin in z-direction are recorded. The force-displacement curves are measured regularly every 200 bores and are evaluated by the force/displacement gradient. Further details regarding the evaluation of the mechanical strength of a bore and the test setup are presented in Paragraph 7.1. The mechanical strength results in Figure 6.9 show an overall decreasing bore quality trend, which match the increasing damage values in Figure 6.8 very well.

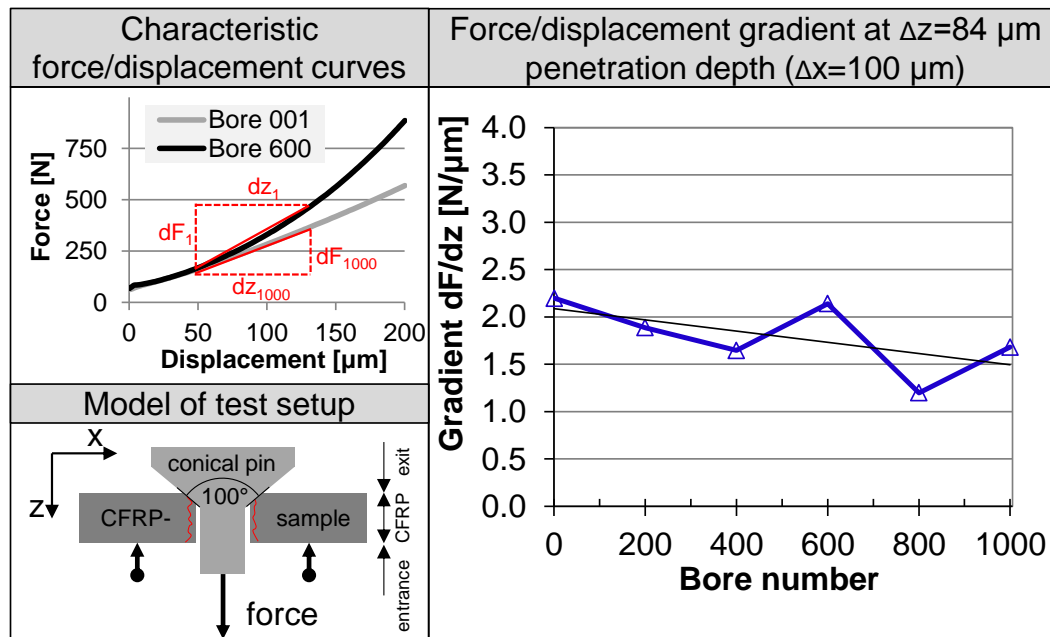


Figure 6.9: Force/displacement gradient of the mechanical strength tests plotted over the number of bores

Comparable to the definition of end of tool life time by theoretical critical thrust force proposed by HO-CHENG and DHARAN [109] and TSAO and HOCHENG [222], a limit of Q_d or each of the five quality values can be defined depending on the application. Once the global quality value or as required one of the five parameters exceeds the determined limit, the tool actually reaches the end of tool life time. Although the proposed quality measurement method is not on-line with the machining operation a regular analysis of bore quality in some interval allows monitoring with a certain time offset. The advantage of direct identification of actual bore exit quality overcomes the disadvantage of time offset especially in development phase of new drilling tool geometries and in research.

Figure 6.10 demonstrates the determination of tool life time based on the exemplary bore exit analysis of the bore series presented in Figure 6.5. In an exemplary application with a countersinking process subsequently to the drilling operation, the limits for damages in the vicinity of the bore may be $D_{max} < 9 \text{ mm}$ and $A_d < 10 \text{ mm}^2$ resulting in $F_{nd} < 0.3$ and $F_{A_d} < 0.43$ respectively. Not to harm the countersinking operation a maximum amount of 10 uncut fibre bundles, covering not more than 9 mm^2 and a maximum circumferential length of 9 mm constitute the limits, resulting in $F_{L,95\%} < 0.45$, $F_n < 0.58$ and $F_{A_{cov}} < 0.28$. These exemplary limits show the applicability and are marked with a red dotted area in the background of the bars in the diagram in Figure 6.10. An arrow points the number of bore for each quality parameter, which just meets the limit for this application. In this example with an relatively wide analysing interval of 200 bores the actual maximum tool life time for the explained application is 400 bores; At 600th bore the delamination in the vicinity of the bore (F_{nd}) and the number of uncut fibre bundles (F_n) exceed the limits. To increase the precision of the tool life time declaration if necessary, a narrower analysing interval – in extreme case, up to 100% monitoring – can be chosen. Determining the tool life time in this way gives detailed information about the actual development of bore quality and it is possible to distinguish between various defects at bore exits.

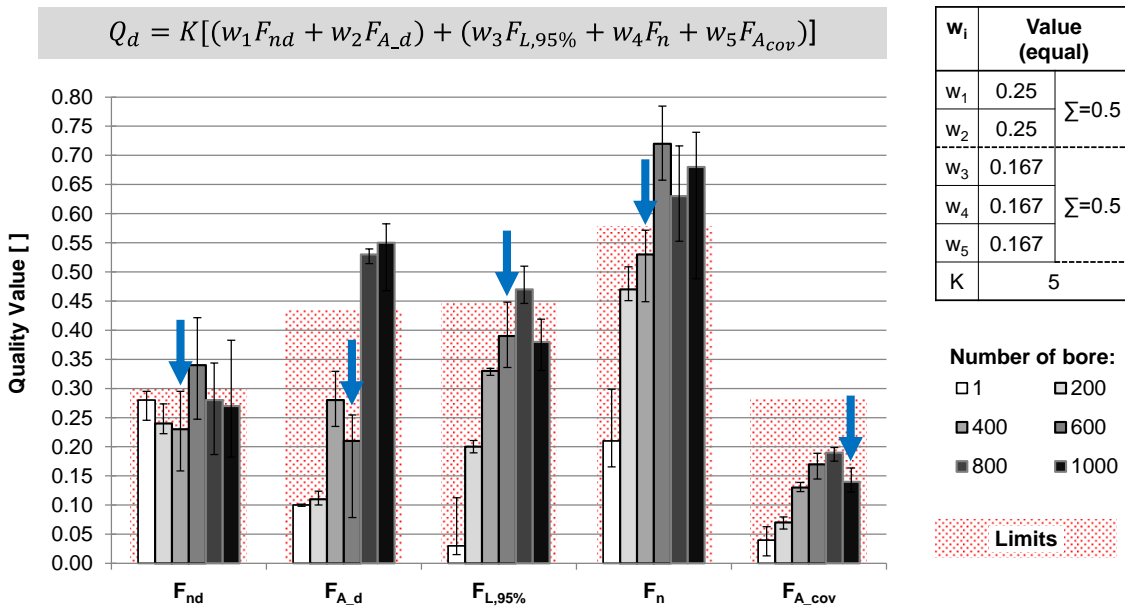


Figure 6.10: Exemplary limits (marked red, dotted area) to define end of tool lifetime for each of the five parameters of damage description: F_{nd} , F_{A_d} , $F_{L,95\%}$, F_n , $F_{A_{cov}}$; published in [234]

6.4 Conclusion of bore exit evaluation approach

Equation (118) with proposed parameters describing the residual defects at the entrance or exit and uncut fibres inside a bore hole serves as universal damage value to describe the quality after a drilling operation in fibre reinforced polymers (FRP). Depending on the material and the weave of the fibres, single parameters might have a different influence on the overall quality. For the presented drilling experiments in unidirectional CFRP two possible sets of weighting factors are shown, one with an equal distribution and one based on the thrust force increase. Within one bore series the weighting factors need to remain constant to enable direct comparability and constitute a development with tool wear.

The analysis presented above shows that the existing delamination factors F_d , F_{da} and F_{ed} are unsuitable to describe the bore quality in unidirectional CFRP, which tend to single delaminated and uncut fibres. The final course of the proposed damage value Q_d reflects the bore quality in agreement with the microscope pictures of the bore exits, the thrust force, the mechanical strength/expansion tests of the bores and the tool wear. Overall Q_d matches the actual bore exit quality, including the effects of uncut fibres much better than the existing delamination factors.

The proposed universal damage value Q_d is the perfect complement to the cutting edge quality value Q_{crit} presented by HENERICHS et al. [101, 232]. First experimental evaluations in [232] show certainly a correlation of the cutting edge quality (Q_{crit}) compared to the bore quality (Q_d). In future work with extensive tests it is necessary to find correlations between single cutting edge micro-geometry parameters presented in [101, 232] and the damage values presented in this approach. The following chapter 6.5 discusses this correlation.

Each of the five parameters in Q_d presented in equations (119) to (123) describes a significant quality aspect of the bore exit. While F_{nd} is sensitive to D_{max} due to single, far delaminated or spalled fibres, F_{A_d} is negatively correlated to D_{max} . The weighted summation of both parameters (F_{nd} and F_{A_d}) describes the effect of damages around the bore on the drilling quality adequately. For various drilling series in unidirectional CFRP the sophisticated

combination of the three parameters $F_{L,95\%}$, $F_{A_{cov}}$ and F_n proved the feasibility to distinguish whether a drill generates wide or small, long or short and many or few uncut fibres. Due to irregular damages in drilling unidirectional CFRP the analyses of the bore exit quality should be based at least on three different bore exit samples per analysing step to get uniform and representative results for a drilling series. For the analysis of these drilling experiments an infinite focus measurement device showed its suitability and the detailed analyses of the geometry data were conducted using a *Matlab*® GUI.

6.5 Correlation of the damage value Q_d and tool micro-geometry

In an extensive drilling series with eleven different diamond-coated drilling tools, the characteristic micro-geometry parameters are determined having the biggest influence on the machining quality. Part of the research presented in this chapter is published in [232] and the cutting edge micro-geometry characterisation is presented in detail by HENERICHS [101]. Figure 6.11 represents this objective by visually comparing both approaches.

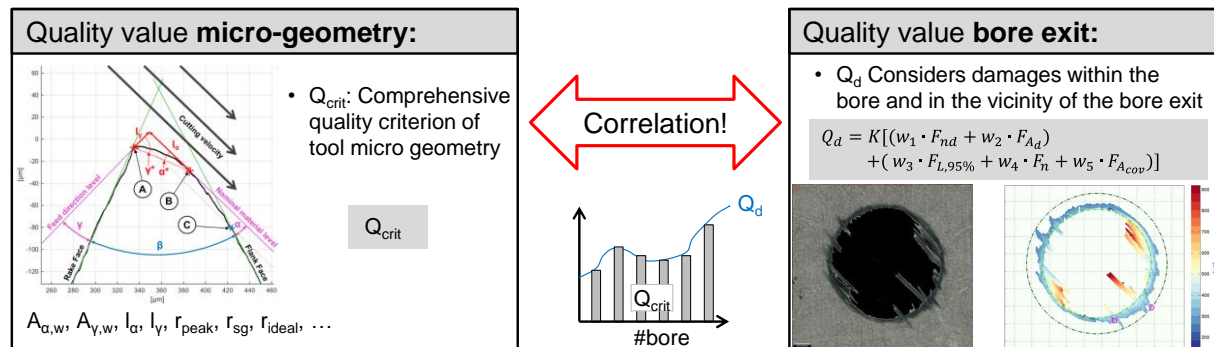


Figure 6.11: Objective of this chapter: Correlation between cutting edge micro-geometry evaluation (left) and proposed bore exit evaluation (right); published in [232]

Based on machining experiments with detailed micro-geometry analyses, these cutting edge micro-geometry parameters are identified, which correlate the machining quality of the drills best. It is noteworthy that a suitable tool macro-geometry (e.g. tip angle, helix angle, α and γ) is prerequisite for good drilling quality. According to the fundamental machining studies with variable tool geometry by HENERICHS et al. [102] and partly presented in chapter 4, large rake and clearance angle are beneficial for good machining qualities and tool lifetime in CFRP machining: Clearance angle in the range of $\alpha=21^\circ$ generate lower process forces and good machining quality. Increasing the rake angle to approximately $\gamma=20^\circ$ - 30° shows similar improvements but with lower influence compared to the clearance angle variation.

For a new CFRP tool with good acuity, the separation point (2) and the point of maximum compression (3), illustrated in Figure 4.11, are close to each other resulting in rather small values for l_{α} and l_{γ} and high level of symmetry. In this case, the load on the CFRP material is focussed on the tip of the cutting edge, exceeding the shear and bending strength of the CFRP-material with relatively low process forces. It is well known that with progressing tool wear the cutting edges in CFRP machining form a waterfall profile. Consequently, the lengths l_{γ} and especially l_{α} increase and the point of maximum compression (3) is in a certain distance to the separation point (2). In order to cut the CFRP material and generate flawless

quality, the peak radius r_{peak} and the length l_γ are getting more important with increasing wear. The following conclusions can be stated:

- A small peak radius r_{peak} is necessary but not sufficient for good machining quality; Shear and bending strength of the CFRP is exceeded at a lower force level because of higher stress concentration
- The smaller l_γ the lower is the growth of compressive stress from point (2) to point (3)
 - For tools with small l_γ , the material is separated in (2) and conveyed along the rake face
 - For unfavourably worn tools with large l_γ , the majority of the CFRP material is compressed underneath the cutting edge, causing high normal forces and tool wear
- The smaller r_{sg} the higher is the stress concentration in the point of maximum compression (3) and cracks may be introduced into the workpiece
 - Tools with large r_{sg} likewise generate a better machining surface by ensuring a uniform compression of the material in the area of negative clearance angle

Extensive drilling experiments show that the length l_α , locating the point of maximum compression on the flank face, does not directly influence the machining quality: Good machining results can even be achieved with tools showing intensive flank face wear as long the curvature of the worn flank face approaches a straight line. Tool A is an example for this finding, as presented in Table 6.3 in combination with Figure 6.12 and Figure 6.13. The length $l_\alpha=232.4 \mu\text{m}$ is comparatively large at the 1000th bore but simultaneously $r_{sg}=1325 \mu\text{m}$ is high and the tool still generates a very good bore exit quality, represented by a small damage value of $Q_d=0.17$. Accordingly, the micro-geometry quality values l_γ and r_{peak} as well as r_{sg} with significant direct influence on the actual machining quality are considered in the comprehensive cutting edge quality criterion

$$Q_{crit} = w_1 v_1 l_\gamma + w_2 v_2 \frac{1}{r_{sg}} + w_3 v_3 r_{peak}, \quad (124)$$

In this equation, the length l_γ , r_{sg} and r_{peak} should be inserted in micrometre. The w_i describe the weighting values, subordinate to the condition $\sum w_i = 1$ and the v_i values represent the scaling factors. Q_{crit} in the range of zero represents a perfect micro-geometry, while large values indicate an unsuitable geometry for CFRP machining. To improve the intuitiveness, the scaling factors v_i are chosen in this exemplary evaluation that the limit of sufficient workpiece quality is approximately reached with $Q_{crit}=1$, as proposed by HENERICHS [101]. For $Q_{crit}<1$, the micro-geometry of the main cutting edge shows good cutting conditions and the CFRP machining quality is at least sufficient. Quality values above the critical quality value $Q_{crit}>1$ show poor machining quality and the micro-geometry is insufficient for CFRP machining. Therefore, the scaling and weighting factors are determined the following way by means of the drilling data: To ensure an equal magnitude of the three separate terms $v_i \cdot x_i$, firstly, the scaling factors v_i are calculated by means of a first guess $v_i \cdot x_{i,max}=5$. Choosing a value of 5 has proven itself for this study, but since the v_i values are re-adjusted later on anyways, other values are also fine. Subsequently, the three weighting factors w_i are calculated with the ordinary least square method based on the bore exit quality data Q_d of the drilling series. Finally, the scaling factors are equally re-adjusted that the above described limit of sufficient micro-geometry $Q_{crit}=1$ meets the workpiece quality $Q_d=1$. Applying the

above described procedure to the extensive machining data, results in the set of weighting and scaling values for (43) presented in Table 6.3. Indicated by a high weighting factor $w_1=0.45$, the length l_v has a large influence on the micro-geometry quality value Q_{crit} . The peak radius r_{peak} is weighted with $w_3=0.35$ and the surface generation radius r_{sg} is of minor importance ($w_2=0.2$). When transferring the quality equation of tool micro-geometry Q_{crit} to CFRP materials with different physical and mechanical properties, dissimilar tool wear may arise and the material may tolerate unfavourable micro-geometries differently. Consequently, the scaling and weighting factors would need to be adjusted. The adaptation for other materials is subject of future research.

Subsequently, the correlation results are shown based on the selection of three exemplary tools. Figure 6.12 shows the bore exits of these three drilling tools with completely different machining qualities. Table 6.2 presents the comprehensive quality criterion Q_{crit} for the three tools A, B and C at the three analysing steps based on equation (124). The diamond coating failure on the rake face of tool B causes rounding of the exposed carbide, represented by comparatively high peak radii of 6–8 μm at 600th and 1000th bore; at the same time the length l_v is larger compared to the other two tools. These parameters result in a worn micro-geometry value of $Q_{crit}>1$ and consequently in insufficient bore exit quality. In contrast to tool B, tool A generates the best bore exit quality after the 300th bore in test: With increasing wear the peak radius r_{peak} decreases strongly, the radius of surface generation r_{sg} increases and the length l_v remains comparatively small with values between 19 and 34 μm . Based on this beneficial micro-geometry features cutting edge quality criteria of $Q_{crit}=0.73\text{--}0.88$ arise for the worn tool A.

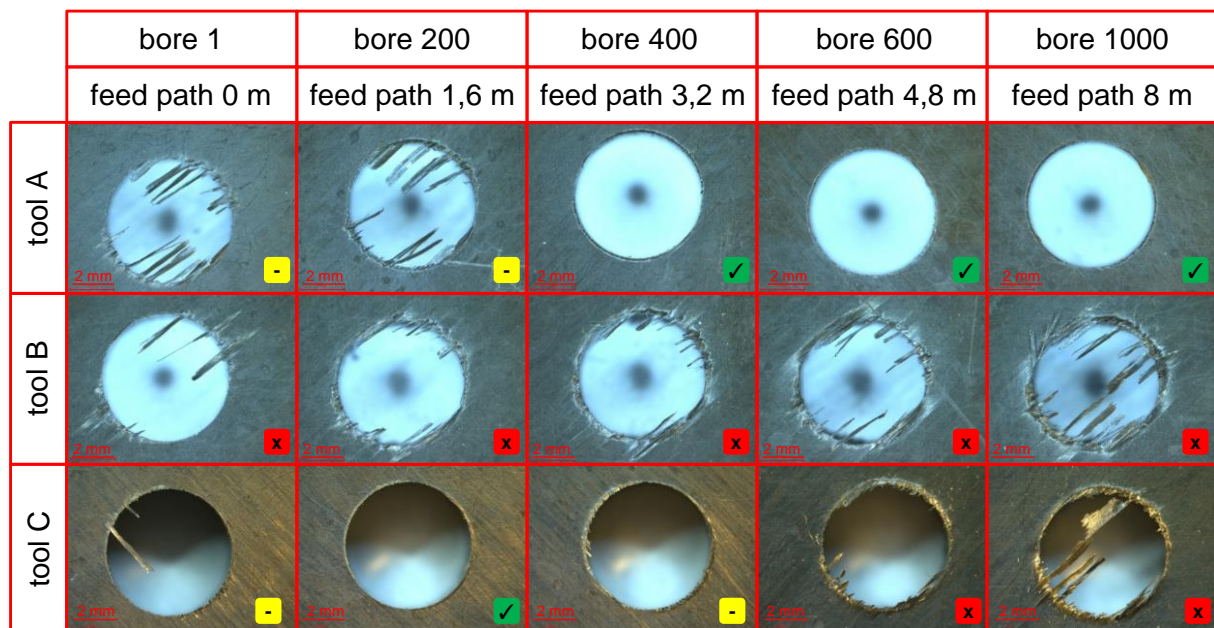


Figure 6.12: Optical microscope images of bore exits for three exemplary tools A, B, C; published in [232]

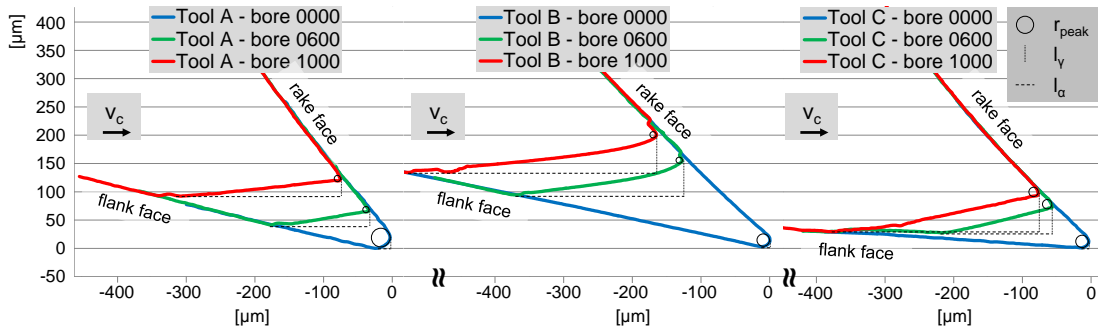


Figure 6.13: Cutting edge profiles of tools A, B, C at 80% of radius with r_{peak} , l_v and l_α ; published in [232]

Table 6.3: Values of micro-geometry quality for tool A, B and C

	# bore	l_α [μm]	l_v [μm]	r_{sg} [μm]	r_{peak} [μm]	Q_{crit} [-]	w_i [-]	v_i [-]
tool A	0	21.3	19.4	24.5	16.6	1.04	$w_1=0.45$ $w_2=0.20$ $w_3=0.35$	$v_1=0.05$ $v_2=10$ $v_3=0.09$
	600	143.6	27.4	$12 \cdot 10^{11}$	2.5	0.73		
	1000	232.4	33.4	1325	2.8	0.88		
tool B	0	12	10.6	12.2	12.2	0.78		
	600	241.2	63	75.2	6.1	1.72		
	1000	359.8	74.6	267.7	8.2	2.04		
tool C	0	12	11.7	14.3	11	0.75		
	600	162.9	38.9	198.4	2.5	1.01		
	1000	300.4	65.6	525.4	3.0	1.66		

Figure 6.14 illustrates the cutting edge quality Q_{crit} and the bore exit damage value Q_d for the three drilling tools. The diagram enables comparison of the comprehensive cutting edge quality and the resulting bore exit quality. While the profile measurements of the cutting edges are conducted under new condition, after 600 and after 1000 bores (hatched bars), the measurements of bore exit quality are implemented every 200 bores (solid lines). The determined bore exit damage values Q_d represent the bore exit microscopy in Figure 6.12 very well. Although the bore exit quality varies widely among the presented tools ($0.09 < Q_d < 2.21$), the evaluation of cutting edge geometry by Q_{crit} shows a good correlation to the machining results. Tools with good bore exit quality, represented by low Q_d at a certain wear state, have a microgeometry with a low Q_{crit} value. This observation is consistent for tools A and C as well as partially for tool B. The comparison of the cutting edge quality of tool B in the new state with promising $Q_{crit}=0.78$ in Figure 6.14 and the actual bore exit qualities represents an outlier. Unfortunately, too rare 3D tool wear analyses exist during the first few hundred bores to explain this effect of tool B based on parameters of the CEA approach. But microscope images of tool B right after drilling the first bores show breakouts of the diamond coating on the rake face close to the cutting edge corner. This unfavourable and rapid change of cutting edge micro-geometry explains the insufficient bore quality. For future studies, it is recommended to conduct more dense 3D-analysing steps and measure the micro-geometry on more than one position of the cutting edge. Evaluating these results, it definitely needs to be considered that additional parameters to the micro-geometry, such as variable tool macro-geometry and point angle, also influence the bore quality. Nevertheless, a correlation between Q_d and Q_{crit} can be shown.

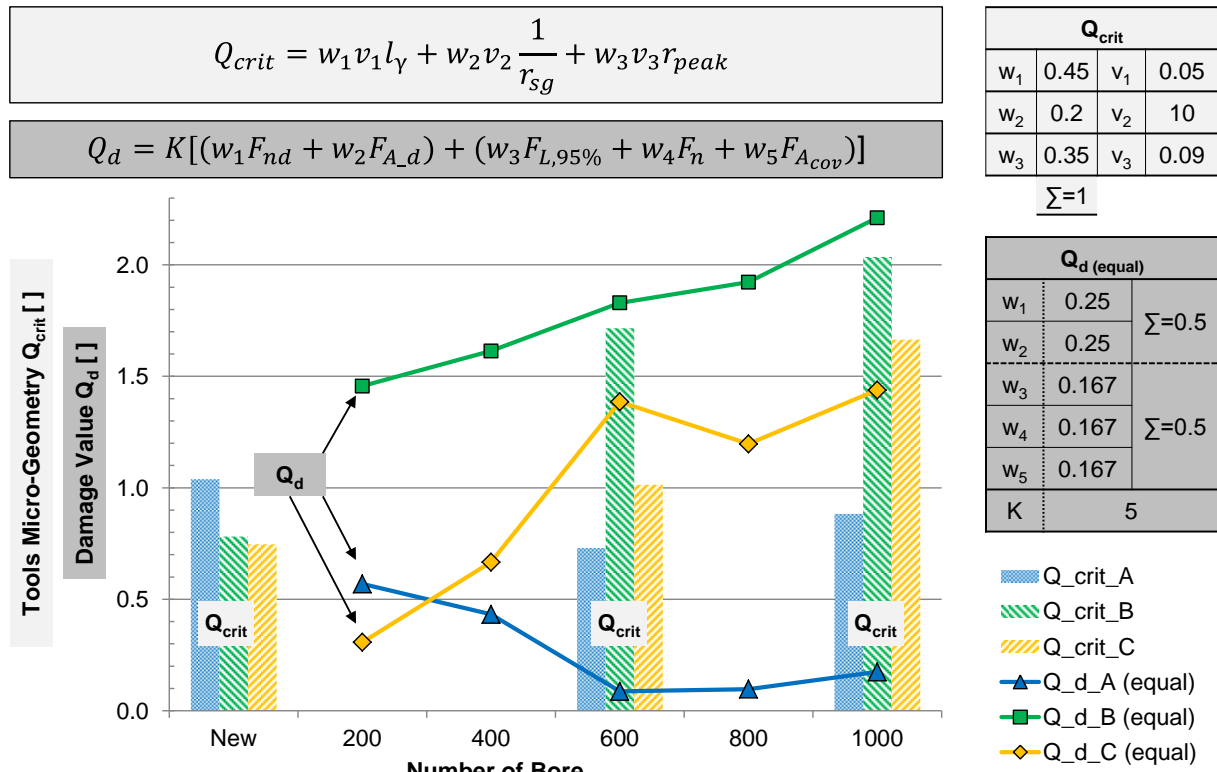


Figure 6.14: Bore exit quality evaluated with damage value Q_d and quality of micro geometry Q_{crit} according to equation (43); published in [232]

7 Drilling experiments in CFRP

The foregoing fundamental experiments, analyses and theoretical approaches have the objective to better understand the relationship between tool geometry and chip formation in CFRP machining. This data and knowledge may be applied to more complex processes e.g. drilling and helps to improve tools for CFRP machining. To validate the improved drilling tools concerning bore quality, process forces and wear it is necessary to obtain experimental data. Therefore, it is precondition to use a test rig setup and analysing procedure with high repeatability. The new approach for bore exit evaluation in Chapter 6 and the *Cutting Edge Analyser* approach by HENERICHS [101] for micro-geometry evaluation as well as the test rigs in 7.2.1 and 7.3.1 fulfill these criteria. In this way optimisation of drilling tools by cutting edge treatment and development of orbital drilling tools for difficult to machine materials is enabled.

In this chapter the optimisation ability of drilling tools is presented and experimentally proven in hard to machine UD CFRP/epoxy material. In a first experimental series, drilling tools with intentionally local ablated diamond coating are tested in unidirectional CFRP material. The local dislodging of the diamond coating aims for provoking the so-called *self-sharpening effect* from the first bore on. This effect is explained in Chapter 7.2.

Moreover, in a second experimental series conventional and orbital drilling processes are conducted in hard to machine UD CFRP/epoxy material. Tool wear tests with up to 1000 bores are carried out with both processes and are compared in terms of bore quality, process forces and processing time. It is explained in Chapter 7.3 that orbital drilling may be an alternative for conventional drilling.

7.1 Measuring equipment

Tool wear progression is analysed in regular intervals with an optical *Leica* MZ16 A microscope, which allows for up to 160x magnification. Therefore, the tools are regularly (at least every 200 bores) taken out of the machine tool, cleaned in an ultrasonic bath and positioned under the microscope by means of a rectangular prism. The focus of this analysis is on the rake and flank face to identify potential damages of the diamond coating. In contrast to precise 3D microscopy of single positions of the cutting edges, this method gives an overview of the regularity of abrasive wear and the occurrence/frequency of coating breakouts. The same microscope MZ16 A is utilised to generate images of the bore exits in CFRP. Although the images only allow for rough comparison of bore quality, it rather provides an overview and quality trend for the drilling series of 1000 bores. Objective comparisons according to the method in Chapter 6 require 3D microscopy of the bore exits, which is explained in detail in Chapter 6.2 and Figure 6.2.

For detailed tool wear analysis and micro-geometry evaluation a 3D infinite focus microscope is used. Generally the main cutting edge is measured at 80% of the tool radius in the new state, after 600 and after 1000 bores. For this precise analysis 20x magnification is used with vertical and lateral resolutions of 0.2 μm and 2 μm respectively. Afterwards 2D profiles are generated, averaged over a width of 50 μm and evaluated by means of the *Cutting Edge Analyser* (CEA) approach presented by HENERICHS et al. [101, 232]. The schematic analysing sequence is shown in Figure 7.1.

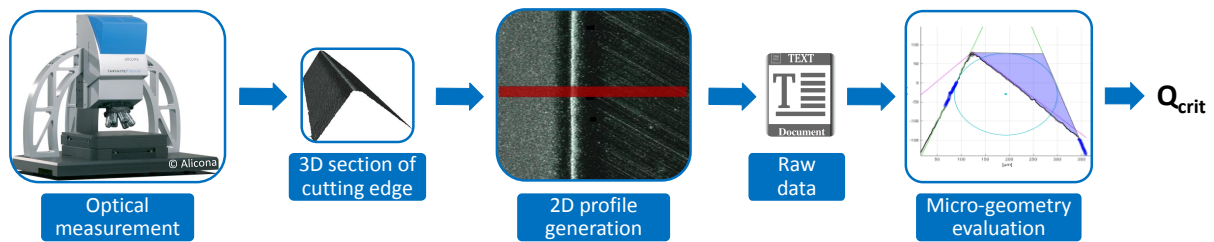


Figure 7.1: Micro-geometry analysing sequence with infinite focus microscope.

Bore diameter measurements are performed using a coordinate measurement machine *Leitz PMM 864*. The setup and measurement routine is shown in Figure 7.2. Three consecutive bores are regularly measured (at least every 200 bores) with a coordinate measurement machine. A vice (blue) is used for fixation of the CFRP stripe and a mechanical end stop ensures reproducible positioning of a new test stripe. The stripes are orientated with the bore exit side to the bottom and tactile measurement is conducted from the bore entrance side. In this way potential uncut fibres do not harm the measurements. A round probe of $\varnothing=3$ mm is used to measure on three levels in the bore channel with each eight measuring points. The bore diameter and roundness are evaluated by averaging over the three separate measuring levels per bore. The desired bore diameter in this thesis is 6.35 mm ($1/4''$), which is a typical value in the aerospace industry.

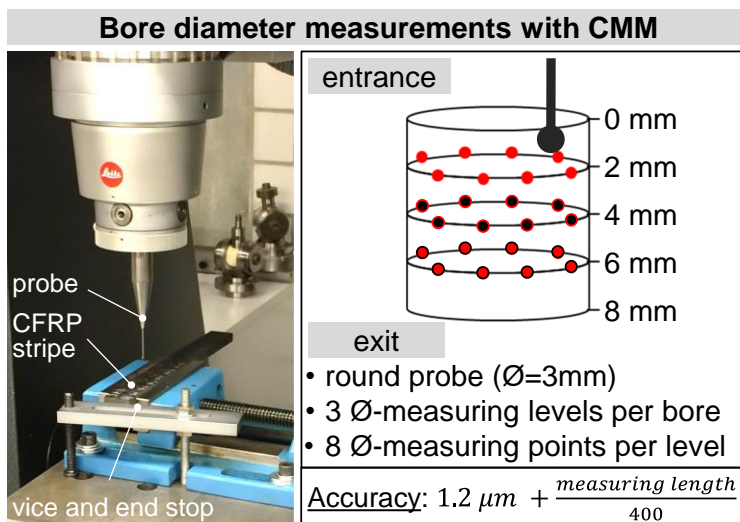


Figure 7.2: Bore diameter measurements on Coordinate Measuring Machine (CMM)

Micrographs of the bores are prepared to identify damages introduced by the drilling operation below the surface. Different approaches show that micrographs perpendicular to the bore axis display the damages at the bore edge best. Therefore, regularly every 200 bores a sample of approximately $24 \times 15 \times 8 \text{ mm}^3$ is cut out with the bore in the centre, embedded in transparent epoxy with the bore exit side to the bottom and grinded after curing at the bottom side. The grinding and polishing strategy with the *Struers Abramin* machine is shown in the table in Figure 7.3 and an exemplary sample with two micrographs is shown at the bottom of Figure 7.3. It is well known from fundamental experiments [230] that fibre cutting angles in the range of $\phi=90^\circ$ and $\phi=135^\circ$ are sensitive for subsurface fibre cracks, fibre pull-outs and saw teeth profiles. Accordingly, the analysed micrographs focus on these fibre cutting angles. In general maximum damages up to a depth of approximately $100 \mu\text{m}$ from the bore edge have been found.

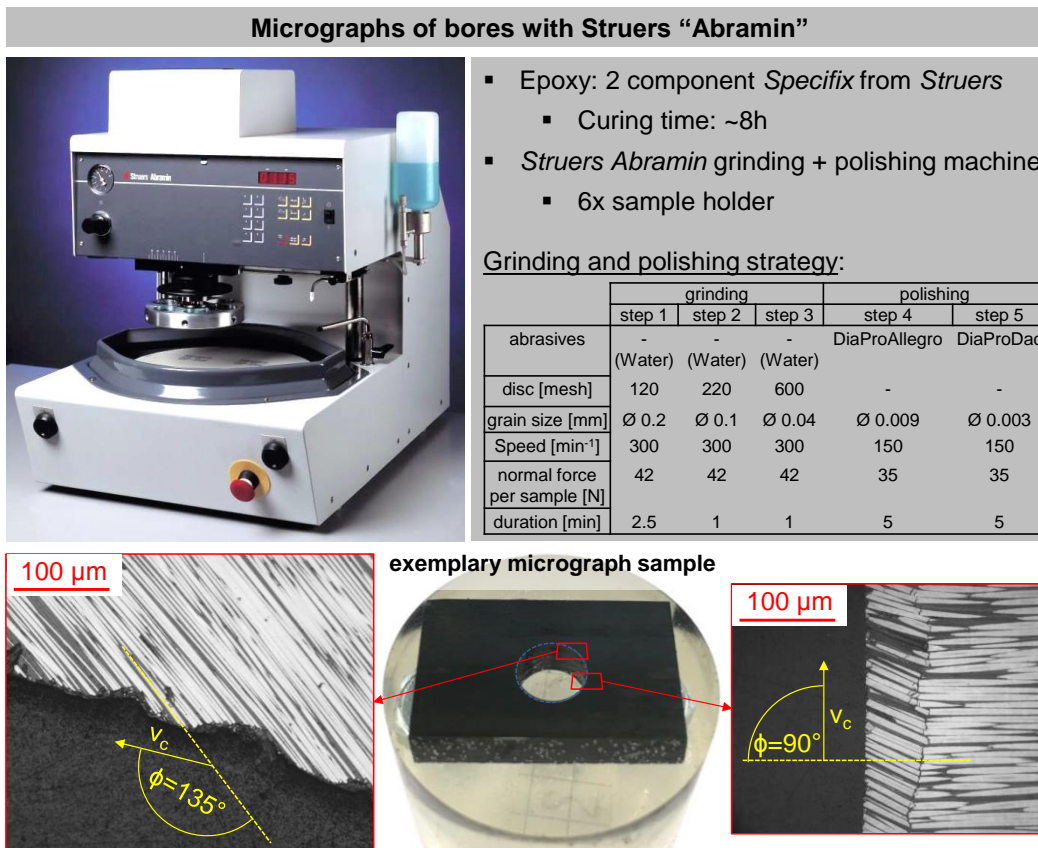


Figure 7.3: Micrograph generation of exemplary bore

According to HENERICHS et al. [99], the residual mechanical strength of a bore is examined by means of a conical pin pull-through-test with a *Schenk* static material testing machine modified and modernised by *Zwick/Roell*. A CVD diamond-coated pin with 100° cone angle is used to expand the bore hole from the drill entrance or exit side as chosen while the force and displacement of the pin in Z direction is recorded, as shown in Figure 7.4. Since the maximum damages in the presented drilling experiments occur at the bore exit side, this is where the mechanical strength tests are implemented. In preparation of the analysis the samples of approximately $24 \times 14 \times 8 \text{ mm}^3$, with the bore to be tested in the centre, are ground at the bore entrance side. In this way the sample has one planar surface, where it is put onto the testing machine table, to prevent setting effects during load initiation. The conical pin is made of cemented carbide with a CVD diamond coating to withstand the wear during relative movement between pin and CFRP while expanding the bore. The cylindrical part of the pin inside the bore has a diameter of $\text{Ø}=6 \text{ mm}$ for good centricity during testing. A 100° cone proved to be suitable. Typical force-displacement curves are measured regularly every 200 bores by means of a load cell and position sensors in the testing machine and are shown in Figure 7.4 (middle). Measurement starts at a pre-load in Z direction of 50 N and ends, when a force of 4800 N is reached (not displayed). The upper limit is chosen, because the analysis does not aim to test total failure of the probe but to display damages at the bore-channel and -exit, which were introduced by the drilling process. Micrographs detect damages at the bore edge up to a depth of $100 \mu\text{m}$. Based on this maximum expected damage depth, the force/displacement gradients are evaluated in this range of $\Delta x=100 \mu\text{m}$, exemplarily presented for two drilling tools in the right graph in Figure 7.4.

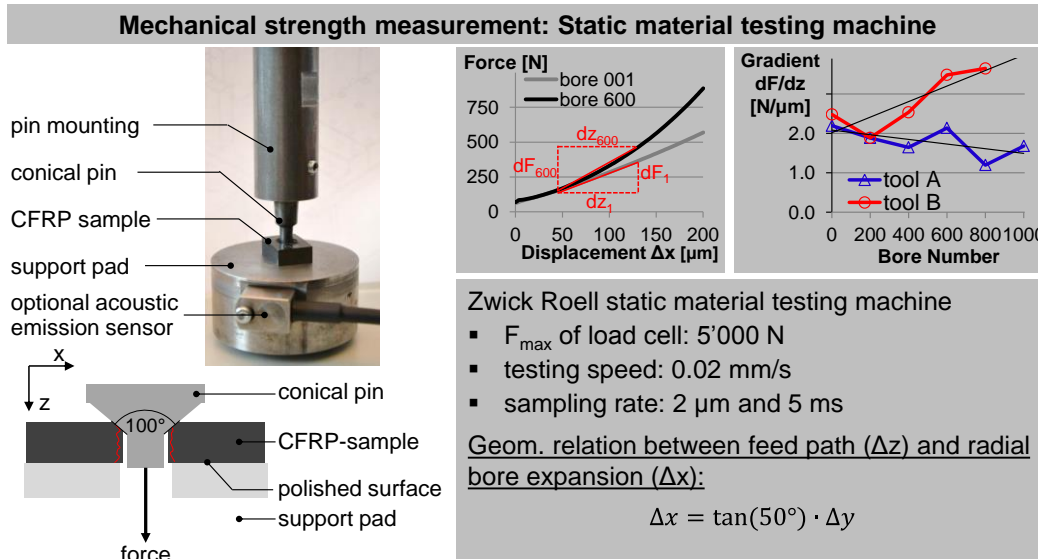


Figure 7.4: Mechanical strength measurement setup

7.2 Cutting edge treatment of diamond-coated drilling tools

According to HENERICHS et al. [101] optimised carbide drilling tool geometries with diamond coating show an initial run-in period, during which the tools cause certain damages at bore exits and manual rework is necessary. Subsequently the drilling tools show a so called self-sharpening effect. The latter effect is characterised by an intensively wearing flank face, while the rake face with heavy loads is still protected by the CVD diamond coating, which results in a resetting and sharpening of the cutting edges. Figure 7.5 shows the bore exit quality development of two exemplary diamond-coated carbide drilling tools, namely geometry A and geometry B, for 1000 bores. These tools show the a run-in period: It takes about 150 bores for geometry A and 250 bores for geometry B to generate good bore exit quality. Afterwards the bore exits are free from uncut fibres or delamination at least until the 1000th bore. Measurements of the cutting edge radius after coating, after 600th and 1000th bore in cutting edge profiles at 80% of the tool radius show a strong decrease with tool wear. Obviously the cutting edge sharpness increases with wear and the bore quality becomes better. Entrance delamination does not occur in general with these drills.

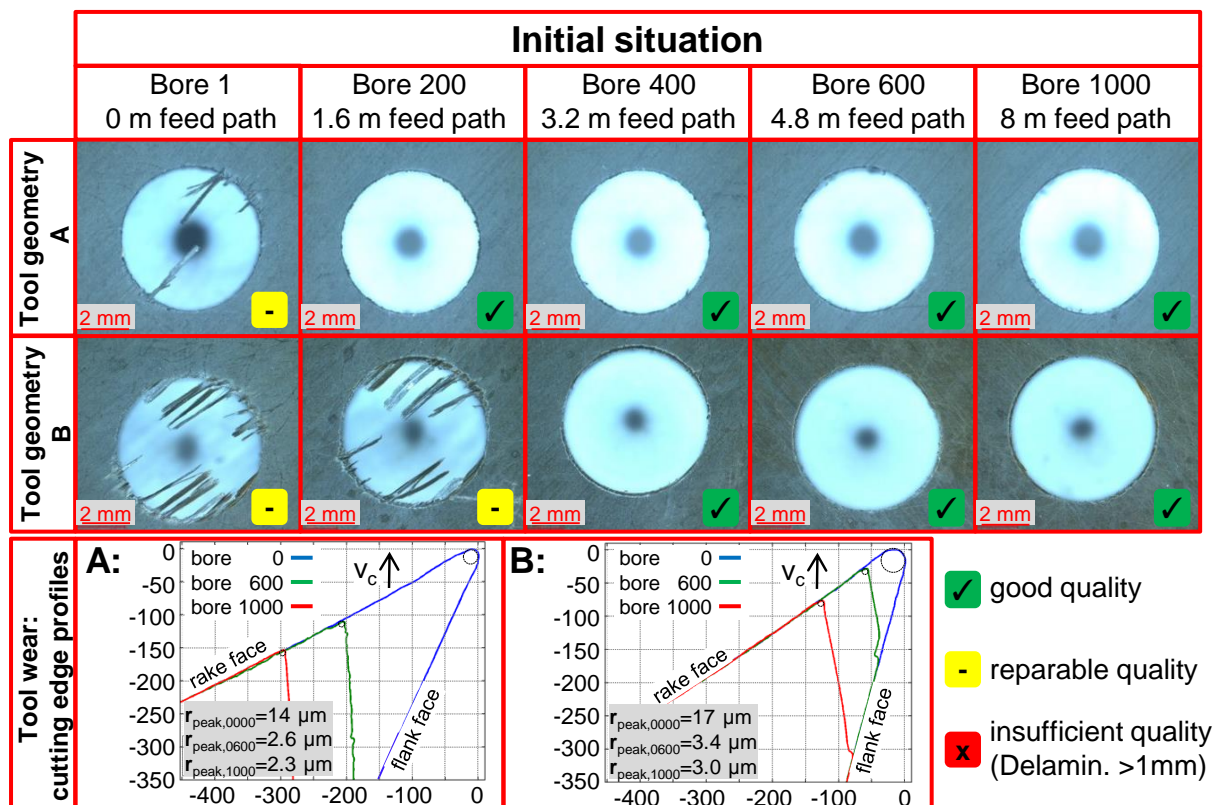


Figure 7.5: Initial bore exit quality of diamond-coated tools and wear profiles; published in [231]

The above mentioned costly extra drilling operations should be avoided in application-ready CFRP drilling tools. It aims to develop diamond-coated CFRP drilling tools, which create initially a good bore quality. Therefore the following trade-off needs to be addressed: On the one hand to benefit from the enhanced tool lifetime by diamond coatings and on the other hand to reduce large peak radii of diamond-coated tools. In this Chapter 7.2 two cutting edge treatment methods subsequent to the diamond coating process of CFRP drilling tools are presented: Tangential laser ablation and abrasive sandblasting. These methods aim to intentionally weaken or abrade the diamond coating locally on the flank face to enable the

self-sharpening effect from the first bore on. The treated cutting edges are tested in CFRP and compared to non-treated diamond-coated tools, which show the above explained initial run-in period with subsequent self-sharpening effect. Analyses with infinite focus microscopy, force measurement and optical microscopy enable evaluation of the two different methods. Part of the following research was published in [231].

7.2.1 Experimental setup

To evaluate the bore quality and tool lifetime of different conventional drilling tools, tests are carried out on a *Mikron VC1000* 3-axis machining centre. The test rig setup and specifications are presented in Figure 7.6. The drilling experiments are conducted under dry machining conditions in CFRP sheet material with a thickness of 8 mm. A schematic illustration of the setup is presented in Figure 7.7, in which two machining positions are distinguished.

- Position one describes the wear tests of up to 1000 bores with $\varnothing=6.35$ mm. These bores are conducted in CFRP sheets of $230 \times 230 \times 8$ mm³, resulting in a total feed path of 8 m. To prevent collision with the surrounding aluminium workpiece fixtures, a distance of the bore centre to the workpiece edges of 15 mm is adhered. Taking a bore distance of 9 mm with square packing into account enables for a maximum of 23 bores per row. The web thickness between the bores is 2.65 mm, so damages between the bores are generally not affecting each other.
- In regular intervals, generally all 200 bores, three consecutive force measurements are conducted at the second machining position in CFRP stripes of $230 \times 24 \times 8$ mm³. Such a stripe is positioned on top of the Kistler dynamometer type 9272 by means of an aluminium fixture, which allows for defined positioning of the probe. Drilling position is in the centre of the dynamometer.

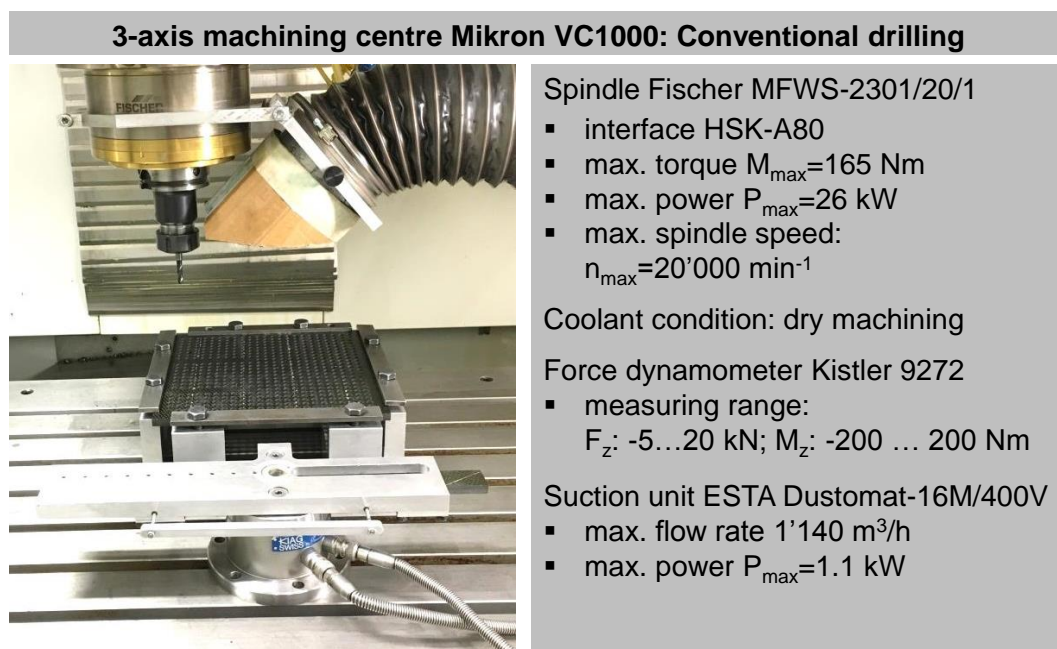


Figure 7.6: Experimental setup and specifications of the machining centre used for drilling tests

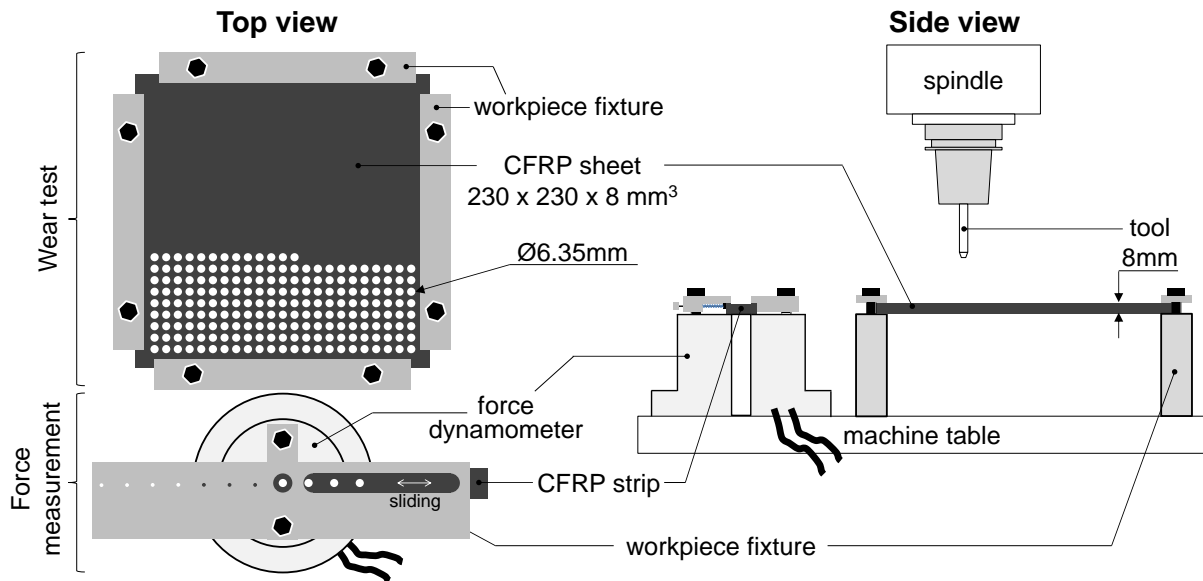


Figure 7.7: Schematic illustration of the setup used for conventional drilling experiments

The examined CFRP multilayer material M21/34%/UD194/IMA-12K with IMA fibres is made of unidirectional prepregs with 66% (by weight) fibre content. It is widely utilized in the aerospace industry. Each layer has a thickness of approximately 180 μm and the matrix material is an epoxy resin HexPly[®] M21. The composite material shows a tensile strength in fibre direction (0°) of 3050 N/mm^2 . The tensile modulus in fibre direction is 178'000 N/mm^2 (0°) and the density is $\rho=1.58 \text{ g}/\text{cm}^3$. An original stack of 44 unidirectional prepreg fibre layers with symmetrical layout $[0^\circ_{11}, \pm 45^\circ_{22}, 90^\circ_{11}]_s$ and epoxy resin is cured in autoclave and cut to plates of dimensions: 230x230x8 mm^3 . These test plates have one rather rough and one polished-like side. The latter is chosen as bore exit side to provoke heavy push out delamination. A top layer of woven glass fibre, which is known to lower delamination defects, is absent in the experiments to ensure all tool wear and material defects are being generated only by the CFRP. Table 7.1 displays the physical and mechanical properties of the machined work piece material.

Table 7.1. Physical and mechanical properties of IMA-12K fibres

Physical properties	fibre	weave/UD	fibre mass [g/m^2]	fibre volume [%]	laminate density [g/cm^3]	glass trans. temp. [$^\circ\text{C}$]
	IMA	UD	194	59.2	1.58	195
Mech. properties	tensile	tensile strength [MPa]	tensile modulus [GPa]	compression	compr. strength [MPa]	compr. modulus [GPa]
	method EN6032	3050	178	method EN2561 B	1500	146

Two different drilling tool geometries, namely A and B, with the same nano-crystalline diamond coating of slightly different thickness and different carbide material (both 6% Co) are tested. The WC-Co-substrate material of geometry A is MG12 of the company *Ceratizit* with a grain size of 0,5 - 0,8 μm and a Vickers hardness of 1790 HV30, while the WC-Co-substrate of geometry B is EMT 100 of the company *Extramet* with an average grain size of 0,8 μm and the same Vickers hardness of 1790 \pm 50 HV30. Both geometries are spiral drills with similar point and helix angles and two main cutting edges. The chisel edge shows an

intensive web thinning, as being common in CFRP machining for delamination reduction. Figure 7.8 shows the tool specifications.

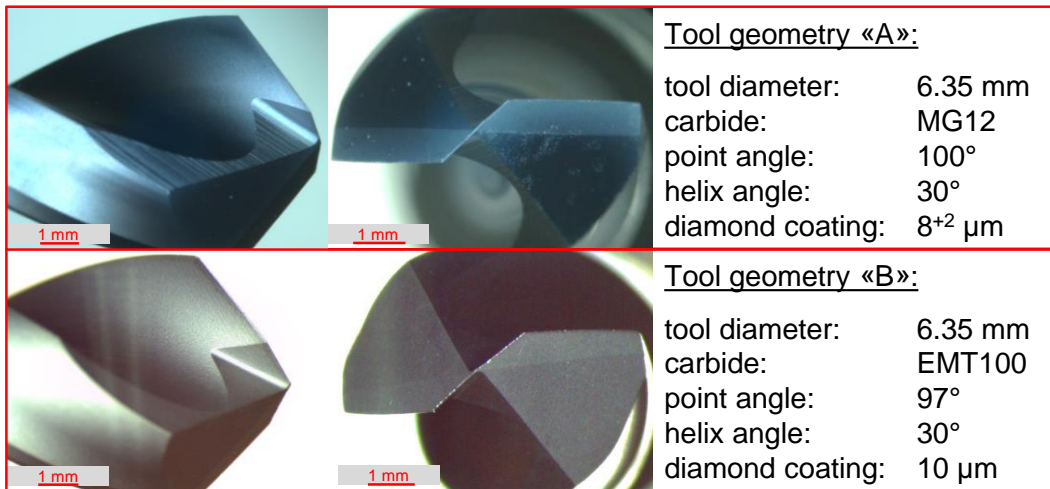


Figure 7.8: Tool geometries and coating thickness; published in [231]

Tangential Laser Ablation

This treatment method is conducted on a modified *EWAG* Laser Line. The machine is equipped with an Nd:YVO₄ ultrashort pulsed laser of the company Time-Bandwidth (Fuego™) which emits light in a wavelength of 1064 nm. The laser beam is guided through a hurrySCAN II® scan head of *Scanlab* with two axes and feed speeds up to 7 m/s. The material at the cutting edge is removed by tangential laser ablation process from the tools flank face with reciprocating movement of the laser beam parallel to the cutting edge; see Figure 7.9 and Figure 7.10. The infeed in X-direction between the three separate tangential ablation processes is 15 μm for one roughing and 10 μm for each of the two dressing steps. Laser parameters used: Power of 28.3 W, 800 kHz pulse frequency, 0.6 mm/s vertical feed and 500 mm/s scanner feed, ~0.5 mm Rayleigh length, ~30 μm focus diameter.

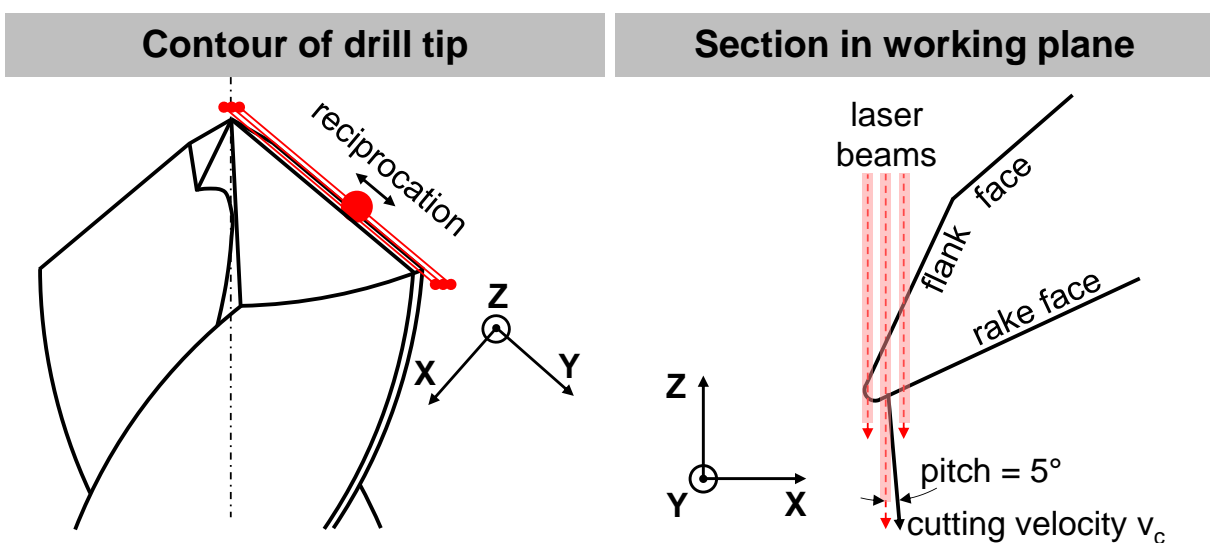


Figure 7.9: Schematic illustration of laser beam control during laser ablation; published in [231]

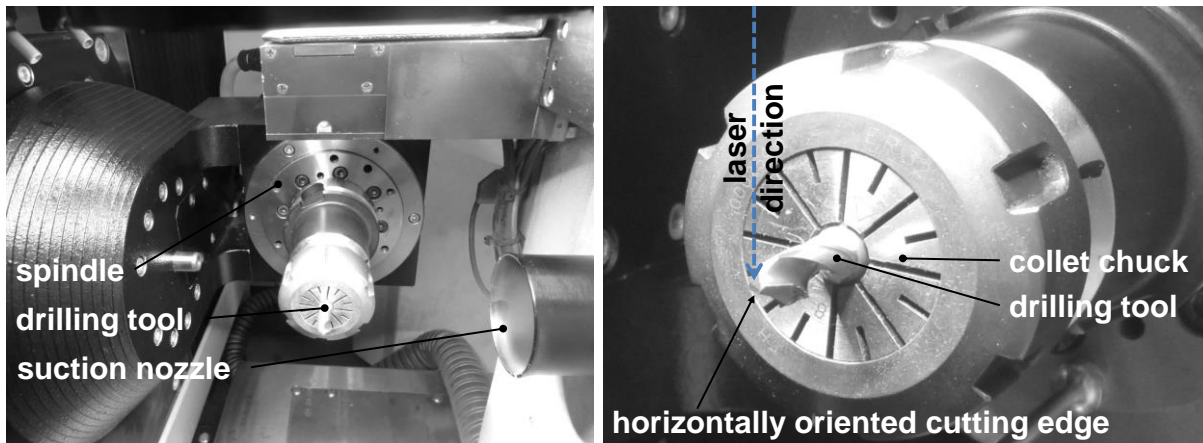


Figure 7.10: Overview of drilling tool in the chuck of the *EWAG Laser line* (left) and vertical direction of laser beam (right)

Sandblasting

Selective sandblasting of the cutting edges is applied to induce cracks in the coating on the flank face or erode it locally to shorten the run-in period. The jet nozzle with 1.8 mm diameter is mounted onto a six axes robot, which orients the sandblast vertically on one cutting edge flank face, shown on the right in Figure 7.12. During sandblasting the robot performs a reciprocating motion parallel to the cutting edge, as illustrated in Figure 7.11. This serves for 2D distribution of fluctuations in the abrasive grain density of the sandblast. The sandblasting parameters, presented in Table 7.2, are evaluated in a foregoing parameter study and are in accordance with analyses by WYEN [254]. This parameter study showed that high air pressure of 6 bars is necessary to erode the CVD diamond coating with the Al_2O_3 particles (F320 mesh). A nozzle distance of 15 mm generates maximum removal. A reciprocating motion with 5 mm/s feed rate and 360 times overrun resulting in 3 min duration of sandblasting on each position along the flank face is applied to harm the CVD diamond coating. The turning points of the reciprocation are situated 3 mm outside of the component.

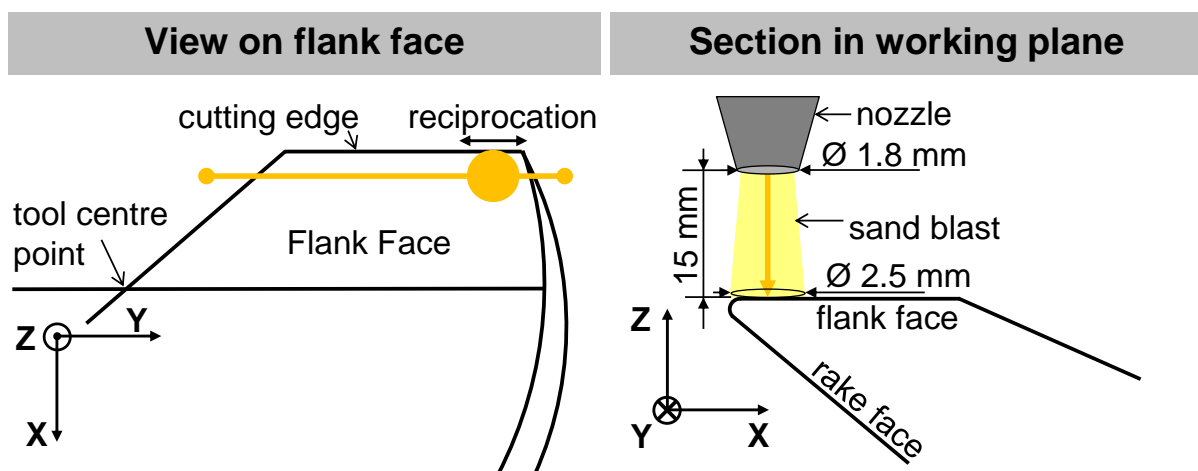


Figure 7.11: Schematic illustration of control during sandblasting; published in [231]

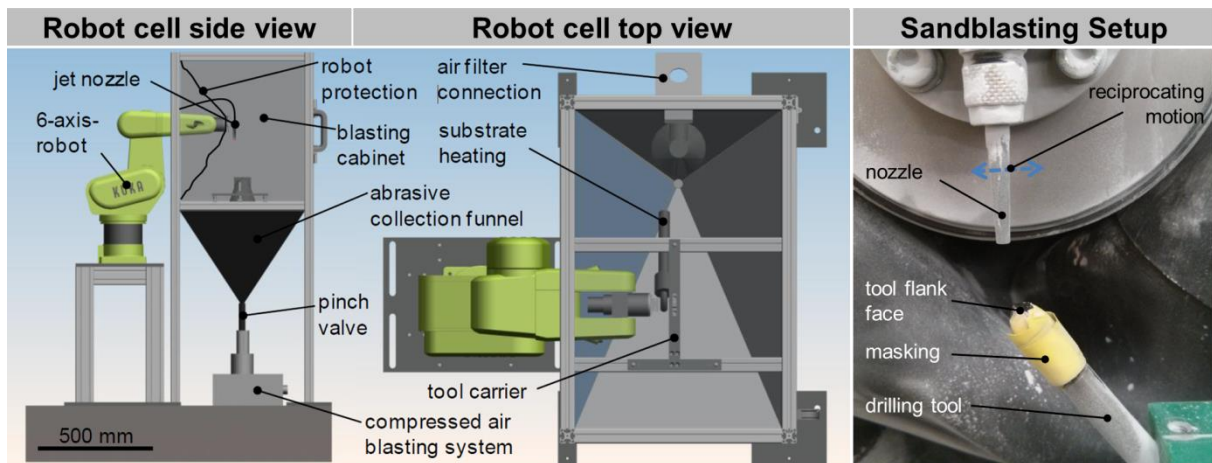


Figure 7.12: Sandblasting robot cell and setup for reproducible erosion of diamond coating, according to WYEN [254].

Table 7.2: Parameter-set for the sandblasting process

Parameter	Value
Abrasive material	Al_2O_3
Grain size	F320
Nozzle width	1,8 mm
Blasting angle	90° -normal to flank face-
Feed	5 mm/s
Nozzle distance	15 mm
Air pressure	6 bar

7.2.2 Drilling results

Standard diamond-coated drilling tools are compared with those treated by the two methods explained above subsequent to the coating process. The first two rows in Figure 7.13 show the diamond-coated tools after treatment. While the tangentially lasered tools A2L and B2L show an evenly reset cutting edge with exposed carbide material shining on the flank face and faultless diamond coating on the rake face, the sandblasted tool A3S has multiple irregular break-outs of the diamond coating all along the cutting edge. The diamond coating on the rake face of the tool – being averted to the sandblast – shows chipping defects up to 30 μm distant to the original cutting edge. It is hardly possible to fit a peak radius in the cutting edge profile (bottom of Figure 7.13) after sandblasting ($r_{\text{peak}} \approx 5.7 \mu\text{m}$). Although the sandblast ($\varnothing \approx 2.5 \text{ mm}$) treated a 2.5 mm wide zone parallel to the cutting edge, the diamond coating in the residual zone of the flank face does not seem to be affected.

The 3rd and 4th row in Figure 7.13 show the wear status of A2L, A3S and B2L after drilling 200 bores in 8 mm thick CFRP. The analysis of the micro-geometry at 80% of the radius of each tool is presented in the 5th row after coating (blue), cutting edge preparation (green) and machining (red). Coloured bars in the pictures of the 1st and 3rd row mark the respective profile analysis position. The breakouts of A3S become worse after drilling 200 bores and the exposed carbide shows rounding up to 10 μm radius. The lasered tools show an even wear on the flank face being proportional to the length of cut. A break out of the $8^{+2} \mu\text{m}$ thick

coating of A2L occurs on the rake face at the cutting edge corner, which certainly affects the machining quality. In this area of the cutting edge, which generates the final bore surface, the carbide is no longer protected by the coating and starts to be rounded. Tool B2L does not show such an error. It cannot conclusively be stated if initial damages in the coating are introduced by the laser operation, process forces exceed the coating stability due to specific tool geometry A, or the different substrate materials of geometry A and B influence the coating adhesion. Besides this single defect the remaining diamond-coated cutting edge of A2L becomes even sharper with wear: $r_{\text{peak},50}=2.2 \mu\text{m}$ (not displayed) and $r_{\text{peak},200}=2.3 \mu\text{m}$. The same effect – increasingly getting sharper cutting edge with tool wear – occurs at tool B2L: The cutting edge radius after laser preparation is about $3 \mu\text{m}$ and after drilling 200 bores even smaller with $r_{\text{peak},200}=2.8 \mu\text{m}$.

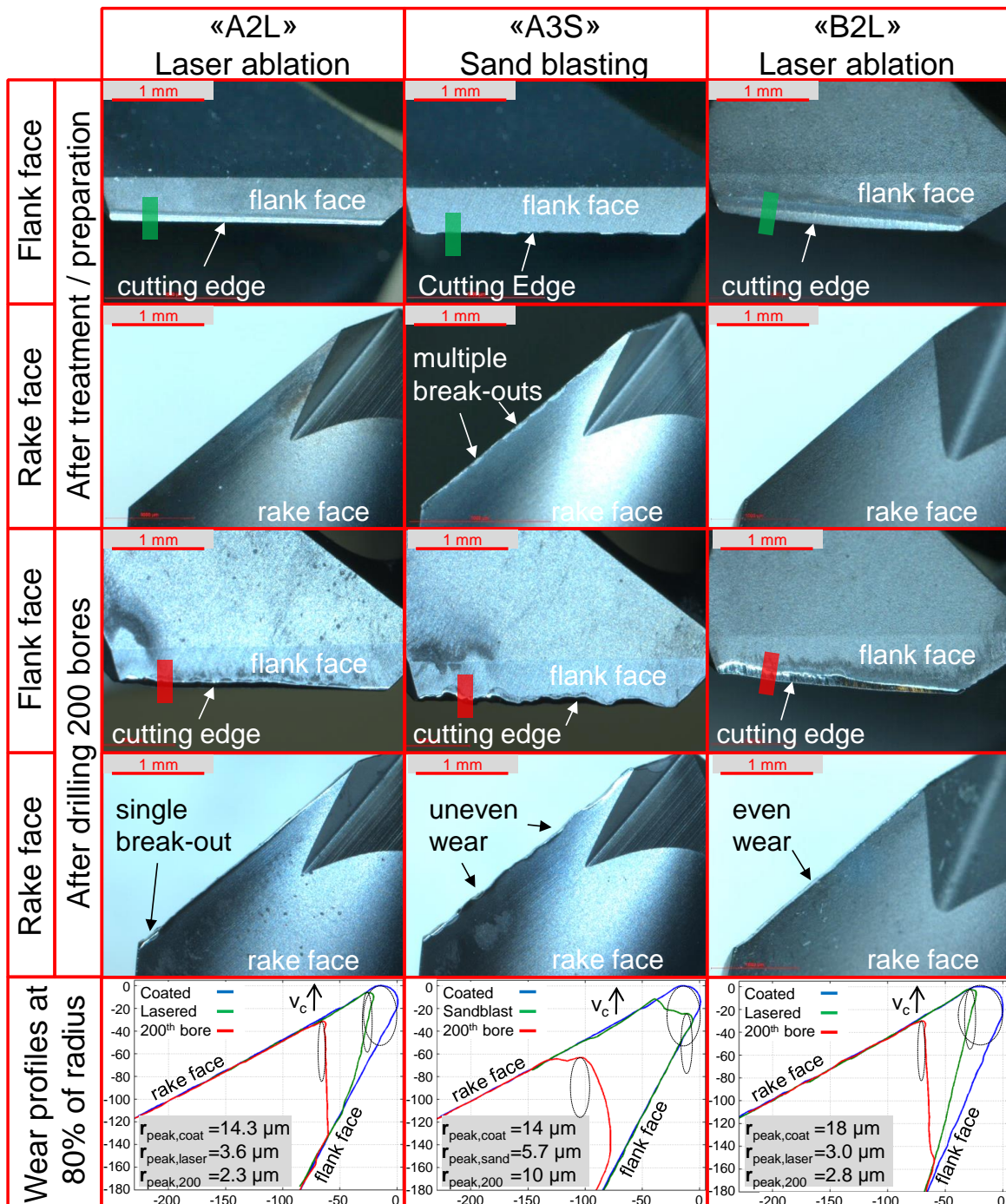


Figure 7.13: Microscopy of cutting edges and wear profiles; published in [231]

Figure 7.14 shows the associated thrust forces (solid lines) and torques (dashed lines) of the prepared tools in comparison to the reference tools B1R and A1R. Due to the above described favourable micro-geometry the thrust forces for the laser prepared tool B2L are constantly 15-20 N below the reference B1R. The laser treated tool A2L is 10-17 N below the reference A1R for the first 100 bores and subsequently equal to A1R. While the torque of the tool B2L is reduced by 1 - 2.3 Ncm during first 200 bores, the torque of A2L reduced by even 5 - 6 Ncm for 50 bores. Subsequently the effect of laser treatment on the torque fades and the tool is equal to the reference. The thrust force of the sandblasted tool A3S starts on the same level as the reference tool A1R but increases rapidly within 50 bores from 59.6 N to 85.1 N (+43%) due to adverse wear and cutting edge rounding; The same effect but on a weaker scale can be recognized for the torque of A3S.

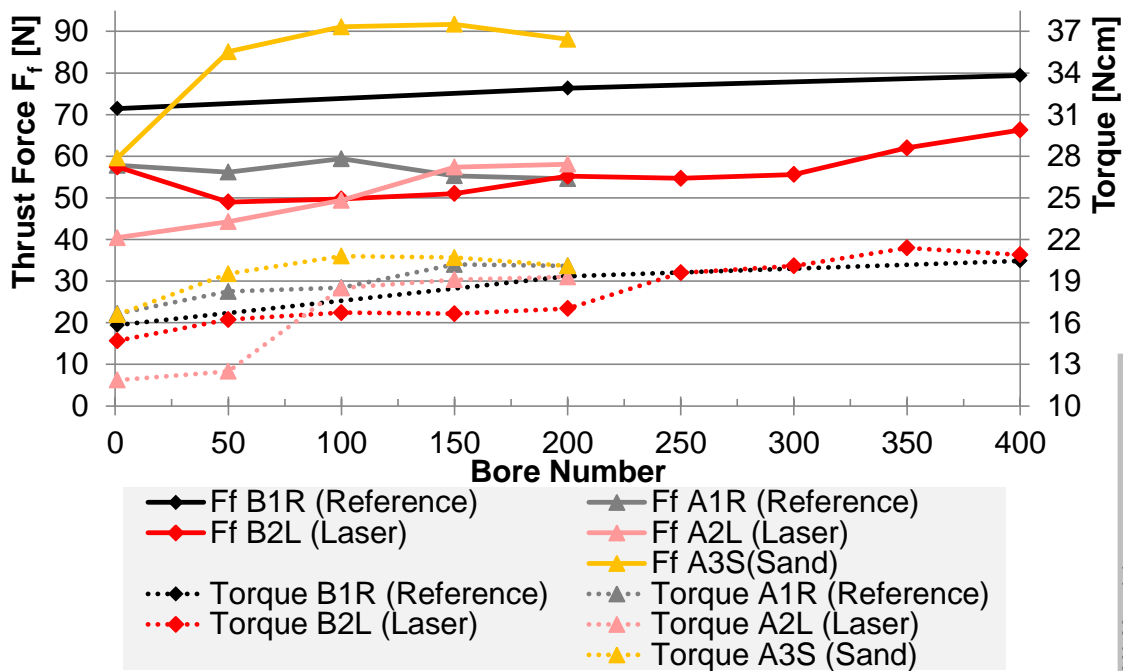


Figure 7.14: Thrust force and torque measurements; published in [231]

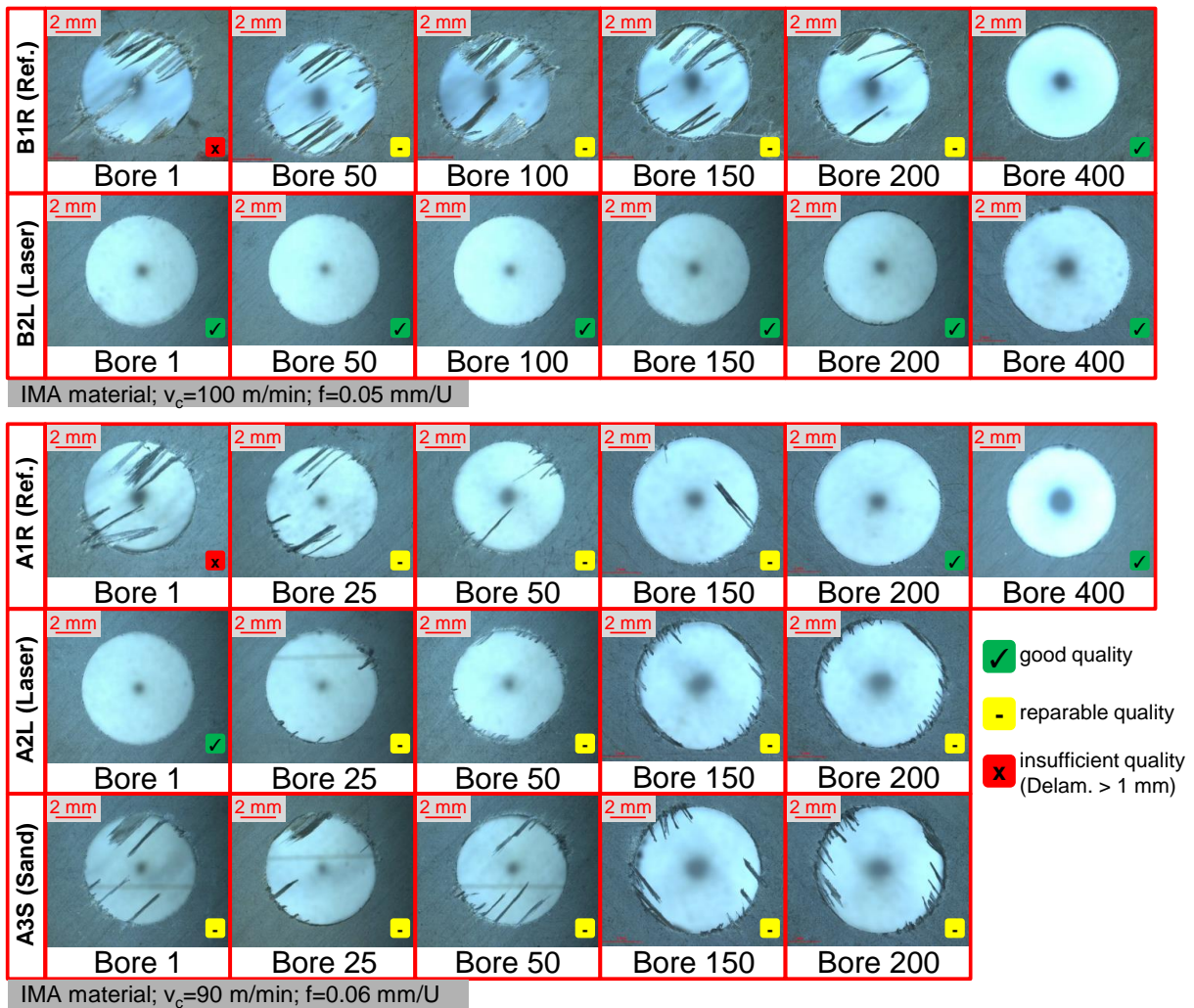


Figure 7.15: Comparison of bore exit qualities for differently-prepared tools; published in [231]

Figure 7.15 verifies the favourable micro-geometry of the laser prepared tool B2L and at least initially of A2L, with increased bore exit quality compared to the reference tools. Especially B2L with thick coating and MG12 carbide convinces by extraordinary drilling results from the first bore on without uncut fibres nor delamination at the bore exits. The comparison of the profile analysis in Figure 7.13 and Figure 7.5 at the state of 200 bores shows that a constant wear status is reached and the period of poor bore quality is actually skipped for the laser-treated tool. Tool A2L with identical laser treatment, but 8^{+2} μm coating thickness and MG12 substrate, shows also an initially increased bore exit quality. But due to the breakout on the rake face and an increasingly rounded cutting edge in this area the amount of uncut fibres increases after the 1st bore of A2L. The bore exit quality of the sandblasted tool A3S is worse compared to the reference A1R corresponding to the wear pattern in Figure 7.13 and the process forces in Figure 7.14.

7.2.3 Conclusion cutting edge treatment

Precondition for the laser-treated cutting edges, generating improved results, is that the tool macro-geometry is basically suitable for machining the chosen CFRP material. Best results are achieved if the tool shows a sharpening effect with progressing wear. Self-sharpening occurs, when the tool wear generates a suitable micro-geometry and the iterating process is self-stabilising with increasing tool wear. A generally suitable micro-geometry for CFRP

machining is characterised by a small cutting edge radius (range: 2-4 μm) in combination with a short length l_v , as being explained by HENERICHS [101]. In this way, damages in the workpiece may be avoided. MAEGAWA et al. [151] describe the self-sharpening effect being based on different wear progressions of a thin coating with high hardness and a softer carbide.

Summarising the results, it is possible to increase the sharpness of diamond-coated cutting tools by picosecond laser ablation: Cutting edge radii of 3-4 μm are achievable with diamond coating still protecting the rake face, resulting in outstanding bore qualities in CFRP. The phase with poor bore quality during initial bores of diamond-coated tools is completely skipped. The thrust forces are reduced durably by 20 - 30% (-14 N to -21 N) compared to a diamond-coated reference tool. In contrast to the laser process, the presented selective sandblasting process harms the coating along the cutting edge and rake face, resulting in declining bore quality. Consequently, sandblasting with the described process is unsuitable to improve the tool micro-geometry of the cutting edge. The influence of the treatment method on the overall tool lifetime has not been examined.

7.3 Orbital drilling vs. conventional drilling

Hard to machine CFRP materials and material combinations with specific unidirectional layups with high fibre content are widely used in the aerospace industry, to reach the high mechanical specifications of structural components. Inter alia BOLDT and CHANANI [18] as well as TETI [218] indicated the possibility of reducing bore exit damages by tool geometry and process optimisation to some degree. Even though conventional drilling processes in CFRP are in the focus of research and the corresponding tools are further improved, in high-end applications with advanced material combinations this process pushes more and more to its limits; e.g. in drilling particular unidirectional CFRPs and countermeasures against delamination upon exit like back-up support or glass fibre top-layers are unfeasible. In these cases the economics show the limits, due to insufficient bore quality and necessary manual rework. Main reason for conventional drilling to cause bore exit delamination is the critical intervention condition with zero-speed in the tool centre, explained by LINDQVIST et al. [149].

Orbital drilling, in which the tool travels along a helical path is also heavily investigated [20, 56, 130, 149, 150, 166] and offers itself as suitable alternative in the above mentioned hard to machine materials. Orbital drilling supposed to generate better bore quality due to advantageous chip extraction and cutting conditions. In this Chapter the two different methods conventional and orbital drilling are compared in terms of bore quality, tool wear, diameter variances as well as cycle times. Therefore detailed analyses of bore-exit and -channel quality by micrographs, 3D microscopy and conical expansion tests are conducted. The comparison with optimised diamond-coated tools and process parameters enables direct evaluation of the two different drilling processes. Part of this section is published in [233].

7.3.1 Experimental setup

Conventional drilling and orbital drilling experiments have each been conducted on a similar test rig and in the same difficult-to-machine CFRP material. While the conventional drilling experiments are conducted on a *Mikron* VC1000 milling machine tool, shown in Figure 7.6, the orbital drilling experiments are conducted on a highly dynamic parallel kinematic Hexaglide machine tool, shown in Figure 7.16. This machine tool is developed at the Institute of Machine Tools and Manufacturing (IWF) at ETH Zurich and further details can be found in the doctoral thesis of HEBSACKER [93]. Force measurement is implemented at the workpiece using Kistler dynamometers type 9272 (conv. drilling) and type 9254 (orb. drilling). In conventional drilling thrust forces and torque are measured, while in orbital drilling one axial and two lateral process forces are recorded.

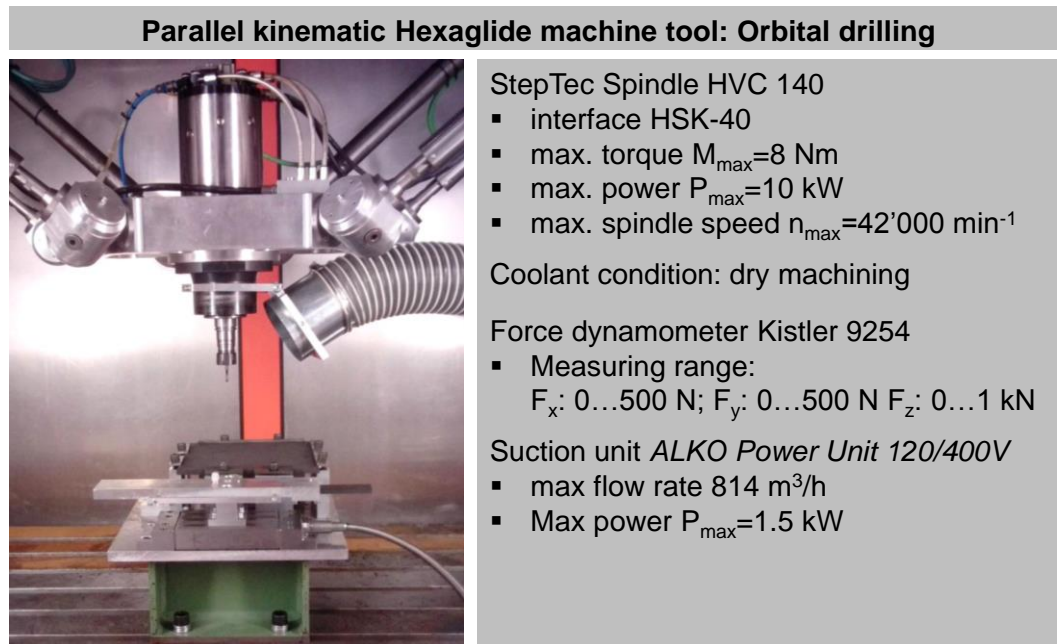


Figure 7.16: Conventional and orbital drilling test rigs

The examined CFRP multilayer material (AS4 fibres) is known to be challenging to drill and made of unidirectional prepregs with 62% (by volume) fibre content. Each layer has a thickness of approximately 0.12 mm and epoxy resin has been chosen as matrix material. This composite material shows a tensile strength in fibre direction (0°) of 2'137 N/mm² and perpendicular to fibre direction (90°) of 81 N/mm². The tensile modulus in fibre direction is 141'000 N/mm² (0°) and the density is $\rho=1.6$ g/cm³. An original stack of 68 unidirectional prepreg fibre layers with symmetrical layout $[0^{\circ}_{32}, \pm 45^{\circ}_{24}, 90^{\circ}_{12}]_s$ and epoxy resin is cured in autoclave and cut to plates of dimensions: 230x230x8 mm³. These test plates have one rather rough and one polished-like side. The latter is chosen as bore exit side to provoke heavy push out delamination.

Cemented carbide spiral drills, displayed in Figure 7.17, with nano-crystalline diamond coating of 8+2 μ m thickness are used for conventional drilling. The tool diameter is 6.35 mm and the geometry is adapted to CFRP machining. A typical cutting speed of 90 m/min and a feed of 60 μ m/rot are set for the experiments. The same geometry is applied for the drilling experiments for validation of the bore exit evaluation approach in 6.3.

The orbital drilling endmill tools of $\varnothing=5$ mm are also made of cemented carbide to drill bores of $\varnothing=6.35$ mm. The same diamond coating as for the conventional drilling tools is applied. Tools with 3 teeth are chosen, because a foregoing parameter study resulted in an underperformance of 4 or more-fluted tools regarding bore quality due to disadvantageous chip evacuation. Orbital drilling tools with just 2 teeth show a rapid decrease of bore diameter with wear. Based on this parameter study the following values are sufficient for this application: Cutting speed of 160 m/min ($n_{\text{rot}}=10'190$ /min); revolution in clockwise direction (up-milling) with eccentricity of 0.675 mm; axial feed velocity of $v_{f,a,h}=105$ mm/min and tangential feed velocity of $v_{f,t,h}=535$ mm/min resulting in a helical pitch of 11.12° ($n_{\text{rev}}=126.1$ /min). These parameters result in an axial and tangential feed per tooth of $f_{z,a}=3.44$ μ m/rot/tooth and $f_{z,t}=82.3$ μ m/rot/tooth. Each tool is tested for 1000 bores or a total axial feed path of 8 m.

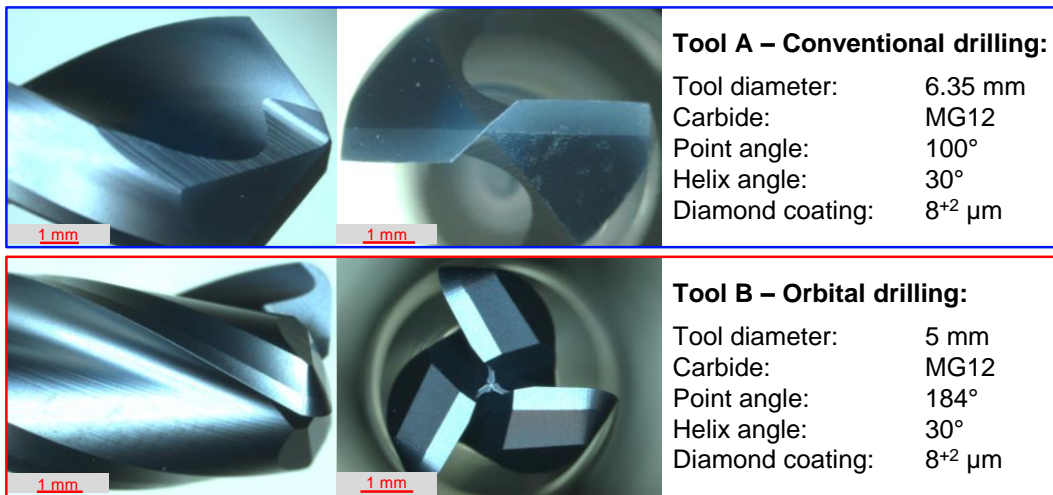


Figure 7.17: Side view and top view of diamond-coated conventional (A) and orbital drilling (B) tools; published in [233]

7.3.2 Drilling results

The pictures in Figure 7.18 clearly show some uncut fibres and delamination at the bore exits of the unidirectional CFRP material. The first row presents regular bore exit qualities of the conventional drilling Tool A for a series of 1000 bores. With increasing bore number the amount of uncut fibres increases, as well as the extent of delamination in the vicinity of the bores, distinguishable by miscoloured height information. The second row shows the bore exit quality of the orbital drilling process with Tool B. At a first glance the general quality of Tool B seems to be better than with conventional drilling and it even improves with increasing number of bores.

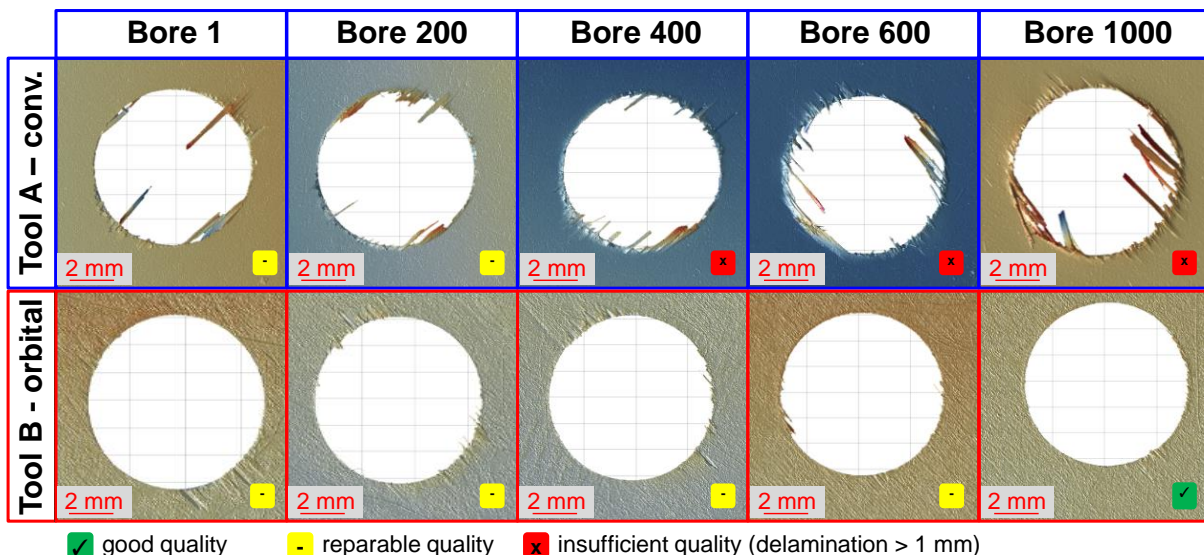


Figure 7.18: 3D microscope pictures (miscoloured) of bore exits; published in [233]

The bore exit quality can be described by the comprehensive damage value Q_d with equal weighting of the damages inside and outside the bore as presented in Chapter 6; the applied equation is presented in Figure 7.19. The diagram shows a comparison of Q_d and the common delamination factor F_d introduced by CHEN [44] for both drilling processes. This factor is represented by dashed lines and apparently is unsuitable for quality evaluation in unidirectional CFRP; Scattering of the maximum extend of delamination superimposes the

bore quality. In fact a better correspondence to the microscope images in Figure 7.18 is shown by the damage value Q_d . Conventional drilling with Tool A generates a decreasing quality over 1000 bores with increasing damage value $Q_{d,0001}=0.73$ to $Q_{d,1000}=1.5$. The orbital drilling process shows a lower damage level between $0.07 \leq Q_d \leq 0.61$, with an initially decreasing quality between 1st and 200th bore. Afterwards the quality is continuously getting better until the 1000th bore.

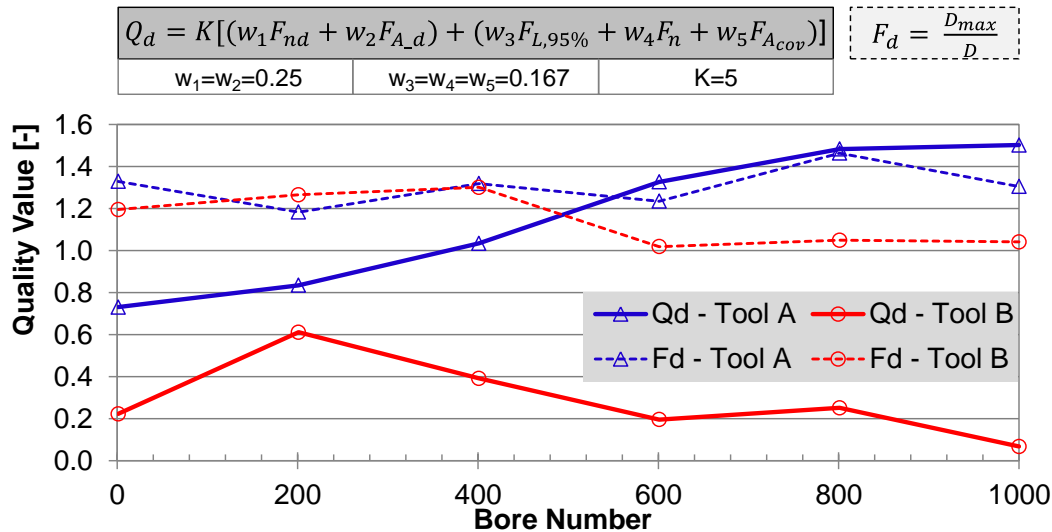


Figure 7.19: Evaluation of bore exit quality by Q_d and F_d ; published in [233]

Figure 7.20 shows the axial thrust forces (solid lines) as well as the torque for Tool A and the lateral thrust forces for Tool B (dashed lines). The analyses are based on three consecutive measurements every 200 bores. Due to heavy tool wear, the thrust force in conventional drilling increases progressively, while the torque increases almost linearly. The high thrust forces of Tool A (conv. drilling) cause the immense delamination and uncut fibres, presented in Figure 7.18 and Figure 7.19. The axial thrust forces of Tool B remain on a low level over 1000 bores (<66N), due to avoidance of zero-speed on tool axis by relief groove and orbital drilling process. Simultaneously an almost linear increase of the lateral thrust force $F_{f,l}$ arises from 9 N to 25 N at 1000th bore.

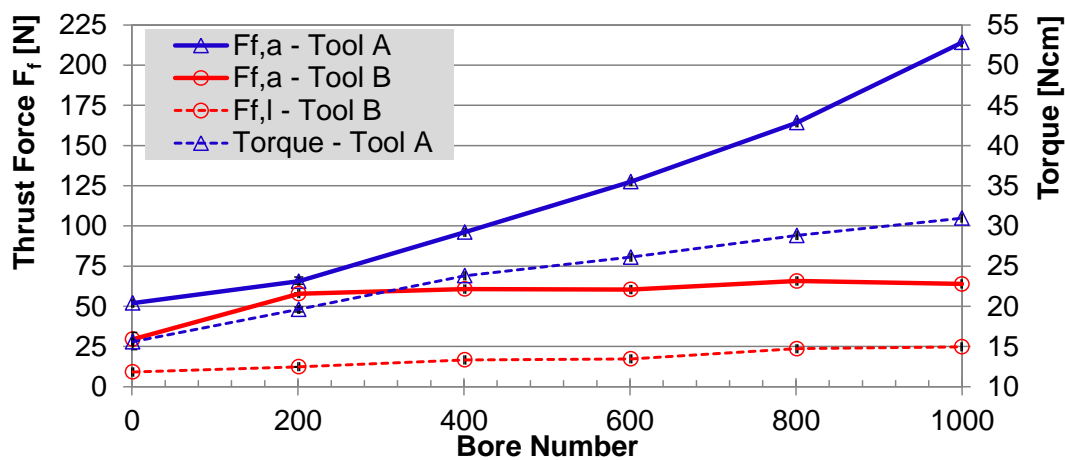


Figure 7.20: Thrust force ($F_{f,a}$) and torque of conventional drilling (Tool A); axial ($F_{f,a}$) and lateral force ($F_{f,l}$) of orbital drilling (Tool B); published in [233]

Micrographs perpendicular to the bore axis have been prepared regularly every 200 bores for both machining processes. Fibre cutting angles of $\phi=90^\circ$ and $\phi=135^\circ$ are known to be

sensitive for subsurface fibre cracks, fibre pull-outs and saw teeth profiles [230]. Figure 7.21 shows a selection of the most sensitive fibre cutting angle for the 1st, 400th and 1000th bore of each machining process. The microscope images in the lower two rows show a smooth and almost damage free bore channel for the orbital drilling process (Tool B) over 1000 bores; Only single fibre pull-outs occur. The microscope images in the upper two rows in Figure 7.21 present a worse bore channel quality of conventional drilling in comparison to orbital drilling below: Especially at the 400th and 1000th bore fibre cracks occur up to 40 μm below the surface. For $\phi=90^\circ$ the fibres are bend in cutting velocity direction up to 100 μm below the surface, presumably due to high mechanical load. For $\phi=135^\circ$ and the 1000th bore of Tool A, single saw teeth are introduced.

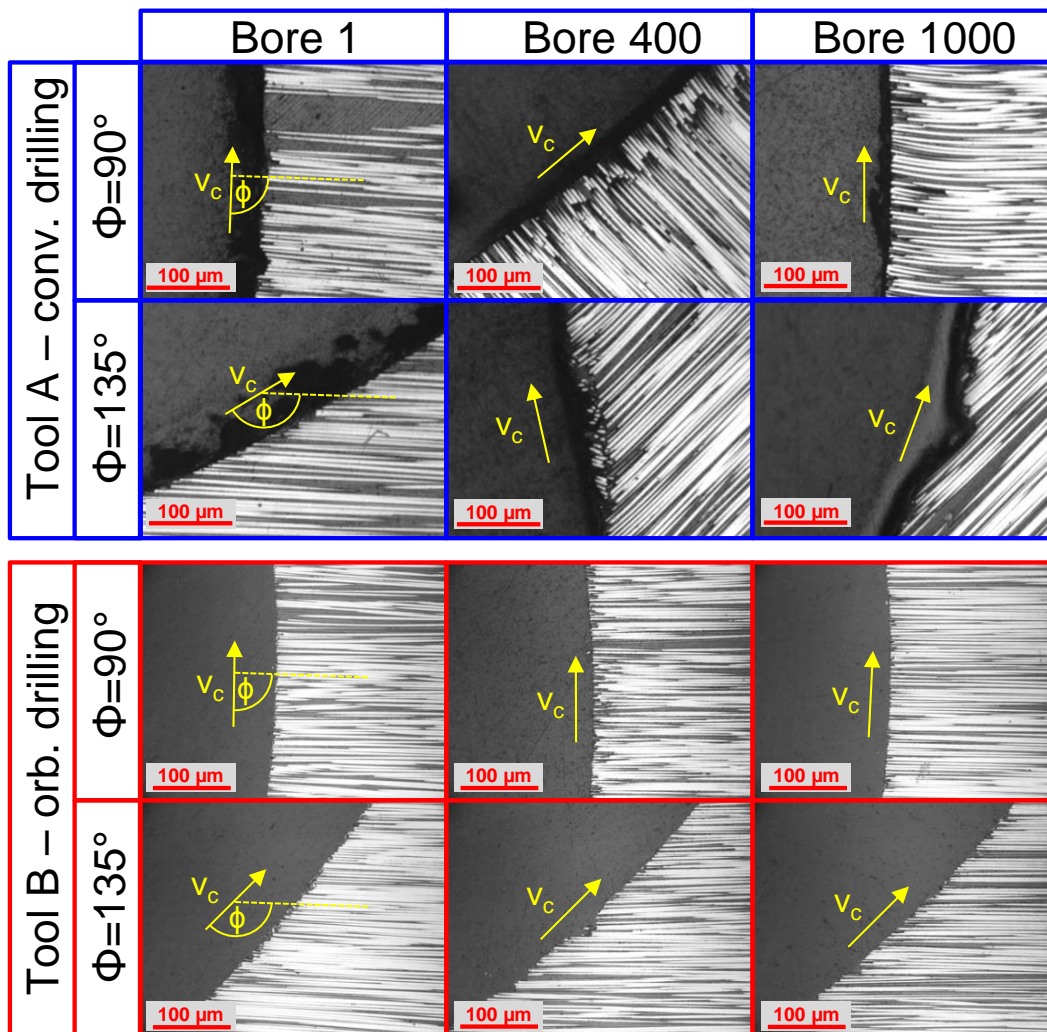


Figure 7.21: Comparison of micrographs at 1st, 400th and 1000th bore with critical fibre cutting angles $\phi=90^\circ$ and $\phi=135^\circ$; published in [233]

Additional analyses of the resulting material strength at the bore exit have been used to compare the quality in conventional and orbital drilling of CFRP. Typical force-displacement curves are measured regularly every 200 bores and are evaluated by the force/displacement gradient in the maximum expected damage depth of $\Delta x=100 \mu\text{m}$, according to the micrographs. The first 200 bores of Tool B show a decreasing gradient, meaning the strength of the 200th bore is lower than that of the first bore. Afterwards the strength is continuously increasing. Tool A shows an overall trend of decreasing strength, in general below the strength of the bores generated by orbital drilling. Interestingly the force/displacement

gradients of Tool B and at least partially of Tool A show a very good correlation to the quality value Q_d , presented in Figure 7.19. This fact proves the suitability of the mechanical strength tests with conical expansion devices for bore quality evaluation in CFRP drilling.

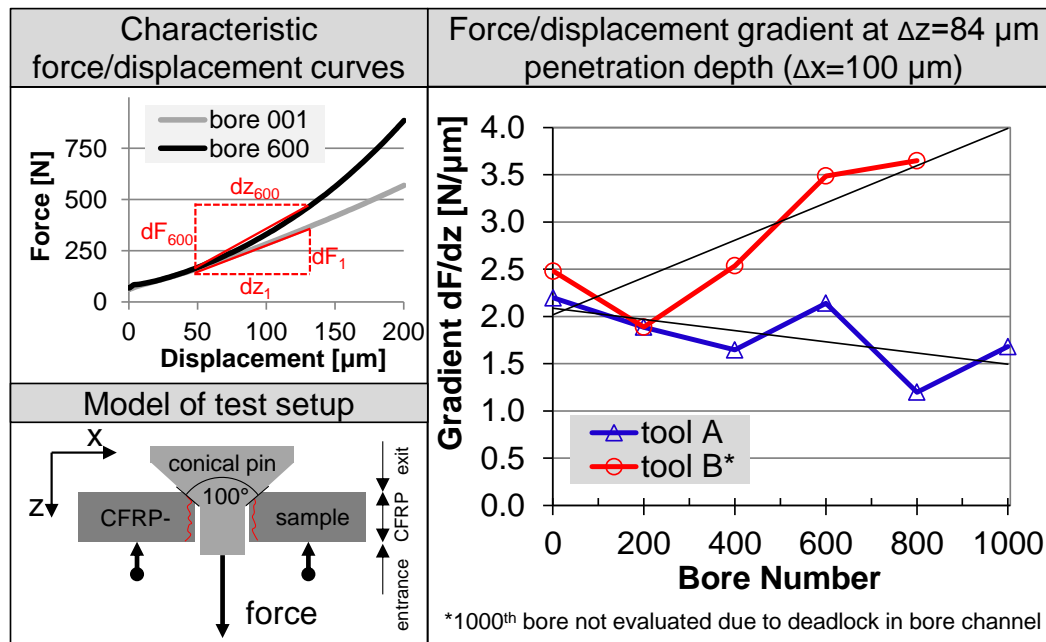


Figure 7.22: Expansion tests of bore exits with conical pin for strength analysis according to HENERICHS et al. [83]; published in [233]

Besides bore channel and bore exit quality, the achievable diameter tolerance is a critical value to choose a machining process for a certain application. Usually the bore diameters are decreasing with progressive tool wear. In conventional drilling of CFRP, heavy wear appears on the flank faces of the main cutting edges, as presented by microscopy of tool wear in Figure 7.24. In conventional drilling the peripheral lands wear less, compared to orbital drilling with interrupted cuts at peripheral edges, typically resulting in smaller diameter deviations. In this series a diameter variance of $14.9 \mu\text{m}$ (IT7) occurs in conventional drilling with diamond-coated Tool A over 1000 bores, presented in Figure 7.23. The orbital drilling process with Tool B generates a higher bore diameter variance of $39.1 \mu\text{m}$ (IT10) over 1000 bores. However, regular diameter measurements show that for the first 800 bores the diameter variance ($\Delta\varnothing_{\text{orb.,0-800}}=14.6 \mu\text{m}$) is in the same small range as in conventional drilling ($\Delta\varnothing_{\text{conv.,0-800}}=14.9 \mu\text{m}$); A heavy decrease occurs only after the 800th bore. This effect is caused by the failure of the diamond coating on the peripheral cutting edges of Tool B, shown by microscope images at the wear state after the 1000th bore in Figure 7.24.

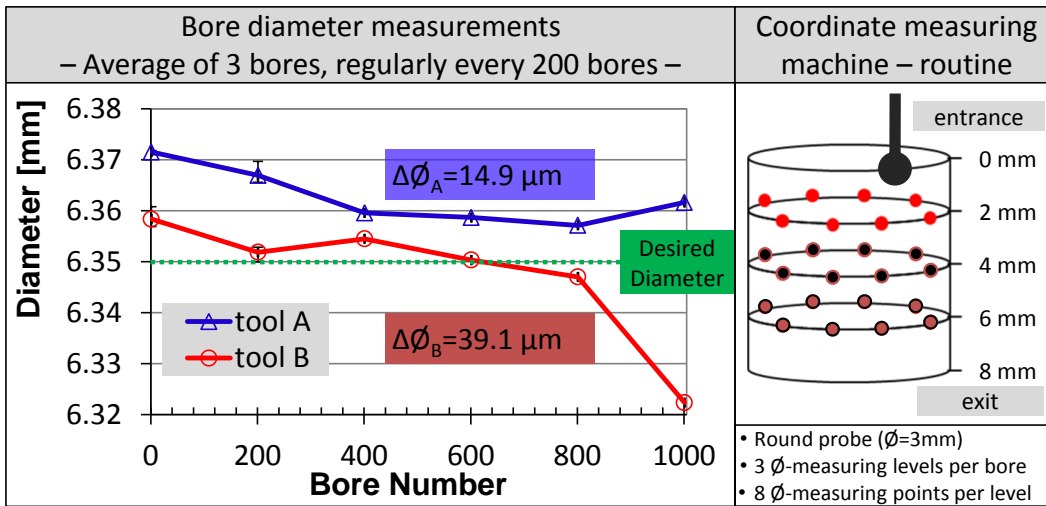


Figure 7.23: Bore diameter measurements with coordinate measuring machine; published in [233]

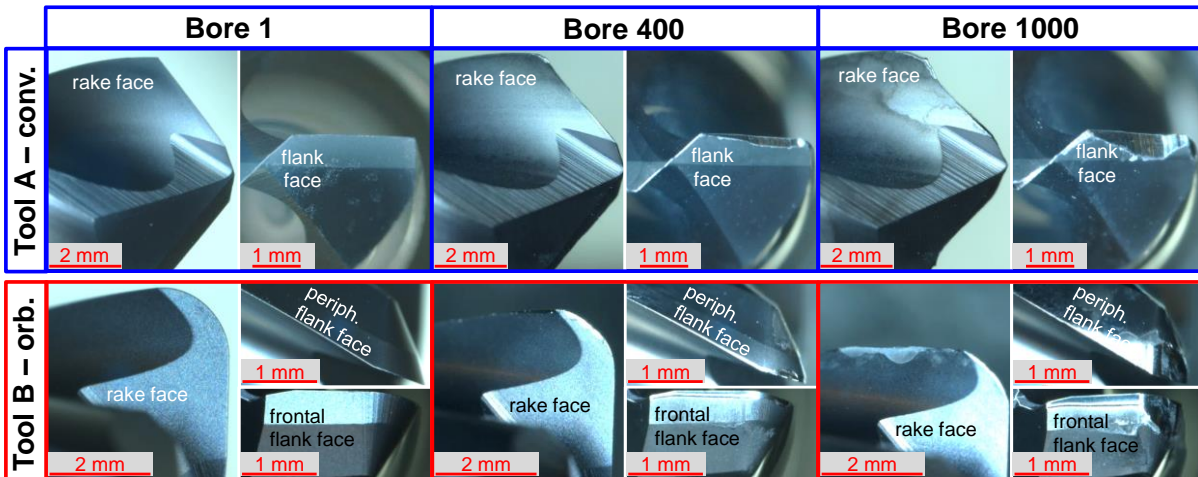


Figure 7.24: Microscope images of tool wear for Tools A and B; published in [233]

The chosen process parameters, described in section 7.3.1 are common for the presented machining task and influence directly the processing time. Assuming each 1 mm safety distance on the entry and exit side, 2 mm drill tip length and 8 mm material thickness sum up to 12 mm feed path per bore, see right side in Figure 7.25. The diagram (left) shows a comparison of processing time for one bore with conventional drilling in contrast to orbital drilling: For this application orbital drilling takes 8 s (=100%), while the conventional process takes 3.8 s (47.5%).

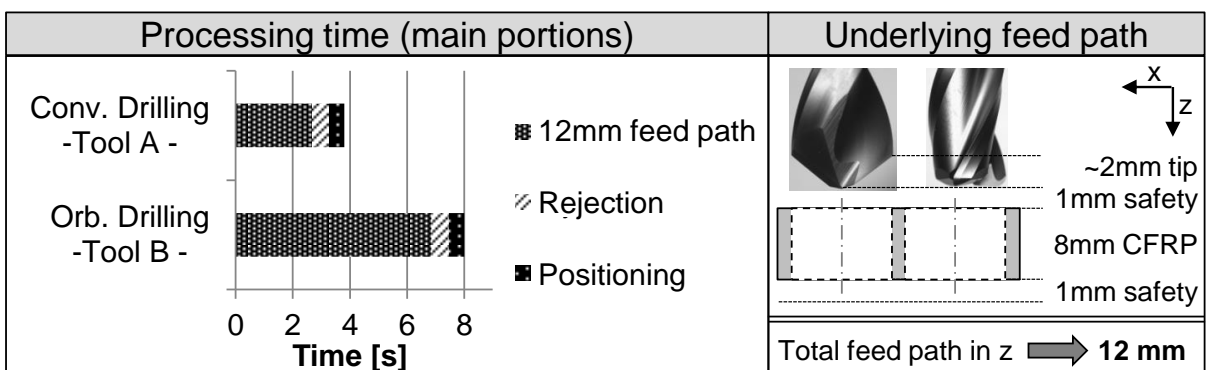


Figure 7.25: Processing time comparison for conv. drilling vs. orb drilling; published in [233]

7.3.3 Conclusion of process strategy comparison

The presented analyses compare conventional and orbital drilling in the same hard to machine CFRP material and highlight the differences between the two processes. These results with the following key findings allow for selection of the appropriate process for CFRP applications:

- Up to 3.3x higher axial thrust forces occur in conventional drilling, compared to orbital drilling; After initial wear, the axial thrust forces in orbital drilling remain constant
- Significantly less bore exit damages (delamination or uncut fibres) and less bore channel damages (fibre cracks, pull-out and bending) occur in orbital drilling
- The higher amount of damages in conventional drilling causes lower material strength
- Process time of orb. drilling is 210% of the process time of conv. drilling (influenced by number of flutes & feed rates)

Briefly, orbital drilling generates a better bore quality with lower process forces but necessitates a more complex/dynamic machine tool and longer process times. Thus orbital drilling is the right choice if sufficient quality, cannot be achieved with conventional drilling (rework necessary) even after geometry and process parameter optimisation. As soon as the diamond coating at the peripheral cutting edge of orbital drilling tools fail, the bore- \emptyset decreases significantly. Preferably, the bore diameter decrease in orbital drilling due to tool wear should be compensated by machine control, as the quality seems not to be the lifetime limiting factor. The effect of increasing bore exit quality with progressing wear in orbital drilling in contrast to decreasing quality in conventional drilling is influenced by advantageous diamond coating wear.

8 Overall conclusion and outlook

Today, CFRP materials are used for high performance engineering parts in the aerospace and automotive industry as well as energy and sports & leisure applications. With CFRP it is possible to adapt the component properties to the application by choosing appropriate fibre and matrix materials as well as by orienting the fibre in the component. Typically, the material is produced near-net-shape, which means that drilling and milling operations are only necessary at the end of the manufacturing process. During these machining operations intensive tool wear and insufficient machining quality are the main challenges, leading to limitation of the applicability of CFRP. It is desirable to optimise the machining processes in order to be able to apply CFRP material with its advantageous properties to the desired extent. Optimisation of CFRP machining has many different influencing factors, some of which have been addressed in this work. The main goal of this work is to improve the drilling process in CFRP by enhancing the understanding of chip formation mechanisms and optimising drilling strategies and tool geometries.

Initially, the fundamental experiments, carried out in collaboration with HENERICHS [101], elementarily expanded the process understanding of chip formation in CFRP machining. These experiments enabled tool wear description on micro-geometrical basis by means of five repeatedly measurable parameters l_α , l_γ , γ^* , α^* , b_c . In combination with the evaluation of the friction coefficient close to a machining operation these results enabled for a development of a micro-mechanical and analytical force model. In contrast to existing models, not only the *fibre orientation*, *material properties*, *initial tool geometry* and *feed rate* but also the *actual tool wear* is considered. The model is characterized by considering distinct micro-mechanical chip formation mechanisms, which are simulated in separate sub-models depending on the specific fibre orientation. Initially developed for orthogonal cutting with one individual fibre orientation and tool geometry during a single experiment, a superior consistency between model and measured values could be demonstrated. In summary, the proposed analytical force model provides additional data for process optimisation, such as the origin and share of the arising forces at the cutting edge.

Because this model considers distinct chip formation mechanisms and variable cutting edge micro-geometries, in future the model can be transferred to various processes, such as drilling operations. For a further optimization, it is planned to mathematically describe the relationship between tool wear and influencing variables such as feed rate, cutting speed, fibre orientation as well as original tool geometry, which actually is an input to the force model.

Similar to the initially conducted fundamental orthogonal cutting experiments, the machining quality needs to be reproducibly evaluated during the optimisation of drilling processes. Since no standard or satisfactory scheme existed, one focus of this thesis is on the development of a comprehensive bore exit quality (BEQ) evaluation method. Therefore five parameters have been combined to a damage value Q_d , which reflects the bore quality based on damages protruding inside a bore and surrounding the bore exit. It has been shown that Q_d is less sensitive to scattering by individual delaminated fibres compared to existing factors, especially in UD material. A comparison of the Cutting Edge Analyser (CEA) approach by Henerichs with the proposed BEQ approach in 6.5 shows a good correlation. Best machining quality is achieved with tools showing small peak radii r_{peak} and short lengths

l_v . A large radius of surface generation r_{sg} leads to a uniform compression and smooth stress distribution in the CFRP material.

Using this advantageous BEQ evaluation method, several drilling experiments have been carried out with the aim of improving the bore quality by means of tool geometry, diamond coating and process strategy optimisation. One very successful development approach for high quality rivet bore generation in CFRP aims for post-coating cutting edge treatment of CVD diamond-coated carbide spiral drills with a picosecond laser ablation. This newly developed local treatment method of diamond-coated carbide tools enables for a sharp cutting edge with diamond coating protecting on the rake face. The cutting edges produced by laser operation with beam exit on the cutting edge are sharp with radii down to 3-4 μm , resulting in outstanding bore exit qualities in hard to machine unidirectional CFRP materials. In combination with the unaffected diamond coating on the rake face and a geometry adapted for the self-sharpening effect, the proposed treatment method promises an extraordinary long tool lifetime. The well-known run-in behaviour of untreated diamond-coated tools, with initial bores of insufficient quality, could be avoided.

A further lever, besides cutting geometry and diamond coating improvement is the machining strategy. In certain applications the process-related disadvantages of conventional drilling, such as the adverse chip transport and pressing effects instead of cutting in the tool centre, are predominant. In these cases, a bore with sufficient quality cannot be generated with conventional drilling even by applying the above-mentioned improvements and drilling with defensive cutting parameters. In an extensive comparison between conventional and orbital drilling both strategies are compared regarding bore quality, tool wear, diameter variances and cycle time. Each machining strategy is conducted with diamond-coated carbide tools, in which the tool geometry is optimised based on the findings from the initially presented fundamental orthogonal turning experiments. Accordingly, on the one hand orbital drilling achieved better bore exit and bore channel qualities resulting in higher static strength of the bore. But on the other hand, conventional drilling shows less bore diameter deviations, does not require a highly dynamic machine tool or orbital drilling spindle and is usually the faster process. By means of the revealing analyses and comparisons it is possible to find the optimum process for a certain drilling application.

IV Bibliography

- [1] P. Albrecht, 1960, New developments in the theory of the metal-cutting process: part I. The ploughing process in metal cutting, *Journal of Manufacturing Science and Engineering*. **82**(4): pp. 348-357.
- [2] Q. An, W. Ming, X. Cai and M. Chen, 2015, Study on the cutting mechanics characteristics of high-strength UD-CFRP laminates based on orthogonal cutting method, *Composite Structures*. **131**: pp. 374-383.
- [3] D. Arola and M. Ramulu, 1994, Machining-induced surface texture effects on the flexural properties of a graphite/epoxy laminate, *Composites*. **25**(8): pp. 822-834.
- [4] D. Arola, M. Ramulu and D.H. Wang, 1996, Chip formation in orthogonal trimming of graphite/epoxy composite, *Composites Part A: applied science and manufacturing*. **27**(2): pp. 121-133.
- [5] D. Arola and M. Ramulu, 1997, Orthogonal cutting of fiber-reinforced composites: a finite element analysis, *International journal of mechanical sciences*. **39**(5): pp. 597-613.
- [6] D. Arola, M.B. Sultan and M. Ramulu, 2002, Finite element modeling of edge trimming fiber reinforced plastics, *Journal of manufacturing science and engineering*. **124**(1): pp. 32-41.
- [7] D.D. Arola and M. Ramulu, 1998, Net-shape machining and the process-dependent failure of fiber-reinforced plastics under static load, *ASTM Journal of Composites Technology & Research (USA)*. **20**(4): pp. 210-220.
- [8] S. Arul, L. Vijayaraghavan, S. Malhotra and R. Krishnamurthy, 2006, The effect of vibratory drilling on hole quality in polymeric composites, *International Journal of Machine Tools and Manufacture*. **46**(3): pp. 252-259.
- [9] J.C. Aurich, M. Zimmermann and L. Leitz, 2011, The preparation of cutting edges using a marking laser, *Production Engineering*. **5**(1): pp. 17-24.
- [10] J.C. Aurich, B. Kirsch, C. Müller and L. Heberger, 2014, Quality of Drilled and Milled Rivet Holes in Carbon Fiber Reinforced Plastics, *Procedia CIRP*. **24**: pp. 56-61.
- [11] M.G. Bader and R.M. Ellis, 1974, The effect of notches and specimen geometry on the pendulum impact strength of uniaxial CFRP, *Composites*. **5**(6): pp. 253-258.
- [12] E. Bassett, J. Köhler and B. Denkena, 2012, On the honed cutting edge and its side effects during orthogonal turning operations of AISI1045 with coated WC-Co inserts, *CIRP Journal of Manufacturing Science and Technology*. **5**(2): pp. 108-126.
- [13] C. Becke, 2011, Prozesskrafttrichtungsangepasste Frässtrategien zur schädigungsarmen Bohrungsbearbeitung an faserverstärkten Kunststoffen, (Diss.) Karlsruher Institut für Technologie (KIT), Karlsruhe.
- [14] N. Bhatnagar, N. Ramakrishnan, N.K. Naik and R. Komanduri, 1995, On the machining of fiber reinforced plastic (FRP) composite laminates, *International Journal of Machine Tools and Manufacture*. **35**(5): pp. 701-716.
- [15] N. Bhatnagar, I. Singh and D. Nayak, 2004, Damage investigation in drilling of glass fiber reinforced plastic composite laminates, *Materials and manufacturing processes*. **19**(6): pp. 995-1007.
- [16] D. Biermann and I. Terwey, 2008, Cutting edge preparation to improve drilling tools for HPC processes, *CIRP Journal of Manufacturing Science and Technology*. **1**(2): pp. 76-80.
- [17] M. Biot, 1922, Bending of an infinite beam on an elastic foundation, *Zeitschrift für Angewandte Mathematik und Mechanik*. **2**(3): pp. 165-184.
- [18] J. Boldt and J. Chanani, 1987, Solid tool machining and drilling, engineered materials handbook, *ASM International*. **1**(9): pp. 867-872.
- [19] K.-D. Bouzakis, N. Michailidis, N. Vidakis, K. Efstathiou, T. Leyendecker, G. Erkens, R. Wenke and H.-G. Fuss, 2000, Optimization of the cutting edge radius of PVD coated inserts in milling considering film fatigue failure mechanisms, *Surface and Coatings Technology*. **133**: pp. 501-507.

- [20] E. Brinksmeier and S. Fangmann, 2007, Orbital drilling of high tolerance boreholes, International Conference on Applied Production Technology (APT '07), Bremen. pp. 75-84.
- [21] E. Brinksmeier, S. Fangmann and I. Meyer, 2008, Orbital drilling kinematics, Production Engineering. **2**(3): pp. 277-283.
- [22] E. Brinksmeier, S. Fangmann and R. Rentsch, 2011, Drilling of composites and resulting surface integrity, CIRP Annals-Manufacturing Technology. **60**(1): pp. 57-60.
- [23] E. Brinksmeier, Machinability of Carbon-Fiber-Reinforced and GLARE Materials, Section in: CIRP Encyclopedia of Production Engineering, Editors: L. Laperrière and G. Reinhart, 2014, Springer Berlin Heidelberg: pp. 782-787.
- [24] O. Byelyayev, 2008, Erhöhung der Leistungsfähigkeit von HSS-Spiralbohrern durch Einsatz der magnetabrasiven Bearbeitung, (Diss.) Univ. Magdeburg, Magdeburg.
- [25] G. Byrne, D. Dornfeld and B. Denkena, 2003, Advancing cutting technology, CIRP Annals-Manufacturing Technology. **52**(2): pp. 483-507.
- [26] K.A. Calzada, S.G. Kapoor, R.E. DeVor, J. Samuel and A.K. Srivastava, 2012, Modeling and interpretation of fiber orientation-based failure mechanisms in machining of carbon fiber-reinforced polymer composites, Journal of Manufacturing Processes. **14**(2): pp. 141-149.
- [27] E. Capello, 2004, Workpiece damping and its effect on delamination damage in drilling thin composite laminates, Journal of Materials Processing Technology. **148**(2): pp. 186-195.
- [28] G. Caprino and R. Teti, 1994, Quantitative acoustic emission for fracture behavior of center-hole GFRP laminates, Journal of composite materials. **28**(13): pp. 1237-1249.
- [29] G. Caprino and R. Teti, 1995, Residual strength evaluation of impacted GRP laminates with acoustic emission monitoring, Composites science and technology. **53**(1): pp. 13-19.
- [30] G. Caprino and L. Nele, 1996, Cutting forces in orthogonal cutting of unidirectional GFRP composites, Journal of engineering materials and technology. **118**(3): pp. 419-425.
- [31] G. Caprino, L. Nele and L. Santo, 1996, Effect of tool wear on cutting forces in the orthogonal cutting of unidirectional glass fibre-reinforced plastics, Composites Part A: Applied Science and Manufacturing. **27**(5): pp. 409-415.
- [32] G. Caprino and A. D'Amore, 1998, Flexural fatigue behaviour of random continuous-fibre-reinforced thermoplastic composites, Composites Science and Technology. **58**(6): pp. 957-965.
- [33] G. Caprino and L. Santo, 1998, Interpretation of size effect in orthogonal machining of composite materials. Part II. Sheet moulding compound, Composites Part A: Applied Science and Manufacturing. **29**(8): pp. 893-897.
- [34] G. Caprino, L. Santo and L. Nele, 1998, Interpretation of size effect in orthogonal machining of composite materials. Part I: Unidirectional glass-fibre-reinforced plastics, Composites Part A: Applied Science and Manufacturing. **29**(8): pp. 887-892.
- [35] G. Caprino and G. Giorleo, 1999, Fatigue lifetime of glass fabric/epoxy composites, Composites Part A: Applied Science and Manufacturing. **30**(3): pp. 299-304.
- [36] G. Caprino, V. Lopresto, C. Scarponi and G. Briotti, 1999, Influence of material thickness on the response of carbon-fabric/epoxy panels to low velocity impact, Composites Science and Technology. **59**(15): pp. 2279-2286.
- [37] G. Caprino and V. Lopresto, 2001, On the penetration energy for fibre-reinforced plastics under low-velocity impact conditions, Composites Science and Technology. **61**(1): pp. 65-73.
- [38] G. Caprino, A. Langella and V. Lopresto, 2003, Indentation and penetration of carbon fibre reinforced plastic laminates, Composites Part B: Engineering. **34**(4): pp. 319-325.
- [39] G. Caprino, A. Langella and V. Lopresto, 2003, Prediction of the first failure energy of circular carbon fibre reinforced plastic plates loaded at the centre, Composites Part A: Applied Science and Manufacturing. **34**(4): pp. 349-357.
- [40] G. Caprino, R. Teti and I. De Iorio, 2005, Predicting residual strength of pre-fatigued glass fibre-reinforced plastic laminates through acoustic emission monitoring, Composites Part B: Engineering. **36**(5): pp. 365-371.

- [41] N.D. Chakladar, S.K. Pal and P. Mandal, 2012, Drilling of woven glass fiber-reinforced plastic—an experimental and finite element study, *The International Journal of Advanced Manufacturing Technology*. **58**(1): pp. 267-278.
- [42] L.-W. Chang, S.-S. Yau and T.-W. Chou, 1987, Notched strength of woven fabric composites with moulded-in holes, *Composites*. **18**(3): pp. 233-241.
- [43] G. Chardon, O. Klinkova, J. Rech, S. Drapier and J.-M. Bergheau, 2015, Characterization of friction properties at the work material/cutting tool interface during the machining of randomly structured carbon fibers reinforced polymer with Poly Crystalline Diamond tool under dry conditions, *Tribology International*. **81**: pp. 300-308.
- [44] W.-C. Chen, 1997, Some experimental investigations in the drilling of carbon fiber-reinforced plastic (CFRP) composite laminates, *International Journal of Machine Tools and Manufacture*. **37**(8): pp. 1097-1108.
- [45] F.Y. Cheung, Z. Zhou, A. Geddam and K. Li, 2008, Cutting edge preparation using magnetic polishing and its influence on the performance of high-speed steel drills, *Journal of materials processing technology*. **208**(1): pp. 196-204.
- [46] K.L. Chien, 1953, The influence of tool sharpness on the mechanics of metal cutting, (Diss.) Massachusetts Institute of Technology, Cambridge.
- [47] K. Colligan and M. Ramulu, 1991, Delamination in surface plies of graphite/epoxy caused by the edge trimming process, *Processing and Manuf. of Composite Materials*, **1**: pp. 113-125.
- [48] K. Colligan and M. Ramulu, 1992, The effect of edge trimming on composite surface plies, *Manufacturing Review (USA)*. **5**(4): pp. 274-283.
- [49] C.J. Cortés-Rodríguez, 2009, Cutting edge preparation of precision cutting tools by applying micro-abrasive jet machining and brushing, (Diss.) Kassel University, Kassel.
- [50] J.P. Davim and P. Reis, 2003, Study of delamination in drilling carbon fiber reinforced plastics (CFRP) using design experiments, *Composite structures*. **59**(4): pp. 481-487.
- [51] J.P. Davim and P. Reis, 2003, Drilling carbon fiber reinforced plastics manufactured by autoclave - experimental and statistical study, *Materials & design*. **24**(5): pp. 315-324.
- [52] J.P. Davim and P. Reis, 2005, Damage and dimensional precision on milling carbon fiber-reinforced plastics using design experiments, *Journal of materials processing technology*. **160**(2): pp. 160-167.
- [53] J.P. Davim, J.C. Rubio and A. Abrao, 2007, A novel approach based on digital image analysis to evaluate the delamination factor after drilling composite laminates, *Composites Science and Technology*. **67**(9): pp. 1939-1945.
- [54] J.P. Davim, 2009, *Machining Composite Materials*, John Wiley & Sons, Hoboken, NJ (USA).
- [55] B. Denkena, T. Friemuth, S. Fedorenko and M. Groppe, 2002, *An der Schneide wird das Geld verdient, Werkzeugtechnik+Verfahren*,
- [56] B. Denkena, D. Boehnke and J.H. Dege, 2008, Helical milling of CFRP-titanium layer compounds, *CIRP Journal of Manufacturing Science and Technology*. **1**(2): pp. 64-69.
- [57] B. Denkena, L. de Leon and J.H. Dege, 2008, Kinematik und Spanungsformen beim Zirkularfräsen, *Materialwissenschaft und Werkstofftechnik*. **39**(9): pp. 610-615.
- [58] B. Denkena, L. Leon-Garcia and E. Bassett, 2008, Preparation of designed cutting edge microgeometries by simultaneous 5-axes brushing, *Proceedings of the 3rd International Conference on Manufacturing Engineering (ICMEN) and EUREKA Brokerage Event*, **1**(3).
- [59] B. Denkena, L. de Leon, E. Bassett and M. Rehe, 2010, Cutting edge preparation by means of abrasive brushing, *Key Engineering Materials*, **438**: pp. 1-7.
- [60] B. Denkena and D. Biermann, 2014, Cutting edge geometries, *CIRP Annals-Manufacturing Technology*. **63**(2): pp. 631-653.
- [61] C. Dharan and M. Won, 2000, Machining parameters for an intelligent machining system for composite laminates, *International Journal of Machine Tools and Manufacture*. **40**(3): pp. 415-426.

- [62] C. Dold, M. Henerichs, L. Bochmann and K. Wegener, 2012, Comparison of ground and laser machined polycrystalline diamond (PCD) tools in cutting carbon fiber reinforced plastics (CFRP) for aircraft structures, *Procedia CIRP*. 1: pp. 178-183.
- [63] L.M.P. Durao, J.M.R. Tavares, A. Goncalves de Magalhaes, A.T. Marques and A.P.M. Baptista, 2008, Damage analysis of carbon/epoxy plates after drilling, *International Journal of Materials and Product Technology*. **32**(2-3): pp. 226-242.
- [64] L.M.P. Durão, D.J. Gonçalves, J.M.R. Tavares, V.H.C. de Albuquerque, A. Aguiar Vieira and A. Torres Marques, 2010, Drilling tool geometry evaluation for reinforced composite laminates, *Composite structures*. **92**(7): pp. 1545-1550.
- [65] G.W. Ehrenstein, 2006, *Faserverbund-Kunststoffe : Werkstoffe - Verarbeitung - Eigenschaften*, Hanser, München.
- [66] M. Emonts and H. Janssen, 2011, *Neue Technologien der Faserverbundtechnik*, WZL RWTH Aachen, Aachen.
- [67] E.D. Eneyew, 2014, *Experimental Study of Damage and Defect Detection during Drilling of CFRP Composites*, (Diss.) University of Washington, Washington (USA).
- [68] M. Ester, H.-P. Kriegel, J. Sander and X. Xu, 1996, A density-based algorithm for discovering clusters in large spatial databases with noise, *Conference on Knowledge Discovery and Data Mining (KDD)*, Portland, Oregon. **96**: pp. 226-231.
- [69] G.C. Everstine and T.G. Rogers, 1971, A theory of machining of fiber-reinforced materials, *Journal of Composite Materials*. **5**(1): pp. 94-106.
- [70] S. Fangmann, I. Meyer and E. Brinksmeier, 2011, Erweiterte Theorie zum Orbitalbohren (helikales Bohrfräsen), *Materialwissenschaft und Werkstofftechnik*. **42**(6): pp. 506-518.
- [71] S. Fangmann, 2012, *Orbitalbohrstrategien in seriellen Werkstoffverbunden*, (Diss.) Universität Bremen, Bremen.
- [72] A. Faraz, D. Biermann and K. Weinert, 2009, Cutting edge rounding: An innovative tool wear criterion in drilling CFRP composite laminates, *International Journal of Machine Tools and Manufacture*. **49**(15): pp. 1185-1196.
- [73] N. Feito, J. Díaz-Álvarez, A. Díaz-Álvarez, J.L. Cantero and M.H. Miguélez, 2014, Experimental Analysis of the Influence of Drill Point Angle and Wear on the Drilling of Woven CFRPs, *Materials*. **7**(6): pp. 4258-4271.
- [74] M. Feldhoff, 2012, *Modellgestützte Werkzeug-und Prozessentwicklung des Bohrschleifens faserverstärkter Duromere*, (Diss.) Vulkan-Verlag,
- [75] J. Ferreira, N. Coppini and G. Miranda, 1999, Machining optimisation in carbon fibre reinforced composite materials, *Journal of materials processing technology*. **92**: pp. 135-140.
- [76] H. Fischer, 1897, Die Größe der Widerstände gegen das Abheben von Metallspänen, *VDI-Zeitung*. **41**: pp. 504-508.
- [77] M. Flemming, G. Ziegmann and S. Roth, 2013, *Faserverbundbauweisen: Fertigungsverfahren mit duroplastischer matrix*, Springer Verlag, Berlin.
- [78] L. Fong and S. Advani, Resin transfer molding, Section in: *Handbook of Composites*, Editor S.T. Peters, 1998, Springer Verlag, Mountain View, California (USA): pp. 433-455.
- [79] S. Frenz, 2006, *Theoretische und experimentelle Untersuchungen glasfaserverstärkter Verbundwerkstoffplatten unter dynamischer Belastung*, (Diss.) RWTH Aachen, Faculty of Mechanical Engineering, Aachen.
- [80] T. Friemuth, 2002, *Herstellung spanender Werkzeuge*, (Diss.) Universität Hannover, Hannover.
- [81] W. Gawehn, 1985, *FORTRAN IV/77-Programm zur Finite-Elemente-Methode: Ein FEM-Programm für die Elemente Stab, Balken und Scheibendreieck*, Springer Verlag, Berlin.
- [82] M. GhasemiNejhad and T. Chou, 1990, Compression behaviour of woven carbon fibre-reinforced epoxy composites with moulded-in and drilled holes, *Composites*. **21**(1): pp. 33-40.

- [83] P. Ghidossi, M. El Mansori and F. Pierron, 2004, Edge machining effects on the failure of polymer matrix composite coupons, *Composites Part A: Applied Science and Manufacturing*. **35**(7): pp. 989-999.
- [84] A. Gilpin, 2009, Tool solutions for machining composites, *Reinforced Plastics*. **53**(6): pp. 30-33.
- [85] R. Gradinger, 2009, Herausforderungen bei der industriellen Umsetzung des Legierungskonzeptes Scalmalloy für Flugzeuganwendungen, Springer Verlag, BHM, Berlin.
- [86] P. Grass, 1988, Bohren faserverstärkter Duromere, (Diss.) RWTH Aachen, WZL RWTH Aachen, Aachen.
- [87] A.A. Griffith, 1921, The phenomena of rupture and flow in solids, *Philosophical transactions of the royal society of london. Series A: containing papers of a mathematical or physical character*. **221**: pp. 163-198.
- [88] T. Grilo, R. Paulo, C. Silva and J. Davim, 2013, Experimental delamination analyses of CFRPs using different drill geometries, *Composites Part B: Engineering*. **45**(1): pp. 1344-1350.
- [89] P. Guegan, 1994, Contribution a` la qualification de l'usinage de mate´riaux composites a` matrice organique, (Diss.) Ecole Centrale de Nantes, Nantes.
- [90] M. Hagino and T. Inoue, 2013, Effect of Carbon Fiber Orientation and Helix Angle on CFRP Cutting Characteristics by End-Milling, *Journal ref: International Journal of Automation Technology*. **7**(3): pp. 292-299.
- [91] W. Hake and R. Zemann, 2014, Insights of parameter experiments for cfrp machining (Erkenntnisse aus Parameterversuchen bei der CFK Zerspanung), 2. Workshop FIBRECUT, Wien.
- [92] S.C. Han, Y. Chen, J.H. Xu and J.W. Zhou, 2014, Experimental study of tool wear in milling multidirectional CFRP laminates, *Materials Science Forum*, **770**: pp. 276-280.
- [93] M. Hebsacker, 2000, Entwurf und Bewertung Paralleler Werkzeugmaschinen-das Hexaglide, (Diss.) Eidgenössisch Technische Hochschule Zürich (ETH), Nr. 13467, Zürich.
- [94] L. Heckmann, 2010, Systematische Analyse der Schneidkantenarchitektur mit Hilfe der Finite-Elemente-Methode, kassel university press GmbH,
- [95] S. Heimbs, S. Schmeer, J. Blaurock and S. Steeger, 2013, Static and dynamic failure behaviour of bolted joints in carbon fibre composites, *Composites Part A: Applied Science and Manufacturing*. **47**: pp. 91-101.
- [96] M. Henerichs, C. Dold, R. Voss and K. Wegener, 2013, Performance of Lasered PCD-and CVD-Diamond Cutting Inserts for Machining Carbon Fiber Reinforced Plastics (CFRP), *Int. Mechanical Engineering Congress and Exposition, San Diego, California (USA)*. pp. 64-72.
- [97] M. Henerichs, M. Egeter, T. Liebrich, R. Voss and K. Wegener, 2014, Evaluation of the IWF-Wunder Reproduction Method for Generating Positive Replica, *International Journal of Automation Technology*. **8**(1): pp. 49-56.
- [98] M. Henerichs, R. Voss, D. Harsch, F. Kuster and K. Wegener, 2014, Tool Life Time Extension with Nano-Crystalline Diamond Coatings for Drilling Carbon-Fibre Reinforced Plastics (CFRP), *Procedia CIRP*. **24**: pp. 125-129.
- [99] M. Henerichs, R. Voss, H. Tanaka, F. Kuster and K. Wegener, 2014, Analysis of Material Weakening in CFRP after a Drilling Operation, *Procedia CIRP*. **24**: pp. 44-48.
- [100] M. Henerichs, R. Voss, S. Übelin and K. Wegener, 2014, Analyse von Werkstoffschäden in gewebeartig gelegtem CFK-Material nach einer Bohrbearbeitung, *International Chemnitz Manufacturing Colloquium ICMC*. **80**: pp. 701-718.
- [101] M. Henerichs, 2015, Bohrbearbeitung von CFK unter besonderer Berücksichtigung der Schneidkantenmikrogeometrie, (Diss.) Eidgenössische Technische Hochschule Zürich (ETH), Nr. 22629, Zürich.
- [102] M. Henerichs, R. Voss, F. Kuster and K. Wegener, 2015, Machining of carbon fiber reinforced plastics: Influence of tool geometry and fiber orientation on the machining forces, *CIRP Journal of Manufacturing Science and Technology*. **9**: pp. 136-145.

- [103] M. Hetényi, 1946, *Beams on Elastic Foundation: Theory with Applications in the Fields of Civil and Mechanical Engineering*, University of Michigan press, Ann Arbor.
- [104] Hexcel-Corporation, Product Data: HexPly M21, [cited 09.02.2015]; Available from: http://www.hexcel.com/Resources/DataSheets/Prepreg-Data-Sheets/3501-6_eu.pdf.
- [105] Hexcel-Corporation, Product Data: AS4/3501-6 Epoxy Matrix, [cited 09.02.2015]; Available from: http://www.hexcel.com/Resources/DataSheets/Prepreg-Data-Sheets/3501-6_eu.pdf.
- [106] Hexcel-Corporation, HexTow Carbon Fibre Selector Guide, [cited 01.2016]; Available from: http://www.hexcel.com/Resources/SelectorGuides/CarbonFiber_SelectorGuide_us.pdf.
- [107] W. Hintze, D. Hartmann and C. Schütte, 2011, Occurrence and propagation of delamination during the machining of carbon fibre reinforced plastics (CFRPs)—An experimental study, *Composites Science and Technology*. **71**(15): pp. 1719-1726.
- [108] W. Hintze and D. Hartmann, 2013, Modeling of delamination during milling of unidirectional CFRP, *Procedia CIRP*. **8**: pp. 444-449.
- [109] H. Hocheng and C. Dharan, 1990, Delamination during drilling in composite laminates, *Journal of Manufacturing Science and Engineering*. **112**(3): pp. 236-239.
- [110] H. Hocheng and H. Puw, 1992, On drilling characteristics of fiber-reinforced thermoset and thermoplastics, *International Journal of Machine Tools and Manufacture*. **32**(4): pp. 583-592.
- [111] H. Hocheng, H. Puw and K. Yao, 1992, Experimental aspects of drilling of some fiber-reinforced plastics, *Proceedings of the Machining of Composite Materials Symposium*, Chicago, IL (USA). pp. 127-138.
- [112] H. Hocheng, H. Puw and Y. Huang, 1993, Preliminary study on milling of unidirectional carbon fibre-reinforced plastics, *Composites Manufacturing*. **4**(2): pp. 103-108.
- [113] H. Hocheng and C. Tsao, 2003, Comprehensive analysis of delamination in drilling of composite materials with various drill bits, *Journal of Materials Processing Technology*. **140**(1): pp. 335-339.
- [114] H. Hocheng and C. Tsao, 2005, The path towards delamination-free drilling of composite materials, *Journal of materials processing technology*. **167**(2): pp. 251-264.
- [115] H. Hocheng and C. Tsao, 2006, Effects of special drill bits on drilling-induced delamination of composite materials, *International Journal of Machine Tools and Manufacture*. **46**(12): pp. 1403-1416.
- [116] H. Hocheng, H.A. Kishawy, C.C. Tsao, S.D.E. Wakil, G. Caprino, A. Langella, J. Sheikh-Ahmad, J.P. Davim, K. Palanikumar and e.t. al, 2011, *Machining technology for composite materials: principles and practice*, Woodhead Publishing Limited, Oxford.
- [117] V. Hohensee, 1991, *Umrißbearbeitung faserverstärkter Kunststoffe durch Fräsen und Laserschneiden*, (Diss.) Hannover University, IFW, Hannover.
- [118] K. Horejsi, R. Schledjewski, J. Noisternig and O. Koch, 2013, Cost-saving potentials for CFRP parts in early design stages, *International Conference on Composite Materials (ICCM)*, Montreal, Canada. **19**: pp. 8439-8446.
- [119] C. Hwu and C. Fan, 1998, Sliding punches with or without friction along the surface of an anisotropic elastic half-plane, *The Quarterly Journal of Mechanics and Applied Mathematics*. **51**(1): pp. 159-177.
- [120] C. Hwu and C. Fan, 1998, Contact problems of two dissimilar anisotropic elastic bodies, *Journal of applied mechanics*. **65**(3): pp. 580-587.
- [121] D. Iliescu, D. Gehin, M.E. Gutierrez and F. Girot, 2010, Modeling and tool wear in drilling of CFRP, *International Journal of Machine Tools and Manufacture*. **50**(2): pp. 204-213.
- [122] S. Jain and D.C. Yang, 1994, Delamination-free drilling of composite laminates, *Journal of Manufacturing Science and Engineering*. **116**(4): pp. 475-481.
- [123] S.Å. Johansson, G.C. Ossbahr and T. Harris, 2002, *A study of the influence of drilling method and hole quality on static strength and fatigue life of carbon fiber reinforced plastic aircraft material*, SAE Aerospace Automated Fastening, Chester, England: pp. 171-177.
- [124] K.L. Johnson, 1985, *Contact Mechanics*, Cambridge University Press, Cambridge.

- [125] Y. Karpat, O. Bahtiyar, B. Değer and B. Kaftanoğlu, 2014, A mechanistic approach to investigate drilling of UD-CFRP laminates with PCD drills, *CIRP Annals-Manufacturing Technology*. **63**(1): pp. 81-84.
- [126] Y. Karpat, B. Değer and O. Bahtiyar, 2014, Experimental evaluation of polycrystalline diamond tool geometries while drilling carbon fiber-reinforced plastics, *The International Journal of Advanced Manufacturing Technology*. **71**(5-8): pp. 1295-1307.
- [127] Y. Karpat and O. Bahtiyar, 2016, Energy Based Investigation of Process Parameters While Drilling Carbon Fiber Reinforced Polymers, *Procedia CIRP*. **46**: pp. 59-62.
- [128] C.P. Keferstein and W. Dutschke, 2010, *Fertigungsmesstechnik*, Springer,
- [129] M. Keuerleber, 2006, Bestimmung des Elastizitätsmoduls von Kunststoffen bei hohen Dehnraten am Beispiel von PP, (Diss.) University of Stuttgart, Fakultät für Energie-, Verfahrens- und Biotechnik, Stuttgart.
- [130] H. Kihlman, I. Eriksson and M. Ennis, 2002, *Robotic Orbital Drilling of Structures for Aerospace Applications*, SAE Aerospace Automated Fastening, Chester, England: pp. 85-91.
- [131] F. Klocke and C. Würtz, 1998, The use of PCD tools for machining fibre reinforced materials, *Proceedings of the ECCM, Naples, Italy*. **8**: pp. 509-515.
- [132] F. Klocke and W. König, 2008, *Fertigungsverfahren 1: Drehen, Fräsen, Bohren*, Springer Verlag, Berlin.
- [133] D. Knoll, 1990, Verkleben von glasfaserverstärkten Duroplasten, *Adhäsion–Kleben & Dichten*. **34**(5): pp. 36-39.
- [134] K. Knothe and H. Wessels, 2013, *Finite Elemente: eine Einführung für Ingenieure*, Springer Verlag, Berlin.
- [135] W. König, C. Wulf, P. Grass and H. Willerscheid, 1985, Machining of fibre reinforced plastics, *CIRP Annals-Manufacturing Technology*. **34**(2): pp. 537-548.
- [136] W. König and P. Grass, 1989, Quality definition and assessment in drilling of fibre reinforced thermosets, *CIRP Annals-Manufacturing Technology*. **38**(1): pp. 119-124.
- [137] A. Koplev, A. Lystrup and T. Vorm, 1983, The cutting process, chips, and cutting forces in machining CFRP, *Composites*. **14**(4): pp. 371-376.
- [138] T. Kraus and M. Kühnel, Der globale CFK-Markt, [cited 01.01.2016]; Available from: http://www.avk-tv.de/files/20151214_20150923_composites_marktbericht_gesamt.pdf.
- [139] T. Kraus and M. Kühnel, Der globale CFK-Markt, [cited 01.01.2017]; Available from: http://www.avk-tv.de/files/20161128_marktbericht_2016deutsch.pdf.
- [140] G. Kress, 2012, *Skriptum: Mechanik der Faserverbundwerkstoffe*, Zentrum für Strukturtechnologien, Zürich.
- [141] S. Lafaye, C. Gauthier and R. Schirrer, 2005, A surface flow line model of a scratching tip: apparent and true local friction coefficients, *Tribology international*. **38**(2): pp. 113-127.
- [142] S. Lafaye, C. Gauthier and R. Schirrer, 2006, The ploughing friction: analytical model with elastic recovery for a conical tip with a blunted spherical extremity, *Tribology Letters*. **21**(2): pp. 95-99.
- [143] A. Langella and M. Durante, 2008, Comparison of tensile strength of composite material elements with drilled and molded-in holes, *Applied Composite Materials*. **15**(4-6): pp. 227-239.
- [144] R. Lässig, M. Eisenhut, A. Mathias, R.T. Schulte, F. Peters, T. Kühmann, T. Waldmann and W. Begemann, 2012, *Serienproduktion von hochfesten Faserverbundbauteilen*, Roland Berger, VDMA.
- [145] F. Latger, T. Harris and S. Björklund, 2002, *Drilling Cost Model*, SAE Aerospace Automated Fastening, Chester, England: pp. 55-61.
- [146] M.-B. Lazar, 2012, *Cutting Force Modelling for Drilling of Fiber-Reinforced Composites*, (Diss.) EPFL Lausanne, Nr. 5289, Lausanne.

- [147] M. Li, S. Soo, D. Aspinwall, D. Pearson and W. Leahy, 2014, Influence of lay-up configuration and feed rate on surface integrity when drilling carbon fibre reinforced plastic (CFRP) composites, *Procedia CIRP*. **13**: pp. 399-404.
- [148] H. Lin and Y. Lee, 1992, Strength of composite laminates with continuous fiber around a circular hole, *Composite structures*. **21**(3): pp. 155-162.
- [149] R. Lindqvist, I. Eriksson and M. Wolf, *Orbital Drilling of Sandwich Constructions for Space Applications*, SAE Aerospace Automated Fastening, 2001. DOI: 10.4271/2001-01-2571.
- [150] R. Lindqvist and H. Kihlman, *Orbital Drilling - Implementation and Evaluation*, SAE Aerospace Manufacturing and Automated Fastening, 2004. DOI: 10.4271/2004-01-2814.
- [151] S. Maegawa, S. Hayakawa, F. Itoigawa and T. Nakamura, Development of novel tool for cutting of carbon-fiber-reinforced plastics (Positive use of abrasive wear at tool edge for reduction in cutting force), *Mechanical Engineering Journal*, 2015. **2**(6). DOI: 10.1299/mej.15-00295.
- [152] S. Maegawa, Y. Morikawa, S. Hayakawa, F. Itoigawa and T. Nakamura, 2015, Effects of Fiber Orientation Direction on Tool-Wear Processes in Down-Milling of Carbon Fiber-Reinforced Plastic Laminates, *International Journal of Automation Technology*. **9**(4): pp. 356-364.
- [153] S. Maegawa, S. Hayakawa, F. Itoigawa and T. Nakamura, 2016, Two-Layer Tool with Hardness Distribution Around Tool Edge for Reducing Cutting Forces in CFRP Machining, *Int. J. of AutomationTechnology*. **10**(3): pp. 364 - 371.
- [154] M. Mahdi and L. Zhang, 2001, An adaptive three-dimensional finite element algorithm for the orthogonal cutting of composite materials, *Journal of Materials Processing Technology*. **113**(1): pp. 368-372.
- [155] M. Mahdi and L. Zhang, 2001, A finite element model for the orthogonal cutting of fiber-reinforced composite materials, *Journal of Materials Processing Technology*. **113**(1): pp. 373-377.
- [156] A.T. Marques, L.M. Durao, A.G. Magalhaes, J.F. Silva and J.M.R.S. Tavares, 2009, Delamination analysis of carbon fibre reinforced laminates: evaluation of a special step drill, *Composites Science and Technology*. **69**(14): pp. 2376-2382.
- [157] C.M. Mate, G.M. McClelland, R. Erlandsson and S. Chiang, *Atomic-scale friction of a tungsten tip on a graphite surface*, Section in: *Scanning Tunneling Microscopy*, 1993, Springer: pp. 226-229.
- [158] J. Mathew, N. Ramakrishnan and N. Naik, 1999, Trepanning on unidirectional composites: delamination studies, *Composites Part A: Applied Science and Manufacturing*. **30**(8): pp. 951-959.
- [159] S. Matsunaga, T. Matsubara, W.-X. Wang and Y. Takao, Effects of reciprocation number on the friction behaviors of carbon/epoxy for various fiber orientations and high contact pressures, *Int. Conference on Composite Materials (ICCM)*, 2001. **13**. ID 1446.
- [160] J. Mayer, R. Tognini, M. Widmer, H. Zerlik, E. Wintermantel and S.-W. Ha, *Faserverbundwerkstoffe*, Section in: *Medizintechnik – Life Science Engineering*, Editors: E. Wintermantel and S.-W. Ha, 2009, Springer Verlag, Berlin: pp. 299-342.
- [161] M. Mehta, T. Reinhart and A. Soni, 1992, Effect of fastener hole drilling anomalies on structural integrity of PMR-15/Gr composite laminates, *Machining of Composite Materials*, Chicago, Illinois (USA). pp. 113-126.
- [162] J. Miller, 1987, *Drilling graphite/epoxy at Lockheed*, *American Machinist & Automated Manufacturing*. **131**(10): pp. 70-71.
- [163] A. Mondelin, B. Furet and J. Rech, 2010, Characterisation of friction properties between a laminated carbon fibres reinforced polymer and a monocrystalline diamond under dry or lubricated conditions, *Tribology International*. **43**(9): pp. 1665-1673.
- [164] N. Naik and R.S. Kumar, 1999, Compressive strength of unidirectional composites: evaluation and comparison of prediction models, *Composite structures*. **46**(3): pp. 299-308.
- [165] D. Nayak, N. Bhatnagar and P. Mahajan, 2005, Machining studies of UD-FRP composites part 2: finite element analysis, *Machining Science and Technology*. **9**(4): pp. 503-528.

- [166] W. Ni, Orbital drilling of aerospace materials, SAE Technical Paper, 2007. DOI: 10.4271/2007-01-3814.
- [167] X. Ning and M.R. Lovell, 2002, On the sliding friction characteristics of unidirectional continuous FRP composites, *Journal of tribology*. **124**(1): pp. 5-13.
- [168] K. Ohta, H. Tanaka and R. Takizawa, 2012, Development of Tilted Planetary Drilling System, *Procedia CIRP*. **1**: pp. 681-682.
- [169] O. Pecat, R. Rentsch and E. Brinksmeier, 2012, Influence of Milling Process Parameters on the Surface Integrity of CFRP, *Procedia CIRP*. **1**: pp. 466-470.
- [170] E. Persson, I. Eriksson and L. Zackrisson, 1997, Effects of hole machining defects on strength and fatigue life of composite laminates, *Composites Part A: Applied Science and Manufacturing*. **28**(2): pp. 141-151.
- [171] S.T. Peters, 1998, Introduction, composite basics and road map, Chapman & Hall, Handbook of composites, London.
- [172] W.D. Pilkey, Contact Stresses (Chapter 9), Section in: *Formulas for Stress, Strain and Structural Matrices*, 2008, John Wiley & Sons, Hoboken, New Jersey (USA): pp. 413-449.
- [173] R. Piquet, B. Ferret, F. Lachaud and P. Swider, 2000, Experimental analysis of drilling damage in thin carbon/epoxy plate using special drills, *Composites Part A: Applied Science and Manufacturing*. **31**(10): pp. 1107-1115.
- [174] H. Puls, F. Klocke and D. Lung, 2012, A new experimental methodology to analyse the friction behaviour at the tool-chip interface in metal cutting, *Production engineering*. **6**(4-5): pp. 349-354.
- [175] H. Puw and H. Hocheng, 1999, Milling of polymer composites, *MANUFACTURING ENGINEERING AND MATERIALS PROCESSING*. **53**: pp. 267-294.
- [176] H.Y. Pwu and H. Hocheng, 1998, Chip formation model of cutting fiber-reinforced plastics perpendicular to fiber axis, *Journal of manufacturing science and engineering*. **120**(1): pp. 192-196.
- [177] Z. Qi, K. Zhang, H. Cheng, D. Wang and Q. Meng, 2015, Microscopic mechanism based force prediction in orthogonal cutting of unidirectional CFRP, *The International Journal of Advanced Manufacturing Technology*. **79**(5-8): pp. 1209-1219.
- [178] M. Ramesh, K. Seetharamu, N. Ganesan and M. Sivakumar, 1998, Analysis of machining of FRPs using FEM, *Int. Journal of Machine Tools and Manufacture*. **38**(12): pp. 1531-1549.
- [179] C. Ramirez, G. Poulachon, F. Rossi and R. M'Saoubi, 2014, Tool wear monitoring and hole surface quality during CFRP drilling, *Procedia CIRP*. **13**: pp. 163-168.
- [180] M. Ramulu, C. Wern and J. Garbini, 1993, Effect of fibre direction on surface roughness measurements of machined graphite/epoxy composite, *Composites Manufacturing*. **4**(1): pp. 39-51.
- [181] M. Ramulu, 1997, Machining and surface integrity of fibre-reinforced plastic composites, *Sadhana*. **22**(3): pp. 449-472.
- [182] M. Ramulu, T. Branson and D. Kim, 2001, A study on the drilling of composite and titanium stacks, *Composite Structures*. **54**(1): pp. 67-77.
- [183] G.V.G. Rao, P. Mahajan and N. Bhatnagar, 2007, Micro-mechanical modeling of machining of FRP composites—cutting force analysis, *Composites science and technology*. **67**(3): pp. 579-593.
- [184] G.V.G. Rao, P. Mahajan and N. Bhatnagar, 2007, Machining of UD-GFRP composites chip formation mechanism, *Composites Science and Technology*. **67**(11–12): pp. 2271-2281.
- [185] S. Reichmann, 2011, Themenspecial: Läppen und Hohnen; Komplette Oberflächenbehandlung durch Magnetfinish, Fachverlag Moeller,
- [186] W. Reimann, 1991, Hochgeschwindigkeitsfräsen von kohlenstoffaserverstärkten Kunststoffen, (Diss.) Hanser München, Darmstadt.

- [187] T.J. Reinhart, Overview of composite materials, Section in: Handbook of Composites, 1998, Springer: pp. 21-33.
- [188] R. Rentsch, E. Brinksmeier and O. Pecat, 2012, Surface Integrity of Machined CFRP Structures, 15th European Conference on Composite Materials (ECCM15), Venice, Italy. **24**(28.6): pp. 1-6.
- [189] D. Richardson, The fundamental principles of composite material stiffness predictions, [cited 05.08.2016]; Available from: <http://www.swcompositesgateway.co.uk/Property-Prediction.pdf>.
- [190] G. Riegert, A. Gleiter, H. Gerhard and G. Busse, 2007, Active thermography for defect detection in carbon fiber reinforced composite materials, Review of Progress in Quantitative Nondestructive Evaluation, **894**(1): pp. 1044-1051.
- [191] L. Romoli and G. Dini, 2008, Experimental study on the influence of drill wear in CFRP drilling process, CIRP International Conference on Intelligent Computation in Manufacturing Engineering Naples, Italy. **6**: pp. 1-6.
- [192] E. Roos and K. Maile, 2006, Werkstoffkunde für Ingenieure: Grundlagen, Anwendung, Prüfung, Springer-Verlag, Berlin.
- [193] S. Rummenholler, 1996, Werkstofforientierte Prozeßauslegung für das Fräsen kohlenstoffaserverstärkter Kunststoffe, (Diss.) RWTH Aachen, Shaker Verlag, Aachen.
- [194] A. Ruosi, M. Valentino, V. Lopresto and G. Caprino, 2002, Magnetic response of damaged carbon fibre reinforced plastics measured by a HTS-SQUID magnetometer, Composite structures. **56**(2): pp. 141-149.
- [195] A. Sahraie Jahromi and B. Bahr, 2010, An analytical method for predicting cutting forces in orthogonal machining of unidirectional composites, Composites Science and Technology. **70**(16): pp. 2290-2297.
- [196] S. Sakamoto and H. Iwasa, 2012, Effect of cutting revolution speed on cutting temperature in helical milling of CFRP composite laminates, Key Engineering Materials, **523**: pp. 58-63.
- [197] K. Sakuma and M. Seto, 1978, Tool wear in cutting glass-fibre-reinforced plastics: The effect of physical properties of tool materials (Japanese), **44**(381): pp. 1752.
- [198] K. Sakuma, Y. Yokoo and M. Seto, 1984, Study on Drilling of Reinforced Plastics (GFRP and CFRP): Relation between Tool Material and Wear Behavior, Bulletin of JSME. **27**(228): pp. 1237-1244.
- [199] K. Sakuma, M. Seto, M. Taniguchi and Y. Yokoo, 1985, Tool wear in cutting carbon-fiber-reinforced plastics: The effect of physical properties of tool materials, Bulletin of JSME. **28**(245): pp. 2781-2788.
- [200] R. Schomaker, R. Pedwell and B. Knickrehm, 2014, Methodology for Classification of Shim Materials, SAE International Journal of Aerospace. **7**(2): pp. 255-262.
- [201] M. Schoßig, C. Bierögel, W. Grellmann, R. Bardenheier and T. Mecklenburg, 2006, Einfluss der Dehnrates auf das mechanische Verhalten von glasfaserverstärkten Polyolefinen, Tagung Werkstoffprüfung, Bad Neuenahr, Germany: pp. 445-450.
- [202] V. Schulze and C. Becke, 2011, Analysis of machining strategies for fiber reinforced plastics with regard to process force direction, Procedia Engineering. **19**: pp. 312-317.
- [203] H. Schürmann, 2008, Konstruieren mit Faser-Kunststoff-Verbunden, Springer, Berlin.
- [204] C. Schütte, 2014, Bohren und Hobeln von kohlenstoffaserverstärkten Kunststoffen unter besonderer Berücksichtigung der Schneide-Faser-Lage, (Diss.) Technische Universität Hamburg-Harburg, IPMT, Hamburg.
- [205] J.Y. Sheikh-Ahmad, 2009, Machining of Polymer Composites, Springer-Verlag, Abu Dhabi, United Arab Emirates.
- [206] D. Smolenicki, J. Boos, F. Kuster, H. Roelofs and C. Wyen, 2014, In-process measurement of friction coefficient in orthogonal cutting, CIRP Annals-Manufacturing Technology. **63**(1): pp. 97-100.

- [207] P. Sreejith, R. Krishnamurthy, S. Malhotra and K. Narayanasamy, 2000, Evaluation of PCD tool performance during machining of carbon/phenolic ablative composites, *Journal of Materials Processing Technology*. **104**(1): pp. 53-58.
- [208] P.S. Steif, 1988, A simple model for the compressive failure of weakly bonded, fiber-reinforced composites, *Journal of composite materials*. **22**(9): pp. 818-828.
- [209] A. Stöckle, 2014, Effizient in Composites 40 Jahre Erfahrungen aus dem Hubschrauberbau, Airbus Helicopters, Fachtagung Carbon Composites 2014.
- [210] B. Storch and A. Zawada-Tomkiewicz, 2012, Distribution of unit forces on the tool edge rounding in the case of finishing turning, *The International Journal of Advanced Manufacturing Technology*. **60**(5-8): pp. 453-461.
- [211] A.N. Stroh, 1958, Dislocations and cracks in anisotropic elasticity, *Philosophical magazine*. **3**(30): pp. 625-646.
- [212] N.-H. Sung and N.P. Suh, 1979, Effect of fiber orientation on friction and wear of fiber reinforced polymeric composites, *Wear*. **53**(1): pp. 129-141.
- [213] H. Takeyama and N. Iijima, 1988, Machinability of glassfiber reinforced plastics and application of ultrasonic machining, *CIRP Annals-Manufacturing Technology*. **37**(1): pp. 93-96.
- [214] H. Tanaka, K. Ohta, R. Takizawa and K. Yanagi, 2012, Experimental Study on Tilted Planetary Motion Drilling for CFRP, *Procedia CIRP*. **1**: pp. 443-448.
- [215] H. Tanaka, K. Ota, R. Takizawa and K. Yanagi, 2013, Experimental Study on Inclined Planetary Mechanism Drilling for Carbon Fiber Reinforced Plastic, *International Symposium on Ultraprecision Engineering and Nanotechnology (ISUPEN)*, Tokyo, Japan. pp. 23-28.
- [216] I. Terwey, 2011, Steigerung der Leistungsfähigkeit von Vollhartmetallwendelbohrern durch Strahlspanen, (Diss.) Technische Universität Dortmund, Vulkan Verlag, Essen.
- [217] R. Teti and N. Alberti, 1990, Ultrasonic identification and measurement of defects in composite material laminates, *CIRP Annals-Manufacturing Technology*. **39**(1): pp. 527-530.
- [218] R. Teti, 2002, *Machining of Composite Materials*, *CIRP Annals - Manufacturing Technology*. **51**(2): pp. 611-634.
- [219] F. Tikal, 2009, *Schneidkantenpräparation: Ziele, Verfahren und Messmethoden: Berichte aus Industrie und Forschung*, kassel university press GmbH, Kassel.
- [220] H.K. Toenshoff and B. Denkena, 2013, *Basics of cutting and abrasive processes*, Springer, Berlin.
- [221] H. Tönshoff, A. Ostendorf, C. Kulik and F. Siegel, 2003, Finishing of cutting tools using selective material ablation, *Proceedings of 1 st International CIRP Seminar on Micro and Nano Technology*, Copenhagen, Denmark.
- [222] C. Tsao and H. Hocheng, 2003, The effect of chisel length and associated pilot hole on delamination when drilling composite materials, *International journal of machine tools and manufacture*. **43**(11): pp. 1087-1092.
- [223] C. Tsao and H. Hocheng, 2004, Taguchi analysis of delamination associated with various drill bits in drilling of composite material, *International Journal of Machine Tools and Manufacture*. **44**(10): pp. 1085-1090.
- [224] C. Tsao and H. Hocheng, 2005, Computerized tomography and C-Scan for measuring delamination in the drilling of composite materials using various drills, *International Journal of Machine Tools and Manufacture*. **45**(11): pp. 1282-1287.
- [225] C. Tsao and H. Hocheng, 2007, Effect of tool wear on delamination in drilling composite materials, *International journal of mechanical sciences*. **49**(8): pp. 983-988.
- [226] C. Tsao, 2008, Thrust force and delamination of core-saw drill during drilling of carbon fiber reinforced plastics (CFRP), *The International Journal of Advanced Manufacturing Technology*. **37**(1-2): pp. 23-28.
- [227] C. Tsao, K. Kuo and I. Hsu, 2012, Evaluation of a novel approach to a delamination factor after drilling composite laminates using a core-saw drill, *The International Journal of Advanced Manufacturing Technology*. **59**(5-8): pp. 617-622.

- [228] S. Usui, J. Wadell and T. Marusich, 2014, Finite Element Modeling of Carbon Fiber Composite Orthogonal Cutting and Drilling, *Procedia CIRP*. **14**: pp. 211-216.
- [229] D.J. Vaughan, Fiberglass reinforcement, Section in: *Handbook of Composites*, 1998, Springer: pp. 131-155.
- [230] R. Voss, M. Henerichs, F. Kuster and K. Wegener, 2014, Chip root analysis after machining carbon fiber reinforced plastics (CFRP) at different fiber orientations, *CIRP HPC*, Berkeley (US). **14**: pp. 217-222.
- [231] R. Voss, M. Henerichs, G. Capricano, F. Kuster and K. Wegener, 2016, Post-Coating Treatment of Cutting Edge for Drilling Carbon Fibre Reinforced Plastics (CFRP), *Procedia CIRP*, **46**: pp. 161-164.
- [232] R. Voss, M. Henerichs, D. Harsch, F. Kuster and K. Wegener, 2016, Optimised approach for characterisation of cutting edge micro-geometry in drilling carbon fibre reinforced plastics (CFRP), *The International Journal of Advanced Manufacturing Technology*. **90**(1): pp. 457-472.
- [233] R. Voss, M. Henerichs and F. Kuster, 2016, Comparison of conventional drilling and orbital drilling in machining carbon fibre reinforced plastics (CFRP), *CIRP Annals - Manufacturing Technology*. **65**(1): pp. 137-140.
- [234] R. Voss, M. Henerichs, S. Rupp, F. Kuster and K. Wegener, 2016, Evaluation of bore exit quality for fibre reinforced plastics including delamination and uncut fibres, *CIRP Journal of Manufacturing Science and Technology*. **12**: pp. 56-66.
- [235] R. Voss, M. Henerichs, C. Walch, F. Kuster and K. Wegener, 2016, Friction Analysis between Carbon Fibre Reinforced Plastic and Diamond Coating with Cutting Process Tribometer, *International Conference on Precision Engineering*, Hamamatsu, Japan.
- [236] R. Voss, L. Seeholzer, F. Kuster and K. Wegener, 2017, Cutting Process Tribometer Experiments for Evaluation of Friction Coefficient Close to a CFRP Machining Operation, *Procedia CIRP*. **66**: pp. 204-209.
- [237] B. Wang, H. Gao, S.P. Zhang and Y.J. Bao, 2012, Study on friction coefficient between carbon/epoxy composites and a monocrystalline diamond under different temperatures, *Advanced Materials Research*, **565**: pp. 627-632.
- [238] D. Wang, M. Ramulu and C. Wern, 1992, Orthogonal cutting characteristics of graphite/epoxy composite material, *North American Manufacturing Research Inst. of SME*, **20**: pp. 159-165.
- [239] D. Wang, M. Ramulu and D. Arola, 1995, Orthogonal cutting mechanisms of graphite/epoxy composite. Part II: multi-directional laminate, *International Journal of Machine Tools and Manufacture*. **35**(12): pp. 1639-1648.
- [240] D. Wang, M. Ramulu and D. Arola, 1995, Orthogonal cutting mechanisms of graphite/epoxy composite. Part I: unidirectional laminate, *International Journal of Machine Tools and Manufacture*. **35**(12): pp. 1623-1638.
- [241] D.H. Wang, 1994, *Machining characteristics of graphite/epoxy composite*, (Diss.) University of Washington, Seattle.
- [242] X. Wang and L. Zhang, 2003, An experimental investigation into the orthogonal cutting of unidirectional fibre reinforced plastics, *International journal of machine tools and manufacture*. **43**(10): pp. 1015-1022.
- [243] X. Wang, Y.L. He and J.Y. Wang, 2013, A Delamination Factor Prediction Model for Drilling of Composite Materials, *Advanced Materials Research*. **601**: pp. 41-45.
- [244] X. Wang, P.Y. Kwon, C. Sturtevant, D. Kim and J. Lantrip, 2013, Tool wear of coated drills in drilling CFRP, *Journal of Manufacturing Processes*. **15**(1): pp. 127-135.
- [245] K. Wegener, M. Henerichs, R. Voss and D. Harsch, 2014, Schneidkantenmikrogeometrie entscheidet über die Standzeit beim Bohren von CFK, *Diamant Hochleistungswerkzeuge (DIHW)*, Harnisch.
- [246] K. Weinert and C. Kempmann, 2004, Cutting temperatures and their effects on the machining behaviour in drilling reinforced plastic composites, *Advanced Engineering Materials*. **6**(8): pp. 684-689.

- [247] C. Wern, M. Ramulu and A. Shukla, 1994, Investigation of stresses in the orthogonal cutting of fiber-reinforced plastics, *Experimental Mechanics*. **36**(1): pp. 33-41.
- [248] E. Winkler, 1867, *Die Lehre von der Elastizität und Festigkeit (The Theory of Elasticity and Stiffness)*, H. Dominicus, Prague.
- [249] E. Witten, 2014, *Handbuch Faserverbundkunststoffe/Composites: Grundlagen, Verarbeitung, Anwendungen*, Springer-Verlag, Frankfurt am Main.
- [250] T. Wong, S. Wu and G. Croy, 1982, An analysis of delamination in drilling composite materials, 14th National SAMPE Technical Conference, **47**: pp. 1-483.
- [251] S. Wu, Multifacet drills, Section in: *Handbook of High-Speed Machining Technology*, 1985, Springer, University of Wisconsin, Madison: pp. 305-316.
- [252] C. Würtz, 2000, *Beitrag zur Analyse der Staubemissionen bei der Fräsbearbeitung von Bauteilen aus kohlenstoffaserverstärkten Kunststoffen*, (Diss.) Shaker, WZL, RWTH Aachen, Aachen.
- [253] C.-F. Wyen and K. Wegener, 2010, Influence of cutting edge radius on cutting forces in machining titanium, *CIRP Annals - Manufacturing Technology*. **59**(1): pp. 93-96.
- [254] C.-F. Wyen, 2011, *Rounded cutting edges and their influence in machining titanium*, (Diss.) Eidgenössische Technische Hochschule ETH Zürich, DMAVT, Zürich.
- [255] C.-F. Wyen, W. Knapp and K. Wegener, 2012, A new method for the characterisation of rounded cutting edges, *The International Journal of Advanced Manufacturing Technology*. **59**(9-12): pp. 899-914.
- [256] G. Xu, 1996, *Einfluss der Schneidkantenform auf die Oberflächenausbildung beim Hochgeschwindigkeitsfräsen mit Feinkornhartmetall*, (Diss.) TH Darmstadt, Shaker Verlag, Shaker Verlag, Aachen.
- [257] W. Xu and L. Zhang, 2014, On the mechanics and material removal mechanisms of vibration-assisted cutting of unidirectional fibre-reinforced polymer composites, *International Journal of Machine Tools and Manufacture*. **80-81**: pp. 1-10.
- [258] W. Xu and L. Zhang, 2016, Mechanics of fibre deformation and fracture in vibration-assisted cutting of unidirectional fibre-reinforced polymer composites, *International Journal of Machine Tools and Manufacture*. **103**: pp. 40-52.
- [259] Y.L. Xu and K.L. Reifsnider, 1993, Micromechanical modeling of composite compressive strength, *Journal of Composite Materials*. **27**(6): pp. 572-588.
- [260] S.-S. Yau and T.-W. Chou, 1988, Strength of woven-fabric composites with drilled and molded holes, *Composite Materials: Testing and Design*, **8**: pp. 423-437.
- [261] W.C. Young and R.G. Budynas, 2002, *Roark's formulas for stress and strain*, McGraw-Hill, New York.
- [262] N. Yusefian, P. Koshy, S. Buchholz and F. Klocke, 2010, Electro-erosion edge honing of cutting tools, *CIRP Annals-Manufacturing Technology*. **59**(1): pp. 215-218.
- [263] L. Zackrisson, I. Eriksson and J. Bäcklund, 1994, Method and tool for machining a hole in a fiber-reinforced composite material, Swedish Patent, Sweden.
- [264] R. Zemann, J. Sacherl, W. Hake and F. Bleicher, 2015, New Measurement Processes to Define the Quality of Machined Fibre Reinforced Polymers, *Procedia Engineering*. **100**: pp. 636-645.
- [265] H.J. Zhang, W.Y. Chen, D.C. Chen and L.C. Zhang, 2001, Assessment of the exit defects in carbon fibre-reinforced plastic plates caused by drilling, *Key Eng. Materials*. **196**: pp. 43-52.
- [266] J.G. Zhang, B. Wang, F.H. Sun and H. Gao, 2012, Improvement on the Cutting Performance of CVD Diamond Coated Drills in Drilling CFRP, *Key Engineering Materials*, **499**: pp. 366-371.
- [267] L. Zhang, 2001, *Solid mechanics for engineers*, Macmillan Press, Basingstoke, UK.
- [268] L. Zhang, L. Wang and X. Liu, 2001, A mechanical model for predicting critical thrust forces in drilling composite laminates, *Proceedings of the Institution of Mechanical Engineers, Part B: Journal of Engineering Manufacture*. **215**(2): pp. 135-146.

-
- [269] L.C. Zhang, H.J. Zhang and X.M. Wang, 2001, A force prediction model for cutting unidirectional fibre-reinforced plastics, *Machining Science and Technology*. **5**(3): pp. 293-305.
- [270] L.C. Zhang, 2009, Cutting composites: A discussion on mechanics modelling, *Journal of materials processing technology*. **209**(9): pp. 4548-4552.

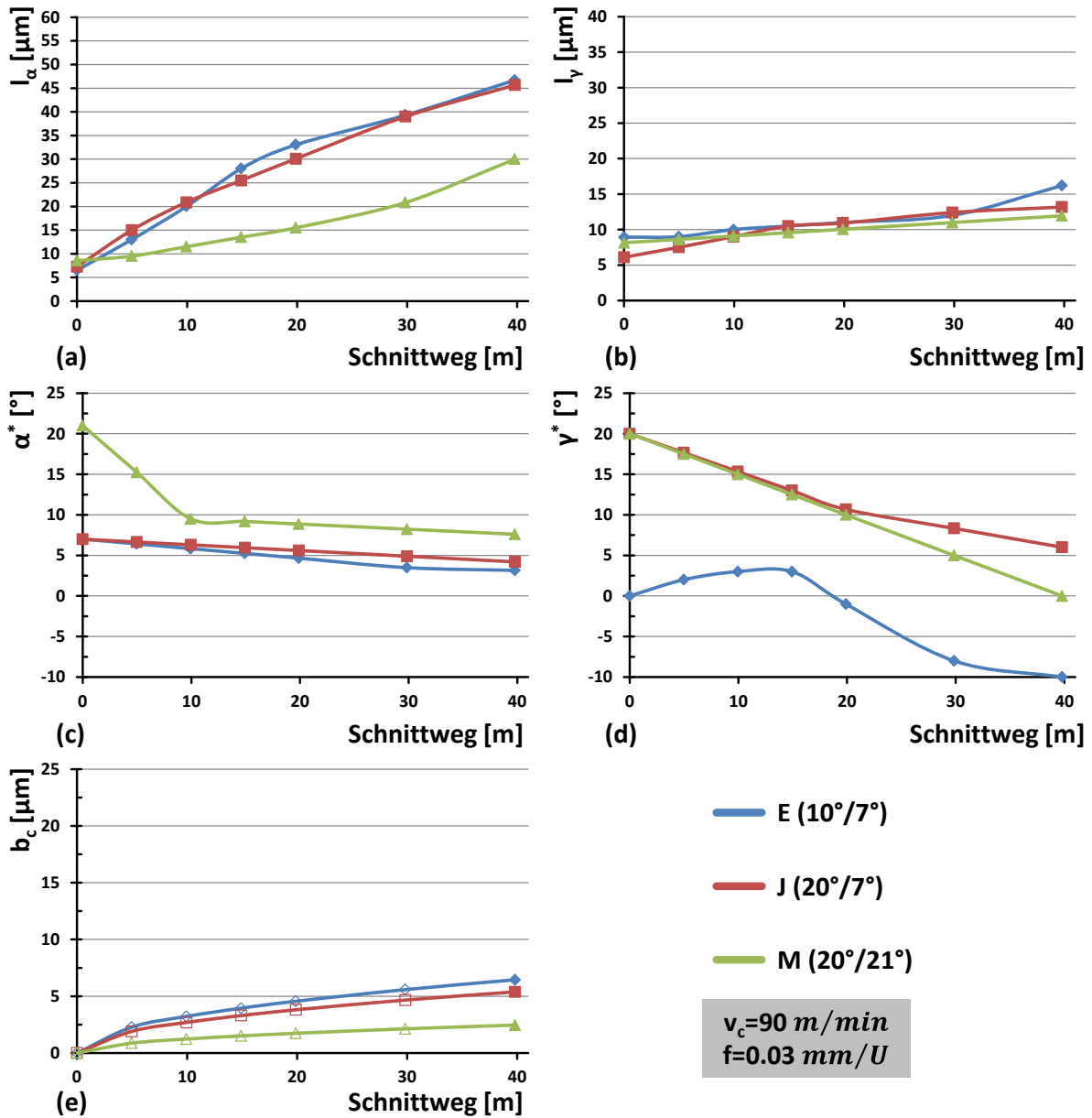
V Appendix

A.1. Table of tool wear parameters considered in the force model

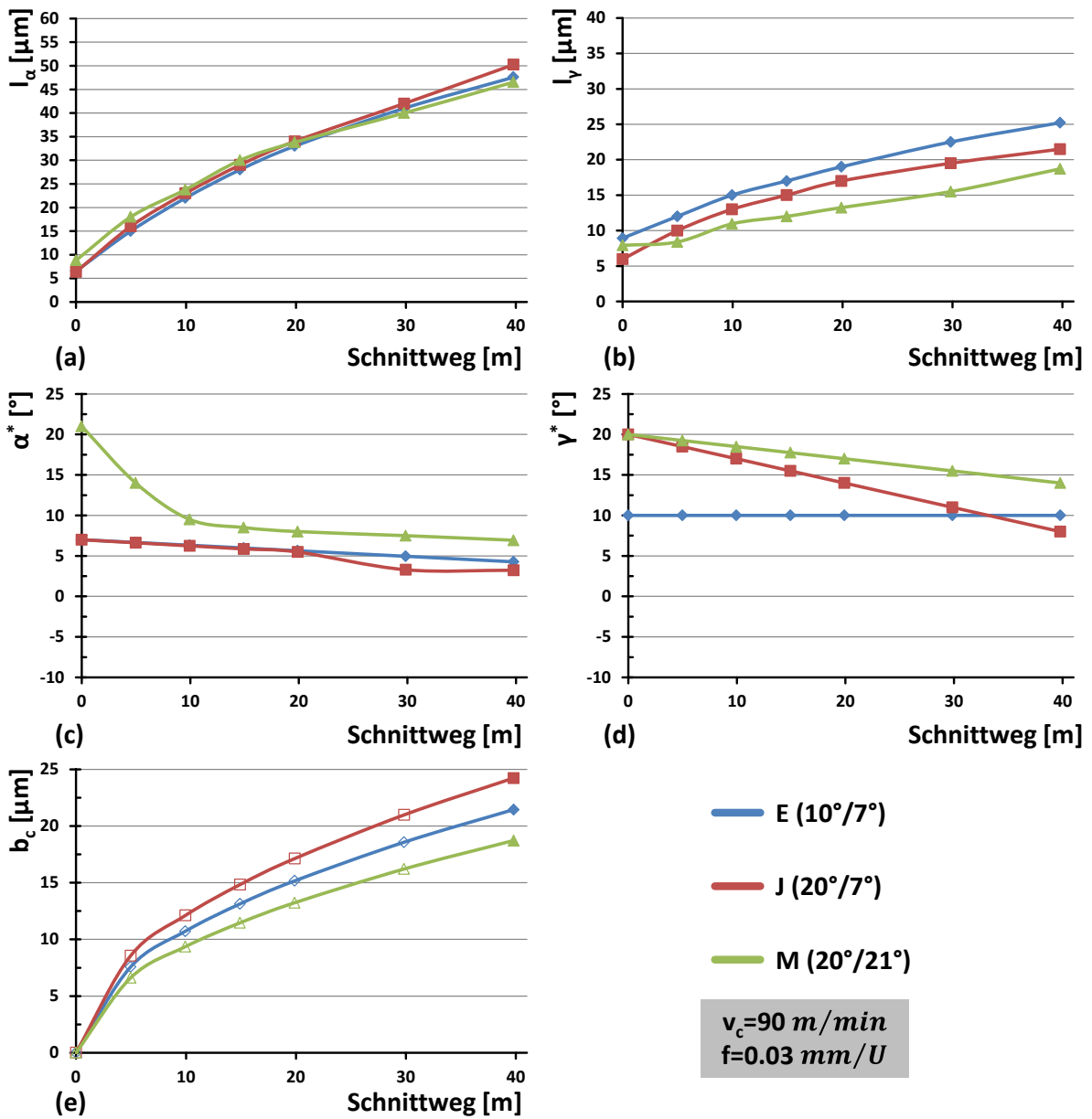
		Wear States		0	I	II	III	IV	V	VI
		Feed travel [mm]		0	0.25	0.5	0.75	1	1.5	2
		Cutting length [m]		0	5	10	15	20	30	40
Material	Tool	Parameter								
0°	E14B $\gamma=10^\circ/\alpha=7^\circ$	l_α		6.53	13.0	20.0	28.0	33.0	39.3	46.7
		l_γ		8.93	9.00	10.0	10.5	11.0	12.0	16.2
		b_c		/	2.28	3.23	3.95	4.56	5.59	6.45
		α^*		7.00	6.42	5.83	5.25	4.66	3.49	3.15
		γ^*		0.00	2.00	3.00	3.00	-1.00	-8.00	-10.0
	J14A $\gamma=20^\circ/\alpha=7^\circ$	l_α		7.27	15.00	20.88	25.50	30.09	39.00	45.65
		l_γ		6.10	7.50	9.00	10.50	10.92	12.40	13.17
		b_c		/	1.90	2.69	3.30	3.81	4.66	5.39
		α^*		7.00	6.65	6.30	5.95	5.60	4.90	4.20
		γ^*		20.00	17.67	15.33	13.00	10.67	8.33	6.00
	M14A $\gamma=20^\circ/\alpha=21^\circ$	l_α		8.54	9.50	11.50	13.50	15.50	20.83	30.00
		l_γ		8.14	8.62	9.09	9.57	10.04	10.99	11.94
		b_c		/	0.87	1.23	1.51	1.74	2.13	2.46
		α^*		21.00	15.25	9.50	9.18	8.87	8.23	7.60
		γ^*		20.00	17.50	15.00	12.50	10.00	5.00	0.00
30°	E11B** $\gamma=10^\circ/\alpha=7^\circ$	l_α		6.53	15.00	22.00	28.00	33.00	41.00	47.57
		l_γ		8.93	12.00	15.00	17.00	19.00	22.50	25.22
		b_c		/	7.58	10.73	13.14	15.17	18.58	21.45
		α^*		7.00	6.66	6.32	5.98	5.64	4.95	4.27
		γ^*		10.00	10.00	10.00	10.00	10.00	10.00	10.00
	J14B $\gamma=20^\circ/\alpha=7^\circ$	l_α		6.38	16.00	23.00	29.00	34.00	42.00	50.24
		l_γ		5.96	10.00	13.00	15.00	17.00	19.50	21.49
		b_c		/	8.57	12.12	14.84	17.13	20.98	24.23
		α^*		7.00	6.62	6.24	5.86	5.48	3.29	3.23
		γ^*		20.00	18.50	17.00	15.50	14.00	11.00	8.00
	M14B $\gamma=20^\circ/\alpha=21^\circ$	l_α		8.81	18.00	23.78	30.00	33.80	40.00	46.54
		l_γ		7.92	8.39	10.95	12	13.24	15.5	18.71
		b_c		/	6.62	9.36	11.46	13.24	16.21	18.72
		α^*		21.00	14.00	9.50	8.50	8.00	7.50	6.93
		γ^*		20.00	19.25	18.5	17.75	17.00	15.50	14.00
60°	E15A $\gamma=10^\circ/\alpha=7^\circ$	l_α		5.86	12.50	18.94	/	28.24	/	50.64
		l_γ		9.56	15.13	18.78	/	21.74	/	33.95
		b_c		/	7.64	10.80	/	15.27	/	21.60
		α^*		7.00	6.20	5.20	/	4.24	/	2.70
		γ^*		10.00	9.75	9.50	/	9.00	/	8.00

	J15A $\gamma=20^\circ/\alpha=7^\circ$	l_α		6.48	9.69	16.00	/	26.00	/	43.17
		l_γ		5.89	10.85	13.97	/	18.00	/	25.39
		b_c		/	7.05	9.97	/	14.10	/	19.94
		α^*		7.00	6.63	6.25	/	3.25	/	2.38
		γ^*		20.00	19.75	19.50	/	19.00	/	18.00
	M15A $\gamma=20^\circ/\alpha=21^\circ$	l_α		8.98	15.38	22.00	/	34.48	/	58.75
		l_γ		8.38	10.40	12.00	/	17.64	/	25.21
		b_c		/	2.13	3.01	/	4.26	/	6.02
		α^*		21.00	21.00	21.00	/	14.80	/	11.00
		γ^*		20.00	19.88	19.75	/	19.50	/	19.00
90°	E15B $\gamma=10^\circ/\alpha=7^\circ$	l_α		5.85	16.00	24.14	/	31.65	/	44.80
		l_γ		6.00	13.02	18.00	/	22.00	/	29.63
		b_c		/	5.24	7.41	/	10.47	/	14.81
		α^*		7.00	6.10	5.25	/	4.47	/	3.67
		γ^*		1.00	1.13	1.25	/	1.50	/	2.00
	J15B $\gamma=20^\circ/\alpha=7^\circ$	l_α		6.50	16.00	22.00	/	30.57	/	43.00
		l_γ		5.87	11.16	14.00	/	18.09	/	24.70
		b_c		/	4.37	6.18	/	8.73	/	12.35
		α^*		7.00	6.48	5.96	/	4.21	/	2.94
		γ^*		20.00	19.50	19.00	/	18.00	/	16.00
	M15B $\gamma=20^\circ/\alpha=21^\circ$	l_α		8.81	18.77	24.98	/	31.96	/	42.52
		l_γ		7.20	13.16	19.11	/	22.38	/	25.65
		b_c		/	0.71	1.00	/	1.41	/	2.00
		α^*		21.00	21.00	21.00	/	21.00	/	21.00
		γ^*		20.00	19.38	18.75	/	17.50	/	15.00
150°	H14A $\gamma=10^\circ/\alpha=14^\circ$	l_α		4.23	6.50	8.00	/	11.00	/	12.77
		l_γ		9.54	8.81	8.07	/	7.84	/	7.53
		b_c		/	0.00	0.00	/	0.00	/	0.00
		α^*		14.00	14.00	14.00	/	14.00	/	14.00
		γ^*		10.00	9.13	8.25	/	6.50	/	3.00
	I14B $\gamma=10^\circ/\alpha=21^\circ$	l_α		7.63	8.59	9.54	/	11.45	/	15.27
		l_γ		8.68	8.76	8.85	/	9.02	/	9.37
		b_c		/	0.00	0.00	/	0.00	/	0.00
		α^*		21.00	21.00	21.00	/	21.00	/	21.00
		γ^*		10.00	9.13	8.25	/	6.50	/	3.00
	L14B $\gamma=20^\circ/\alpha=14^\circ$	l_α		5.43	7.38	9.33	/	10.16	/	11.83
		l_γ		5.65	5.76	5.87	/	6.09	/	6.54
		b_c		/	0.08	0.12	/	0.17	/	0.24
		α^*		14.00	14.00	14.00	/	14.00	/	10.50
		γ^*		20.00	18.63	17.25	/	14.50	/	9.00

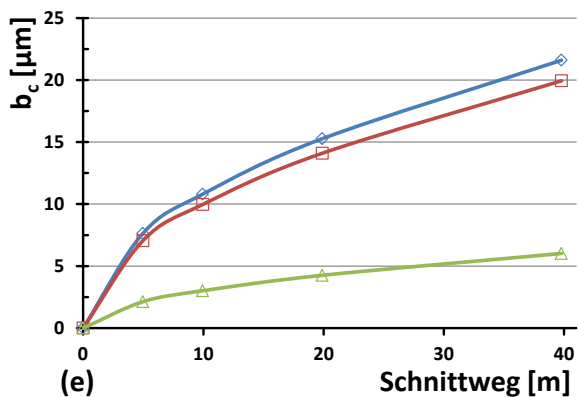
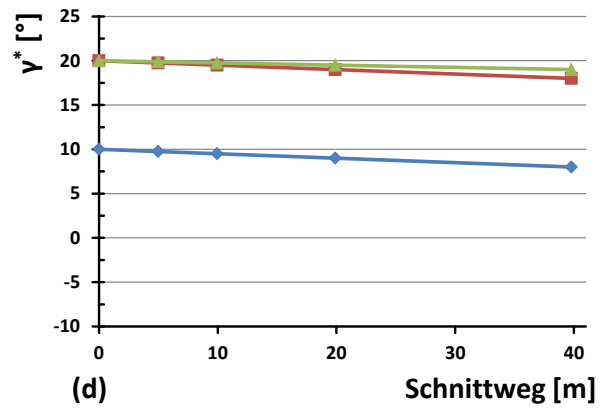
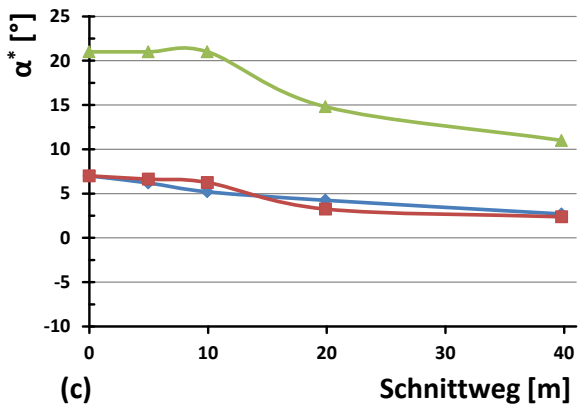
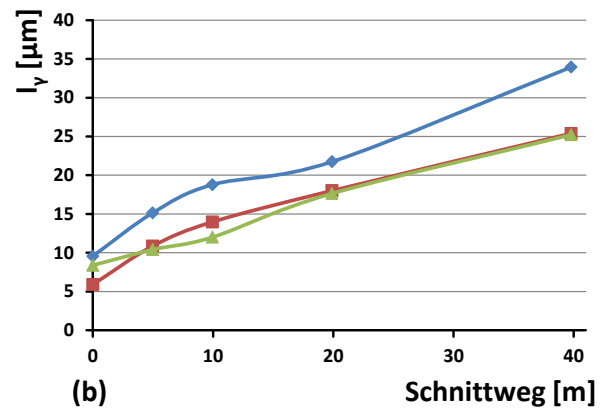
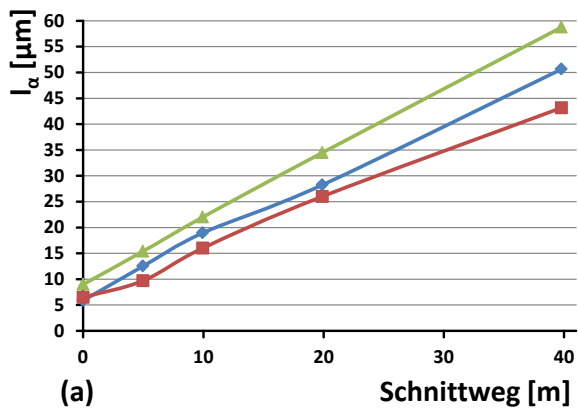
** different strategy: Without interrupting the process at different wear states → fitted data

A.2. Graphical evaluation of tool *micro-geometry* for $\theta=0^\circ$ Tool micro-geometry for $\theta=0^\circ$ 

Tool micro-geometry for $\theta=30^\circ$



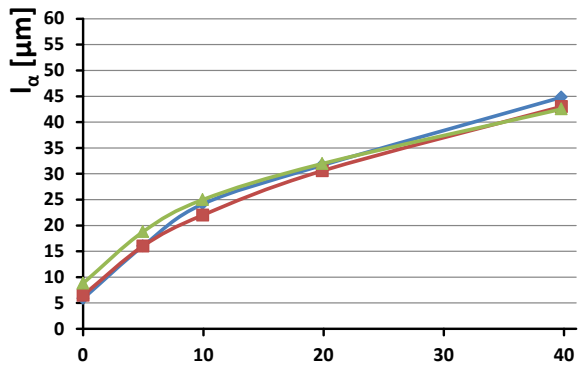
Tool micro-geometry for $\theta=60^\circ$



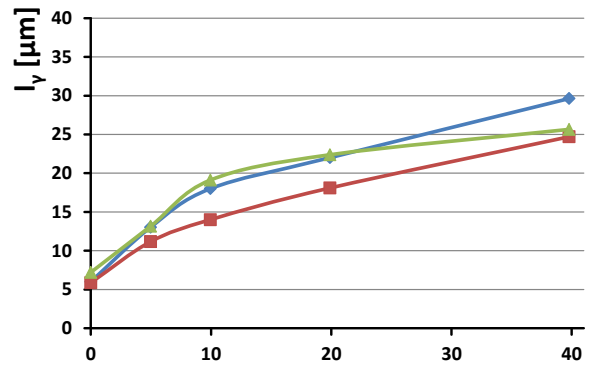
- E (10°/7°)
- J (20°/7°)
- M (20°/21°)

$v_c = 90 \text{ m/min}$
 $f = 0.03 \text{ mm/U}$

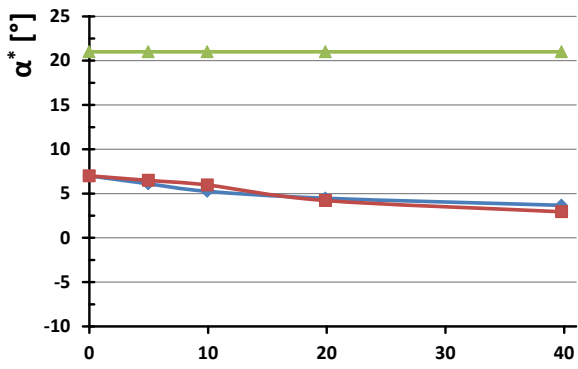
Tool micro-geometry for $\theta=90^\circ$



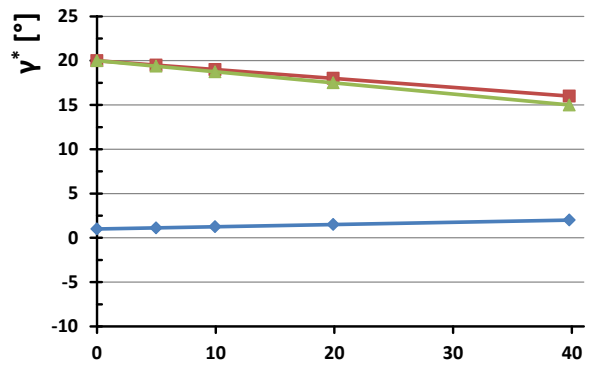
(a)



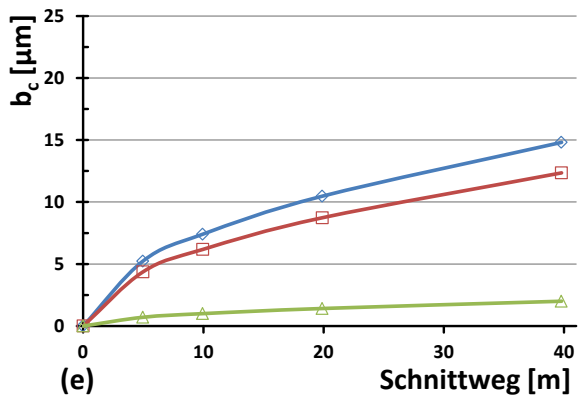
(b)



(c)



(d)

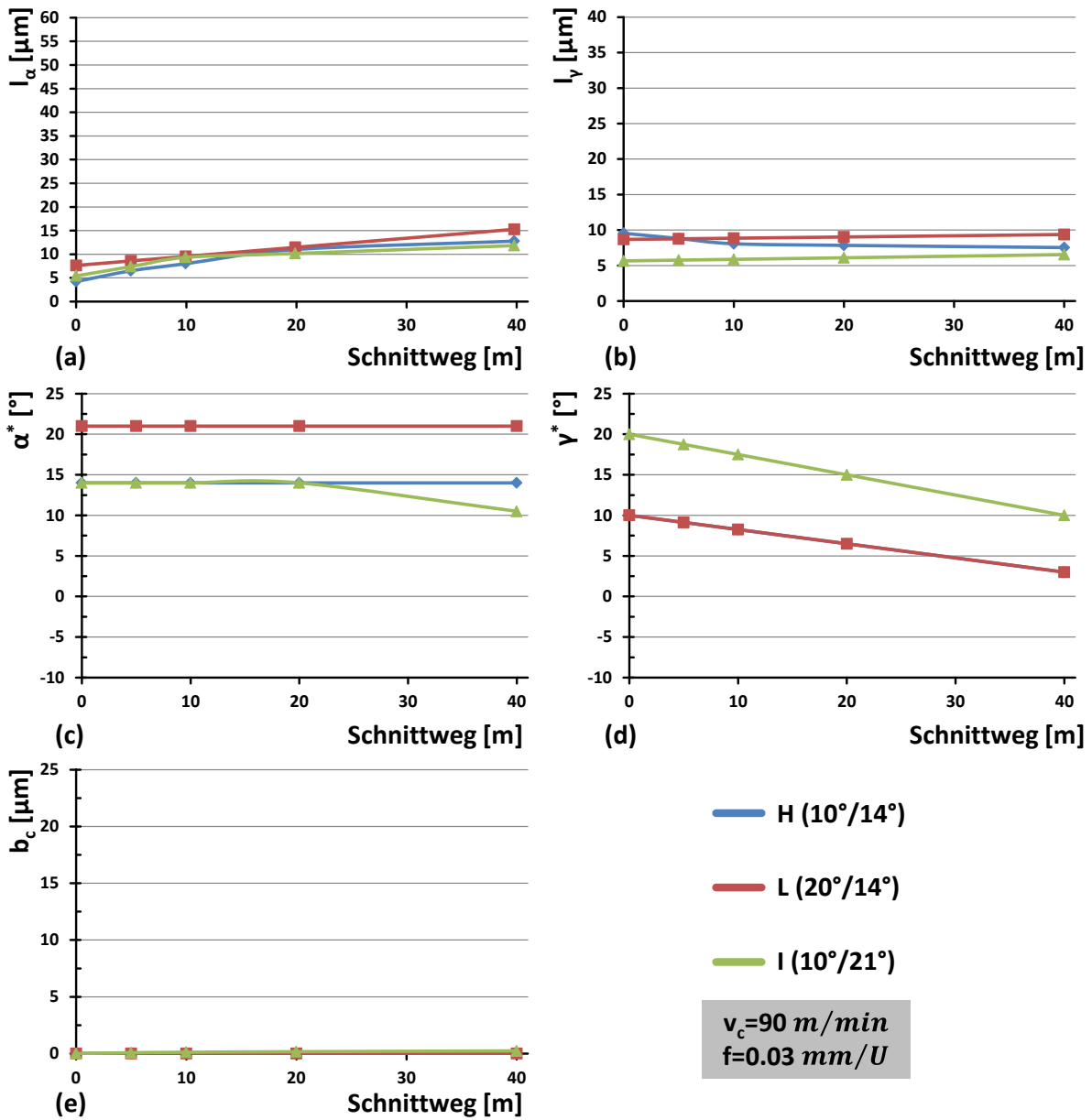


(e)

—◆— E ($10^\circ/7^\circ$)
—■— J ($20^\circ/7^\circ$)
—▲— M ($20^\circ/21^\circ$)

 $v_c=90 \text{ m/min}$
 $f=0.03 \text{ mm/U}$

Tool micro-geometry for $\theta=150^\circ$

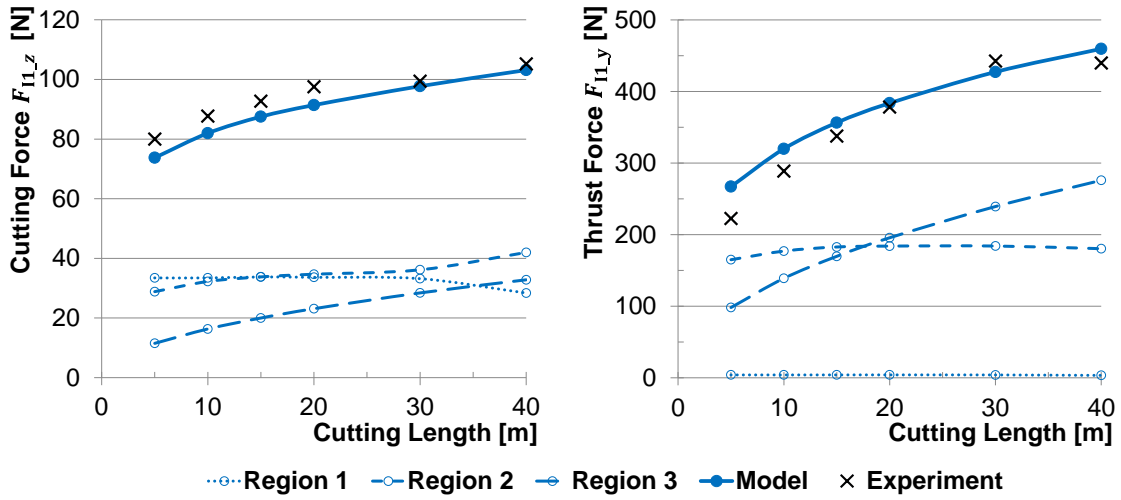


A.3. Material properties, process parameters and fitting variables of the force model according to [104, 106, 177, 189, 257]

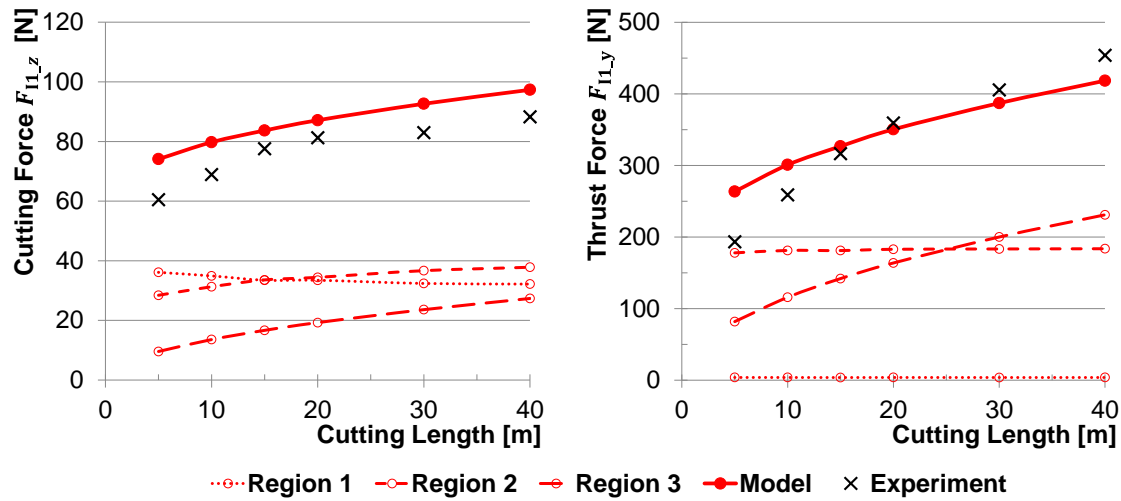
Material Properties			
Carbon Fibre		Epoxy Matrix	
Designation	IMA-12k	Designation	M21/34%
<i>Young's Modulus (axial) – E_{f1}</i>	297 GPa	<i>Young's Modulus – E_{m_0}</i>	3.5 GPa
<i>Young's Modulus (transv.) – E_{f2}</i>	15 GPa	<i>Shear modulus – G_m</i>	1.02 GPa
<i>Shear modulus – G_f</i>	8.96 GPa	<i>Poisson's ratio – ν_m</i>	0.318
<i>Poisson's ratio – ν_f</i>	0.2	<i>Shear strength – τ_c</i>	62 MPa
<i>Fibre volume fraction – V_f</i>	0.592	<i>Bonding WINKLER konstant - k_b</i>	115 GPa/m
<i>Fibre radius – r_f</i>	3.5 μm		
<i>Tensile strength – σ_{T_f0}</i>	4900 MPa		
Divers			
<i>Friction coefficient – μ</i>	0.12	<i>Radius of RVE – r_{fm}</i>	5.85 μm
<i>Parameter for matrix slippage – ξ</i>	0.02		
<i>Parameter for interfacial fibre-matrix bonding – η</i>	1.98		
Process Parameters			
<i>Cutting speed – v_c</i>	90 m/min	<i>Feed rate – f</i>	30 $\mu\text{m/rot}$
Fitting Variables			
<i>Correction factor micro-buckling – K_f</i>	0.33	<i>Factor tensile fibre strength– $K_{\sigma_{Tf}}$</i>	3.5
<i>Height sub-region 2.2 (in I1) – $H_{2.2}$</i>	2.625 μm	<i>Fitted compr. fibre strength – $\sigma_{Pr_{cr}}$</i>	8500 MPa
<i>Young's Modulus CFRP region 2 – E_{c2}</i>	17 GPa	<i>Factor Young's modulus matrix – K_{Em}</i>	3
<i>Young's Modulus CFRP region 3 – E_{c3}</i>	17 GPa		
<i>Cushion factor of elastic foundation (in I2) – k_{cush}</i>	3.414		
<i>Critical deflection of fibre (in I3) – $\omega_{z'_{cr}}$</i>	0.26 μm		
<i>normalized elastic foundation factor (in I4) – \hat{k}</i>	0.1085 MPa		

A.4. Simulated process forces over cutting length for $\theta=0^\circ$

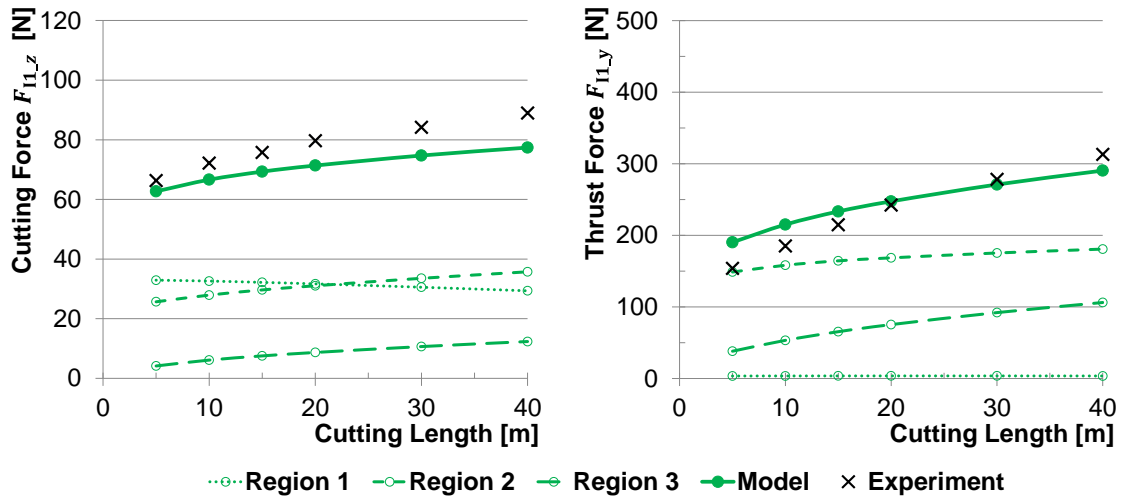
Tool E ($10^\circ/7^\circ$) – Sub-Model $\theta=0^\circ$ (I)



Tool J ($20^\circ/7^\circ$) – Sub-Model $\theta=0^\circ$ (I)

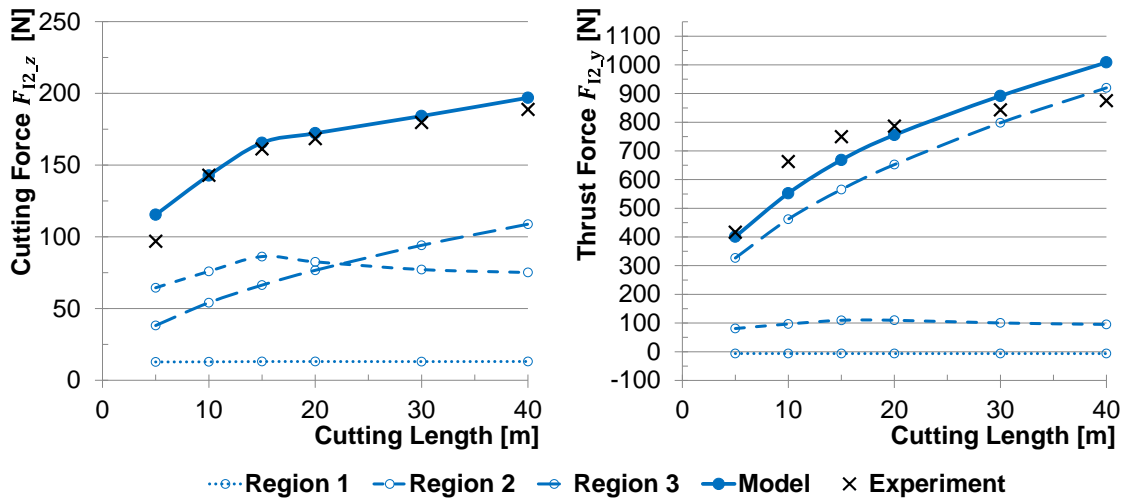


Tool M ($20^\circ/21^\circ$) – Sub-Model $\theta=0^\circ$ (I)

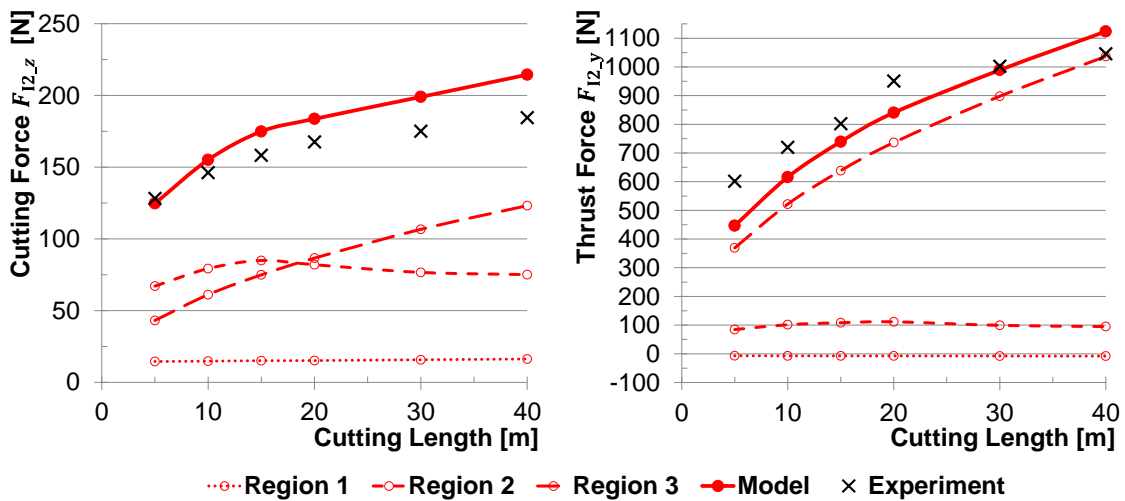


A.5. Simulated process forces over cutting length for $\theta=30^\circ$

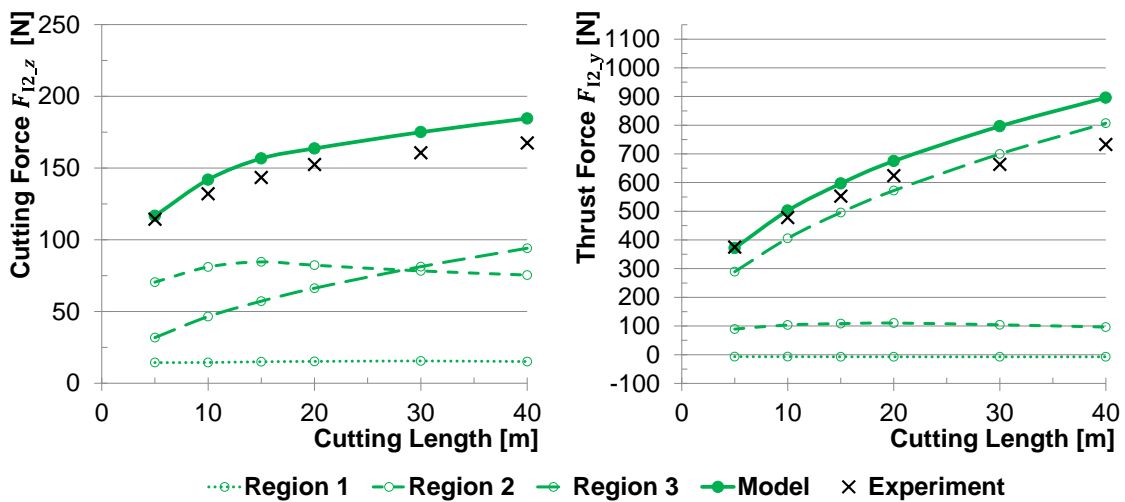
Tool E ($10^\circ/7^\circ$) – Sub-Model $15^\circ \leq \theta \leq 75^\circ$ (II) ($\theta=30^\circ$)



Tool J ($20^\circ/7^\circ$) – Sub-Model $15^\circ \leq \theta \leq 75^\circ$ (II) ($\theta=30^\circ$)

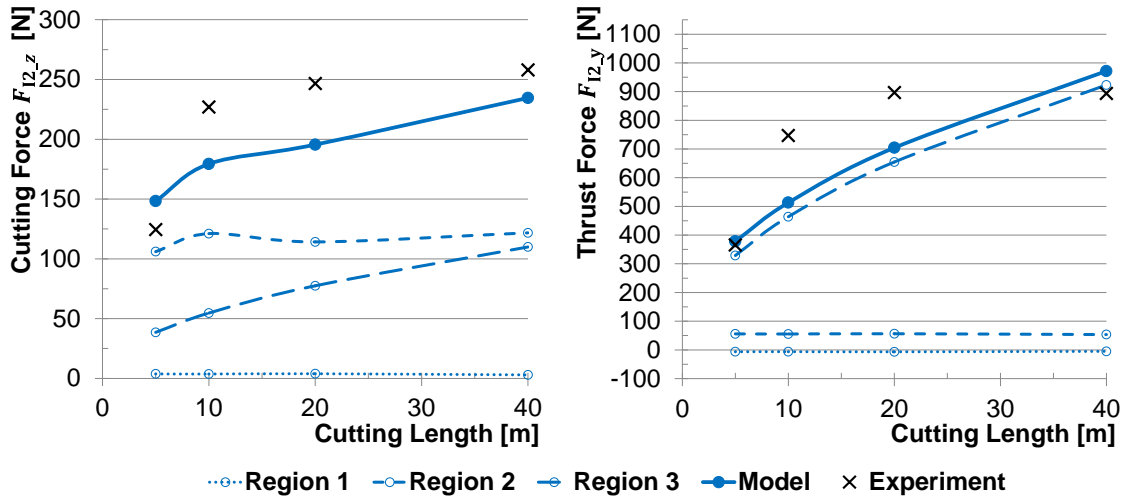


Tool M ($20^\circ/21^\circ$) – Sub-Model $15^\circ \leq \theta \leq 75^\circ$ (II) ($\theta=30^\circ$)

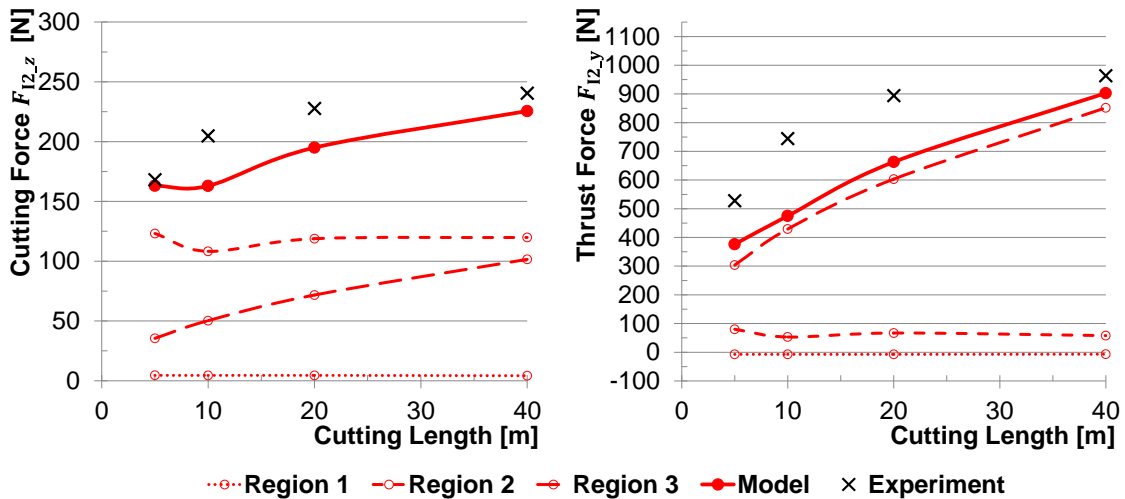


A.6. Simulated process forces over cutting length for $\theta=60^\circ$

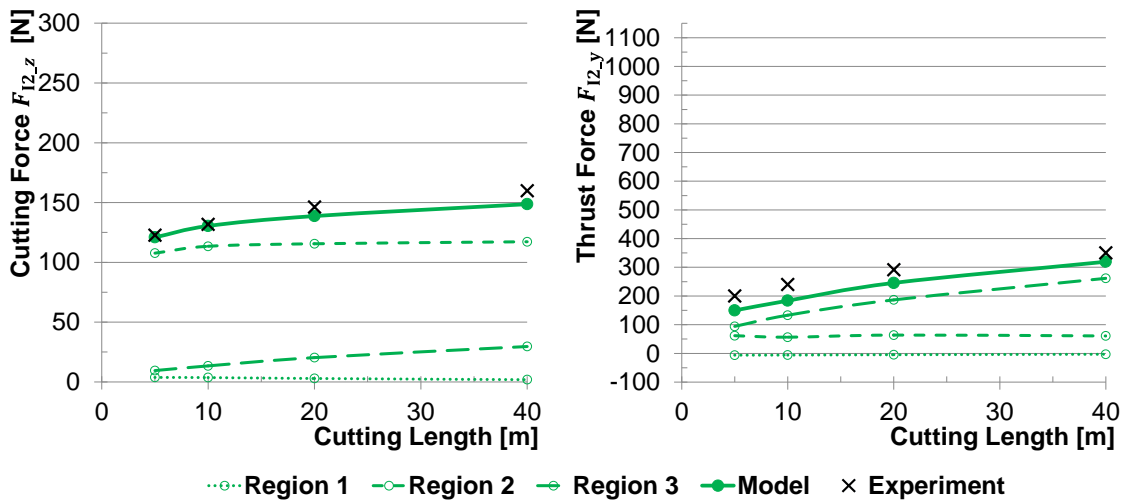
Tool E ($10^\circ/7^\circ$) – Sub-Model $15^\circ \leq \theta \leq 75^\circ$ (II) ($\theta=60^\circ$)



Tool J ($20^\circ/7^\circ$) – Sub-Model $15^\circ \leq \theta \leq 75^\circ$ (II) ($\theta=60^\circ$)

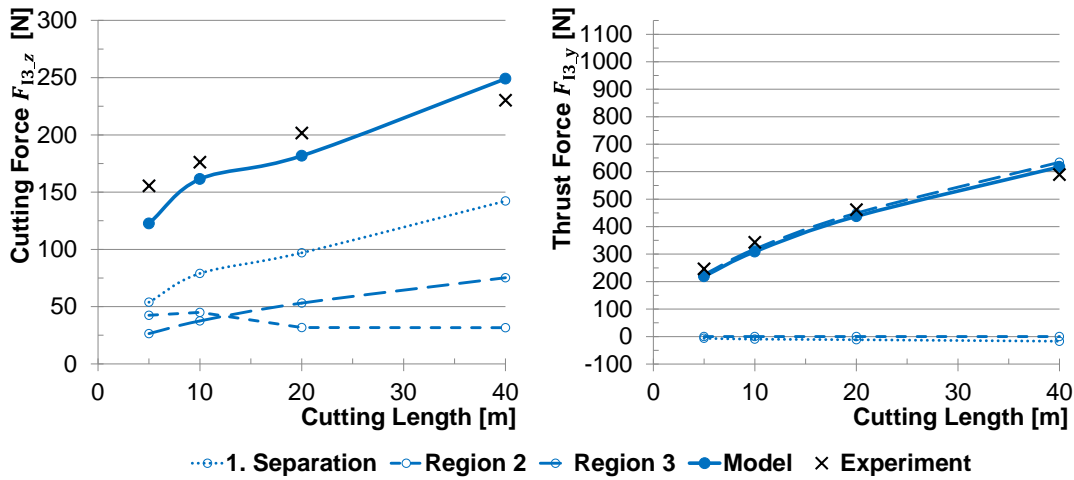


Tool M ($20^\circ/21^\circ$) – Sub-Model $15^\circ \leq \theta \leq 75^\circ$ (II) ($\theta=60^\circ$)

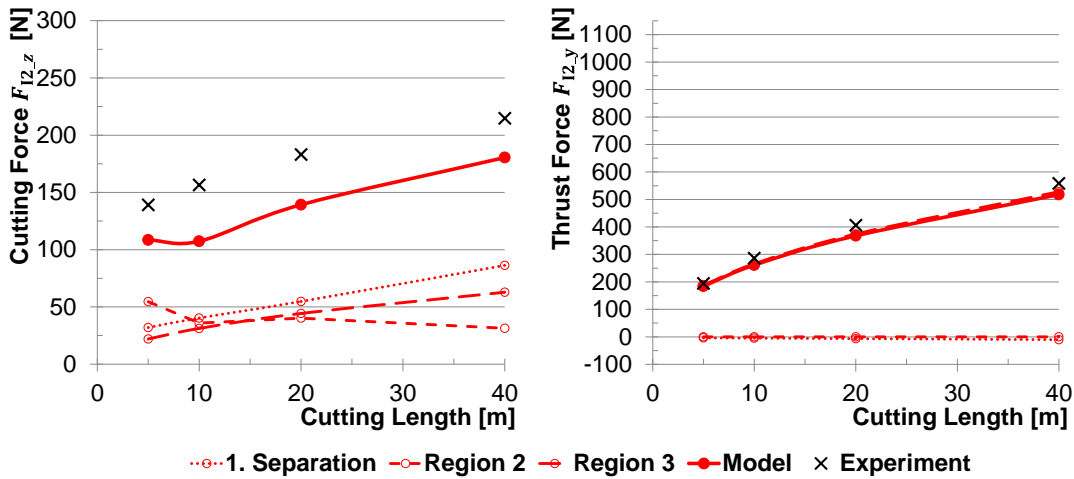


A.7. Simulated process forces over cutting length for $\theta=90^\circ$

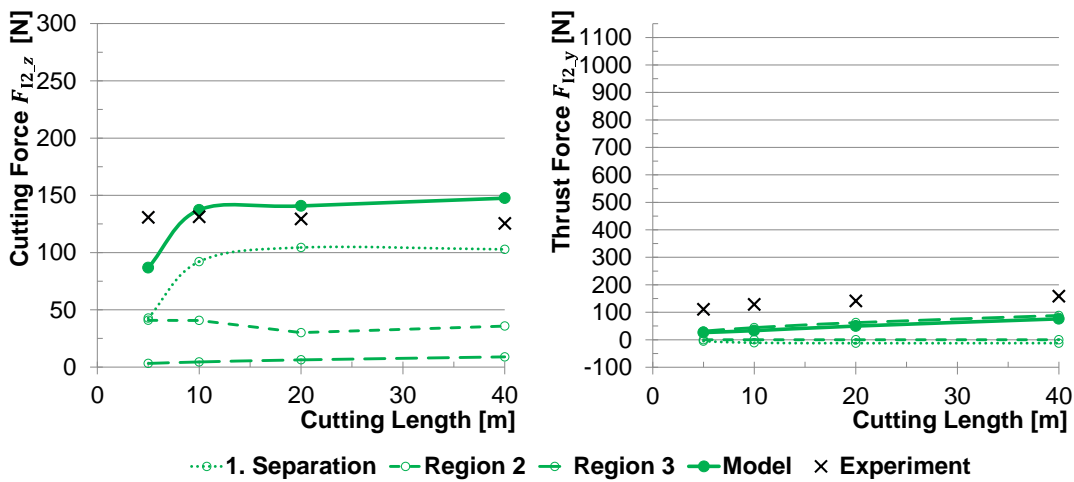
Tool E ($10^\circ/7^\circ$) – Sub-Model $\theta=90^\circ$ (III)



Tool J ($20^\circ/7^\circ$) – Sub-Model $\theta=90^\circ$ (III)

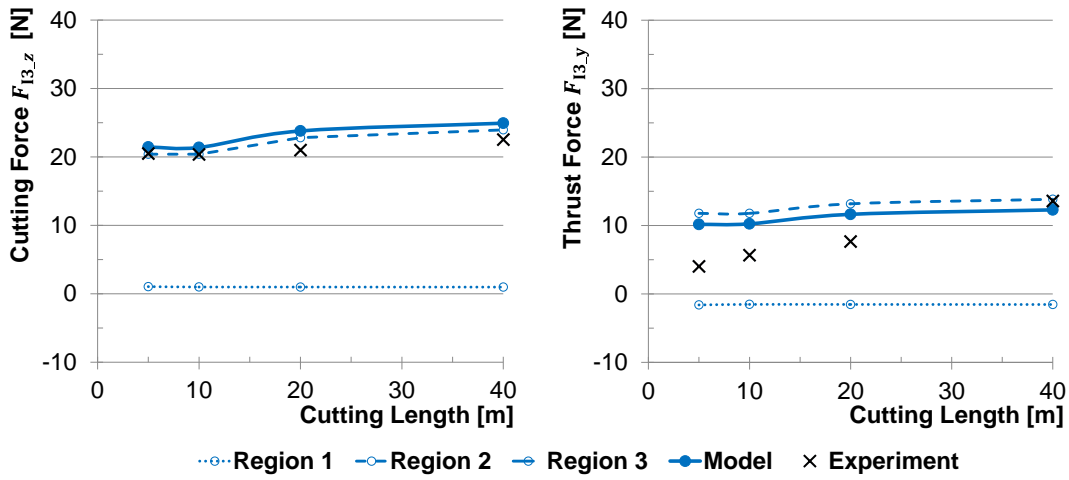


Tool M ($20^\circ/21^\circ$) – Sub-Model $\theta=90^\circ$ (III)

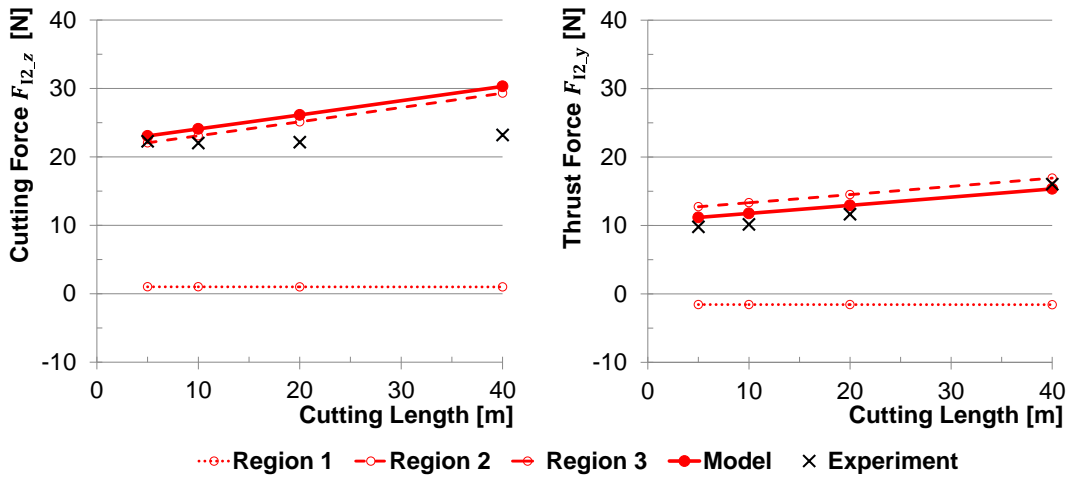


A.8. Simulated process forces over cutting length for $\theta=150^\circ$

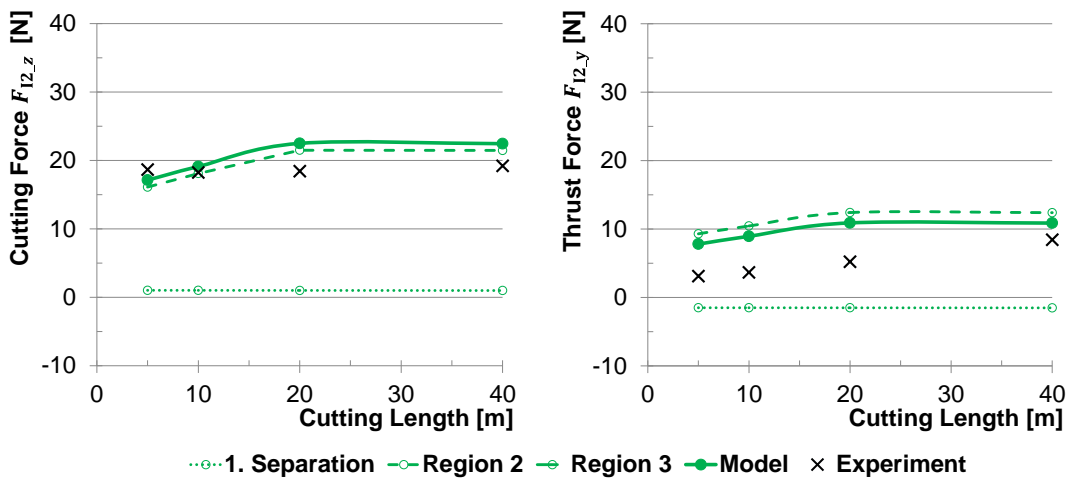
Tool H (10°/14°) – Sub-Model $\theta=150^\circ$ (IV)



Tool I (10°/21°) – Sub-Model $\theta=150^\circ$ (IV)



Tool L (20°/14°) – Sub-Model $\theta=150^\circ$ (IV)



A.9. Parameters for use in (95) and (97), according to PILKEY [172] (Part I)

A/B	n_a	n_b	n_c	n_d
1.000000	1.000000	1.000000	1.000000	1.000000
0.965467	1.013103	0.987137	0.999929	0.999952
0.928475	1.025571	0.975376	0.999684	0.999714
0.893098	1.038886	0.963238	0.999306	0.999279
0.851780	1.055557	0.948729	0.998565	0.998574
0.805934	1.075967	0.931815	0.997404	0.997442
0.767671	1.094070	0.917565	0.996134	0.996124
0.727379	1.114909	0.901981	0.994404	0.994407
0.699686	1.130480	0.890831	0.992984	0.992988
0.640487	1.166370	0.866782	0.989130	0.989123
0.594383	1.198061	0.847158	0.985274	0.985223
0.546919	1.234696	0.826174	0.980321	0.980224
0.514760	1.262333	0.811413	0.976303	0.976163
0.465921	1.309532	0.788097	0.968956	0.968738
0.416913	1.364990	0.763293	0.959796	0.959415
0.384311	1.407560	0.745894	0.952481	0.951928
0.351726	1.455592	0.727797	0.943952	0.943170
0.335659	1.481904	0.718443	0.939264	0.938324
0.319620	1.510007	0.708906	0.934183	0.933087
0.303612	1.540072	0.699179	0.928689	0.927396
0.287810	1.572253	0.689231	0.922811	0.921331
0.272153	1.606769	0.679051	0.916524	0.914773
0.264330	1.625029	0.673890	0.913167	0.911272
0.256632	1.643925	0.668646	0.909749	0.907690
0.241289	1.684020	0.658001	0.902457	0.900066
0.233648	1.705308	0.652595	0.898573	0.895998
0.226114	1.727405	0.647099	0.894613	0.891797
0.218611	1.750463	0.641548	0.890467	0.887432
0.211182	1.774490	0.635922	0.886181	0.882914
0.203782	1.799603	0.630236	0.881699	0.878199
0.196453	1.825817	0.624468	0.877067	0.873296
0.189191	1.853208	0.618615	0.872278	0.868186
0.182010	1.881858	0.612675	0.867328	0.862885
0.174887	1.911914	0.606661	0.862155	0.857378
0.167809	1.943479	0.600570	0.856755	0.851609
0.153928	2.011419	0.588084	0.845392	0.839398
0.147127	2.048051	0.581680	0.839412	0.832932

A.10. Parameters for use in (95) and (97), according to PILKEY [172] (Part II)

A/B	n_a	n_b	n_c	n_d
0.140401	2.086717	0.575179	0.833169	0.826193
0.133739	2.127590	0.568576	0.826653	0.819118
0.120723	2.216622	0.555000	0.812859	0.804111
0.114362	2.265238	0.548013	0.805555	0.796099
0.108093	2.316993	0.540894	0.797927	0.787713
0.095880	2.431163	0.526202	0.781687	0.769785
0.084137	2.562196	0.510823	0.764043	0.750170
0.078432	2.635404	0.502862	0.754578	0.739598
0.067433	2.800291	0.486269	0.734380	0.716896
0.056978	2.996047	0.468688	0.712143	0.691708
0.047131	3.232638	0.449900	0.687586	0.663652
0.043365	3.341996	0.442004	0.676968	0.651460
0.039714	3.461481	0.433842	0.665896	0.638702
0.036174	3.592781	0.425404	0.654286	0.625283
0.034451	3.663353	0.421060	0.648302	0.618329
0.031090	3.816109	0.412142	0.635818	0.603838
0.029457	3.898845	0.407545	0.629345	0.596298
0.026283	4.079175	0.398062	0.615852	0.580534
0.024745	4.177734	0.393165	0.608814	0.572309
0.023243	4.282607	0.388149	0.601581	0.563839
0.021771	4.394598	0.383020	0.594100	0.555076
0.020340	4.514196	0.377744	0.586438	0.546068
0.017583	4.780675	0.366775	0.570311	0.527108
0.016262	4.929675	0.361046	0.561848	0.517130
0.014980	5.091023	0.355138	0.553092	0.506793
0.013737	5.266621	0.349046	0.543983	0.496048
0.012536	5.458381	0.342741	0.534527	0.484885
0.011377	5.668799	0.336203	0.524695	0.473265
0.010261	5.901168	0.329419	0.514415	0.461124
0.009191	6.159118	0.322351	0.503678	0.448458
0.008168	6.447475	0.314966	0.492433	0.435174
0.007192	6.772417	0.307225	0.480617	0.421232
0.006266	7.142177	0.299092	0.468127	0.406537
0.005391	7.567233	0.290498	0.454903	0.391004
0.004570	8.062065	0.281372	0.440832	0.374507
0.003805	8.647017	0.271621	0.425766	0.356910